Publishing House ASV

begell house, inc. publishers

PAACH

Scientific coordination is carried out by the Russian Academy of Architecture and Construction Sciences (RAACS)

Volume 19 • Issue 1 • 2023

ISSN 2588-0195 (Online)
ISSN 2587-9618 (Print) Continues ISSN 1524-5845

International Journal for

Computational Civil and Structural Engineering

Международный журнал по расчету гражданских и строительных конструкций

http://raasn.ru/public.php
http://ijccse.iasv.ru/index.php/IJCCSE

DOI: 10.22337/2587-9618
GICID: 71.0000.1500.2830

PUBLISHER

ASV Publishing House
(ООО «Издательство АСВ»)
19/1,12, Yaroslavskoe Shosse, 120338, Moscow, Russia
Tel. +7(925)084-74-24; E-mail: iasv@iasv.ru; Интернет-сайт: http://iasv.ru/

ADVISORY EDITORIAL BOARD

TECHNICAL EDITOR

EDITORIAL TEAM

INVITED REVIEWERS

AIMS AND SCOPE

The aim of the Journal is to advance the research and practice in structural engineering through the application of computational methods. The Journal will publish original papers and educational articles of general value to the field that will bridge the gap between high-performance construction materials, large-scale engineering systems and advanced methods of analysis.

The scope of the Journal includes papers on computer methods in the areas of structural engineering, civil engineering materials and problems concerned with multiple physical processes interacting at multiple spatial and temporal scales. The Journal is intended to be of interest and use to researches and practitioners in academic, governmental and industrial communities.

ОБЩАЯ ИНФОРМАЦИЯ О ЖУРНАЛЕ

International Journal for Computational Civil and Structural Engineering

(Международный журнал по расчету гражданских и строительных конструкций)

Международный научный журнал "International Journal for Computational Civil and Structural Engineering (Международный журнал по расчету гражданских и строительных конструкций)" (IJCCSE) является ведущим научным периодическим изданием по направлению «Инженерные и технические науки», издаваемым, начиная с 1999 года (ISSN 2588-0195 (Online); ISSN 2587-9618 (Print) Continues ISSN 1524-5845). В журнале на высоком научно-техническом уровне рассматриваются проблемы численного и компьютерного моделирования в строительстве, актуальные вопросы разработки, исследования, развития, верификации, апробации и приложений численных, численно-аналитических методов, программно-алгоритмического обеспечения и выполнения автоматизированного проектирования, мониторинга и комплексного наукоемкого расчетно-теоретического и экспериментального обоснования напряженно-деформированного (и иного) состояния, прочности, устойчивости, надежности и безопасности ответственных объектов гражданского и промышленного строительства, энергетики, машиностроения, транспорта, биотехнологий и других высокотехнологичных отраслей.

В редакционный совет журнала входят известные российские и зарубежные деятели науки и техники (в том числе академики, члены-корреспонденты, иностранные члены, почетные члены и советники Российской академии архитектуры и строительных наук). Основной критерий отбора статей для публикации в журнале − их высокий научный уровень, соответствие которому определяется в ходе высококвалифицированного рецензирования и объективной экспертизы, поступающих в редакцию материалов.

Журнал входит в Перечень ВАК РФ ведущих рецензируемых научных изданий, в которых должны быть опубликованы основные научные результаты диссертаций на соискание ученой степени кандидата наук, на соискание ученой степени доктора наук по научным специальностям и соответствующим им отраслям науки:

- 1.1.8 – Механика деформируемого твердого тела (технические науки),
- 1.2.2 – Математическое моделирование численные методы и комплексы программ (технические науки),
- 2.1.1 – Строительные конструкции, здания и сооружения (технические науки),
- 2.1.2 – Основания и фундаменты, подземные сооружения (технические науки),
- 2.1.5 – Строительные материалы и изделия (технические науки),
- 05.23.07 – Гидротехническое строительство (технические науки),
- 2.1.9 – Строительная механика (технические науки)

В Российской Федерации журнал индексируется Российским индексом научного цитирования (РИНЦ).

Журнал входит в базу данных Russian Science Citation Index (RSCI), полностью интегрированную с платформой Web of Science. Журнал имеет международный статус и высылается в ведущие библиотеки и научные организации мира.

Издатели журнала – *Издательство Ассоциации строительных высших учебных заведений /АСВ/* (Россия, г. Москва) и до 2017 года *Издательский дом Begell House Inc*. (США, г. Нью-Йорк). Официальными партнерами издания является *Российская академия архитектуры и строительных наук* (РААСН), осуществляющая научное курирование издания, и *Научно-исследовательский центр СтаДиО* (ЗАО НИЦ СтаДиО).

Цели журнала – демонстрировать в публикациях российскому и международному профессиональному сообществу новейшие достижения науки в области вычислительных методов

решения фундаментальных и прикладных технических задач, прежде всего в области строительства.

Задачи журнала:

• предоставление российским и зарубежным ученым и специалистам возможности публиковать результаты своих исследований;

• привлечение внимания к наиболее актуальным, перспективным, прорывным и интересным направлениям развития и приложений численных и численно-аналитических методов решения фундаментальных и прикладных технических задач, совершенствования технологий математического, компьютерного моделирования, разработки и верификации реализующего программно-алгоритмического обеспечения;

• обеспечение обмена мнениями между исследователями из разных регионов и государств.

Тематика журнала. К рассмотрению и публикации в журнале принимаются аналитические материалы, научные статьи, обзоры, рецензии и отзывы на научные публикации по фундаментальным и прикладным вопросам технических наук, прежде всего в области строительства. В журнале также публикуются информационные материалы, освещающие научные мероприятия и передовые достижения Российской академии архитектуры и строительных наук, научно-образовательных и проектно-конструкторских организаций.

Тематика статей, принимаемых к публикации в журнале, соответствует его названию и охватывает направления научных исследований в области разработки, исследования и приложений численных и численно-аналитических методов, программного обеспечения, технологий компьютерного моделирования в решении прикладных задач в области строительства, а также соответствующие профильные специальности, представленные в диссертационных советах профильных образовательных организациях высшего образования.

Редакционная политика. Политика редакционной коллегии журнала базируется на современных юридических требованиях в отношении авторского права, законности, плагиата и клеветы, изложенных в законодательстве Российской Федерации, и этических принципах, поддерживаемых сообществом ведущих издателей научной периодики.

За публикацию статей плата с авторов не взымается. Публикация статей в журнале бесплатная. На платной основе в журнале могут быть опубликованы материалы рекламного характера, имеющие прямое отношение к тематике журнала.

Журнал предоставляет непосредственный открытый доступ к своему контенту, исходя из следующего принципа: свободный открытый доступ к результатам исследований способствует увеличению глобального обмена знаниями.

Индексирование. Публикации в журнале входят в системы расчетов индексов цитирования авторов и журналов. «Индекс цитирования» – числовой показатель, характеризующий значимость данной статьи и вычисляющийся на основе последующих публикаций, ссылающихся на данную работу.

Авторам. Прежде чем направить статью в редакцию журнала, авторам следует ознакомиться со всеми материалами, размещенными в разделах сайта журнала (интернет-сайт Российской академии архитектуры и строительных наук (http://raasn.ru); подраздел «Издания РААСН» или интернет-сайт Издательства АСВ (http://iasv.ru); подраздел «Журнал IJCCSE»): с основной информацией о журнале, его целями и задачами, составом редакционной коллегии и редакционного совета, редакционной политикой, порядком рецензирования направляемых в журнал статей, сведениями о соблюдении редакционной этики, о политике авторского права и лицензирования, о представлении журнала в информационных системах (индексировании), информацией о подписке на журнал, контактными данными и пр. Журнал работает по лицензии Creative Commons типа cc by-nc-sa (Attribution Non-Commercial Share Alike) – Лицензия «С указанием авторства – Некоммерческая – Копилефт».

Рецензирование. Все научные статьи, поступившие в редакцию журнала, проходят обязательное двойное слепое рецензирование (рецензент не знает авторов рукописи, авторы рукописи не знают рецензентов).

Заимствования и плагиат. Редакционная коллегия журнала при рассмотрении статьи проводит проверку материала с помощью системы «Антиплагиат». В случае обнаружения многочисленных заимствований редакция действует в соответствии с правилами COPE.

Подписка. Журнал зарегистрирован в Федеральном агентстве по средствам массовой информации и охраны культурного наследия Российской Федерации. Индекс в общероссийском каталоге РОСПЕЧАТЬ − 18076.

По вопросам подписки на международный научный журнал “International Journal for Computational Civil and Structural Engineering (Международный журнал по расчету гражданских и строительных конструкций)” обращайтесь в Агентство «Роспечать» (Официальный сайт в сети Интернет: http://www.rosp.ru/) или в издательство Ассоциации строительных вузов (АСВ) в соответствии со следующими контактными данными:

ООО «Издательство АСВ»

Юридический адрес: 129337, Россия, г. Москва, Ярославское ш., д. 26, офис 705;

Фактический адрес: 129337, Россия, г. Москва, Ярославское ш., д. 19, корп. 1, 5 этаж, офис 12 (ТЦ Соле Молл);

Телефоны: +7 (925) 084-74-24, +7 (926) 010-91-33;

Интернет-сайт: www.iasv.ru. Адрес электронной почты: iasv@iasv.ru.

Контактная информация. По всем вопросам работы редакции, рецензирования, согласования правки текстов и публикации статей следует обращаться к главному редактору журнала члену-корреспонденту РААСН *Сидорову Владимиру Николаевичу* (адреса электронной почты: sidorov.vladimir@gmail.com, sidorov@iasv.ru, iasv@iasv.ru, sidorov@raasn.ru) или к техническому редактору журнала советнику РААСН *Кайтукову Таймуразу Батразовичу* (адреса электронной почты: tkaytukov@gmail.com; kaytukov@raasn.ru). Кроме того, по указанным вопросам, а также по вопросам размещения в журнале рекламных материалов можно обращаться к генеральному директору ООО «Издательство АСВ» *Никитиной Надежде Сергеевне* (адреса электронной почты: iasv@iasv.ru, nsnikitina@mail.ru, ijccse@iasv.ru).

Журнал становится технологичнее. Издательство АСВ с сентября 2016 года является членом Международной ассоциации издателей научной литературы (Publishers International Linking Association (PILA)), осуществляющей свою деятельность на платформе CrossRef. Оригинальным статьям, публикуемым в журнале, будут присваиваться уникальные номера (индексы DOI – Digital Object Identifier), что значительно облегчит поиск метаданных и местонахождение полнотекстового произведения. DOI – это система определения научного контента в сети Интернет.

С октября 2016 года стал возможен прием статей на рассмотрение и рецензирование через онлайн систему приема статей Open Journal Systems на сайте журнала (электронная редакция): http://ijccse.iasv.ru/index.php/IJCCSE.

Автор имеет возможность следить за продвижением статьи в редакции журнала в личном кабинете Open Journal Systems и получать соответствующие уведомления по электронной почте.

В феврале 2018 года журнал был зарегистрирован в Directory of open access journals (DOAJ) (это один из самых известных поисковых сервисов в мире, который предоставляет открытый доступ к материалам и индексирует не только заголовки журналов, но и научные статьи), в сентябре 2018 года включен в продукты EBSCO Publishing.

В ноябре 2020 года журнал начал индексироваться в международной базе Scopus.

International Journal for
Computational Civil and Structural Engineering
(Международный журнал по расчету гражданских и строительных конструкций)
Volume 19, Issue 1 ***2023***

Scientific coordination is carried out by the Russian Academy of Architecture and Construction Sciences (RAACS)

CONTENTS

International Journal for
Computational Civil and Structural Engineering
(Международный журнал по расчету гражданских и строительных конструкций)
Volume 19, Issue 1 ***2023***

Scientific coordination is carried out by the Russian Academy of Architecture and Construction Sciences (RAACS)

СОДЕРЖАНИЕ

DOI:10.22337/2587-9618-2023-19-1-14-22

HYDRODYNAMIC STABILITY OF SWIRLING FLOWS WITH AXIAL RECIRCULATION ZONES

Vadim K. Akhmetov
Moscow State University of Civil Engineering, Moscow, RUSSIA

Abstact. The problem of the motion of a viscous incompressible swirling flow in an axisymmetric channel has been numerically investigated. Various flow regimes have been obtained, including those with the formation of the axial recirculation zones. In the framework of linear theory, the stability of the obtained calculated flows with respect to non-axisymmetric perturbations is investigated on the assumption of local parallelism. The growth rates and phase velocities of unstable disturbances are calculated. In the presence of a reverse flow zone, the disturbances growth rates are increased significantly.

Keywords: theory of hydrodynamic stability, swirling flows, growth rates factors, phase velocities

ГИДРОДИНАМИЧЕСКАЯ УСТОЙЧИВОСТЬ ЗАКРУЧЕННЫХ ПОТОКОВ С ПРИОСЕВЫМИ ЗОНАМИ РЕЦИРКУЛЯЦИИ

В.К. Ахметов
Национальный исследовательский Московский государственный строительный университет, г. Москва, РОССИЯ

Аннотация. Численно исследована задача о движении закрученного потока вязкой несжимаемой жидкости в осесимметричном канале. Получены различные режимы течений, в том числе с образованием приосевых рециркуляционных зон. В рамках линейной теории на основе гипотезы локальной параллельности потока исследована задача об устойчивости полученных расчетных течений по отношению к неосесимметричным возмущениям. Рассчитаны коэффициенты усиления и фазовые скорости неустойчивых возмущений. При наличии в потоке зоны возвратного течения коэффициенты усиления возмущений существенно возрастают.

Ключевые слова: гидродинамическая теория устойчивости, закрученные течения, коэффициенты усиления, фазовые скорости

1. INTRODUCTION

Swirling flows have a wide area of applications in various technical field. They are used to intensify heat and mass transfer processes, purify gases and liquids from impurities, stabilize combustion processes, extinguish energy in hydraulic structures, and etc. The swirl has a significant effect on all the main characteristics of the flow, including its stability. In this case, a critical point (stagnation point) with zero velocity is formed on the flow axis or near it. Behind of this point, a reverse flow zone is formed. The emerging instability leads to the formation of secondary vortex motions, and can also be the cause of the collapse of the vortex.

The phenomenon of collapse (destruction) of a vortex (vortex breakdown) was first discovered in aerodynamic studies during the flow around the wings of a large sweep. Disturbances of the vortex decay type are characterized by a sudden deviation of the vortex axis from its original direction or a sharp increase in the vortex core.
The existing results on the study of vortex decay are systematized in review [1]. Most of the experiments were carried out in weakly expanding axisymmetric tubes. Currently, eight types of vortex decay have been recorded. Their detailed classification is presented in [2]. Two types of vortex breakdown are most common: bubble breakdown and spiral breakdown. Bubble breakup is characterized by a critical point on the flow axis, followed by an almost axisymmetric shell of

the recirculation zone. In problems related to combustion, such recirculation regions serve as a kind of flame holder [3]. In other technical devices such as presented [4, 5], the formation of counter flow zones is undesirable, since it can lead to excessive deceleration of the main flow. After axisymmetric decay, as a rule, spiral decay follows. Although, they can be observed independently. Spiral decay is characterized by a sharp break in the vortex axis, after which a corkscrew-like swirling of the flow occurs.

Thus, when the vortex is destroyed, a significant rearrangement of the initial flow occurs. In particular, it was experimentally established [6] that after the collapse of a vortex, the flow, as a rule, becomes turbulent.

The phenomenon of vortex decay is closely related to the development of flow instability. The problem of the stability of a free vortex whose velocity profiles can be obtained from the self-similar Batchelor solution for a viscous swirling wake was studied in [7–12]. In the paper [9], selective calculations were performed for the first three instability modes of a free vortex. And a new viscous instability mode was discovered for the first time. Detailed studies of that are presented in [10]. In the paper [11], the instability of the flow under study was presented for large values of the swirling parameter of the flow. There, the existence of up to eight unstable modes simultaneously was established. The branching of eigensolutions is discovered and the filling of the region of admissible values in the space of free parameters by instability modes is studied.

The paper [12] provides a study on the stability of a swirling flow in an unbounded medium, the velocity profiles of which were obtained by numerically solving the complete system of Navier–Stokes equations. This study was based on the hypothesis of local parallelism of the flow. It is shown that in the presence of a recirculation zone in the flow, the strongest instability was observed. The oscillation frequencies corresponding to the most unstable wavenumber are consistent with the results on the stability of vortices coming off the trailing edge of an aircraft wing and with research data on the spectral characteristics of swirling flows in an expanding channel [13].

This paper aims to study the problem of the stability of an internal swirling flow in an axisymmetric channel, using a similar approach.

2. STATEMENT OF THE PROBLEM ON THE MOTION OF A SWIRLING FLOW

The paper considers the problem of the development of a swirling flow in an axisymmetric channel of radius. Axisymmetric laminar flows of a viscous incompressible fluid are described by the Navier–Stokes system of equations. In a cylindrical coordinate system r, φ, z with respect to the stream function ψ, the vorticity Ω and the azimuthal velocity V_φ can be represented as follows

$$\frac{1}{r}\frac{\partial^2\psi}{\partial z^2}+\frac{\partial}{\partial r}\left(\frac{1}{r}\frac{\partial\psi}{\partial r}\right)=-\Omega \tag{1}$$

$$\frac{\partial\Omega}{\partial t}+\frac{\partial}{\partial z}(V_z\Omega)+\frac{\partial}{\partial r}(V_r\Omega)= =\frac{1}{\mathrm{Re}}\left[\frac{\partial^2\Omega}{\partial z^2}+\frac{\partial^2\Omega}{\partial r^2}+\frac{\partial}{\partial r}\left(\frac{\Omega}{r}\right)\right]+G^2\frac{1}{r}\frac{\partial(V_\varphi)^2}{\partial z} \tag{2}$$

$$\frac{\partial V_\varphi}{\partial t}+\frac{\partial}{\partial z}(V_zV_\varphi)+\frac{1}{r}\frac{\partial}{\partial r}(rV_rV_\varphi)+\frac{V_rV_\varphi}{r}= =\frac{1}{\mathrm{Re}}\left[\frac{\partial^2V_\varphi}{\partial z^2}+\frac{1}{r}\frac{\partial}{\partial r}\left(r\frac{\partial V_\varphi}{\partial r}\right)-\frac{V_\varphi}{r^2}\right] \tag{3}$$

$$V_r=-\frac{1}{r}\frac{\partial\psi}{\partial z},\quad V_z=\frac{1}{r}\frac{\partial\psi}{\partial r},\quad \Omega=\frac{\partial V_r}{\partial z}-\frac{\partial V_z}{\partial r} \tag{4}$$

The system of equations (1)–(4) is written in a conservative dimensionless form. The axial V_z and radial V_r velocities are related to the characteristic value U_0. The azimuthal velocity V_φ is related to the characteristic value W_0. The coordinates are related to the radius r_0, and the time is related to the value r_0/U_0. The system of equations (1)–(4) contains two dimensionless parameters:

Reynolds number $\mathrm{Re} = U_0 r_0 / \nu$, in which ν is the kinematic viscosity, and spin parameter is $G = W_0 / U_0$.

The solution of the problem under consideration is determined in the area D: $0 \le z \le z_k$, $0 \le r \le 1$. At the input $z = 0$, the following distributions for the axial and azimuthal velocity components (the radial velocity in the initial section is assumed to be zero) were set:

$$\begin{aligned} &V_{z0}(r) = D_0 + D_1 \exp(-B_1 r^2), \\ &V_{\varphi 0}(r) = \frac{A}{r}(1 - \exp(-B_2 r^2)), \ 0 \le r \le r_0, \\ &V_{z0}(r) = a_0 + a_1 r + a_2 r^2, \\ &V_{\varphi 0}(r) = b_0 + b_1 r + b_2 r^2, \qquad r_0 \le r \le 1. \end{aligned} \tag{5}$$

These profiles are consistent with experiments [6]. For $0 \le r \le r_0$, the distribution of velocities (5) corresponds to a free vortex. The constant B_2 characterizes the value r at which the azimuth velocity is maximum. By selecting D_0, D_1, a corollary or jet type flow can be gotten. In the equations (5), the coefficients of the polynomials a_i, b_i are found from the no-slip conditions at 1 and the continuity of the velocities $V_{z0}(r)$, $V_{\varphi 0}(r)$, and their derivatives at the point r_0.

The set of boundary conditions, including setting velocity profiles $V_{z0}(r)$, $V_{\varphi 0}(r)$ at the input $z = 0$, no-slip conditions on the channel walls, symmetry conditions on the axis $r = 0$, and soft boundary conditions in the outlet section $z = z_k$, for this problem can be represented as:

$$\begin{aligned} &\psi = \psi_0(r), V_\varphi = V_{\varphi 0}(r), \frac{\partial \psi}{\partial z} = 0, \ 0 \le r \le 1, \ z = 0 \\ &\psi = \psi_0 = \mathrm{const}, V_\varphi = 0, \frac{\partial \psi}{\partial r} = 0, \ 0 \le z \le z_k, \ r = 1 \\ &\psi = 0, V_\varphi = 0, \Omega = 0, \ 0 \le z \le z_k, \ r = 0 \\ &\frac{\partial \psi}{\partial z} = \frac{\partial \Omega}{\partial z} = \frac{\partial V_\varphi}{\partial z} = 0, \quad 0 \le r \le 1, \quad z = z_k \end{aligned} \tag{6}$$

For the numerical solution of the boundary value problem (1)–(4) with boundary conditions (6), the finite difference method was used, which was tested and successfully applied in [14–17] to calculate swirling flows of various types. In these calculations, the following values were accepted:

$$\begin{aligned} &D_0 = 1, \ D_1 = 0, \ B_1 = 0, \ B_2 = 14, \\ &A = 0.419, \ r_0 = 0.75, \ z_k = 10 \end{aligned} \tag{7}$$

3. RESULTS

The calculations of the flow fields corresponding to the boundary value problem (1) – (4), (6), (7) were carried out at $\mathrm{Re} = 100$, 150, 300, 500 in the swirl range $0 \le G \le 3$. The most characteristic patterns of streamlines are shown in Fig.1. Further, the main properties of the calculated flows are considered in detail.

At a sufficiently large swirl value (depending on the value of the number Re), a reverse flow zone appears in the axial part of the channel, limited by stagnation points (z_1, z_2) located on the symmetry axis. This recirculation region has a toroidal structure with closed current lines. An example of such a flow at $\mathrm{Re} = 100$, $G = 2.1$ is shown in Fig.1, b. As the swirl increases, the diameter d_0 of the return flow region increases, the recirculation region shifts upstream, and the rear stagnation point z_2 slightly shifts towards the front one z_1.

If Reynolds number is higher of 150, G= 2.2, the return flow region is formed somewhat closer to the input section and its length in the direction z decreases (Fig. 1, c). With an increase in swirl G=2.4, the rear stagnation point approaches the anterior one, and the streamlines behind the recirculation zone acquire a zigzag shape. With a further increase in swirl G=2.6 (figure 1, d) downstream of the first region of the return flow, a second recirculation zone is formed. It also has a toroidal structure, but with a lower recirculation rate and a smaller diameter. The length of the

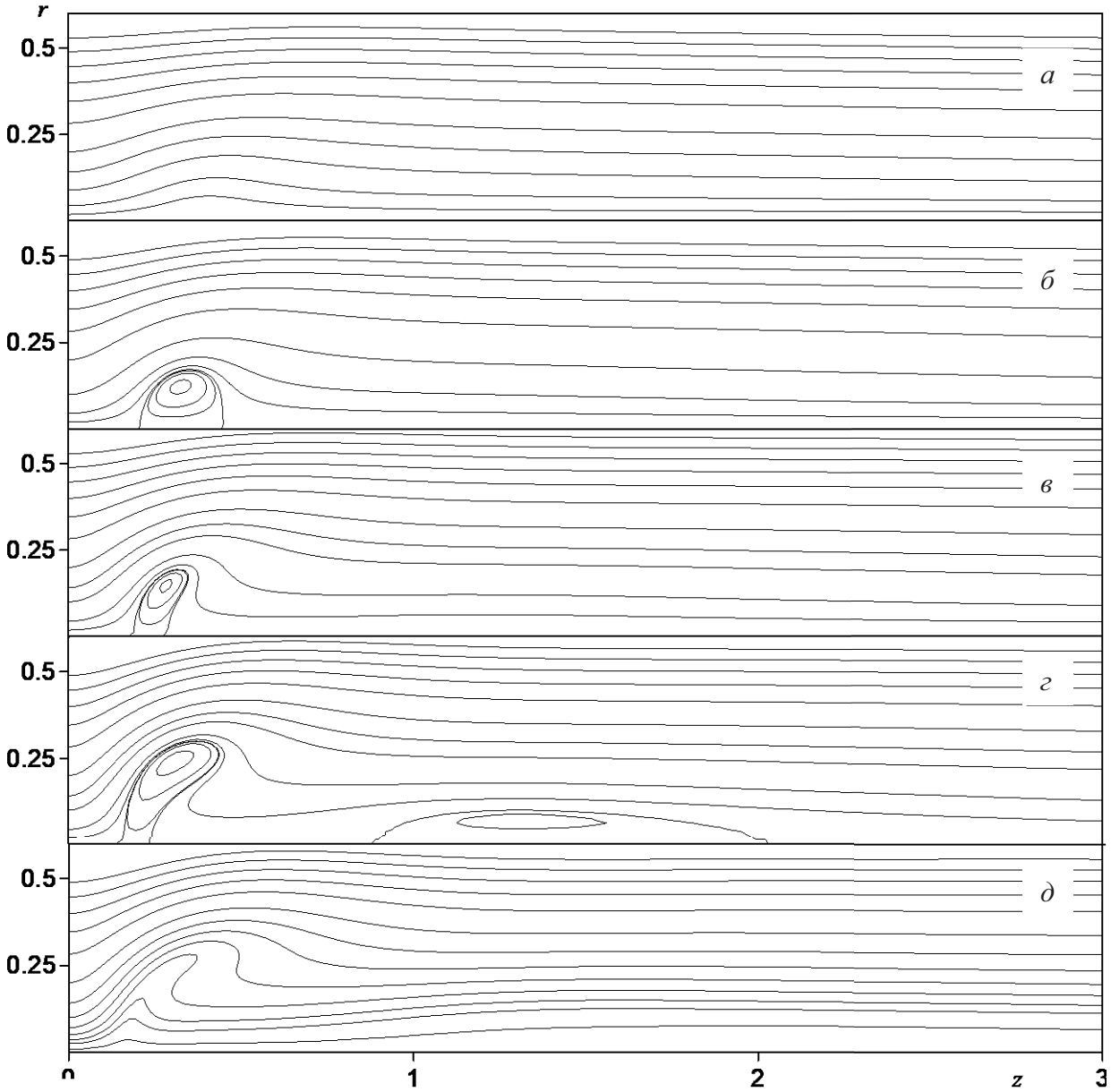

Figure 1. Streamlines for Re=100, G=1.7 (а), G=2.1 (б); Re=150, G=2.2 (в), G=2.6 (г); Re=300, G=2.4 (д)

second reverse flow zone is much longer than the first.

A further increase in the Reynolds number Re=300 leads to a qualitative change in the flow pattern. With a sufficiently high swirl 2.4 (Fig.1, e), the first recirculation zone on the channel axis is not formed (the flow directly in the axial part for $r \le 0.05$ moves forward). In contrary, a separation region with a reverse flow is formed at a distance of $r \approx 0.1$–0.3 from the symmetry axis.

4. FLOW STABILITY

Further, the small perturbations of a swirling flow with given velocity profiles are considered

$$V_z = U(r), \qquad V_\varphi = W(r), \qquad V_r = 0 \qquad (8)$$

as solutions of the linearized Navier–Stokes equations of the traveling wave type (normal modes)

$$\{V_z', V_r', V_\varphi', p'\} = \\ = \{F, iS, H, P\}\exp[i(\alpha z + n\varphi - \alpha ct)], \quad (9)$$

in which p is the pressure; alpha is the wave number; n is the perturbation mode $(n = 0; \pm 1; \pm 2; ...)$; c is the speed of wave propagation; i is an imaginary unit. For complex amplitude functions F(r), S(r), H(r), P(r) a system of equations are obtained:

$$r^2\gamma F + \alpha r^2 P + r^2 SU' = \\ = \frac{1}{i\,\mathrm{Re}}\left[r\left(rF'\right)' - \left(\alpha^2 r^2 + n^2\right)F\right],$$

$$r^2\gamma S + 2rHW - r^2 P' = \\ = \frac{1}{i\,\mathrm{Re}}\left[r\left(rG'\right)' - \left(\alpha^2 r^2 + n^2 + 1\right)S - 2nH\right], \quad (10)$$

$$r^2\gamma H + r^2 S\left(W' + \frac{W}{r}\right) + rnP = \\ = \frac{1}{i\,\mathrm{Re}}\left[r\left(rH'\right)' - \left(\alpha^2 r^2 + n^2 + 1\right)H - 2nS\right],$$

$$\alpha rF + \left(rS\right)' + nH = 0,$$

where $\gamma = \alpha(U - c) + nW/r$. Prime means a derivative with respect to r. For system (10) at r = 0, the boundary conditions are derived from the requirements for the regular behavior of the solution near the axis and have the form

$$S(0) = H(0) = 0, \\ F(0), P(0) - \textit{restricted for } n = 0; \\ S(0) \pm H(0) = 0, \\ F(0) = P(0) = 0 - \text{при } n = \pm 1; \quad (11) \\ S(0) = H(0) = F(0) = P(0) = 0 - \textit{for } |n| > 1; \\ S(1) = H(1) = F(1) = 0.$$

Let's consider perturbations (9) periodic in z, whose amplitude varies with time. Then α is a real number ($\alpha = 2\pi/\lambda$, where λ is the perturbation wavelength), and $c = c_r + ic_i$ is the complex one; c_r is the velocity of propagation of the perturbation in the direction z (phase velocity), c_i is the rate of rise of the perturbation in time, $\omega_i = \alpha c_i$ is the amplification factor of the perturbations, and $\omega_r = \alpha c_r$ is the oscillation frequency. For $c_i < 0$, the perturbation amplitudes (9) decay (the flow is stable), and for $c_i > 0$, they increase with time (the flow is unstable).

The method for calculation of eigenvalues is described in [9-10], and testing of the method is presented in [11].

For the calculated swirling flows, the maximum value of the radial velocity component is smaller over order than the corresponding values for the axial and azimuthal components. In the distributions $V_z(r,z)$, $V_\varphi(r,z)$, the relation with z is significantly manifested only in the very initial section near the inlet section. Therefore, the problem of the stability of the obtained flows with respect to non-axisymmetric perturbations (9) at r=-1 is considered under the assumption that the flow is locally parallel. For this purpose, in the system of equations (10) take profiles $V_z(r,z_0)$, $V_\varphi(r,z_0)$ as $U(r)$, $W(r)$, from calculations in the system of equations (10). Here z_0 is a parameter.

First, the case was studied, for which the initial swirling of the flow is insufficient to form a reverse flow zone. Only a slight swelling of the streamlines is observed in the axial part of the flow. An example of such a flow at Re=100, G=1.7 is shown in figure 1, a. Figure 2, a show the dependences of the gains ω_i and the corresponding phase velocities ω_r on the wave number α obtained in different cross sections of the flow z=const for this case. In the initial section z=0 (curve 1), a very slight flow instability is observed with a maximum value of $\omega_i^* = \max\omega_i = 0.0027$ in a narrow range of the wave number $3.18 \le \alpha \le 3.55$. In the next section, at z=0.31 (curve 2), the instability increases and at z=2.5 (curve 4) it becomes the largest. Further downstream, the instability

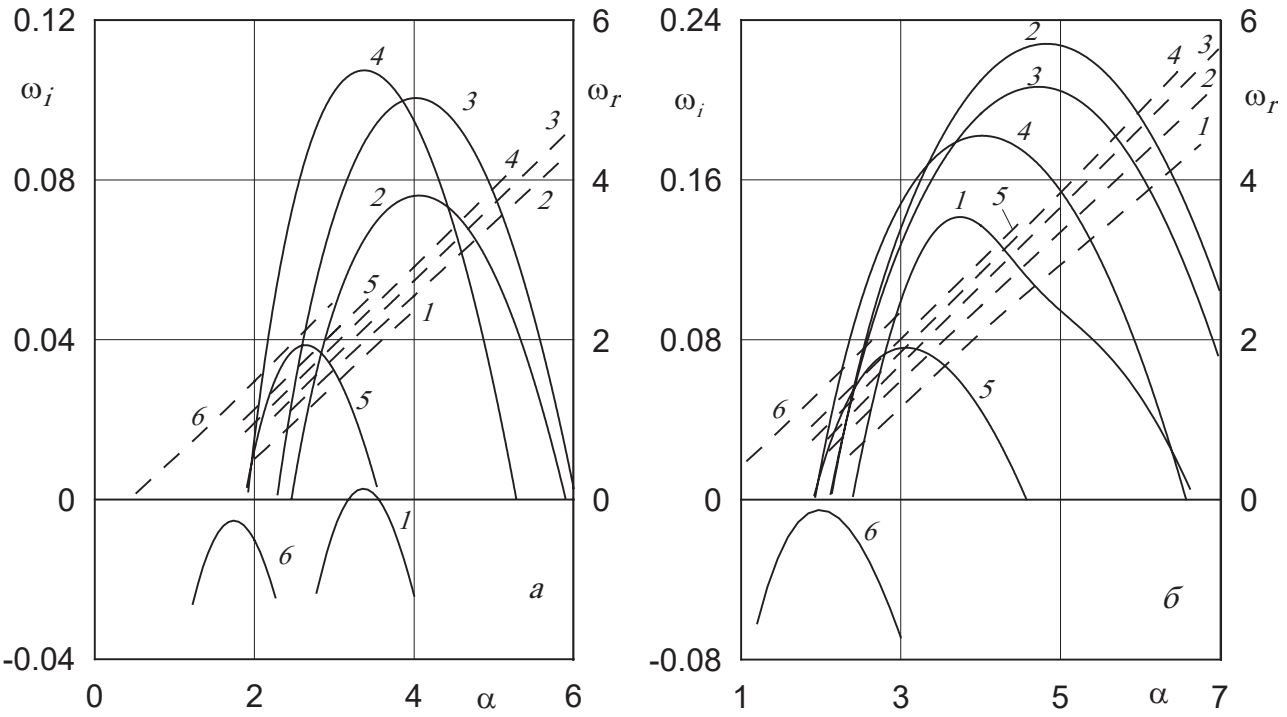

Figure 2. Amplification factors - wave number (_____) and oscillation frequency - wave numbers (_ _ _) diagrams for добавить Re и G ..... in the sections z=0, 0.31, 0.62, 2.5, 5, 10 (curves 1-6)

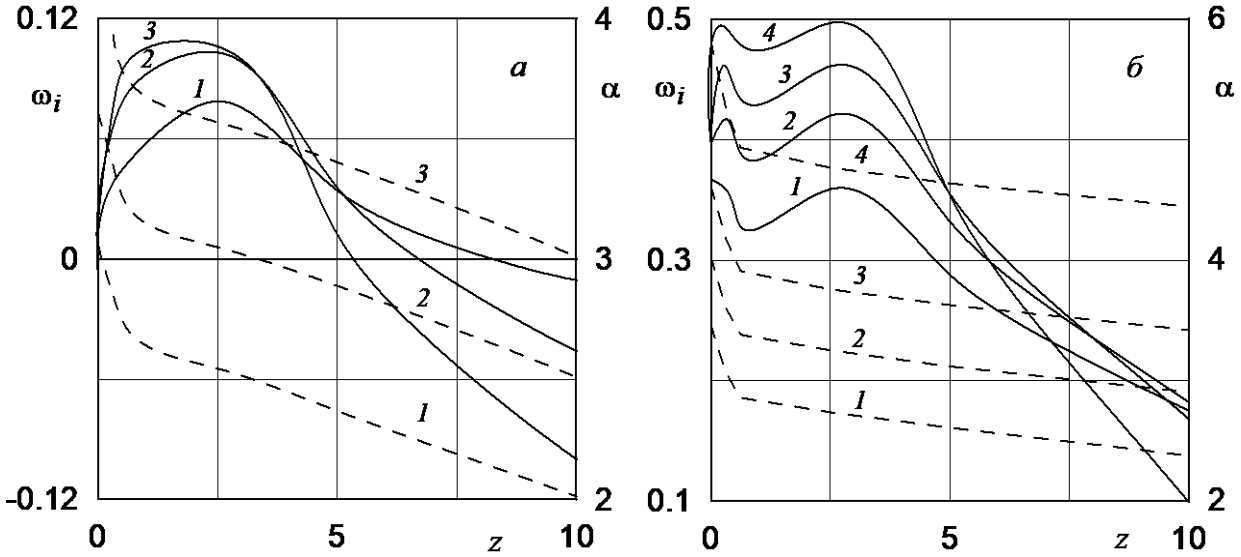

Figure 3. Amplification factors - axis coordinate (_____) and wave numbers – axis coordinate (_ _ _) diagrams for добавить *Re* и *G* ..... for fixed oscillation frequencies

decreases, and at z=10 (curve 6) at the channel outlet, the flow becomes stable ($\omega_i < 0$).

Figure 3, a show the change in amplification factors ω_i and wave numbers α along the flow axis for perturbations (9) with a fixed oscillation frequency ω_r. All diagrams $\omega_i(z)$ show a local maximum at $z \approx 2.5$.

Thus, swirling of the flow leads to instability of the flow before the formation of the recirculation zone. The axial velocity profiles in this case are characterized by a large velocity defect on the ($V_* \approx 0.1$) axis, have an inflection

point at $z \approx 0.25$, and differ significantly from the parabolic distribution.

At Re=100, G=2.1, there is a paraxial zone of reverse stream in the flow at $0.207 \le z \le 0.448$ (figure 1, b). The calculated amplification factors and oscillation frequencies for a given flow are shown in Fig.2, b. In the initial section z=0 (curve 1), the flow is unstable with a maximum amplification factor of $\omega_i^* = 0.141$ at $\alpha_* = 3.74$. In the region of the reverse flow at z=0.31 (curve 2), the strongest instability is noted. At $0.6 \le z \le 2.5$, the maximum values of the amplification factors change insignificantly. Further downstream, the instability decreases and at the outlet at z=10 (curve 6), the flow becomes stable ($\omega_i < 0$).

Таким образом, закрутка потока приводит к неустойчивости

Characteristic relations for the change in the amplification factors along the flow axis for flows with a recirculation zone are shown in Fig.3, b. The distribution $\omega_i(z)$ has two local maxima. One of them at $z \approx 2.5$ is observed in all calculated unstable flows and is associated with the swirl effect. The other, located upstream at $z \approx 0.3$, is due to the presence of a reverse flow zone in the flow. The values of the amplification factors at the points of local maxima are close to each other. In contrast to the flow without the formation of a recirculation zone, the velocity V_z profiles in the axial region have two inflection points at $r \approx 0.1$; 0.3. As can be seen from figures 3, a, b, the values of the wavelengths corresponding to the most growing disturbances in the first and second zones differ insignificantly.

At Re=150 or more intense initial swirl G=2.6 in the flow, a second axial region of the return flow is formed (figure 1, d). It has a large length along z, and the recirculation rate is less. In this case, the distribution $\omega_i(z)$ is completely similar to the previous case and has two local maxima, each of which is observed in the region of the reverse flow zones. Moreover, instability in the first recirculation zone leads to the formation of a more pronounced maximum for the second zone.

The results obtained are consistent with the calculations of the spatiotemporal instability of swirling flows in an unbounded medium [18, 19], which show that the strongest flow instability is observed in the region of bubble-like decay and in its wake with the formation of a spiral form of decay.

5. CONCLUSION

The provided studies on the swirling flows show that there are two mechanisms of instability. The first one is related with the effect of flow swirl, the second one with the formation of reverse flow zones. The traveling wave of perturbations successively passes through two zones, in which its amplitude grows most rapidly. This effect can contribute to the destruction of the vortex.

REFERENCES

1. **Lucca-Negro O., O'Doherty T.** Vortex breakdown: a review // Progr. in Energy and Comb. Sci. 2001. V. 27. P. 431-481.
2. **Alekseenko S.V., Kuibin P.A., Okulov V.L.** Introduction to theory of concentrated vortices. Moskow–Izhevsk: Institute of Computer Science. 2005. 504 p.
3. **Gupta A.K, Lilley D.G, Syred N.** Swirl Flows 1984 (Abacus Press)
4. **Akhmetov V.K., Shkadov V.Ya., Konon P.N.** Aerodynamics of building structures for flue gas removal. Magazine of Civil Engineering. 2018. 81(5). Pp. 81-92.
5. **Akhmetov V.K.** Method of effective parameters for calculations of turbulent swirling flows in engineering constructions // IOP Conf. Series: Materials Science and Engineering. 2020. V. 869. 052020.
6. **Faler J.H., Leibovich S.** An experimental map of the internal structure of a vortex

breakdown // J. Fluid Mech. 1978. V. 86. № 2. P. 313-335.
7. **Lessen M., Paillet F.** The stability of a trailing line vortex. Part 2. Viscous theory // J. Fluid Mech. 1974. V. 65. Pt. 4. P. 769-779.
8. **Mayer E.W., Powell K.G.** Viscous and inviscid instabilities of a trailing vortex // J. Fluid Mech. 1992. V. 245. P. 91-114.
9. **Akhmetov V.K., Shkadov V.Ya.** Stability of a free vortex // Moscow University Mechanics Bulletin. 1987. V. 42. № 2. P. 17-22.
10. **Akhmetov V.K.** Structure and branching of unstable modes in a swirling flow // Mathematics. 2022. V.10(1). 99.
11. **Akhmetov V.K., Shkadov V.Ya.** Instability of a free vortex for large swirl numbers // Moscow University Mechanics Bulletin. 2003. T. 58. № 1. C. 23-27.
12. **Akhmetov V.K.** Development and stability of swirling flows // Fluid Dynamics. 1988. V. 23. № 4. P. 485-492.
13. **Garg A.K., Leibovich S.** Spectral characteristics of vortex breakdown flowfields // Phys. Fluids. 1979. V. 22. P. 2053-2064.
14. **Akhmetov V.K.** Numerical and asymptotic flow stability analysis of vortex structures // E3S Web of Conferences. 2021. V. 263. 03003.
15. **Akhmetov V.K., Shkadov V.Ya**. Atomization of a powder by a swirling flow with a recirculation zone // Fluid Dynamics. 2000. V. 35. № 6. P. 791-802.
16. **Akhmetov V.K., Akhmetova V.V.** Mathematical Modelling of Vortex Dust Separator // IOP Conf. Series: Materials Science and Engineering. 2019. 661.
17. **Akhmetov V.K., Medvedev Yu.V., Shkadov V.Ya.** Effect of the Inertia Terms in Sliding Bearing Calculation Problems // Fluid Dynamics. 2014. Vol.49. №3. P.320-329.
18. **Herrada M. A., R. Fernandez-Feria R.** On the development of three-dimensional vortex breakdown in cylindrical regions // Phys. Fluids. 2006. V. 18. 084105. 15 p.
19. **Gallaire F., Ruith M., Meiburg E., Chomaz J., Huerre P.** Spiral vortex breakdown as a global mode // J. Fluid Mech. 2006. V. 549. P. 71-80.

СПИСОК ЛИТЕРАТУРЫ

1. **Lucca-Negro O., O'Doherty T.** Vortex breakdown: a review // Progr. in Energy and Comb. Sci. 2001. V. 27. P. 431-481.
2. **Алексеенко С.В., Куйбин П.А., Окулов В.Л.** Введение в теорию концентрированных вихрей. Москва–Ижевск: Институт компьютерных исследований, 2005. 504 с.
3. **Гупта А., Лилли Д., Сайред Н.** Закрученные потоки. М.: Мир, 1987. 588 с.
4. **Ахметов В.К., Шкадов В.Я., Конон П.Н.** Аэродинамика строительных сооружений для удаления дымовых газов // Инженерно-строительный журнал. 2018. № 5(81). С. 81-92.
5. **Akhmetov V.K.** Method of effective parameters for calculations of turbulent swirling flows in engineering constructions // IOP Conf. Series: Materials Science and Engineering. 2020. V. 869. 052020.
6. **Faler J.H., Leibovich S.** An experimental map of the internal structure of a vortex breakdown // J. Fluid Mech. 1978. V. 86. № 2. P. 313-335.
7. **Lessen M., Paillet F.** The stability of a trailing line vortex. Part 2. Viscous theory // J. Fluid Mech. 1974. V. 65. Pt. 4. P. 769-779.
8. **Mayer E.W., Powell K.G.** Viscous and inviscid instabilities of a trailing vortex // J. Fluid Mech. 1992. V. 245. P. 91-114.
9. **Akhmetov V.K., Shkadov V.Ya.** Stability of a free vortex // Moscow University Mechanics Bulletin. 1987. V. 42. № 2. P. 17-22.

10. **Akhmetov V.K.** Structure and branching of unstable modes in a swirling flow // Mathematics. 2022. V.10(1). 99.
11. **Akhmetov V.K., Shkadov V.Ya.** Instability of a free vortex for large swirl numbers // Moscow University Mechanics Bulletin. 2003. T. 58. № 1. C. 23-27.
12. **Akhmetov V.K.** Development and stability of swirling flows // Fluid Dynamics. 1988. V. 23. № 4. P. 485-492.
13. **Garg A.K., Leibovich S.** Spectral characteristics of vortex breakdown flowfields // Phys. Fluids. 1979. V. 22. P. 2053-2064.
14. **Akhmetov V.K.** Numerical and asymptotic flow stability analysis of vortex structures // E3S Web of Conferences. 2021. V. 263. 03003.
15. **Akhmetov V.K., Shkadov V.Ya.** Atomization of a powder by a swirling flow with a recirculation zone // Fluid Dynamics. 2000. V. 35. № 6. P. 791-802.
16. **Akhmetov V.K., Akhmetova V.V.** Mathematical Modelling of Vortex Dust Separator // IOP Conf. Series: Materials Science and Engineering. 2019. 661.
17. **Akhmetov V.K., Medvedev Yu.V., Shkadov V.Ya.** Effect of the Inertia Terms in Sliding Bearing Calculation Problems // Fluid Dynamics. 2014. Vol.49. №3. P.320-329.
18. **Herrada M. A., R. Fernandez-Feria R.** On the development of three-dimensional vortex breakdown in cylindrical regions // Phys. Fluids. 2006. V. 18. 084105. 15 p.
19. **Gallaire F., Ruith M., Meiburg E., Chomaz J., Huerre P.** Spiral vortex breakdown as a global mode // J. Fluid Mech. 2006. V. 549. P. 71-80.

Vadim K. Akhmetov, Doctor of Science, Professor, Department of Computer Science and Applied Mathematics, Moscow State University of Civil Engineering, 26, Yaroslavskoe Shosse, Moscow, 129337, Russia, tel. +7(499) 183-59-94, e-mail: vadim.akhmetov@gmail.com

Ахметов Вадим Каюмович, доктор технических наук, профессор кафедры информатики и прикладной математики Национального исследовательского Московского государственного строительного университета, 129337, г. Москва, Ярославское шоссе, д. 26, тел. +7(499) 183-59-94, e-mail: vadim.akhmetov@gmail.com

International Journal for Computational Civil and Structural Engineering, 19(1) 23–31 (2023)

DOI:10.22337/2587-9618-2023-19-1-23-31

ASSESSMENT OF WEIGHT OF SEDIMENT FORMATION DEPOSIT IN MUNICIPAL COLLECTOR SYSTEM (MCS)

Lyudmila V. Volgina*, *Stanislav A. Sergeev

National Research Moscow State University of Civil Engineering, Moscow, RUSSIA

Abstract: The main purpose of this work is to provide calculations of annual weight of sediment formation deposit in Municipal Collector System (MCS). The article considers two-phases flow in the collector. The storm water collector is small culvert for storm water (rainwater) or for removing the river (creek, stream, flow) underground. The article defines the solid particles in flow as sand, clay, stones, silt, etc. It was found that in case of signif\icant flow rate, then all solid particles move in the pipe. If not, they settle to the bottom and sediment is formed. In this paper, total weight of sediment formation in Moscow collector system is calculated at average annual values. On this ground a consideration can be made that sediment deposit reduces efficiency of the system partially or completely.

Keywords: storm system, storm water pipes, sewage pipes, solid particles, sewerage system, sediment formation

ОЦЕНКА МАССЫ ОТЛОЖЕНИЙ, ФОРМИРУЮЩИХСЯ В ГОРОДСКОЙ КОЛЛЕКТОРНОЙ СИСТЕМЕ

Л.В. Волгина*, *С.А. Сергеев

Национальный исследовательский Московский государственный строительный университет, г. Москва, РОССИЯ

Аннотация. Основная цель настоящей работы расчет массы отложений, формирующихся в городской коллекторной системе ежегодно. Поток в коллекторе рассматривается как двухфазный. Коллектор представляет собой малое водопропускное сооружение (труба) для пропуска ливневой (дождевой) воды или для отвода реки (притока реки или ручья) под землю. В статье рассматриваются твердые частицы такие как галька, песок, глина, ил и т.д. двигающиеся с потоком, в случае значительного расхода воды, и оседают на дно коллектора (образуется осадок), если энергии потока недостаточно. В данной работе общая масса отложений, формирующихся во всей московской коллекторной системе, рассчитана по среднегодовым значениям. На основе полученных данных сформулирован вывод, что образование осадка снижает полностью или частично эффективность работы городской коллекторной системы.

Ключевые слова: система коллекторов, ливневые трубы, канализационные трубы, твердые частицы, канализация, образование отложений

INTRODUCTION

With the increase of urbanization in cities, problems due to storm water become more and more important: floods, overflows, pollution of receiving waters, high exploitation costs due to sediment deposits [1,4,5]. Since the mid-20th Century, the fundamental research of “solid transfer in sewers” has been carried out for improvement urban environment [7, 13].

On the territory of Moscow, the total length of the river network is more than 600 km. About 295 km of them (more than 160 rivers) flow underground (Fig. 1) in tube under industrial and civil constructions and have become part of municipal storm system.

The storm water system is separated from sewer systems in Moscow. The volume of transport and sedimentation inside tubes relates to the concentration and types of solid particles shed into the water or ground.

Figure 1. Moscow underground rivers map

As storm water covers streets and other waterproof surfaces, it transports pollutants such as oil, chemicals, pathogens, and sediments. This pollution is carried by storm water and discharged directly into local waterways, which has a negative impact on water quality. The pollution levels of Moscow consist of four zones: transport, residential, park and industrial. The studies have shown [3,9,11,14] that the main pollutant of surface runoff is suspension and dissolved petroleum products, the source of which is transport and collapsing asphalt road surfaces. The main pollutants arising from the operation of roads are oils, lubricants, propellants, tars, silicones, exhaust gases produced by the fuel combustion, abrasive products of broken car discs and tires, asphalt, ashes, dusts, organic bituminous ingredients, and remnants provided after the maintenance of roads in winter [15,17]. The infrastructure (roads, sidewalks, commercial and residential structures) added during urbanization process is designed to collect storm water in Moskva river water channels. The quality of water is influenced by river suspended particles and pollutants collected on impervious surfaces and that are carried by urban storm water runoff. The flow is caused by the slope. Flows in collectors can be unsteady, irregular with variable roughness coefficient and two-phases with wide list of solid particles [8, 18].

The literature review [2, 4, 6,10,12,16] presents the modern concerning sediment sewer transport

modeling. After a description of solid particles found in tubes and in storm water, the different steps considered in models are described: a transfer through model and a model of deposition (sediment formation) and erosion in sewer pipes.

The design Moscow Collector System (MCS) consisted of two tasks: the main one was protection of floods and the secondary was self-cleaning support.

On the regulation basis, the condition in the tube can be self-cleaning. However, Mosvodostok (Moscow engineering system) removes the main part of sediment deposition manually or mechanically. The main purpose of this work is to provide calculations of annual weight of sediment formation deposit in MCS.

METHODS

At the turn of the 19th-20th century, the city's (municipal) sewerage system appeared in Moscow. Also problems with the storm water collection and water irrigation were solved. Most of now operating collector systems were built in period of 60-80 years of the 20th century. Collectors are used for:

- Storm water collection (to protect the territory from flooding)
- City's development (increasing the territory and district connection)
- Ecological goal (reduced entering pollution from the water flows)

Collector system is extensive, complex net (network) of tubes (tree like), where tubes of smaller diameter are connected to tubes of large diameter. There are two types of collectors in MCS, with or without connection to the sewage treatment plants. In the current work we take into account the collectors with connection straight to the river.

The Data Base (DB) consists of characteristics of 2421 collectors (outlet tubes) of MCS. DB allows us to evaluate the efficiency of work of the whole municipal storm system. The working array was built in eight columns and 2421 lines:

$$\left[S_i^n\right],\left[D_i^n\right],\left[C_i^n\right],\left[R_i^n\right],\left[Q_i^n\right],\left[V_i^n\right],\left[H_i^n\right],\left[P_i^n\right] \qquad (1)$$

where S_i^n – water catchment area for runoff tube, D_i^n – local runoff outlet tube diameter, range 100 to 5000 mm, C_i^n - cross-section parameter – "rectangular" or "round"; R_i^n – ratio – part of water catchment area for local runoff tube (percent):

$$\left[R_i^n\right] = \frac{\left[S_i^n\right]}{S} \cdot 100\% \qquad (2)$$

S – Moscow water catchment area (m^2) = 83.5 acre; D – diameter runoff tube (m), Q_i^n part of rate in local runoff tube (m^3/s), Q – water rate in MCS:

$$\left[Q_i^n\right] = Q\frac{\left[S_i^n\right]}{S} \qquad (3)$$

V_i^n - average flow velocity (m^2/s) and H_i^n – depth flow in tube, P_i^n - condition execution "yes" or "no" parameter. In current work, we used the following condition based on state regulation: "If the flow in collectors has average velocity less than recommended self-cleaning velocity, V_{sc}, solid particles will settle in the bottom and the sediment is formed".

The output rectangular cross-section occurs in 2% of cases (45 pieces) and round in 98% of cases (2376 pieces). The total average annual flow rate can be obtained from the water balance of the Moskva river. The water balance of river catchments is the ratio of the arrival and flow of water over a period of time (Table 1).

Table 1. The total annual water balance of Moskva river

RATE	mln m^3 per year	m^3/s
Storm water	600.00	19.29
Moskva river at the entrance to the city (data collected at the Karamyshevskaya dam)	1 144.76	36.80
Tributaries (Yauza, Setun, Gorodnya, Skhodnya, Nishenka, Desna)	353.32	11.36
Irrigation water	10.00	0.32
Leaks through the tube	-256.23	-8.24
Removal of water from the city, Moskva river (data collected at the Perervinsky dam)	-2 680.56	-86.18
Unaccounted tributaries	828.71	26.64
Balance	0.00	0.00

A part of the flow rate (Q) – average annual flow rate in collectors – is flow rate entering the collector system and is taken as the main calculated flow rate (average annual) passing through the entire collector system (Table 2).

Table 2. Estimated average water rate in MCS

RATE	mln m^3 per year	m^3/s
Storm water (30% of total 600.00)	181.56	5.84
Tributaries in tube (Setun, Gorodnya, Skhodnya, Nishenka)	157.7	5.07
Irrigation water (100% of total 10.00)	10.00	0.32
TOTAL	349.26	11.23

For the average annual flow rate passing through the MCS, 11.23 m^3/s is accepted in this work.

Taking into account the pipeline diameter, the bottom slope and the wall roughness (Chezi formula) for all possible depths of the pipeline, it is possible to plot the dependence of the flow rate (and, consequently, the velocity) on the relative depth H_i^n. Therefore, if the flow rate in each local collector is known, then the average velocity in each one is known.

The process of application of the overall methodology is illustrated in a Fig. 2.

The self-cleaning velocity is in range of 0.7 – 1.6 m/s., and detection condition $V_{sc} > V_i^n$ for average annual flow rate (flow rate in MCS is 11.23 m^3/s in Table 3). In the UK BS 80056 (British Standard) recommends a full pipe velocity of 1 m/s in order to ensure that a velocity of 0.75 m/s is exceeded at least once each day on average [5].

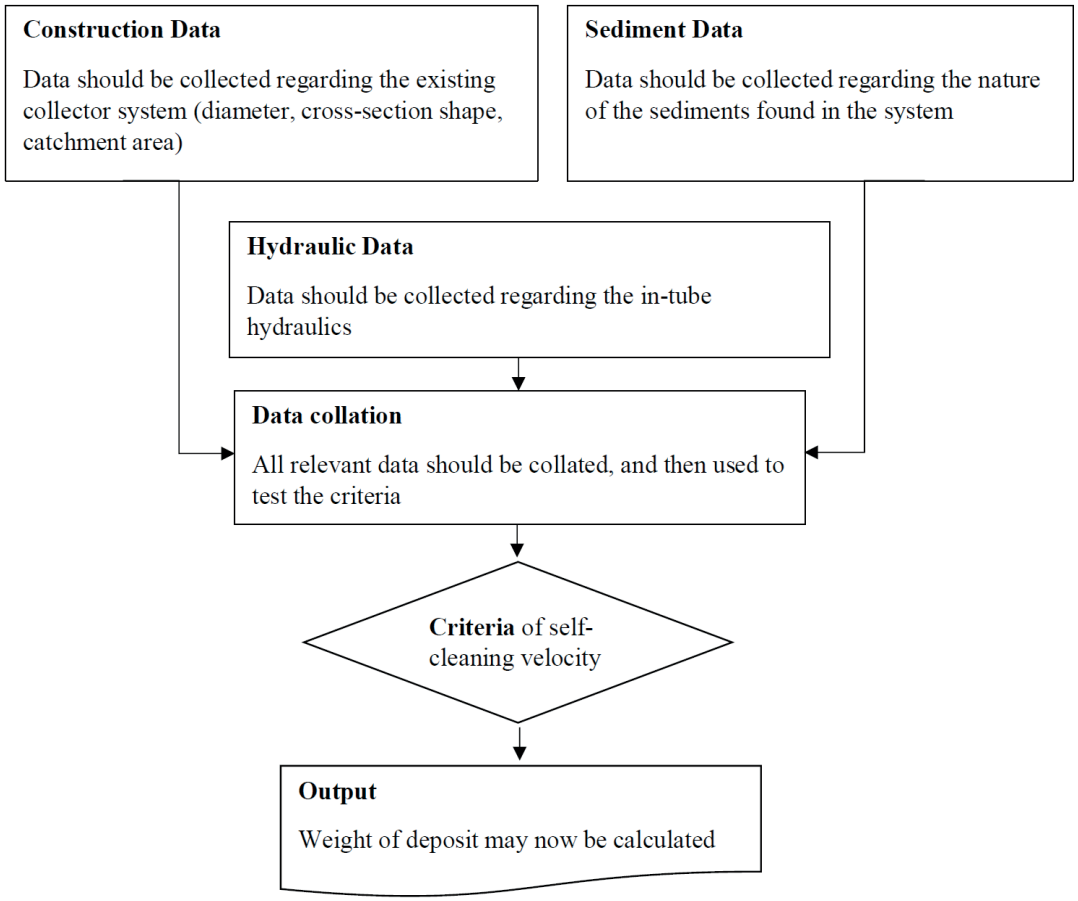

Figure 2. Schematic application of the calculation procedure

Table 3. Velocity analysis

Diameter range mm	Quantity of tubes	Maximum flow rate, m^3/s	Average velocity, V_i^n, m/s	Quantity of tubes with self-cleaning velocity conditions
below 300	513	0.016	to 1	3
from 300 to 400	678	0.03	to 1.5	7
from 400 to 500	165	0.008	to 0.008	2
from 500 to 600	153	0.1	to 2	9
from 600 to 800	132	0.13	to 2.33	7
from 800 to 1000	263	0.23	to 2.72	15
from 1000 to 1200	91	0.13	to 2	12
from 1200 to 2500	122	0.4	to 2.95	10
from 2500 to 5000	304	0.6	to 1.6	10
TOTAL	**2421**			**75**

For the average annual flow rate (in the MCS), the data was estimated as 11.23 m^3/s and for particles brought into the collector system from the outside:

- 97% of solid (silts) particles (diameter up to 5 mm), will settle to the bottom.
- 87.6% of the suspended solids will settle to the bottom.

RESULTS

In 2346 out of 2421 collectors, there is a condition not sufficient for transporting solid particles. Therefore, suspended solid particles deposit in button (in other words, the collector works as a sewage treatment facilities). The condition of calculation can be seen in Table 4.

Table 4. Conditions of calculation

Condition	Setting
Geometry	Cross section shape (circle or rectangular) (0.3 – 5.0) m x (0.3 – 5.0) m
Roughness coefficient	Concrete: 0.011
Slope	0.005
Soil	Density: 2650 kg/m^3 Particle diameter: < 50 mm Concentration: suspended particles 20.78 mg/l petroleum products 0.58 mg/l
Water	Density: 1000 kg/m^3 Dynamic viscosity: 0.001004 Pa·s

The calculation was made to estimate the weight of solid particles depositing in MCS (Table 5). Particle diameter is maximum inlet diameter, regulated by the standard. Concentration date is based on average actual data for 2019 on the volumes of suspended particles entering the sewage plants (Berezovaya Alley, Ivanovskoe, MKAD No.7, Yurlovskaya). Cleaning efficiency is average for Moscow sewage plants used as deposit process parameter.

Table 5. Weight sediment deposit

No	Parameter	Unit	Formula	Quantity
1	Volume of the storm water flow	mln. m^3 per year		254.52
2	Concentration of suspended solid particles	mg/l		20.78
3	Weight of solid particles moving in the flow	thsd. tons	3 = 1*2	5.29
4	Cleaning efficiency	percent		65.83
5	Collectors with low self-cleaning velocity conditions	percent		87.6
6	Weight of suspended solid particles deposit in the bottom	thsd. tons	6 = 3*4*5	3.05
7	Concentration of petroleum products	mg/l		0.58
8	Weight petroleum products particles moving in the flow	thsd. tons	8 = 1*7	0.15
9	Cleaning efficiency	percent		62.16
10	Collectors with low self-cleaning velocity conditions	percent		87.6
11	Weight of petroleum products particles deposit in the bottom	thsd. tons	11 = 8*9*10	0.08
12	Volume of the 4 big branches (tributaries) of the Moskva river	mln. m3 per year		157.7

13	Average solid particles (silt) concentration in rivers	mg/l		369.4
14	Weight of solid particles in rivers	thsd. tons		58.25
15	Cleaning efficiency	percent		65.83
16	Collectors with low self-cleaning velocity conditions	percent		97
17	Weight of particles from rivers settled in the bottom	thsd. tons	17=14*15*16	37.20
18	TOTAL weight of sediment deposit	thsd. tons	18=6+11+17	40.33

CONCLUSIONS

The estimation of the average annual weight of solid particles deposited at the bottom of the tubes in collector system of Moscow is 40.33 thousand tons (based on the average annual level of water consumption, turbidity and dry sediment).

REFERENCES

1. **Abdelaziz, R., Bakr M.** – I (2012), Inverse Modelling of Groundwater Flow of Delta Wadi El-Arish. Jornal of Water Resource and Protection 2012, vol.4, No.7, July 2012
2. **Arthur, S., Ashley, R., Tait, S. and Nalluri, C.** (1999) Sediment Transport in Sewers—A Step towards the Design of Sewers to Control Sediment Problems. Proceedings of the ICE—Water Maritime and Energy, 136, 9-19.
3. **Batica, J., Goubesville, P.** (2011), Collaborative Research on Flood Resilience in Urban Areas: the CORFU project. 34th World Congress of the International Association for Hydro-Environment Research and Engineering: 33rd Hydrology and Water Resources Symposium and 10th Conference on Hydraulics in Water Engineering. 3914-3920.
4. **Bertrand-Krajewski, J.-L., Briat, P., Scriver, O.,** (1993), Sewer sediment production and transport modelling: a literature review. Journal of Hydraulic Research, vol. 31(4), p.435-460.
5. **Butler D., Luu P.N., Karunaratne S.,** Investigation into sediment deposition in the sewers of the London borough of Lambeth. - First Phase Report, Drainage Research Unit, South Bank Polytechnic, July 1989.
6. **Campisano, A.; Creaco, E.; Modica, C.** Numerical modelling of sediment bed aggradation in open rectangular drainage channels. Urban Water J. 2013, 10, 365–376.
7. **Erik C.Poerse,** Stormwater Governance and Future Cities, Water 2013, 5, 29-52; doi:10.3390/w5010029
8. **Erpicum S., Kerger F., Archambeau P., Dewals B., Pirotton M.,** Experimental and Numerical Investigation of Mixed Flow in a Gallery. Engineering 2009.
9. **Fronczyk, J., Radziemska, M., Dynowski, P., Zbigniew, M., Bazydło** (2016), Quality of Water in the Road Drainage Systems in the Warsaw Agglomeration, Poland. Water 2016, vol 8, p. 429-441.
10. **Gopaliya, K.M.; Kaushal, D.R.** Modeling of soil-water slurry flow through horizontal pipe using CFD. J. Hydrol. Hydromech. 2016, 64, 261–272
11. **Göbel, P., Dierks, C., Coldewey, W.G.,** (2007) Storm water runoff concentration matrix for urban areas, Journal of Contaminant Hydrology, vol. 91, p. 26–42
12. **Kim, C.H.; Han, C.H.** Numerical simulation of hydraulic transport of soil–water mixtures in pipelines. Open J. Fluid Dyn. 2013, 3, 266–270

13. **McDermott, R., Strong, A. and Griffiths, P.** (2019) Solid Transfer in Low Flow Sewers, the Distance Travelled So Far Is Not Enough. Journal of Environmental Protection, 10, 164-207. https://doi.org/10.4236/jep.2019.10201
14. **Nabil, T.; EL-Sawaf, I.; EL-Nahhas, K.** Sand-water slurry flow modelling in a horizontal pipeline by computational fluid dynamics technique. Int. Water Technol. J. 2014, 4, 1–17
15. **Saleh, A. W., Hassa, S.** (2013), Pricing of Urban Water Supply Using the Smart Market Approach. Environment and Urbanization ASIA 4(1):221-241, March 2013
16. **Song, Y. Ho, Yun, R., Lee, E.H., Lee, J.Ho.** (2018) Predicting Sedimentation in Urban Sewer Conduits. Water, April 2018, 10, 462-478
17. **Shabbir, Y.; Khokhar, M.F.; Shaiganfar, R.;** Wagner, T. Spatial variance and assessment of nitrogen dioxide pollution in major cities of Pakistan along N5-Highway. J. Environ. Sci. 2016, 43, 4–14. [CrossRef] [PubMed]
18. **Zhen, C.; Tian-Jian, H.; Joseph, C. SedFoam.** A multi-dimensional Eulerian two-phase model for sediment transport and its application to momentary bed failure. Coast. Eng. 2017, 119, 32–50.

СПИСОК ЛИТЕРАТУРЫ

1. **Abdelaziz, R., Bakr M.** – I (2012), Inverse Modelling of Groundwater Flow of Delta Wadi El-Arish. Jornal of Water Resource and Protection 2012, vol.4, No.7, July 2012
2. **Arthur, S., Ashley, R., Tait, S. and Nalluri, C.** (1999) Sediment Transport in Sewers—A Step towards the Design of Sewers to Control Sediment Problems. Proceedings of the ICE—Water Maritime and Energy, 136, 9-19.
3. **Batica, J., Goubesville, P.** (2011), Collaborative Research on Flood Resilience in Urban Areas: the CORFU project. 34th World Congress of the International Association for Hydro-Environment Research and Engineering: 33rd Hydrology and Water Resources Symposium and 10th Conference on Hydraulics in Water Engineering. 3914-3920.
4. **Bertrand-Krajewski, J.-L., Briat, P., Scriver, O.,** (1993), Sewer sediment production and transport modelling: a literature review. Journal of Hydraulic Research, vol. 31(4), p.435-460.
5. **Butler D., Luu P.N., Karunaratne S.,** Investigation into sediment deposition in the sewers of the London borough of Lambeth. - First Phase Report, Drainage Research Unit, South Bank Polytechnic, July 1989.
6. **Campisano, A.; Creaco, E.; Modica, C.** Numerical modelling of sediment bed aggradation in open rectangular drainage channels. Urban Water J. 2013, 10, 365–376.
7. **Erik C.Poerse,** Stormwater Governance and Future Cities, Water 2013, 5, 29-52; doi:10.3390/w5010029
8. **Erpicum S., Kerger F., Archambeau P., Dewals B., Pirotton M.,** Experimental and Numerical Investigation of Mixed Flow in a Gallery. Engineering 2009.
9. **Fronczyk, J., Radziemska, M., Dynowski, P., Zbigniew, M., Bazydło** (2016), Quality of Water in the Road Drainage Systems in the Warsaw Agglomeration, Poland. Water 2016, vol 8, p. 429-441.
10. **Gopaliya, K.M.; Kaushal, D.R.** Modeling of soil-water slurry flow through horizontal pipe using CFD. J. Hydrol. Hydromech. 2016, 64, 261–272
11. **Göbel, P., Dierks, C., Coldewey, W.G.,** (2007) Storm water runoff concentration matrix for urban areas, Journal of Contaminant Hydrology, vol. 91, p. 26–42
12. **Kim, C.H.; Han, C.H.** Numerical simulation of hydraulic transport of soil–water mixtures in pipelines. Open J. Fluid Dyn. 2013, 3, 266–270

13. **McDermott, R., Strong, A. and Griffiths, P.** (2019) Solid Transfer in Low Flow Sewers, the Distance Travelled So Far Is Not Enough. Journal of Environmental Protection, 10, 164-207. https://doi.org/10.4236/jep.2019.10201
14. **Nabil, T.; EL-Sawaf, I.; EL-Nahhas, K.** Sand-water slurry flow modelling in a horizontal pipeline by computational fluid dynamics technique. Int. Water Technol. J. 2014, 4, 1–17
15. **Saleh, A. W., Hassa, S.** (2013), Pricing of Urban Water Supply Using the Smart Market Approach. Environment and Urbanization ASIA 4(1):221-241, March 2013
16. **Song, Y. Ho, Yun, R., Lee, E.H., Lee, J.Ho.** (2018) Predicting Sedimentation in Urban Sewer Conduits. Water, April 2018, 10, 462-478
17. **Shabbir, Y.; Khokhar, M.F.; Shaiganfar, R.;** Wagner, T. Spatial variance and assessment of nitrogen dioxide pollution in major cities of Pakistan along N5-Highway. J. Environ. Sci. 2016, 43, 4–14. [CrossRef] [PubMed]
18. **Zhen, C.; Tian-Jian, H.; Joseph, C. SedFoam.** A multi-dimensional Eulerian two-phase model for sediment transport and its application to momentary bed failure. Coast. Eng. 2017, 119, 32–50.

Lyudmila V. Volgina, PhD, Associate Professor of the Department of Hydraulics and Hydraulic Engineering, National Research Moscow State University of Civil Engineering (NRU MGSU), 129337, Russia, Moscow, Yaroslavskoe shosse, 26, phone +7 (495) -287-49-14 ext. 14-19, e-mail: VolginaLV@mgsu.ru

Волгина Людмила Всеволодовна, доцент, кандидат технических наук, доцент кафедры «Гидравлики и гидротехнического строительства» Национального исследовательского Московского государственного строительного университета (НИУ МГСУ), 129337, г. Москва, Ярославское ш., д. 26, тел. +7 (495)-287-49-14 доб.14-19. e-mail: VolginaLV@mgsu.ru

Stanislav A. Sergeev, PhD, Associate Professor of the Department of Hydraulics and Hydraulic Engineering, National Research Moscow State University of Civil Engineering (NRU MGSU), 129337, Russia, Moscow, Yaroslavskoe shosse, 26, phone +7 (495) -287-49-14 ext. 14-19, e-mail: SergeevSA@mgsu.ru.

Сергеев Станислав Алексеевич, кандидат технических наук, доцент кафедры «Гидравлики и гидротехнического строительства» Национального исследовательского Московского государственного строительного университета (НИУ МГСУ), 129337, г. Москва, Ярославское ш., д. 26, тел. +7 (495)-287-49-14 доб.14-19. e-mail: SergeevSA@mgsu.ru.

International Journal for Computational Civil and Structural Engineering, 19(1) 32–40 (2023)

DOI:10.22337/2587-9618-2023-19-1-32-40

LOCAL STABILITY AND NATURAL MOTIONS OF THE MULTI-FACE DOME ROD STRUCTURE

Alexander A. Zhuravlev, Dmitriy A. Zhuravlev

Don State Technical University, Rostov-on-don, RUSSIA

Abstract: The research object is a cyclically symmetric construction of a two-tier dome in the form of a convex polyhedron. Load and deflection critical parameters were determined for this construction pyramidal element. The behavior features of the conservative system in the dome's central assembly vertical displacement critical region value analysis has been carried out. The elastic rod model fluctuating and construction deviations from its equilibrium state reaction have been researched. System's behavior at natural motions and nonlinear restoring force is refined on the base of the findings carried out.

Keywords: polyhedral dome, rod structure, snap-through, restoring force, motion equation, elliptic integral, modular angel, phase plane

ЛОКАЛЬНАЯ УСТОЙЧИВОСТЬ И СВОБОДНЫЕ КОЛЕБАНИЯ СТЕРЖНЕВОЙ КОНСТРУКЦИИ МНОГОГРАННОГО КУПОЛА

А.А. Журавлев, Д.А. Журавлев

Донской государственный технический университет, г. Ростов-на-Дону, РОССИЯ

Аннотация: В качестве объекта исследования рассматривается циклически симметричная конструкция двухъярусного купола в форме выпуклого многогранника, для пирамидального элемента которой определены параметры критической нагрузки и прогиба. Выполнен анализ особенностей поведения консервативной системы в окрестности критического значения вертикального перемещения центрального узла купола. Исследован процесс колебаний упругой стержневой модели и изучена реакция конструкции на отклонения от ее равновесного состояния. На основании полученных результатов уточняется поведение системы при свободных колебаниях и нелинейной восстанавливающей силе.

Ключевые слова: многогранный купол, стержневая конструкция, прощелкивание, восстанавливающая сила, уравнение движения, эллиптический интеграл, модулярный угол, фазовая плоскость

The equilibrium stability rigorous definition considered as a mechanical system motion particular case was firstly given in the A.M. Lyapunov's work[1]. Rod structures in the form of convex polyhedron are trended to the snap-through according to the sustainability research majority were carried out on the static criterion base [2,3,4].The system fluctuation problem of this type in their possible equilibrium states region in the case when value nodal load goes up to the critical level, requires both theoretical and experimental researches, since the solution of this actual problem is still far from its complete solution. The considered problem has become more acute recently since high sensitivity of the shell type long span rod structure to the snap-through of the both individual and multiply connected assemblies was identified as a result of major disasters.

Circumscribed according to the 320-hedron scheme sphere of spatial rod construction in the form of a two-tier part of a polyhedral dome

whole surface section is chosen as a research object (Fig. 1). A vertical force P is placed at the vertex of the pentagonal pyramidal element. Force P is placed at the joint 1, in which five symmetrical inclined rods 1-2 are connected (Fig. 2).

The inclination rod angel α in comparison with its initial value α_0 changes. Two-tier dome pentagonal circle is assumed inextensible according to the $l_0 \sin\alpha_0 = l \sin\alpha = a$.

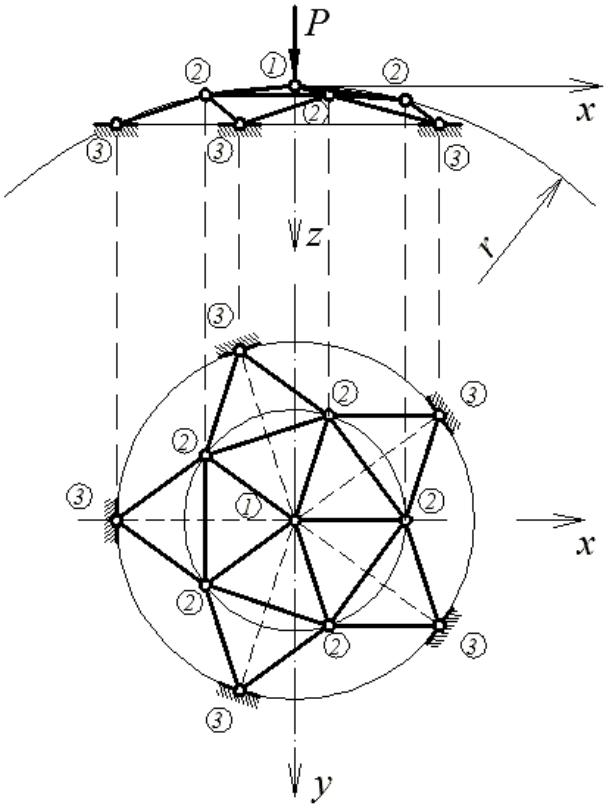

Figure 1. Spatial rod construction in the form of two-tier polyhedral dome

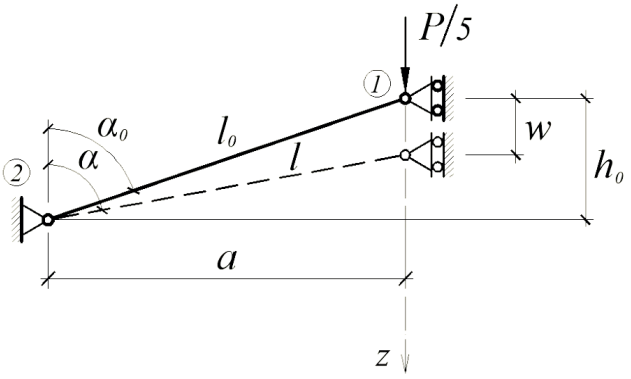

Figure 2. Pentagonal pyramid rod elements design model

Rod structure behavior under the load P_1 and P_2 the forces placed at the joint 1 and 2 have to be analyzed in general case to determine possibility to add the upper tier pentagonal circle non-deformability restriction. The nodal load uneven distribution influence on the local stability of the considered rod system effect must be considered. This distribution is set according to the load transferring area calculated for this joint type on the horizontal domed surface projection for the central joint 1 and five peripheral joints 2. For example, in this case, the ratio of the joint forces is $P_2 / P_1 = 1{,}34$. This situation is clearly depicted on the system equilibrium diagram (Fig. 3), $P_1^* = P_1 / (5EF)$; $\eta_{12} = \eta_1 - \eta_2 = (w_1 - w_2)/l_{12}$ is accepted.

Let us denote that central joint snap-through load level increased by 15% under the force P_2 (curve 1) in comparison with the case when the circle is inextensible (curve 2).

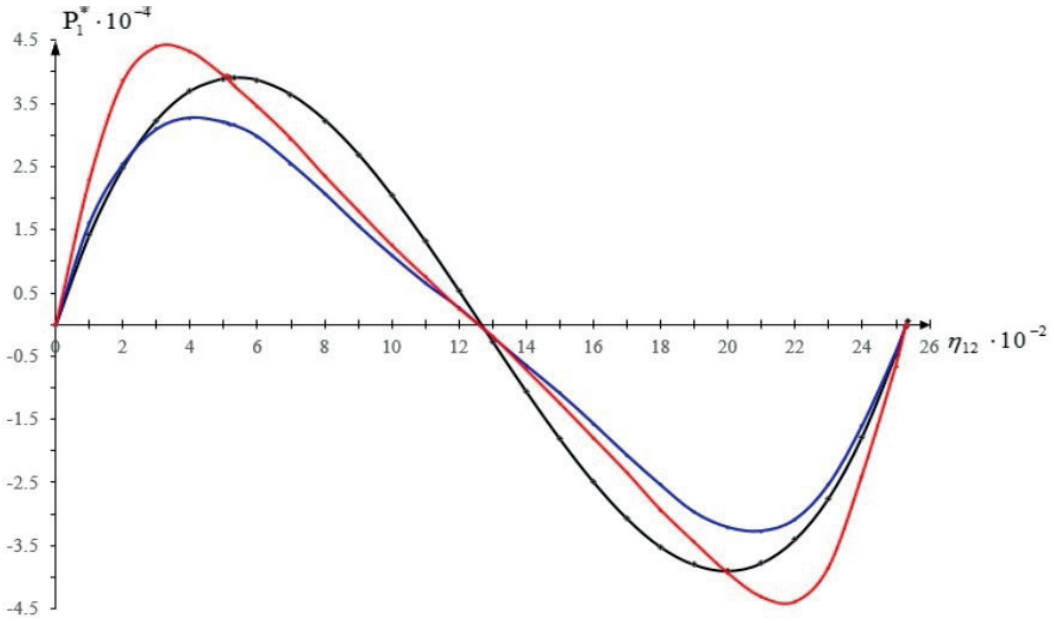

Figure 3. Equilibrium states diagram for a two-tier part rod construction in the form of a 320-hedron

If the coefficient $k = 5P_2 / P_1$ is added then the formula for the critical load changes to [5]:

$$P_{1,cr.} = \frac{10\sqrt{3}}{9}\frac{EF}{1+k}\cos^3\gamma_{23}. \qquad (1)$$

The expression (1) is written as follows in the case of non-deformability pentagonal circle:

$$P_{1,cr.} = \frac{5\sqrt{3}}{9}EF\cos^3\gamma_{12}. \qquad (2)$$

Equating the right-hand sides of the expressions (1) and (2) to each other, the result is:

$$k = 2\left(\cos\gamma_{23}/\cos\gamma_{12}\right)^3 - 1, \qquad (3)$$

whence it follows that $k = 0{,}0723$ and $P_2 = 0{,}014P_1$. In other words, tensile forces take place in the pentagonal circle rod elements only in the case when $P_2 < 0{,}014P_1$

The curve 3 shows rod structure behavior in case when both radial displacement of the nodes 2 in the in the horizontal circle plane and the vertical displacement of the nodes 1,2 are considered. In this case the critical load level is decreased by 11% in comparison with its pentagonal circle non-deformability value.

The curves' 2 and 3 almost complete coincidence is clearly observed in the parameter values interval η_{12} $0 < \eta_{12} < 3\cdot 10^{-3}$.

In this case, the relationship between the force P and the vertical displacement w is expressed:

$$P = 5EF\left(1-\frac{w}{a}\tan\alpha_0\right)\left[\frac{1}{\sqrt{\tan^2\alpha_0+\left(1-\frac{w}{a}\tan\alpha_0\right)^2}}-\cos\alpha_0\right] \qquad (4)$$

After adding a new variable $\xi = 1 - \zeta$,where $\zeta = \frac{w}{a}\tan\alpha_0$, the functional relationship $P = P(\xi)$ is:

$$\hat{P} = \xi\left(\frac{1}{\sqrt{\tan^2\alpha_0 + \xi^2}} - \cos\alpha_0\right). \quad (5)$$

$\hat{P} = P/(5EF)$ is a nondimensional load parameter.

Let us use the condition to determine critical load

$$\frac{d\hat{P}}{d\xi} = 0,$$

and write it in the following manner:

$$\frac{d\hat{P}}{d\xi} = \left(\tan^2\alpha_0 + \xi^2\right)^{-1/2} - \\ -\cos\alpha_0 - \xi^2\left(\tan^2\alpha_0 + \xi^2\right)^{-3/2} = 0 \quad (6)$$

Assuming that $\tan^2\alpha_0 + \xi^2 = z^2$, we determine:

$$z_{кр}^3 = \tan^3\alpha_0\left(\sin\alpha_0\right)^{-1};$$

$$z_{кр} = \tan\alpha_0\left(\sin\alpha_0\right)^{-1/3}. \quad (7)$$

The critical load parameter value $\hat{P}_c$ is equal to

$$\hat{P}_{cr} = \left(1 - \sin^{2/3}\alpha_0\right)^{3/2}. \quad (8)$$

Firstly to determine the value corresponding to the moment when the joint load reaches its critical level we must note that:

$$\xi^2 = \tan^2\alpha_0\sin^{-2/3}\alpha_0\left(1 - \sin^{2/3}\alpha_0\right). \quad (9)$$

On the other hand the equation must be $\xi^2 = (1-\varsigma)^2$ must be.

Equating the right-hand sides of the last two equations to each other, the result is quadratic equation for the nondimensional displacement parameter

$$\varsigma^2 - 2\varsigma + 1 - \tan^2\alpha_0\sin^{-2/3}\alpha_0\left(1 - \sin^{2/3}\alpha_0\right) = 0. \quad (10)$$

The solution of the equation (10) is:

$$\varsigma_{кр} = 1 - \tan\alpha_0\left(\sin^{-2/3}\alpha_0 - 1\right)^{1/2} \quad (11)$$

for the pyramidal element with 320-hedron spatial configuration $\alpha_0 =$ 82.2°. According to this, the numerical values of the trigonometric functions in the initial position of the rod system are:

$$\sin\alpha_0 = 0{,}991950;\ \cos\alpha_0 = 0{,}126591;$$
$$\tan\alpha_0 = 7{,}83586.$$

The vertical displacement nondimensional parameter required value can be found using the values obtained from the expression (11),

$$\varsigma_{cr} = 1 - 0{,}575 = 0{,}425 = 17/40.$$

The rod system equilibrium states diagram, constructed with the dependence (4), is shown in Fig. 4.

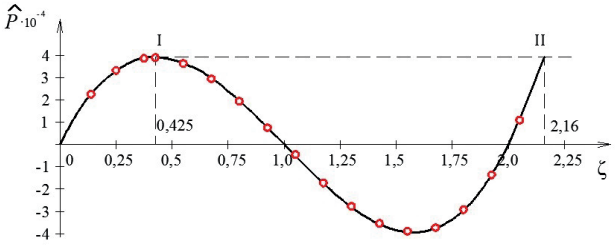

Figure 4. Dependency diagram for a pyramidal element of a rod construction

As we can see, when the maximum load level is reached, the system jumps from the equilibrium state I to the position II. The circles show the equilibrium states diagram for the pyramidal element of a two-tier dome. The stability analysis of this element was carried out in [5] by using the energy method.

Snap-through of the rod construction is not allowed. Let us analyze the stability of its equilibrium state when it is near critical value of the pentagonal pyramidal 320-hedron element top vertical displacement. In other words, let us choose a point on the system equilibrium states curve where the inequation $\varsigma = 2/5 < \varsigma_{cr}$ is valid. The nondimensional displacement parameter value corresponding to this displacement is equal to $\hat{P}(2/5) = 0{,}393 \cdot 10^{-3}$. As for the initial forces of axial compression in the rods, they are determined by the equation

$$S_0 = -\frac{8}{9} EF \cos^2 \alpha \quad . \tag{12}$$

The rod structure of two-tier dome in the form of the 320-hedron fluctuating problem solution is considered only taking account of the fluctuations along the mass m vertical axis held by five meridional direction rods in the regular pentagonal pyramid central joint.

Fluctuating at the initial displacement $(x_0)_{t=0} = x_0$ and without initial speed $(\dot{x}_0)_{t=0} = 0$ at dome pyramidal element central joint deviation from the equilibrium by slight displacement x in the upward vertical mass m motion equation has the following form [6]:

$$\ddot{x} + p^2 f(x) = 0 \quad . \tag{13}$$

Here $f(x)$ means

$$f(x) = 2x + 27\frac{\tan\alpha}{a}x^2 + 9\frac{\tan^2\alpha}{a^2}x^3 \quad . \tag{14}$$

In its turn, $p^2 f(x)$ is nothing other than the restoring force related to the unit mass in the x function displacement.

In this case $\cot\alpha = (3/5)\cot\alpha_0 = 0{,}076571$, it follows that, $\tan\alpha = 13{,}0598$ and $\cos\alpha = 0{,}076348$. The calculation for the p^2 is : $p^2 = 0{,}8216 g/a$.

Mass motion time from the extreme position $(x = x_0)$ to the position $(x = 0)$, when the system goes back to its initial state is determined by the following formula[7]:

$$\tau = -\int_{x_0}^{0} \frac{dx}{\sqrt{2p^2 \int_x^{x_0} f(x)dx}} = \int_0^{x_0} \frac{dx}{\sqrt{2p^2 \int_x^{x_0} f(x)dx}} \quad . \tag{15}$$

Integral radicand according to (14) is:

$$\int_x^{x_0} f(x)dx = \int_x^{x_0} \left(2x + 27\frac{\tan\alpha}{a}x^2 + 9\frac{\tan^2\alpha}{a^2}x^3 \right) dx \quad . \tag{16}$$

As a result of integration and substitution in (15), we have

$$\tau = \frac{\sqrt{2}}{2p} \int_0^1 \frac{dz}{\sqrt{(1-z^2) + 6\gamma(1-z^3) + \gamma^2(1-z^4)}} \quad . \tag{17}$$

Here is: $z = \frac{x}{x_0}$, $\gamma = \frac{3}{2}\frac{x_0}{a}\tan\alpha$.

Further differential $\frac{dz}{\sqrt{R}}$ must be transformed to obtain polynomial under the radical that doesn't contain the variable z uneven degree. Assuming that $u = \sqrt{1-z^2}$ and making a substitution, we obtain $dz = -\frac{u}{\sqrt{1-u^2}} du$

$$\tau = \frac{\sqrt{2}}{2p}\int_0^1 \frac{du}{\sqrt{1-u^2}\sqrt{1+9\gamma+2\gamma^2-\gamma(3+\gamma)u^2}}. \quad (18)$$

In this case we have [8]:

$$\int_0^x \frac{dt}{\sqrt{a^2-t^2}\sqrt{c^2-t^2}} = \frac{1}{c}F\left(\frac{a}{c},\varphi\right). \quad (19)$$

Here $F\left(\frac{a}{c},\varphi\right)$ is the first kind elliptic integral. According to the collating (18) with the standard integral (19) we conclude that

$$a^2 = 1;\ c^2 = \frac{1+9\gamma+2\gamma^2}{\gamma(3+\gamma)},$$
$$\sin\varphi = \frac{x}{a} = 1;\ \varphi = \frac{\pi}{2}.$$

To find the numerical value of γ quantity, let us use the equation $x_0 \tan\alpha_0 / a = 1/40$. As $\tan\alpha_0 = 3\tan\alpha/5$, we determine:

$$\frac{x_0}{a}\tan\alpha = \frac{1}{24};\ \gamma = \frac{3}{2}\frac{x_0}{a}\tan\alpha = \frac{1}{16}.$$

The calculations results:

$$c^2 = \frac{1+\gamma(9+2\gamma)}{\gamma(3+\gamma)} = 8{,}20408;\ c = 2{,}8643;$$
$$\frac{1}{c} = 0{,}3491.$$

Let us find the integral $F(\theta)$ in the case when the amplitude is equal to $\varphi = \pi/2$ and the modulus is equal to $k = 0{,}3491$. The modular angle $\theta = 20{,}43^\circ$ will be determined from the equation $\sin\theta = 0{,}3491$.

The 20° angel corresponds to $F(20^\circ) = 1{,}62003$ and 21° angel corresponds to $F(21^\circ) = 1{,}62523$ according to the table [9] and the amplitude $\varphi = \pi/2$. Assuming that the $F(\theta)$ integral increment is proportional to the angle θ, the result is:

$$\frac{F(20{,}43^\circ) - F(20^\circ)}{F(21^\circ) - F(20^\circ)} = 0{,}43.$$

Whence it follows that $F(20{,}43^\circ) = 1{,}6275$. $\tau = 0{,}918/p$ is to be found with the expression (18).

When deriving the solution numerically, we note that the expression (14) contains the summand x in the first degree and further the motion differential equation (13) is to be written in a slightly modified form:

$$\ddot{\eta} + \overline{p}^2(\eta + \delta_i) = 0. \quad (20)$$

Here is: $\overline{p}^2 = 2p^2$; $\eta = \frac{x}{a}\tan\alpha$ and δ_i means that:

$$\delta_i = \frac{9}{2}\left(3\eta^2 + \eta^3\right).$$

Further let us imagine that the entire time interval τ is divided into a number of small intervals Δt during which the value δ_i is considered constant and equal to its value at the beginning of each of such intervals. The η_i и $\dot{\eta}_i$ are consider as the parameters of displacement and speed at $t_1 = 0$. The equation solution (20) is to be written in the following form:

$$\eta = (\eta_i + \delta_i)\cos\overline{p}t_1 + \frac{\dot{\eta}_i}{\overline{p}}\sin\overline{p}t_1 - \delta_i \quad (21)$$

As a result of time differentiation (21), we got:

$$\frac{\dot{\eta}}{\overline{p}} = -(\eta_i + \delta_i)\sin \overline{p}t_1 + \frac{\dot{\eta}_i}{\overline{p}}\cos \overline{p}t_1 \quad . \quad (22)$$

(21) and (22) are to be squared and summed up. The result is:

$$(\eta + \delta_i)^2 = (\eta_i + \delta_i)^2 + \left(\frac{\eta_i}{\overline{p}}\right)^2 \quad . \quad (23)$$

Thus, we make sure that the equation solution (20) is performed on the $(\eta, \dot{\eta}/\overline{p})$ phase plane of the other circle with the center on the η axis and δ_i coordinate.

Firstly, the value $\ddot{\eta}_0$ is calculated and then the $\dot{\eta}_1$ and η_1 approximate values are determined from [10] at the initial conditions $\eta = \eta_0$ and $\dot{\eta} = 0$ for $t = 0$:

$$\dot{\eta}_1 = \dot{\eta}_0 + \ddot{\eta}_0 \Delta t \; ; \quad \eta_1 = \eta_0 + \frac{\dot{\eta}_0 + \dot{\eta}_1}{2} \quad .$$

Substituting η_1 to the equation (20) instead of η, $\ddot{\eta}_1$ can be found . The most accurate $\dot{\eta}_1$ and η_1 approximations could be derived with this value from the expressions:

$$\dot{\eta}_1 = \dot{\eta}_0 + \frac{\ddot{\eta}_0 + \ddot{\eta}_1}{2}\Delta t \; ; \quad \eta_1 = \eta_0 + \frac{\dot{\eta}_0 + \eta_1}{2} \quad .$$

The values η_2, $\dot{\eta}_2$ and $\ddot{\eta}_2$ for the moment $t_2 = 2\Delta t$ is to be calculated by repeating in order this procedure which was described above.

This values for the moments $t_3 = 3\Delta t$, $t_4 = 4\Delta t$, .., $t_n = n\Delta t$ are calculated analogical.

The numerical integration results are performed on the phase plane (Fig. 5).

Time of the first fluctuation mass cycle m is equal to $\tau = 0{,}939\frac{1}{p}$ with the 2,3% error according to the phase curve shown in the graph. The restoring force grows faster than the deflection in the case when the initial displacement values are increased in this phase curve section. The mass m will take the position indicated by the letter G which corresponds to the central joint vertical displacement critical value at the fluctuation second cycle.

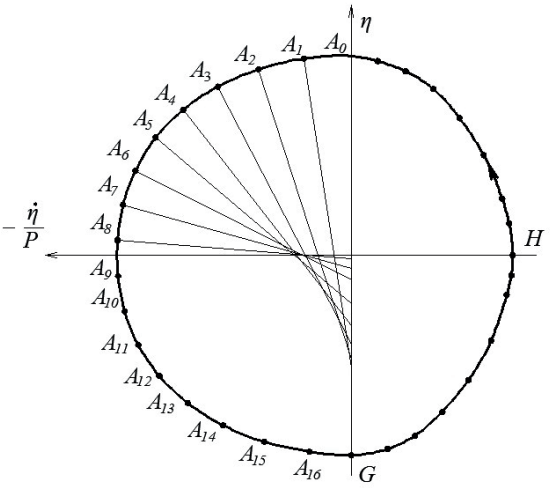

Figure 5. speed-displacement curve on the phase plane for the system fluctuation full cycle

The sign in front of the second summand expression in parentheses is reversed at the phase curve construction for the second fluctuation cycle in the motion equation (20). Due to this operation at increasing its initial displacement value the restoring force growth slows down.

The phase trajectory will have a spiral form instead of a closed curve at the damped fluctuation process. The phase speed will not be equal 0 anywhere in this case, despite it will be continuously decreased as the point approximating to the origin of coordinates.

Comparing the derived data, we come to the conclusion that the two-tier dome part structure snap-through phenomenon can be caused by the rod system fluctuations excitation with a nonlinear restoring force as a result of its central

joint deviation from the equilibrium state in the vertical displacement parameter critical value surroundings.

The fact that fluctuations period is inversely related to the amplitude η_0 in the considered case has to be denoted.

Thus, it could be argued that the danger of its snap-through increases significantly in the case when the rod structure fluctuates with initial speed. Such result in the structure operation is practically inevitable in the case when its carrying capacity is completely exhausted due to the critical load close level. From this it follows that the mass disturbed motion total energy will exceed the difference between the initial potential energy and the potential energy of the system at the considered moment.

REFERENCES

1. **Lyapunov A.M.** Obshhaya zadacha ob ustojchivosti dvizheniya [The general problem of traffic stability]. Leningrad, Moscow, ONTI, 1935. 386 p. (in Russian)
2. **Savel'ev V.A.** Ustojchivost' setchatykh kupolov [Mesh Dome Stability] Metallicheskie konstruktsii. Rabota shkoly prof. N.S. Streletskogo [Metal constructions. School work prof. N.S. Streletsky]. Moscow, Strojizdat, 1966. Pp. 325–339. (in Russian)
3. **Zhuravlev A.A.** Proshhelkivanie sterzhnevoj konstruktsii setchatogo kupola v forme 980-grannika [Clicking the core structure of the mesh dome in the shape of a 980-sided.]. Izvestiya vuzov. Stroitel'stvo [News of Higher Educational Institutions. Construction]. 1983. No. 3. Pp. 34 – 39. (in Russian)
4. **Zhuravlev A.A.** K voprosu o mestnoj ustojchivosti setchatykh kupolov s treugol'noj reshetkoj [On the issue of local stability of mesh domes with a triangular lattice.]. Izvestiya vuzov. Stroitel'stvo i arkhitektura [News of Higher Educational Institutions. Construction and architecture.]. Novosibirsk, 1971. No. 5. Pp. 77–80. (in Russian)
5. **Beskopyl'nyj A., Zhuravlev A., Shilov A.** Buckling analysis of rod structure of the two-tier dome. MATEC Web of Conferences. 2018. No. 193
6. **Bogolyubov N.N., Mitropol'skiy Yu.A.** Asimptoticheskiye metody v teorii nelineynykh kolebaniy [Asymptotic methods in the theory of nonlinear oscillations]. Moscow, Gostekhizdat, 1955. 447 p. (in Russian)
7. **Timoshenko S.P**. Kolebaniya v inzhenernom dele [Fluctuations in engineering]. Moscow, Fizmatgiz, 1959. 439 p. (in Russian)
8. **Sikorskij Yu.S.** Ehlementy teorii ehllipticheskikh funktsij s prilozheniyami k mekhanike [Elements of the theory of elliptic functions with applications to mechanics]. Moscow. 2006. 368 p. (in Russian)
9. **Yanke E., Ehmde F.** Tablitsy funktsij s formulami i krivymi [Function tables with formulas and curves]. Moscow, Fizmatgiz, 1959. 420 p. (in Russian)
10. **Krylov A.N.** Lektsii o priblizhennykh vychisleniyakh [Lectures on approximate calculations]. Leningrad, Moscow, Izdatel'stvo Akademii nauk SSSR [Publishing House of the USSR Academy of Sciences]. 1935. 541 p. (in Russian)

СПИСОК ЛИТЕРАТУРЫ

1. **Ляпунов А.М.** Общая задача об устойчивости движения. ОНТИ. Л.–М.: 1935. – 386 с.
2. **Савельев В.А.** Устойчивость сетчатых куполов // Металлические конструкции. Работа школы проф. Н.С. Стрелецкого. – М.: Стройиздат, 1966. – С. 325–339.
3. **Журавлев А.А.** Прощелкивание стержневой конструкции сетчатого купола в форме 980-гранника. Изв.

вузов. Строительство и архитектура, №3, 1983. – С. 34 – 39.
4. **Журавлев А.А**. К вопросу о местной устойчивости сетчатых куполов с треугольной решеткой. Изв. вузов. Строительство и архитектура, №5, Новосибирск, 1971. – С. 77–80.
5. **Beskopylny A., Zhuravlev A., Shilov A.** Buckling analysis of rod structure of the two-tier dome // MATEC Web of Conferences. 2018. No. 193
6. **Боголюбов Н.Н., Митропольский Ю.А.** Асимптотические методы в теории нелинейных колебаний. – М.: Гостехиздат. – 1955. –447 с.
7. **Тимошенко С.П.** Колебания в инженерном деле. – М.: Физматгиз. – 1959.–439 с.
8. **Сикорский Ю.С.** Элементы теории эллиптических функций с приложениями к механике. – М.: Ком. Книга. – 2006.–368 с.
9. **Янке Е., Эмде Ф.** Таблицы функций с формулами и кривыми. – М.: Физматгиз. – 1959. –420 с.
10. **Крылов А.Н.** Лекции о приближенных вычислениях. – Л.-М.: Изд-во Акад. наук СССР. –1935. – 541 с.

Zhuravlev Alexander Alexandrovich, DSc, Professor Don State Technical University, Russia. +8(8632)918-938; e-mail: heligoland@mail.ru.

Zhuravlev Dmitriy Alexandrovich, PhD, Ass. Professor Don State Technical University, Russia. +8(8632)918-938; e-mail: rodjer1980@mail.ru.

Журавлев Александр Александрович. Профессор кафедры металлических деревянных и пластмассовых конструкций Донского государственного технического университета, доктор технических наук; 344003, г. Ростов-на-Дону, пл. Гагарина, 1; телефон: +8(8632)918-938; e-mail: heligoland@mail.ru.

Журавлев Дмитрий Александрович. Доцент кафедры металлических, деревянных и пластмассовых конструкций Донского государственного технического университета, кандидат технических наук; 344003, г. Ростов-на-Дону, пл. Гагарина, 1; телефон: +8(8632)918-938; e-mail: rodjer1980@mail.ru.

DOI:10.22337/2587-9618-2023-19-1-41-54

COMPARISON OF PHYSICAL AND MECHANICAL TEST METHODS FOR COARSE AGGREGATE ACCORDING TO THE EGYPTIAN AND RUSSIAN STANDARD METHODS

Khalid M. Yousri [1], Dmitrii N. Korotkikh [2,3], Dmitry E. Kapustin [2,3], Luka I. Efishov [2,3]

[1] Housing and Building National Research Center, Cairo, EGYPT
[2] National Research Moscow State University of Civil Engineering, Moscow, RUSSIA
[3] Joint Stock Company "Institute "Orgenergostroy", Moscow, RUSSIA

Abstract: Physical and mechanical test methods for coarse aggregate have been studied under the commercial program of Egyptian and Russian standard test methods comparison. Theoretical and practical research has been carried out using Egyptian raw materials from reputed occurrences. The research shows that the main part of tests is either the same or comparable, which can make the quality assessment easier for both sides provided that the converting rules are followed. Recalculating methods for important geometrical and mechanical properties are proposed. Converting tables, graphics and Russian standards are provided in order to assist Egyptian suppliers with participating in tendering for Al Dabaa NPP project.

Keywords: national specifications comparison, international standards, El-Dabaa NPP, physical and mechanical test methods, concrete aggregate characteristics, raw materials

СОПОСТАВЛЕНИЕ ФИЗИЧЕСКИХ И МЕХАНИЧЕСКИХ МЕТОДОВ ИСПЫТАНИЙ ДЛЯ КРУПНОГО ЗАПОЛНИТЕЛЯ ПО ЕГИПЕТСКИМ И РОССИЙСКИМ СТАНДАРТАМ

Х.М. Йосри [1], Д.Н. Коротких [2,3], Д.Е. Капустин [2,3], Л.И. Ефишов [2,3]

[1] Национальный исследовательский центр жилищного строительства, г. Каир, ЕГИПЕТ
[2] Национальный исследовательский Московский государственный строительный университет, г. Москва, РОССИЯ
[3] Акционерное общество «Институт "Оргэнергострой"», г. Москва, РОССИЯ

Аннотация: В рамках выполненной работы по сопоставлению египетских и российских стандартных методов испытаний были проанализированы методы физико-механических испытаний крупного заполнителя. Теоретические и практические исследования были проведены на материалах, отобранных из наиболее распространенных месторождений Египта. Исследование показывало, что большинство испытаний сопоставимы или одинаковы, что может облегчить мероприятия по оценке качества по стандартам Египта и РФ, при условии соблюдения правил пересчета. Разработаны методы пересчета основных геометрических и механических характеристик. Результаты представлены в виде сопоставительных таблиц и графиков. Российские стандарты представлены для того, чтобы помочь египетским поставщикам участвовать в тендерах по проекту АЭС Аль-Дабаа.

Ключевые слова: сопоставление национальных стандартов, международные стандарты, АЭС Эль-Дабаа, физические и механические методы испытаний заполнителей, характеристики заполнителя для тяжелых бетонов, сырьевые материалы

INTRODUCTION

This study was motivated by the results of analysis and comparison of Russian and Egyptian test methods for fresh concrete, hardened concrete and its raw materials. Technical standards have been analyzed in 2020-2021 as a part of pre-operational work before the construction of the Al-Dabaa NPP.

According to project, fresh and hardened concretes have to be specified in compliance with Russian technical documents. At the same time, it is necessary to use local materials, which are produced and verified according to the Egyptian standards. Preparatory literature review showed only few works about specifications comparison, unfortunately, they are related to metal materials [1-3]. This is why at the pre-construction stage it is important to find a way to compare the specifications of raw materials for concrete (cement, coarse and fine aggregates, chemical and mineral additives) for such a significant project. A reliable recalculating method should be proposed if some of the characteristics cannot be compared without tests.

It was discovered that Egyptian specifications for cement, fresh and hardened concrete are harmonized with the international standards, meaning that the test methods in both countries are the same, which simplifies the quality estimation. The main difficulty appeared with the physical and mechanical characteristics of coarse aggregate. In Egypt, aggregates are still widely examined for compliance with ASTM [4], as it was ordered in ECP 203-2018 [5], despite the fact, that the updated in 2020 version of ECP 203[6] is based on BS EN standard specifications [7]. A transition from US to European standards will take some time for producer to adapt their production, even in 2021 it hard to find aggregates produced according to BS EN 12620. However it is worth mentioning, that distinction between foreign tests is not that big, as it is for Russian specifications. Investigation has shown that the main difference concentrated in the methods of physical tests which are tied up with the geometrical parameters of grains. This is the reason why in this study we have tried to develop a recalculating method for grain size distribution curves gained in accordance with the Egyptian test method. Another reason is that grains size distribution of coarse aggregates affect important characteristics, such as bulk and packing density and mechanical properties (Aggregate Crushing Value (ACV), Ten Percent Fines Value (TFV), Aggregate Impact Value (AIV), Los Angeles Abrasion Resistance).

As an aside, it is important to notice, that the same work was also performed for special types of concrete, including heavy-weight, lightweight and serpentinite concrete for biological shielding. Consideration of these results is beyond the scope of this study.

MATERIAL AND METHODS

Test Methods

Physical and mechanical characteristics of coarse aggregates according to Russian specifications for normal-weight concrete [8] and Egyptian Code of Practice for concrete structures are presented in Table 1. Unlike international standards, the abovementioned Russian standards are available on the internet and it is possible to get familiar with them using machine translation tools. The links are provided in the References section.

According to recent updates the ECP 203-2020 is mainly focused on mechanical requirements for aggregate such as impact value (SZ) and resistance to fragmentation (LA). Recently mentioned ACV and TFV are no longer mandatory. Physical and chemical test methods, such as: water absorption, mean and bulk density and organic impurities have minor distinctions in both countries, due to its nature, and not presented in this study. More accurate information about EN and GOST test methods comparison described by Lyapidevskaya et al. [20]

Table 1. Main physical and mechanical characteristics for coarse aggregates required for both countries

Characteristic	Test method acc. ECP 203-18	Test method acc. ECP 203-20	Test method in Russia
Grain size distribution	ASTM C136-19[9]	EN 933-1:2012	GOST 8269.0-97[10] sec. 4.3
Materials Finer than 75-µm (No. 200) Sieve	ASTM C 117-17[11]	-	GOST 8269.0-97 sec. 4.5.3
Materials Finer than 63-µm Sieve	-	EN 933-1:2012[12]	
Los Angeles abrasion resistance	ASTM C 131/131M-20[13]	BS EN 1097-2:2020[14]	GOST 8269.0-97 sec. 4.10
Impact value	BS 812-112:1990[15]	BS EN 1097-2:2010	GOST 8269.0-97 sec. 4.11 (not obligatory)
Flakiness index	BS 812-105.1:1989[16]	EN 933-3:2012[17]	GOST 8269.0-97 sec. 4.7
Aggregates crushing value (ACV)	BS 812-110:1990[18]	Not carried out	GOST 8269.0-97 sec. 4.8
Ten percent value (TFV)	BS 812-111:1990[19]	Not carried out	Not carried out

According to recent updates the ECP 203-2020 is mainly focused on mechanical requirements for aggregate such as impact value (SZ) and resistance to fragmentation (LA). Recently mentioned ACV and TFV are no longer mandatory. Physical and chemical test methods, such as: water absorption, mean and bulk density and organic impurities have minor distinctions in both countries, due to its nature, and not presented in this study. More accurate information about EN and GOST test methods comparison described by Lyapidevskaya et al. [20]

Grain Size Distribution

In both countries, grain size distribution curves are obtained after screening on control sieves. The main difference lies in the size and shape of sieve openings.

In Russia, grain is sized in accordance with GOST 8269.0-97, sec. 4.3, on sieves with rounded openings of the following sizes: ○ 25, ○ 20, ○ 15, ○ 12.5, ○ 10, ○ 7.5, ○ 5, ○ 2.5, and □ 1.25. After screening, the mass of **retained grains** is to be calculated on each sieve in percentage.

In Egypt, grain is sized in accordance with ASTM C136-19 on sieves with squared openings of the following sizes: □ 37.5, □ 25, □ 19, □ 12.5, □ 9.5, □ 4.75, □ 2.36, and □ 1.18. After screening, the mass of **passed grains** is to be calculated on each sieve in percentage. In EN 933-2 squared openings are also used: □ 31.5, □ 16, □ 8, □ 4, □ 2, □ 1, □ 0.5, □ 0.25, □ 0.125, and □ 0.063.

Materials Finer than 75-µm (No. 200) and 63-µm sieves

The wet sieving method is used both in Russia and Egypt where a control sample is washed on a sieve with a certain opening size. A percentage of passed particles is to be calculated as a difference between the mass of the sample before testing and after washing.

For this test, in Egypt there are following sieves: for ASTM the upper one, with the opening size of 1.18 mm (No. 16), and the bottom one (control sieve), with the opening size of 75-μm (No. 200) or for BS EN - 1 mm (upper sieve) and 63-μm (control sieve). In Russia – 1.25 mm (N125) and 50-μm (N005). In both cases, the upper sieve serves to protect the thin mesh of the control sieve against the pointy edges of coarse aggregate.

Los Angeles Abrasion Resistance

In both countries, the abrasion resistance of coarse aggregates is measured using a shelf drum. A sample of aggregate is loaded into a shelf drum with steel or cast iron spheres (∅ 46…48 mm and m = 390…445 g), then the drum rotates at a constant speed of 30-33 rpm. The number of rotations and abrasion spheres is specified in accordance with the coarse aggregate grading. A percentage of mass loss is to be calculated as a difference between the mass of the sample before testing and after screening on a control sieve.

Both methods are close enough for coarse grades 5 to 10 mm and 10 to 20 mm according to GOST or 6.3 to 9.5 mm (grade C) and 12.5 to 19 mm (grade B) according to ASTM. In either way, the mass of the sample is 5 kg and the number of drum rotations is 500. The difference between the methods is in the size of control sieves' openings – 1.25 mm (N125) in Russia and 1.70 mm (No. 12) in Egypt. Equipment and test procedure according to BS EN is almost identical, except using 1.6 mm sieve as control.

Flakiness Index

Grains with the length three times greater than their width are to be counted as flaky according to the Russian standard. The quantity can be measured either using shell sieves or manually using a shape index caliper.

In Egypt, it was common to use the British approach to define the quantity of flaky grains. Its major difference lies in the alternative collection of samples and the definition of flakiness. Grains are to be considered as flaky if their width is lesser than 0.6 of mean fraction size (D_m) which is calculated as the average of two nearest sieves (Eq. 1):

$$D_m = \frac{d + D}{2}, \tag{1}$$

where D_m is mean grain size of fraction (mm), d is bottom sieve opening size (mm), D is upper sieve opening size (mm).

For each fraction size, sieves with shell openings were designed. Control fractions and sieve shell openings according to the Russian and Egyptian test methods are presented in Table 2.

Latest version of Egyptian Code requires using BS EN 933-3 method, which is a bit simpler. Flaky grains are those with dimensions lesser than $D_i/2$. For each grain size there are certain d_i/D_i groups: 31.5/40, 25/31.5, 20/25, 16/20. 12.5/16, 10/12.5, 8/10, 6.3/8, 5/6.3, 4/5.

Table 2. Aggregate Size-Fraction and Shell Openings

Parameter	Russian method		Egyptian method		
Size-fraction, mm	5-10	10-20	6.3-10	10-14	14-20
Opening L x W, mm	10 x 2.5	20 x 5	30 x 4.9	40 x 7.2	50 x 10.2

Aggregate Crushing Value (ACV)

In both countries, the strength of coarse aggregate is measured after compression test in a special cylinder (Fig. 1).

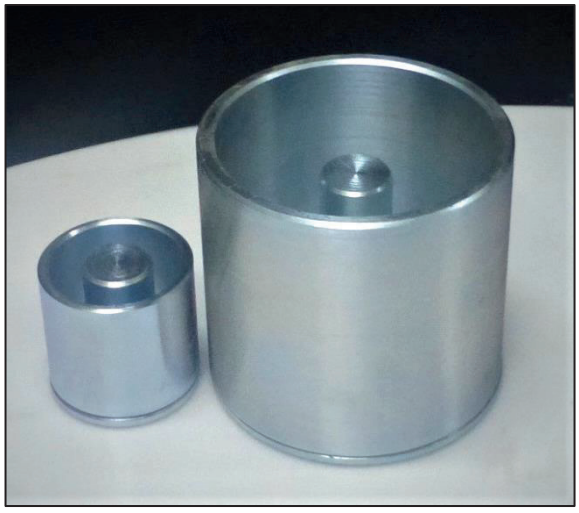

a) Russian Cylinders Ø 75 and Ø 150 mm

b) BS 812:110 Cylinders Ø 154 and Ø 78 mm

Figure 1. Cylinders according to Russian and Egyptian standards

In Russia, ACV is determined using 5 to 10 mm and 10 to 20 mm size fractions. A test sample is put into a cylinder with the inside diameter of 150 mm and the height of 146 mm (Fig. 1a), then the sample is compressed under a 200 kN load at a loading rate of 1…2 kN per second. After the compression is over, ACV is calculated as a difference between the initial mass and the mass after screening on a sieve 2.5 mm for 10 to 20 mm fractions and 1.25 for 5 to 10 mm fractions.

In Egypt, the British test method, which is more concerned about preparation of control samples than the Russian one, was adopted. According to the British method, the main fraction size is 10 to 14 mm. A test sample is put in a cylinder with the inside diameter of 154 mm and the height of 125…140 mm (Fig. 1b), then the sample is compressed under a 400 kN load at the loading rate of 0.67 kN per second. After the compression is over, ACV is calculated as a difference between the initial mass and the mass after screening on a 2.38 mm sieve.

According to Appendix A to BS 812-110:1990, it is possible to use fraction sizes other than 10 to 14 mm. For example, to test 10 to 6.3 mm fractions a small cylinder with the inside diameter of 78 mm, the height of 70…85 mm and compression under the load of 100 kN is used. However, a notable difference remains compared to the Russian method: the load is 50 kN and the height of the test cylinder is 150 mm.

Raw Materials

Control samples for this study were taken from the following occurrences:

- Suez, Attaka (dolomite);
- Matrouh, New Alamein (limestone);
- Matrouh, Al Dabaa (limestone);
- Giza, El Fayoum (basalt).

The chosen occurrences are the main sources of coarse aggregates for civil construction in Egypt. Dolomite aggregates from Attaka, Muhafazah Suez, are considered as the most qualitative due to their stable composition and low alkali reactivity. Then comes moderate limestone from El-Alamein occurrence, Muhafazah Matruh, extended along Wadi-El-Natroon Road. The most changeable physical and mechanical properties are common for limestone from Al-Dabaa region, Muhafazah Suez.

Apart from other materials, there stand igneous rocks rarely used in Egypt as a coarse aggregate for concrete. However, these materials are

essential for the critical structures of nuclear power plants, such as the reactor core containment. Basalt produced in the occurrence near El Fayoum oasis is the most available material in Egypt for this purposes.

Size 67 (4.75 – 19.0 mm), also known on the Egyptian market as Size 1, was chosen as the main grading according to ASTM [4]. The decision was made due to the Al-Dabaa NPP project requirement not to use grains larger than 20 mm. Along with Size 1, Size 2 similar to Size 56 (9.5 to 25.0 mm) is also produced.

THEORETICAL INVESTIGATION

Some characteristics described in Table 1 can be compared based on the theoretical analysis of test methods, e.g. fines content (< 75-μm) and Los Angeles abrasion test.

Materials Finer than 75-μm (No. 200) and 63-μm sievesAs mentioned before, the main difference between the two methods is the size of control sieves' openings. In Egypt, particles less than 75-μm or 63-μm in size are measured, which means that their content will be a bit higher or identical to the value that could be obtained according to the Russian method. Considering the genesis of aggregates in Egypt, it is more likely that fine particles are formed mostly from crushing operations. In case of coarse aggregate, grain size distribution curves are flatter in the 50 to 75 μm range, and the difference is not as crucial as it can be for sands and soils.

As a first estimation, it is recommended to use the results according to the Egyptian standard method from quality certificates without converting them. First, with the Egyptian method, the results could be only a bit higher than with the Russian one, so the project restrictions will not be violated. Second, this approach does not break the ranging of suppliers in accordance with their product quality. Third, control tests according to the Russian and Egyptian standards are to be carried out for the most potential suppliers.

Control examination should be carried out in accordance with the Egyptian method, but using an additional 50-μm sieve (No. 35) from the ASTM E11 [22] set. Since a residue on each sieve is known, it is possible to define the content of particles according to both methods without parallel tests. Furthermore, this approach will give additional information for the rating of aggregates since water demand highly increases after 50-μm rather than 75-μm.

Los AngelesAabrasion Resistance

In both countries, aggregates abrasion resistance is determined using a shelf drum (Los Angeles machine). The drum construction, dimensions, weight of grinding spheres and drum velocity have minimal differences and are within reasonable tolerance limits.

Recalculating is not necessary, however, it is worth to mention that the Russian method requires a sieve with 1.25 mm openings against 1.70 mm or 1.60 mm in Egypt. It is recommended to use an additional sieve No. 16 (1.18 mm) from the standard sieve set [4] for more accurate results.

PRACTICAL INVESTIGATION

The remaining characteristics have to be compared according to practical examination due to the basic distinctions of the test methods, e.g. grain size distribution, flaked and elongated grains content, aggregate crushing value (ACV). However, some results can be converted.

Grain Size DistributionIn Russian and in Egypt, the results of tests are presented graphically as a grain size distribution curve. Between two nearest sieves, the distribution curve is considered continuous. Hence, it is possible to measure the mass of grains for every sieve size inside this interval by means of interpolation. However, this statement is only adequate when the sieve openings have the same shape,

otherwise, if the openings are of the same size the screening area will be different. This means that in order to develop a recalculating method an experimental correspondence between squared and rounded sieve openings should be found.

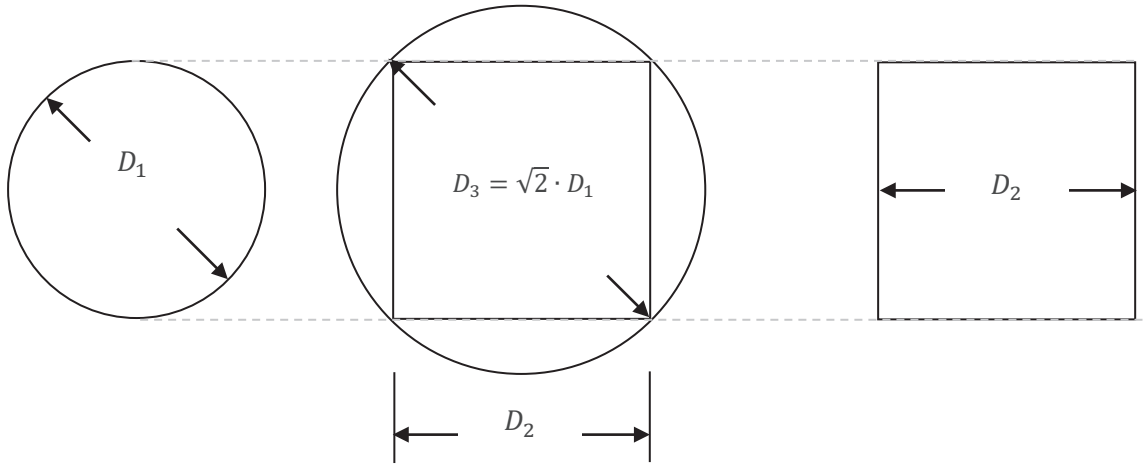

a) Rounded opening with size D_1

b) Diagonal of square opening with size D_2 supposed to be equal to diameter of new rounded opening D_3

c) Squared opening with size D_2

Figure 2. TR 103 Interpretation of Correspondence between Squared and Rounded Openings

In Russia, it is possible to use Technical recommendations [23] to recalculate the results from squared to rounded sieve openings (sec. 4.3.4, Table 2). The correspondence between sieves is established geometrically (Fig. 2b) as an equality between the square's diagonal (D_3) and the corresponding diameter of the rounded opening. However, this method didn't pass experimental verification and cannot be used.

Since the geometric approach was not confirmed during experiments, it was decided to establish a new correspondence between sieves based on the data of sieving materials' samples (see 2.2). Tests were carried out first on Egyptian sieves, then – on Russian. It became possible to establish a new correspondence between the sieves knowing actual grains distribution from the same test samples (Fig. 3).

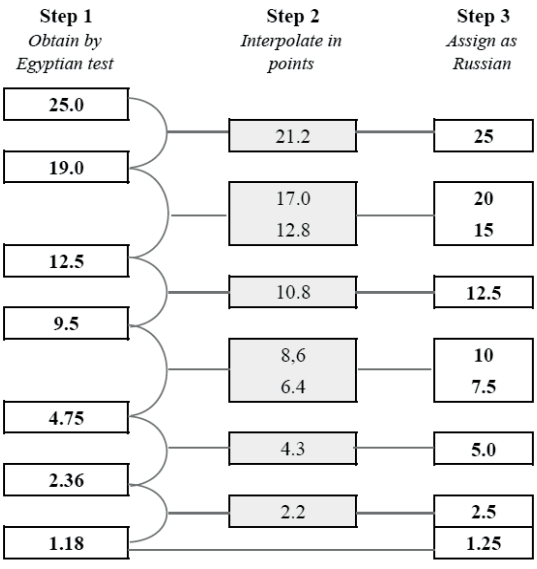

Figure 3. Scheme of Recalculating Results from Egyptian to Russian Sieves

The order of recalculating is as follows:

1. Measure the mass of «passed grains» on Egyptian squared sieves.
2. Convert the obtained values of «passed grains» into «retained grains» via Eq. 2:

$$A_n = 100\% - W_n, \qquad (2)$$

where A_n is the total percentage of retained grains on n-sieve, W_n is the total percentage of passed grains on n-sieve.

3. Find the corresponding points on the curve by means of interpolation using the principle of grain size distribution curve continuity (Fig. 3).
4. Draw a new grain size distribution curve corresponding to Russian rounded sieves.

Fig. 4 (a, b, c, d) presents the actual and recalculated results. As it seems from the graphs, it was not possible to level the error between the different shapes of sieve openings completely. The largest discrepancy is about 10%; however, on the bright side, the curves follow each other's trajectory. The biggest gap can be observed in Fig. 4g showing the results for basalt from El Fayoum with the highest percentage of flaky grains, which most likely increases the discrepancy. In all other cases, the curves are quite close to each other.

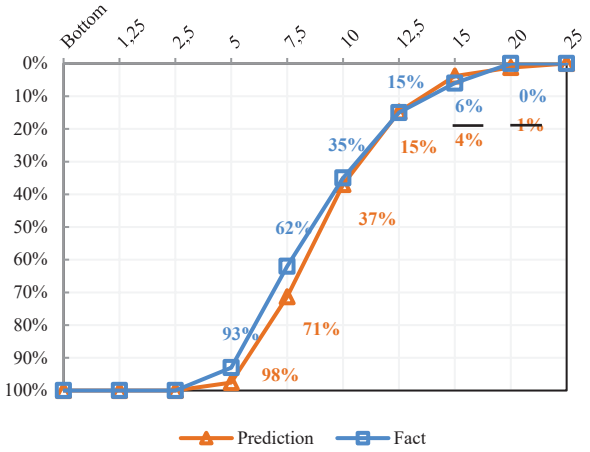

Figure 4a. Suez, Attaka grain size distribution curves

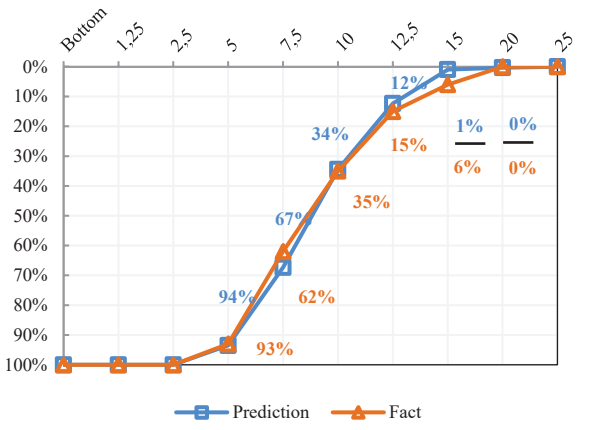

Figure 4b. Matrouh, New Alamein grain size distribution curves

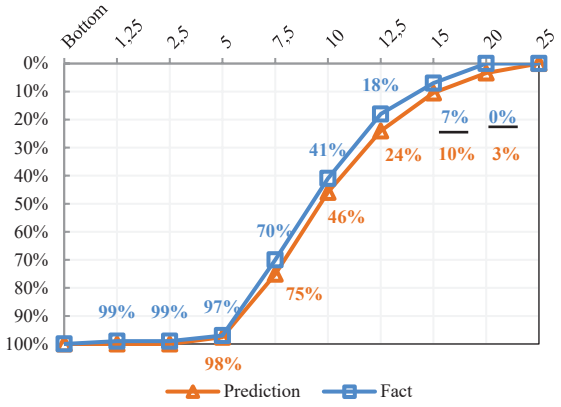

Figure 4c. Matrouh, Al-Dabaa grain size distribution curves

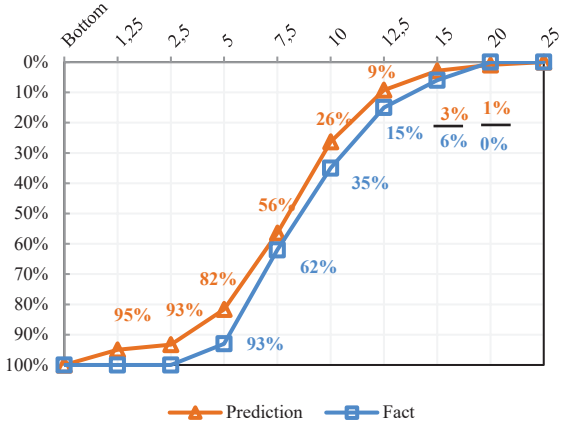

Figure 4d. Giza, El Fayoum grain size distribution curves

Based on the recalculating method results, the following requirements to the interpretation of Russian grain size distributions have been proposed (Table 3).

Table 3. Grading Requirements according to Russian[21] and Egyptian Standards

	Grading	Percentage of passing						
		25.0 mm	19.0 mm	12.5 mm	9.5 mm	4.75 mm	2.36 mm	1.18 mm
Russian	5.0 to10.0 mm	···	···	100	94 - 100	8 - 23	0 - 5	0
	10.0 to 20.0 mm	100	94 - 100	37 - 65	8 - 22	0	···	···
	5.0 to 20.0 mm	100	94 - 100	54 - 78	32 - 58	3 - 14	0 - 4	0
Egyptian	19.0 to 4.75 mm (No. 67 or Size 1)	100	90 - 100	···	20 - 55	0 - 10	0 to 5	0
	25.0 to 9.5 mm (No. 56 or Size 2)	90 - 100	40 - 85	10 - 40	0 - 5	0 - 5	···	···

Field aggregate examination was carried on ASTM sieves; however described recalculating method is also applicable for BS EN sieves. For recalculating additional 22.4 and 11.2 sieves are required from basic group plus sieve set. Recalculating method was used in Voronezh State University on prepared samples in accordance with GOST 32703-2014, which is harmonized with EN 933-1; results are presented in Fig. 4e.

Flakiness and Elongation Indexes

Grains with the length 3-times greater than their width are to be considered in Russia as flaky with no strict differentiation from elongated grains. In Egypt, flaky and elongated grains are to be were determined according to the British standards using mean grain size between two nearest sieves. Grains longer than $0.6 \cdot D_m$.are to be called flaky.

However, no relation between the methods was found after doing the tests due to the significant difference between fractions and mean grain sizes (Table 2). Table 4 shows the results of the tests.

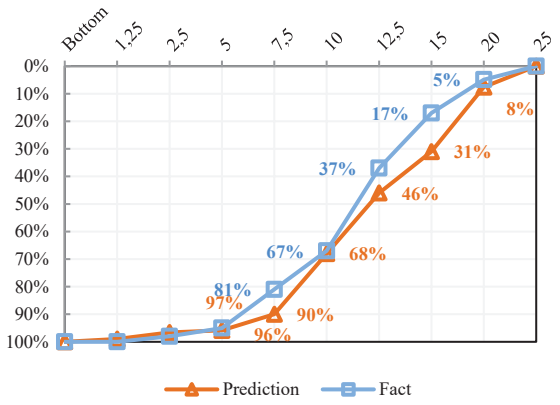

Figure 4e. Experimental EN 933-1 grain size distribution curves

Table 4. Flaky Grains Content Test Results

Region	Grains content (Egyptian method), %		Content of flaky grains (Russian method)[6], %
	Flakiness index[9]	Shape index	
Suez, Attaka (dolomite)	~ 9…12	~ 9	8…10
Matrouh, New Alamein (limestone)	~ 38	~ 22	22…24
Matrouh, Al-Dabaa (limestone)	20...25	12…16	18…22
Giza, El Fayoum (basalt).	~ 38	~ 17	40…46

Aggregate Crushing Value

In Egypt and Russia, ACV is determined by mass loss after compression test in a special cylinder (Fig. 2). Despite the same physical concept and similar testing equipment dimensions, sample preparation and compression force are essentially different.

Results according to the Egyptian method are not comparable with the Russian. However, it is acceptable to convert values using mass loss percentage obtained by Los Angeles machine test. This correspondence is presented in GOST 26633-2015 (see Table A.3). Fig. 5 shows its visual interpretation.

The tests were carried out on the samples described in this study. The results confirmed the adequacy of the correspondence, see Table 5.

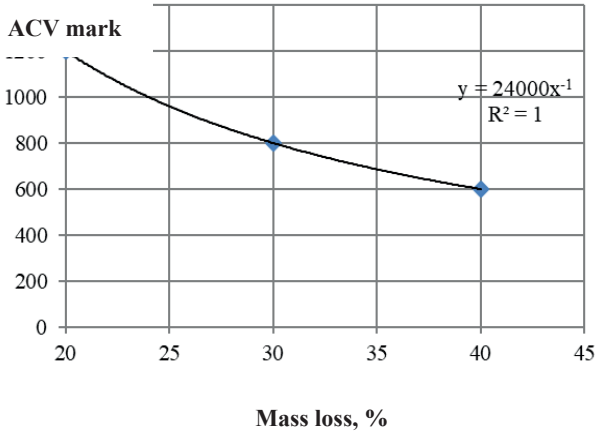

Figure 5. Correspondence between ACV and Percentage of Mass Loss by LA Test

Table 5. LA Machine Test and Russian ACV Test Results

Region	LA mass loss, %	Russian ACV mark	
		expected	actual
Suez, Attaka (dolomite)	19…21	M1200	M1200 (mass loss 9…10%)
Matrouh, New Alamein (limestone)	23…26	M1000	M1000 - 1200 (mass loss 10…12%)
Matrouh, Al-Dabaa (limestone)	35…40	M600	M600 (mass loss 16%)
Giza, El Fayoum (basalt).	~ 16	M1400	M1400 (mass loss ~ 8%)

CONCLUSIONS

The analysis of Egyptian standards as well as their comparison with the Russian technical documents was carried out. It has been found that the standards for fresh and hardened concrete and cement materials are harmonized with international standards in both countries. Main differences appear between coarse and fine aggregates test methods. This study covered only main physical and mechanical tests of coarse aggregate. Experiments have shown that the test methods and their results can be compared provided that the rules of conversion are followed. Most attention must be paid when evaluating the geometric parameters of coarse aggregate grains.

Based on the results of the work it is possible to make the following statements:

- a correspondence between square and round sieves is proposed. However, the prediction accuracy is affected by the content of flaky grains: a higher content increases the gap between the curves. For this reason, the method is recommended only for the initial assessment via quality certificates or when adjustments to crushing processes in production are needed.
- flaky grains content values cannot be converted from Egyptian to Russian method results. The control groups and sizes of shell sieves have essential differences which do not allow avoiding parallel tests.
- an identical approach is used to determine the abrasion resistance. Due to this, it is possible to estimate the aggregate strength (ACV) based on mass loss values obtained by attrition in the Los Angeles machine. Based on the results of the work, the relevance of this dependence was confirmed.

This article can be used as a guidance for Egyptian materials suppliers when it is required to draw up terms of reference or a commercial proposal. Tables for converting requirements and graphical illustrations have been prepared to serve for this purpose.

ACKNOWLEDGES

Presented in this work results were prepared on the basis of experimental investigations, which were carried out in laboratories accredited in accordance with GOST ISO/IEC 17025-2019:

- Housing and Building National Research Center (HBRC), Egypt, Cairo;
- JSC “Institute Orgenergostroy”, Russian Federation, Moscow;
- Center of collective usage named after Professor Yu.M. Borisov in Voronezh State Technical University, Russian Federation, Voronezh, partly supported by the Russian Ministry of Science and High Education, Contract No.075-15-2021-662.

REFERENCES

1. **Boichenko B.M., Nizev K.G., Stoianov A.N.** [et al.] Comparative analysis of quality requirements for metal products and their compliance with world quality standards // Metallurgy of mechanical engineering, Iss. 3, 2018. pp. 21-23 (in Russian).
2. **Polyakova M.A., Gulin A.E., Danilova U.V.** [et al.] Analysis of standard requirements for low-carbon wire // Processing of continuous and laminated materials, Iss. 28, 2012. pp. 75-80 (in Russian).
3. **Petrov A.V, Savin A.V, Lebedjev A.V.** Analysis of the requirements of Russian and European standards for rail joints // Railway and railway household, Iss. 9, 2016. pp. 22-27 (in Russian).
4. ASTM C33-18 Standard Specification for Concrete Aggregates, ASTM International, West Conshohocken, PA, 2018.
5. Egyptian Code of Practice 203-2018 for Design and Construction of concrete structures, Ministry of Development, New Communities, Housing and Building Research center, 2018.
6. ECP 203-2020 Egyptian Code for design and construction of concrete structures,

Ministry of Development, New Communities, Housing and Building Research center, 2020.
7. BS EN 12620:2002+A1:2008, British Standards Institution, London, 2002.
8. GOST 26633-2015 Heavy-weight and sand concretes. Specifications, Standartinform, Moscow, 2019 (in Russian).
9. ASTM C136-19 Standard Test Method for Sieve Analysis of Fine and Coarse Aggregates, ASTM International, West Conshohocken, PA, 2019.
10. GOST 8269.0-97 Mountainous rock road-metal and gravel, industrial waste products for construction works methods of physical and mechanical tests, Standartinform, Moscow, 2019 (in Russian).
11. ASTM C 117-17 Standard Test Method for Materials Finer than 75-μm (No. 200) Sieve in Mineral Aggregates by Washing, ASTM International, West Conshohocken, PA, 2017.
12. BS EN 933-1:2012 Tests for geometrical properties of aggregates - Determination of particle size distribution. Sieving method, British Standards Institution, London, 2012.
13. ASTM C 131/131M-20 Standard Test Method for Resistance to Degradation of Small-Size Coarse Aggregate by Abrasion and Impact in the Los Angeles Machine, ASTM International, West Conshohocken, PA, 2020.
14. BS EN 1097-2:2020 Tests for mechanical and physical properties of aggregates - Methods for the determination of resistance to fragmentation, British Standards Institution, London, 2020.
15. BS 812-112:1989 Testing aggregates. Methods for determination of particle shape. Flakiness index, British Standards Institution, London, 2000.
16. BS 812-105.1:1989 Testing aggregates. Methods for determination of particle shape. Flakiness index, British Standards Institution, London, 1998.
17. BS EN 933-2:2020 Tests for geometrical properties of aggregates - Determination of particle size distribution. Test sieves, nominal size of apertures, British Standards Institution, London, 2000.
18. BS 812-110:1990 Testing aggregates. Methods for determination of aggregate crushing value (ACV), British Standards Institution, London, 1998.
19. BS 812-111:1990 Testing aggregates. Methods for determination of particle shape. Flakiness index, British Standards Institution, London, 1998.
20. **Lyapidevskaya O.B., Bezuglova E.A**. Technical requirements and testing methods of fresh concrete. Comparative analysis of Russian and European standards. // Moscow State University of Civil Engineering, 2013. – 60 p (in Russian).
21. GOST 8267-93 Crushed stone and gravel of solid rocks for construction works. Specifications, Standartinform, 2018.
22. ASTM E11 - 20 Standard Specification for Woven Wire Test Sieve Cloth and Test Sieves, ASTM International, West Conshohocken, PA, 2017.
23. Technical Recommendation 103-07 for a construction and repair of road structures using asphalt concrete, GUPNIIMosstroj, Moscow, 2007.

СПИСОК ЛИТЕРАТУРЫ

1. **Бойченко Б.М., Низев К.Г., Стоянов А.Н.** [и др.] Сравнительный анализ требований к качеству металлопродукции и их соответствие мировым стандартам качеств. // Металлургия машиностроения, № 3, 2018. С. 21-23.
2. **Полякова М.А., Гулин А.Е., Данилова Ю.В.** [и др.] Анализ требований стандартов на низкоуглеродистую проволоку. // Обработка сплошных и слоистых материалов, № 28, 2012. С. 75-80.
3. **Петров А.В, Савин А.В, Лебедев А.В.** Анализ требований российских и европейских стандартов к рельсовым

скреплениям. // Путь и путевое хозяйство, № 9, 2016. С. 22-27.
4. ASTM C33-18 Standard Specification for Concrete Aggregates, ASTM International, West Conshohocken, PA, 2018.
5. Egyptian Code of Practice 203-2018 for Design and Construction of concrete structures, Ministry of Development, New Communities, Housing and Building Research center, 2018.
6. ECP 203-2020 Egyptian Code for design and construction of concrete structures, Ministry of Development, New Communities, Housing and Building Research center, 2020.
7. BS EN 12620:2002+A1:2008, British Standards Institution, London, 2002.
8. ГОСТ 26633-2015 Бетоны тяжелые и мелкозернистые. Технические условия, Стандартинформ, М., 2019.
9. ASTM C136-19 Standard Test Method for Sieve Analysis of Fine and Coarse Aggregates, ASTM International, West Conshohocken, PA, 2019.
10. ГОСТ 8269.0-97 Щебень и гравий из плотных горных пород и отходов промышленного производства для строительных работ методы физико-механических испытаний, Стандартинформ, М., 2019.
11. ASTM C 117-17 Standard Test Method for Materials Finer than 75-μm (No. 200) Sieve in Mineral Aggregates by Washing, ASTM International, West Conshohocken, PA, 2017.
12. BS EN 933-1:2012 Tests for geometrical properties of aggregates - Determination of particle size distribution. Sieving method, British Standards Institution, London, 2012.
13. ASTM C 131/131M-20 Standard Test Method for Resistance to Degradation of Small-Size Coarse Aggregate by Abrasion and Impact in the Los Angeles Machine, ASTM International, West Conshohocken, PA, 2020.
14. BS EN 1097-2:2020 Tests for mechanical and physical properties of aggregates - Methods for the determination of resistance to fragmentation, British Standards Institution, London, 2020.
15. BS 812-112:1989 Testing aggregates. Methods for determination of particle shape. Flakiness index, British Standards Institution, London, 2000.
16. BS 812-105.1:1989 Testing aggregates. Methods for determination of particle shape. Flakiness index, British Standards Institution, London, 1998.
17. BS EN 933-2:2020 Tests for geometrical properties of aggregates - Determination of particle size distribution. Test sieves, nominal size of apertures, British Standards Institution, London, 2000.
18. BS 812-110:1990 Testing aggregates. Methods for determination of aggregate crushing value (ACV), British Standards Institution, London, 1998.
19. BS 812-111:1990 Testing aggregates. Methods for determination of particle shape. Flakiness index, British Standards Institution, London, 1998.
20. **Ляпидевская О.Б., Безгулова Е.А.** Бетонные смеси. Технические требования. Методы испытаний. Сравнительный анализ российских и европейских строительных норм. // Московский государственный строительный университет, Москва, 2013. – 60 С.
21. ГОСТ 8267-93 Щебень и гравий из плотных горных пород для строительных работ. Технические условия, Стандартинформ, М., 2018.
22. ASTM E11 - 20 Standard Specification for Woven Wire Test Sieve Cloth and Test Sieves, ASTM International, West Conshohocken, PA, 2017.
23. Технические рекомендации по устройству и ремонту дорожных конструкций с применением асфальтобетона, ГУП НИИМосстрой, М., 2007

Khalid M. Yousri, Prof., Ph.D, Vice Chairman for Research and Studies Affairs at Housing & Building National Research Centre, 87 Tahrir Street, Dokki, Giza, P.O. Box 1770, Egypt, phone + (202)-33356722 Ext.: 1205. E-mail: kyousri.hbrc@gmail.com.

Dmitrii N. Korotkikh, Prof., Dr.Sc., Head of Responsibility Center "Monolith", JSC "OES", Moscow, Russia. 115114, Russia, Moscow, Derbenevskaya embankment, 7, p. 10; tel +7 (910) 349-86-45; E-mail: korotkih.dmitry@gmail.com

Dmitry E. Kapustin, Cand. Sc., Department of Construction testing, National Research Moscow State University of Civil Engineering, 26, Yaroslavskoye Shosse, Moscow, 129337, Russia; phone +7 (968) 945-73-88; Head of Department of "Construction Examination", JSC "OES", Moscow, Russia. E-mail: kde90@bk.ru

Luka I. Efishov, lecturer., Department of Building Materials science, National Research Moscow State University of Civil Engineering, 26, Yaroslavskoye Shosse, Moscow, 129337, Russia; phone +7 (916) 293-18-95; 1st engineer of Department of "Materials science", JSC "OES", Moscow, Russia. E-mail: efishovli@ioes.ru

Йосри Мохаммед Халид, профессор, доктор философии (Ph.D), вице-председатель по исследовательским и учебным делам в Национальном исследовательском центре жилищного строительства, 1770, Египет, Гиза, ул. Тахрир, д. 87, тел. + (202)-33356722 доб.: 1205. E-mail: kyousri.hbrc@gmail.com

Коротких Дмитрий Николаевич, д.т.н., Директор центра финансовой ответственности (ЦФО) «Монолит», АО "Институт Оргэнергострой", Россия, Москва, 115114, Россия, Москва, Дербеневская набережная, д.7, стр.10; тел +7 (910) 349-86-45; E-mail: korotkih.dmitry@gmail.com

Капустин Дмитрий Егорович, к.т.н., доц. кафедры Испытания сооружений; Национальный исследовательский Московский государственный строительный университет, 129337, Россия, Москва, Ярославское шоссе, д. 26,; тел +7 (968) 945-73-88; Руководитель центра компетенций "Обследование сооружений", АО "Институт Оргэнергострой", Россия, Москва. E-mail: kde90@bk.ru

Ефишов Лука Игоревич, преподаватель кафедры Строительного материаловедения; Национальный исследовательский Московский государственный строительный университет, 129337, Россия, Москва, Ярославское шоссе, д. 26,; тел +7 (916) 293-18-95; инженер 1-й категории отдела Технологии строительных материалов и изделий, АО "Институт Оргэнергострой", Россия, Москва. E-mail: efishovli@ioes.ru

International Journal for Computational Civil and Structural Engineering, 19(1) 55–68 (2023)

DOI:10.22337/2587-9618-2023-19-1-55-68

INTERACTION OF SEA GRAVITY WAVES WITH PORT PROTECTION STRUCTURES IN NUMERICAL MODELS

Izmail G. Kantarzhi, Aleksandr G. Gogin

Moscow State University of Civil Engineering, Moscow, RUSSIA

Abstract. The paper is dedicated to numerical modeling of interaction of sea wind waves with port protective structures. A classification of existing numerical wave models is presented depending on their accuracy and demands on computing power. The main studied effect of the interaction of waves with port protective structures is diffraction of waves in protected water area. In this paper is studied a test case with conservative wave diffraction – two converging breakwaters on a flat bottom with varying of entrance width and approaching waves period. The test case was physically modeled in a wave basin, as well as numerically modeled using the Boussinesq wave model implemented in the MIKE 21 software. As part of setting up the numerical model, the most correct way to model protective structures on the numerical model is proposed and justified – with rejection of wall enclosing sponge layers from entrance section side and with gradual decrease of sponge coefficients towards entrance section. Satisfactory agreement was obtained with a spread of values 10-15% as a result of results comparing of numerical and physical modeling. This made it possible to conclude that the proposed method for protective structures modeling allows to correctly calculate diffraction of waves in protected water area, and the wave model used can be considered verified by results of physical experiments.

Keywords: numerical modeling, wind waves, sea waves, gravity waves, diffraction, breakwaters, sea port, MIKE 21

ЧИСЛЕННАЯ РЕАЛИЗАЦИЯ ВЗАИМОДЕЙСТВИЯ ГРАВИТАЦИОННЫХ ВОЛН С ОГРАДИТЕЛЬНЫМИ СООРУЖЕНИЯМИ МОРСКОГО ПОРТА

И.Г. Кантаржи, А.Г. Гогин

Национальный исследовательский Московский государственный строительный университет (НИУ МГСУ), г. Москва, РОССИЯ

Аннотация. Работа посвящена методу численного моделирования взаимодействия морских ветровых волн с оградительными сооружениями морского порта. Представлена классификация существующих численных волновых моделей в зависимости от их точности и требованиям к вычислительной мощности компьютера. В статье основным исследуемым эффектом взаимодействия волн с гидротехническими сооружениями порта является дифракция волн на защищаемой акватории. Для ее консервативного исследования в работе используется тестовая задача – два сходящихся оградительных сооружения на плоском дне с варьированием шириной входного створа и периодом подходящих волн. Тестовая задача физически смоделирована в волновом бассейне, а также численно с помощью волновой модели Буссинеска, реализованной в ПК MIKE 21. В рамках настройки численной модели предложен и обоснован наиболее корректный способ воспроизведения оградительных сооружений на численной модели – с отказом от ограждающей поглощающие слои стенки со стороны входного створа и постепенным уменьшением коэффициентов поглощения к входному створу. В результате сравнения результатов численного и физического моделирования получено удовлетворительное совпадение с разбросом значений 10-15%. Это позволило сделать вывод о том, что предложенный способ реализации оградительных сооружений позволяет корректно рассчитать дифракцию волн на защищаемой акватории, а используемую волновую модель считать верифицированной результатами физических экспериментов.

Ключевые слова: численное моделирование, ветровые волны, морские волны, гравитационные волны, дифракция, оградительные сооружения, морской порт, MIKE 21

INTRODUCTION

A large-scale work on the reconstruction and construction of maritime transport infrastructure is going in Russia. According to the development program of the Ministry of Transport of Russia, the total capacity of seaports should increase by 25% [1,2] in 2035. One of the important tasks that arises in the implementation of a seaport project is forecasting the development of wind waves in a water area. The height marks of port's hydraulic structures, the possibility and safety of ship processing and servicing, as well as the stability of individual elements of hydraulic structures or, less often, the supporting structures, depend on the parameters of wind waves. Overestimation of the parameters of wind waves can lead to unjustified construction costs. Underestimation causes difficulties in the operation of port for its intended purpose [3].

To protect against storm wind waves, protective structures are installed along port water area perimeter. In gaps between these structures, navigation routes are laid for ships. At the same time, protective structures often become the most expensive objects of seaport due to the need to install them at great depths. Therefore, a top priority is to finding the optimal balance between the length of protective structures and the allowable downtime in the work of port due to excessive wind waves in the water area when performing a feasibility study of the project [4]. Wind waves arise at great depths under action of wind. They propagate to hydraulic structures, near which waves experience transformation processes such as diffraction behind the gap between protective structures, reflection from structures, refraction with decreasing depths in the water area. The final wave regime in port water area is the interference of coming, diffracted and reflected waves, which is schematically presented in Figure 1.

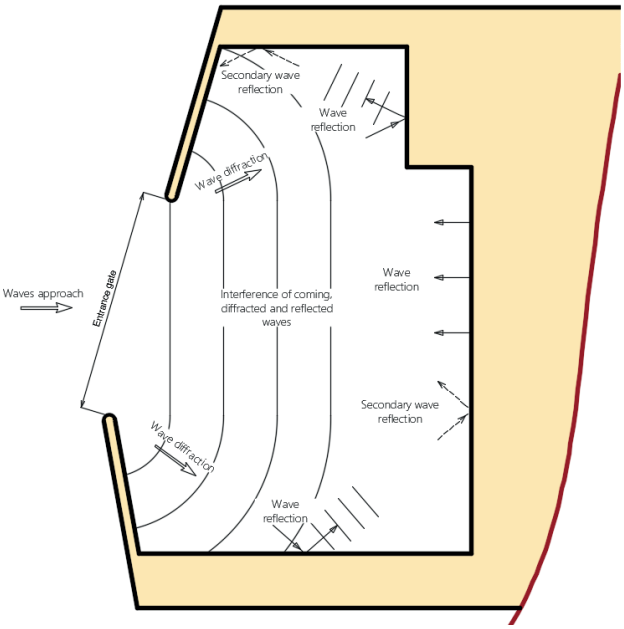

Figure 1. Transformation of wind waves and formation of a wave regime in the water area of seaport

The main process of wave transformation studied in this paper is diffraction. The diffraction means the phenomenon of wave rounding around obstacles, which occurs behind a gap between protective structures and is accompanied by a change in wave heights both up and down. The first methods for calculating diffraction in the water area of seaport were based on the linear theory of waves using the Young principles (energy transfer along the wave front) and Huygens-Fresnel principles (determining the shape of wave fronts). In the Russian scientific literature, the main attention was paid to the method for wave amplitude diffusion. This method was proposed by Malyuzhinets [5] for sea waves on the basis of studies on the diffraction of electromagnetic waves by Leontovich and Fock [6–8]. Further, it was developed by Zagryadskaya [9,10], Krylov et al [11]. In the works of Penny and Price [12], similar transformations were obtained based on the Sommerfeld method for calculating the diffraction of electromagnetic waves [13]. In the middle of the 20th century, the main attention was paid to the energy method for

calculating diffraction, which was developed by Karaushev [14], Galenin [15], Krylov et al. [11], Zavyalov [16] and etc. This method subsequently became the basis of the normative calculation method. Besides, some problems of wave field diffraction allowed to solve the problem using methods based on the mild-slope equations [17, 18].

Currently, to determine the protection of port water area from wind waves, either simplified calculation methods presented in regulatory documents are used. Traditional physical modeling in specially equipped wave pools [19,20], or numerical modeling [21–23] are applied as well. Modern numerical wave models allow predicting the parameters of wind regime in port water area in various configurations and for various wave formation conditions with sufficient efficiency. The main disadvantages of numerical models are the limited applicability of some ones and the need to verify the model for each individual object due to the large number of calibration settings. Thus, although numerical methods are attractive to researchers due to their capabilities and relatively low labor costs, they require accuracy in application and at least partial verification of the results.

Today, there are a large number of numerical wave models designed to simulate the propagation of sea waves in certain conditions. There are some approaches to the systematization of wave models which are presented mainly by foreign authors [24,25]. However, the classifications presented in these papers contain gaps in the nomenclature of existing numerical models. And they can hardly be called final. This paper proposes a classification of existing numerical wave models. The classification is based on their accuracy and resource intensity.

In this study, the main attention is paid to one of the aspects of numerical modeling of the wind waves development in port water area. It is the reproduction of protective structures on a numerical model. The motivation for the study was the spread of the results of calculating wave diffraction in protected water area of port, depending on the method of implementing the head of a protective structure in a computational finite element mesh. Such nuances of numerical simulation strongly affect on the results of diffraction calculation, on the basis of which conclusions are drawn about the protection of port water area and, accordingly, decisions are made about the need for additional costs for the development of the port's protective structures. This makes such studies relevant.

MATERIALS AND METHODS

Classification of numerical waves models

Currently, various numerical wave models are available to simulate the propagation of wind waves both in extensive water areas of the oceans and seas, and in small local water areas of seaports. All of them have their advantages and disadvantages, as well as some restrictions. In the paper, several generalized classes of the most common wave models have been considered.

Spectral wave models based on the law of conservation of wave action solve the wave energy balance equations in the spectral representation and describe the transfer of wave energy in time and space. This class of models is the least demanding on the computing power. Therefore, that is often used to simulate the development of wind waves in vast water areas. Spectral models account all the features of wave generation, their propagation and dissipation. However, this do not consider the phases of individual waves, which makes them inapplicable for accurate calculation, for example, diffraction or reflection of waves near hydraulic structures. Recently, spectral wave models began to include an approximate method for calculating wave diffraction, based on the mild-slope equation obtained at first in the paper [26]. Nevertheless, the use of spectral models has become established in modeling the development of waves in extensive water areas in order to determine the parameters of waves on the way to port. After that, these results are

used as boundary conditions for more accurate models, in which the wave regime is modeled already in port water area.

Wave models based on mild-slope equations are often used directly to simulate the penetration of waves into protected water areas. The use of mild-slope equations, supplemented by the principles of linear wave theory, allows considering of this class of models as quite economical in terms of computing power requirements. The disadvantage of these models is the regular approximation of the simulated waves. As well as those do not allow simulation of the nonlinear waves or the nonlinear interactions between them.

Wave models based on Boussinesq equation are distinguished, first of all, by a more accurate approximation of the distribution of orbital velocities over depth, as well as the possibility of calculating nonlinear effects of wave formation on the free surface of water (for example, wave breaking). The equations, on which this class of models is based, allow to use the frequency and angular distribution of waves by introducing a higher-order dispersion term into the equations. In addition, the Boussinesq equations are also obtained in terms of velocity near the free surface, near the bottom, and at an arbitrary depth [27]. Due to this, models based on the Boussinesq equations are considered as the most flexible for simulation of various specific port areas. Thus, they have become most widespread in recent years.

Non-hydrostatic wave models account non-hydrostatic pressure when simulate sea waves. That allows to accurately simulate the distribution of current velocities and orbital velocities in depth. The basic equations of the model are written in three-dimensional form. That is, the vertical coordinate becomes part of the solution, and is not approximated by some conditions, as in models based on the mild-slope equations or the Boussinesq equations. A significant disadvantage of this class of models is the impossibility of simulating wave breaking. In addition, non-hydrostatic models already have significantly higher requirements for computer processing power, which also limits their application.

Free-surface wave models based on the Navier-Stokes equations are the most expensive in terms of resource consumption. However, they allow accurate modeling of nonlinear wave processes, including wave breaking. Today, this class of models remains practically inapplicable in engineering practice even for the smallest port water areas. These models assume the use of Reynolds-averaged Navier-Stokes equations using turbulent flow models to implement the convergence of the Navier-Stokes equations. Theoretically, the Navier-Stokes equations can also be solved explicitly, considering the turbulence of the flow, but this is still several orders of magnitude more computationally expensive due to the very small spatial and temporal discretization that must be used in this case.

In this paper, the classification of the above and some other classes of wave models according to the criteria "accuracy / required computing resources" was proposed. Figure 2 presents this classification.

The accuracy of the results obtained, which acts as the y-axis, is a debatable parameter in this case. It is based primarily on the number of wave formation and development factors accounted by the model. It should also be noted that some types of models (especially models based on the Boussinesq equations) include a fairly diverse subset of models. The differences between which can also be significant. Thus, the location of models on the chart corresponds to a certain average representation of the types of models relative to other types.

In this paper, a study on the penetration of sea wind waves into the protected water area of port has been performed. The numerical simulation presented in the paper is performed using a numerical wave model based on Boussinesq type equations and implemented in the software MIKE 21, in the module "Boussinesq Waves (BW)". Basic information about that is given in [28].

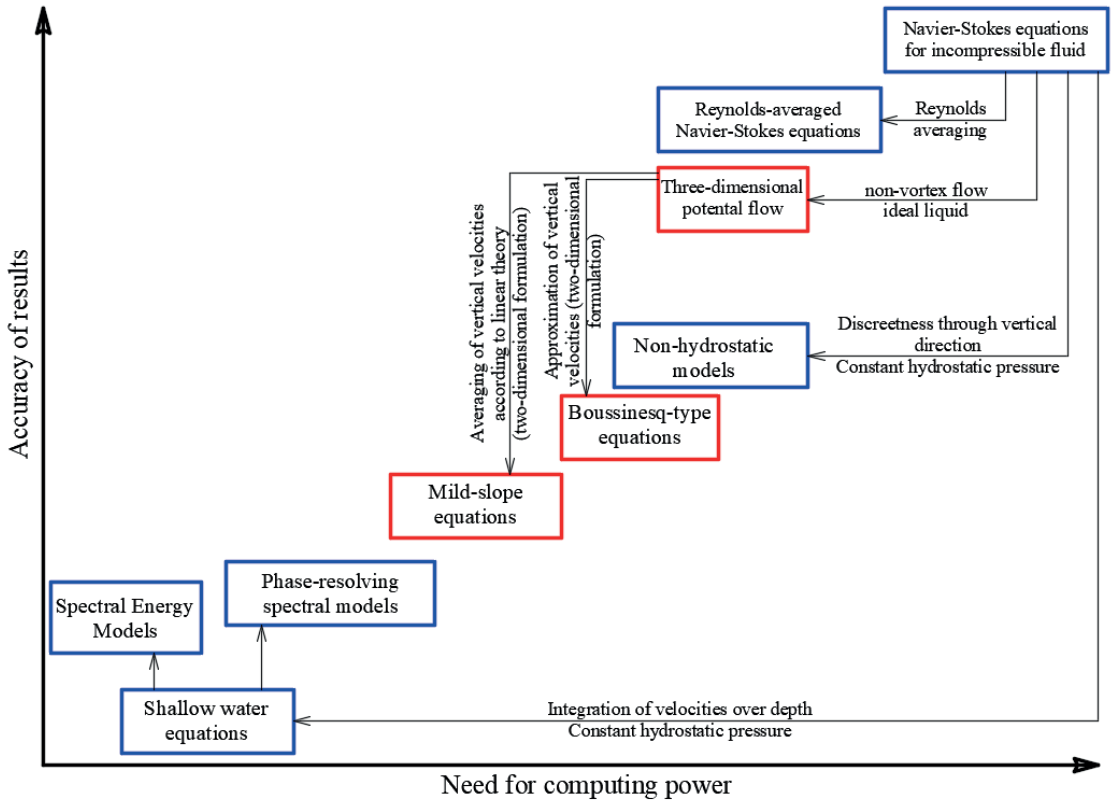

Figure 2. Classification of numerical wave models (models that consider only potential flow are highlighted in red)

Diffraction coefficient

To describe the diffraction pattern in port water area, a wave diffraction coefficient, k_d, which is a dimensionless parameter that characterizes the ratio of the heights of diffracted and approaching waves, is used:

$$k_d = \frac{h_d}{h}, \quad (1)$$

where h_d is the height of the diffracted waves; h is the height of the waves coming to seaport.

Formulation of the test problem

Studies of the diffraction of gravity waves in protected water area were carried out in a specially designed conditional port area, where wave diffraction is of decisive importance, and other effects of wave transformation can be neglected. The conditional port consists of two converging protective structures located on a flat bottom with a depth of 10 m. In total, two widths of the entrance section of 130 and 195 m are considered in the work. As well as five periods of waves coming in the water area are as follows 4.25; 5.65; 7.10; 8.50; and 9.90 s. Thus, within the framework of the study, 10 formulations of the wave diffraction problem were considered. A schematic representation of the test area is shown in Figure 3.

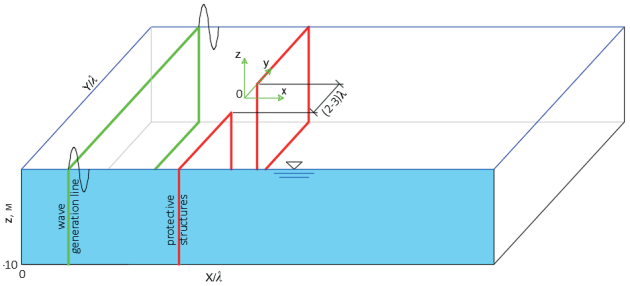

Figure 3. Schematic representation of the test area for wave diffraction studies

Numerical model settings

The first step in setting up a numerical wave model is traditionally the choice of the spatial and time step of the model. The spatial

resolution (or linear dimensions of finite elements) and the time step are chosen in accordance with the so-called Courant number, which means a dimensionless quantity that determines the order of numerical convergence (or sensitivity) of the model. The "physical" meaning of the Courant number is that it determines the number of finite elements that the wave passes in one-time step, and the expression for it is written as follows:

$$Cr = c\frac{\Delta t}{\Delta x}, \quad (2)$$

where $c = \sqrt{gd}$ is the wave propagation speed;
Δt is the time step;
Δx is the size of the finite element.
Satisfactory convergence of the numerical solution is achieved at Cr<1. Based on this condition and taking into account the initial waves, the mesh size was adopted of 2 m, and the time step was 0.14 s. The total simulation time in all models is assumed to be 30 min or 12860 steps. The maximum value of the Courant number was 0.69.
Another feature of numerical simulation is the assignment of boundary conditions on the contour of the model, as well as on some internal elements. For the numerical absorption of energy and wave height in the MIKE 21 BW model, the so-called "sponge" (or absorbing) layers (Sponge layers) proposed in [29] are implemented in the MIKE 21 BW model. They can be installed, for example, along the absorbing elements of the model (beaches) or along the boundaries of the model in order to prevent waves that go beyond the model from returning to the computational domain. Absorbing layers are selected cells of the computational mesh of finite elements, in which the conditions for the sponge coefficient are set, varying from 1 (no absorption) to 10 (maximum absorption). In this case, the numerical implementation of absorption is such that as the wave moves deeper into the absorbing layers, the sponge coefficients should gradually increase exponentially.

The main setting of the numerical model, which became the motivation for this study, was the choice of a method for implementing protective structures on the numerical model. The fact is that the recommendations given by the developers of the software used give dubious results. We mean the head of the protective structure, which was previously recommended to be reproduced, as shown in Figure 4.

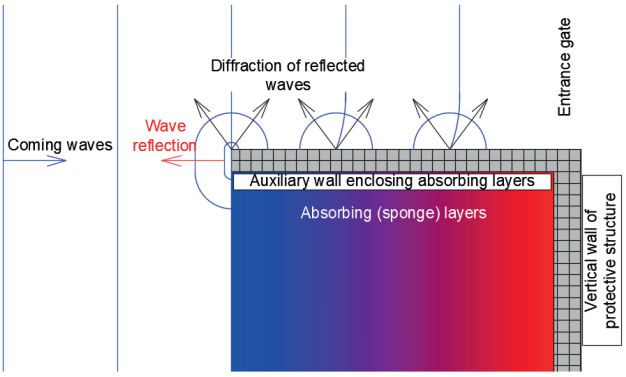

Figure 4. Scheme of the interaction of coming waves with an auxiliary wall enclosing absorbing layers

This option provides for the installation of a certain number of absorbing layers before the construction, which adsorb the energy of coming waves to prevent the development of secondary waves in the water area in front of the construction and in the entrance gate. From the side of the entrance gate, the absorbing layers are covered by a vertical wall, similar to the wall of the protective structure itself. Thus, a kind of channel is formed on the model in the entrance gate, bounded on two sides by walls. This way of implementing protective structures is proposed for use by the developers of the DHI MIKE 21 BW software package. However, it encounters several objections in terms of the correspondence of such a model to real conditions, which is discussed in more detail by the results of a test run of a series of experiments below.
As an alternative to the recommended option, the paper considered three additional options for the implementation of protective structures, shown in Figure 5. Here, option a) is

recommended. The second option (option b)) provides for the implementation of absorbing layers in front of the structure similar to option a), but without the construction of a wall perpendicular to the wall of the protective structure. The third option (option c)) was proposed rather to confirm the fundamental solution on the obligatory arrangement of absorbing layers in front of the structure and is a model of protective structures as close as possible to real conditions. The last option (option d)), as well as option b), provides for the rejection of the wall enclosing the sponge layers from the side of the entrance section, but with a different idea for the implementation of the absorbing layers themselves. It is proposed to gradually reduce the sponge coefficient as it approaches the head of the protective structure. Thus, it allows to avoid the interaction of waves passing through the alignment with layers of "rough" absorption of wave energy, as in the second variant.

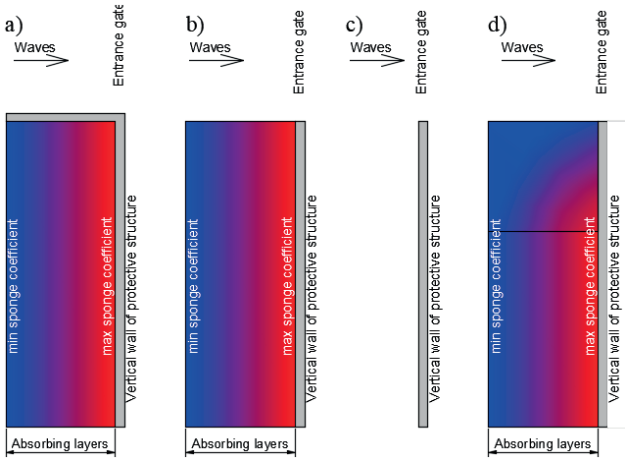

Figure 5. Schemes for the implementation of protective structures and absorbing layers in a numerical experiment

RESULTS

To validate the numerical simulation results, the wave regime was tested in the experimental water areas for all four expected options. Simulation results in the form of isofields of dimensionless diffraction coefficients are presented in Figure 6. The comparison of the results indicates a significant loss of diffraction coefficients and their dependence on a good specification of degree observations. The first considered variant with the formation of a certain entrance channel at the out-of-the-way section gives dubious results. High diffraction coefficients are found near the walls that protect the sponge layers from the inlet section, and a beating is detected in the inlet section itself. The physical meaning of that remains unclear. Most likely, this is the occurrence of behavior under the wave when it hits the auxiliary wall. The wave first diffracts on a single cell of the auxiliary tissue, and then develops, simultaneously being reflected from them and propagating towards the entrance target. Besides, a bending of the wave train is observed on the model of the nearby auxiliary wall in the direction of slowing down the motion of the wave fronts of the walls. Figure 4 presents the exemplary scheme of this mechanism.

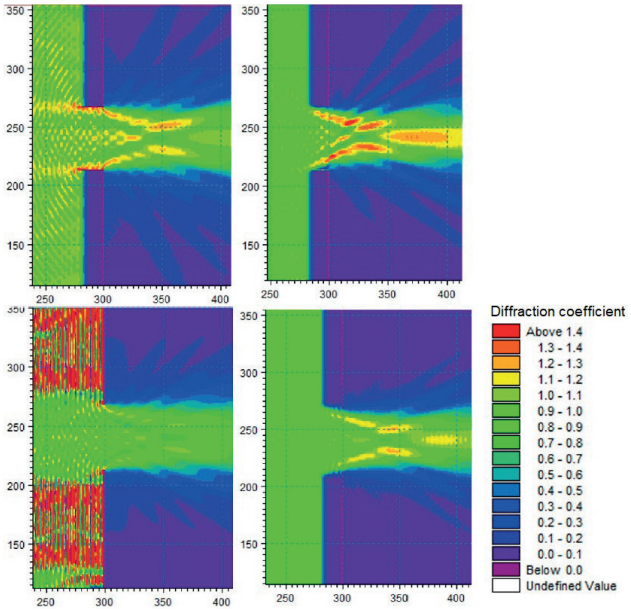

Figure 6. Isofields of diffraction coefficients obtained for different schemes for the implementation of protective structures in the numerical model (top left - option a); top right - b); bottom left - c); bottom right - d))

The above factors of interaction of waves with structures in option a) are the cause of the

appearance of a beat in the entrance section and can be considered a reason for abandoning such a scheme for the execution of protective structures. Calculations according to option c) showed the instability of the model, which did not allow to complete the calculation correctly. At the same time, the obtained results on the distribution of diffraction coefficients in the enclosed water area are close to the accepted assumptions. Despite the high similarity of such a model with the real scheme of experiments, it is difficult to implement such a scheme with stable finding of solutions at each time step in practice.

The results of simulation for options b) and d) showed qualitatively similar results of the distribution of diffraction coefficients in the enclosed water area. The same positions of the extrema of the diffraction coefficients that propagate from the heads of the protective structures to the axis of the entrance section, and the field of large diffraction coefficients at some distance from the entrance section strictly in zone of light. In this case, the maximum diffraction coefficients observed in option b) are about 1.4; in option d) are about 1.2. That is, the quantitative difference in the results is more noticeable. The results obtained on the model in option b) are obviously subject to the influence of secondary waves reflected from layers with "coarse" sponge coefficients, which are considered as a structure with partial absorption / reflection of energy. Thus, at the contact surface of waves with cells with large sponge coefficients, which here, in contrast to option a), are not covered by an auxiliary wall, an interaction mechanism is observed similar to that considered in option a) and shown in Figure 4. In option d), this mechanism also takes place. However, its effect and, consequently, the degree of development of the secondary wave, is significantly less due to the contact of the transmitted waves with the cells with the lowest sponge coefficients. It should also be noted that the results obtained according to variant d) are similar to the results obtained according to variant c), where there are no sponge layers in front of the structures at all.

Thus, the modeling of protective structures presented in Figure 6 (d)), can be recommended as the best in terms of a compromise between the correctness of the results obtained and the stability of the numerical solution.

To verify the results that were obtained by numerical simulation with the accepted option of reproducing protective structures on a numerical model, the same test problem was performed in a wave basin. Physical experiments were carried out at the Research Center "Sea Coast" in Sochi on a scale of 1:50 for 10 statements of the test problem. Figure 7 shows a diagram of a physical experiment, as well as a photograph taken during the experiments.

The experimental data were obtained for all formulations of the test problem at 16 control points. The diffraction coefficients at the points were obtained by the ratio of the recorded wave height at the point to the wave height at control point No. 1 (the closest point to the wave generator).

Comparison of the simulation results and experimental data is provided in figure 7. The line closest to the protective structures is conventionally called "line1", the farthest - "line2". A visual comparison of the results is shown in Figure 8.

Thus, a satisfactory qualitative agreement between the results of numerical and physical modeling is visually noted, with some reservations. First, lower diffraction coefficients are observed everywhere in the zone of light compared to those that were obtained by calculation. On average, the error in the zone of light between experiments and calculations was 18% for all experiments. Secondly, the excess of the "experimental" diffraction coefficients over the "calculated" ones is noted in the zones of the wave shadow. Here the average error was about 10%. According to the comparison, the coincidence of the diffraction coefficients at points located on the boundary of the wave shadow is also noted. On average, for all considered cases, the diffraction coefficients along the wave shadow boundary take values from 0.5 to 0.7.

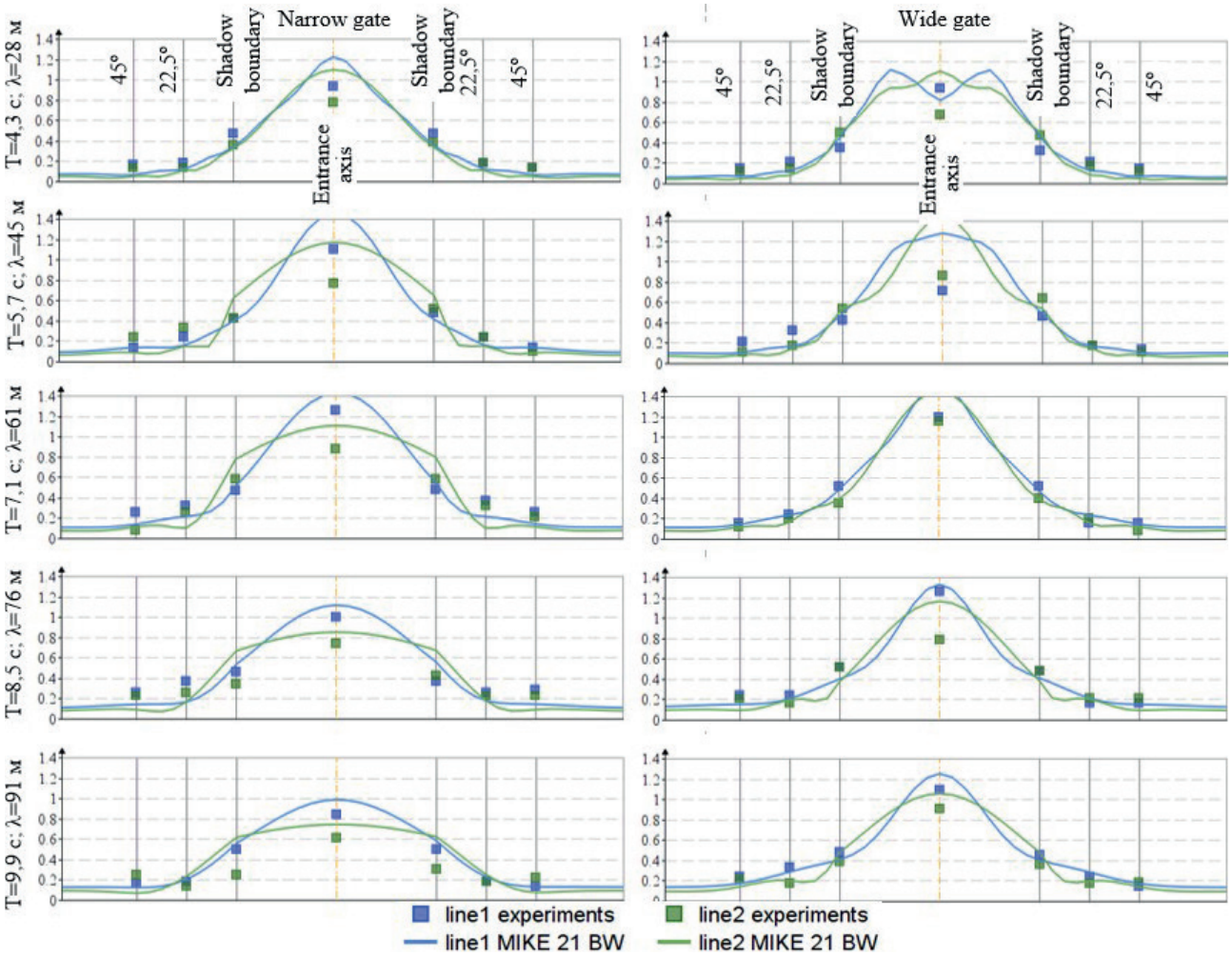

Figure 8. Comparison of the simulation results and the experimental data for all statements of the test problem

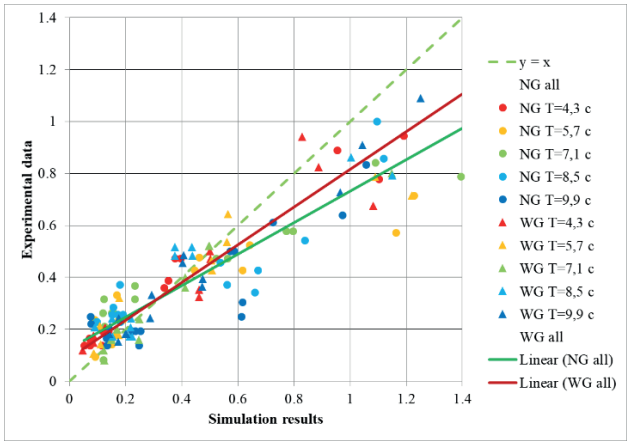

Figure 9. Lines of regression relationship between the diffraction coefficients obtained by physical and numerical modeling (NS - narrow section; WS - wide section)

Regression analysis was performed for quantitative comparison of the obtained results. The results presented above were subjected to statistical processing separately for the narrow gate (NG) and wide gate (WG). As a result of which the regression lines between the "experimental" and "calculated" diffraction coefficients were obtained, shown in Figure 9.

In the zone of deep wave shadow, the diffraction coefficients obtained on the physical model exceed those obtained by simulation. This, first of all, is evidenced by the position of the lower point of the lines of regression relationships, which for all models is above the reference line y=x. Apparently, there was a weak secondary wave in the physical basin due to wave reflection from the model boundaries. Analyzing the results obtained,

the height of the waves formed by the secondary wave was limited to a few millimeters, which gave a significant error at points where the height of the original waves was small (in the zone of deep wave shadow). But it gave a negligible error at points where the height of the original model waves was of the order of centimeters. On the contrary, there is an excess of the diffraction coefficients obtained on the numerical model over those obtained on the physical one at points close to unity of the diffraction coefficients (mainly in the light zone).

The table below presents the results of calculating a set of basic statistical parameters that are commonly used to evaluate the predictive capabilities of wave models, based on the results of comparing the calculated and measured diffraction coefficients.

Table. The main statistical indicators characterizing the degree of coincidence of the results

gate	Regression Equation Coefficients		R	R^2	MSD
	a	b			
narrow	0,606	0,126	0,93	0,86	0,21
wide	0,727	0,089	0,95	0,89	0,16

Thus, the numerical model gives an average error of 10–15% in comparison with the results of physical experiments. Taking into account that the main contribution to the fluctuations of statistical indicators is made by control points in a deep wave shadow, where the influence of the secondary waves is significant, that developed on the physical model. The obtained coincidence of the data allows to recognize the numerical wave model with the chosen method of implementing protective structures applicable for such studies.

CONCLUSION

The analysis presented in the paper allows to build an original classification of numerical wave models depending on their accuracy and the requirements for computer processing power. The proposed classification combines both the most common spectral wave models and modern models that implement the Navier-Stokes equations with a free surface. The resulting classification is presented graphically in Figure 2.

The experiments presented in the paper allows to choose and justify the most correct way to model the seaport protective structures on a numerical model to simulate the diffraction of sea waves in port water area. The proposed option provides for the rejection of the auxiliary wall enclosing the sponge layers from the side of the entrance section, with a gradual decrease in the sponge coefficient towards the head of the protective structure. For substantiation, physical experiments were carried out. The diffraction of waves was studied conservatively for different parameters of the width of the entrance gate and the period of the approaching waves. Comparison of the simulation results and experimental data led to the conclusion that the method proposed in the paper for the modeling of protective structures on the numerical model is justified.

In addition, the obtained satisfactory agreement of the results allows to consider the numerical wave model used in the work, based on the Boussinesq equations and implemented in the MIKE 21 software package, verified by the data of physical experiments. It should be highlighted that both numerical wave models and physical experiments are not ideal in terms of the results obtained, and an error exists in each method. For a physical experiment, the error is primarily due to the accuracy of the measuring equipment and the development of secondary waves in the basin. When performing numerical simulations, the error most strongly depends on the spatial resolution of the finite element mesh. Nevertheless, the diffraction problem considered in the paper, the results for which were obtained by such different methods and coincide with satisfactory accuracy, allows to state with confidence that the numerical model used with the proposed settings is

applicable for modeling waves in water areas where the effects of wave diffraction are strong.

REFERENCES

1. **Popova E.A., Sizova Yu.S.** (2020) Puti realizacii gosudarstvennyh programm razvitiya Severnogo morskogo puti za schet privlecheniya chastnyh investicij [Ways to implement state programs for the development of the Northern Sea Route by attracting private investment]. *Voprosy regional'noj ekonomiki*, no 2, pp. 129–136.
2. **Ruksha V.V.** (2018) Razvitie atomnogo morskogo flota [Development of the nuclear marine fleet]. *Regional'naya energetika i energosberezhenie*, no 2, p. 62.
3. **Kantarzhi I.G., Mordvintsev K.P., Gogin A.G.** (2019) Numerical analysis of the protection of a harbor against waves. *Power technology and engineering*, vol. 5, pp. 45–52.
4. **Gorgutsa Yu.V.** (2020) Metod opredeleniya parametrov pomekh po meteofaktoram obrabotke sudov v morskih portah [Method for determining the parameters of interference by meteorological factors for the processing of ships in seaports]. *Morskie intellektual'nye tekhnologii*, n. 1–1, pp. 107–112.
5. **Malyuzhinets G.D.** (1959) Razvitie predstavlenij o yavleniyah difrakcii (k 130-letiyu so dnya smerti Tomasa YUnga) [Development of ideas about the phenomena of diffraction (to the 130th anniversary of the death of Thomas Young)]. *Uspekhi fizicheskikh nauk*, vol. 69, no 10, pp. 321–334.
6. **Leontovich M.A.** (1944) Ob odnom metode resheniya zadach o rasprostranenii elektromagnitnyh voln vdol' poverhnosti zemli [On one method for solving problems of the propagation of electromagnetic waves along the surface of the earth]. *Izv. Academy of Sciences of the USSR*, vol. 8, no 1, pp. 16–22.
7. **Leontovich M.A., Fok V.A.** (1946) Reshenie zadachi o rasprostranenii elektromagnitnyh voln vdol' poverhnosti Zemli po metodu parabolicheskogo uravneniya [Solving the problem of propagation of electromagnetic waves along the surface of the Earth using the parabolic equation method]. *ZHurnal eksperimental'noj i teoreticheskoj fiziki*, vol. 16, pp. 557–573.
8. **Fok V.A.** (1970) *Problemy difrakcii i rasprostraneniya elektromagnitnyh voln* [Problems of diffraction and propagation of electromagnetic waves]. Moscow: Sov. radio. (in Russian)
9. **Zagryadskaya N.N.** (1995) Primenenie metoda parabolicheskogo priblizheniya v zadachah difrakcii poverhnostnyh voln [Application of the parabolic approximation method in problems of surface wave diffraction]. *ZHurnal tekhnicheskoj fiziki,* vol. 65, no 8, pp. 25–37.
10. **Zagryadskaya N.N.** (2006) *Morskie volny na akvatoriyah i u sooruzhenij vertikal'nogo tipa* [Sea waves in water areas and near vertical structures]. S.-P.: Publishing House of the Polytechnic University. (in Russian)
11. **Krylov Yu.M. et al.** (1986) *Veter, volny i morskie porty* [Wind, waves and seaports]. L.: Gidrometizdat. (in Russian)
12. **Penney W.G. et al.** (1952) Part I. The diffraction theory of sea waves and the shelter afforded by breakwaters. *Philos. Trans. R. Soc. London. Ser. A, Math. Phys. sci. The Royal Society London*, vol. 244, no 882, pp. 236–253.
13. **Sommerfeld A.** (1896) Mathematische theorie der diffraction. *Math. Ann. Springer*, vol. 47, no 2, pp. 317–374.
14. **Krylov Yu.M.** (1966) *Spektral'nye metody issledovaniya i rascheta vetrovyh voln* [Spectral methods of research and calculation of wind waves]. L.: Gidrometeoizdat. (in Russian)
15. **Galenin B.G.** (1988) *Methods for calculating the protection of the water area*

of seaports from waves (PhD Thesis). Moscow.
16. **Zavyalov V.K.** (1976) *Research and calculations of the wave regime in the fenced water areas of ports and outports* (PhD Thesis). Leningrad: LPI M.I. Kalinina.
17. **Berkhoff J.C.W.** (1973) Computation of combined refraction—diffraction. *Coastal Engineering*, pp. 471–490.
18. **Berkhoff J.C.W.** (1976) *Mathematical models for simple harmonic linear water waves: wave diffraction and refraction* (PhD Thesis). Delft: Technische University.
19. **Shelushinin Yu.A.** (2019) Dostovernost' fizicheskogo modelirovaniya gidrotekhnicheskih sooruzhenij na primere ob"ektov imeretinskoj nizmennosti [Reliability of physical modeling of hydraulic structures on the example of objects of the Imereti lowland] // *Olimpijskoe nasledie i krupnomasshtabnye meropriyatiya: vliyanie na ekonomiku, ekologiyu i sociokul'turnuyu sferu prinimayushchih destinacij*, pp. 260–264.
20. **Kantarzhi I.G., Mordvintsev K.P.** (2015) CHislennoe i fizicheskoe modelirovanie v MGSU morskih portovyh gidrotekhnicheskih sooruzhenij [Numerical and physical modeling in MGSU of marine port hydraulic structures]. *Nauka i bezopasnost'*, no 2, pp. 2–16.
21. **Kantarzhi I., Anshakov A., Gogin A.** (2021) Composite modeling of wind waves in designing of port hydraulic structures. Proceedings of the *International Offshore and Polar Engineering Conference*, *Rhodes, 06.2021*, pp. 2254–2261.
22. **Afanasiev K.E. et al.** (2012) CHislennoe modelirovanie raboty opytovogo volnoproduktora odinochnyh voln [Numerical modeling of the operation of an experimental single-wave wave generator]. *Prikladnye tekhnologii gidroakustiki i gidrofiziki*, pp. 201–203.
23. **Zheleznyak M.I.** (2014) CHislennoe modelirovanie rezonansnyh svojstv gavanej s pomoshch'yu nelinejnoj negidrostaticheskoj modeli SWASH [Numerical simulation of the resonant properties of harbors using the non-linear non-hydrostatic SWASH model], *Matematicheskie mashiny i sistemy,* no 3, pp. 78–87.
24. **Komen G.J. et al.** (1996) *Dynamics and modeling of ocean waves*, Cambridge: Cambridge University Press.
25. **Lavidas G., Venugopal V.** (2018) Application of numerical wave models at European coastlines: A review. *Renew. Sustain. Energy Rev*. vol. 92, pp. 489–500.
26. **Holthuijsen L.H., Herman A., Booij N.** (2003) Phase-decoupled refraction–diffraction for spectral wave models. *Coastal Engineering*, vol. 49, no 4, pp. 291–305.
27. **Borsboom M.J.A.** (1998) A Boussinesq-type wave model with improved linear and nonlinear behavior. *Rep. H3203*, vol. 51, paper no X0231.
28. DHI Water Environment (2017) *Boussinesq Waves Module. user guide*. Denmark, DHI Water Environment.
29. **Larsen J., Dancy H.** (1983) Open boundaries in short wave simulations—a new approach, *Coastal Engineering*, vol. 7, no 3. pp. 285–297.

СПИСОК ЛИТЕРАТУРЫ

1. **Попова Э.А., Сизова Ю.С.** Пути реализации государственных программ развития Северного морского пути за счет привлечения частных инвестиций // Вопросы региональной экономики, 2020, № 2. С. 129–136.
2. **Рукша В.В.** Развитие атомного морского флота // Региональная энергетика и энергосбережение, 2018, № 2. С. 62.
3. **Кантаржи И.Г., Мордвинцев К.П., Гогин А.Г.** Численное исследование защищенности акватории порта // Гидротехническое строительство, 2019, № 5. С. 45–52.

4. **Горгуца Ю.В.** Метод определения параметров помех по метеофакторам обработке судов в морских портах // Морские интеллектуальные технологии, 2020, № 1–1. С. 107–112.
5. **Малюжинец Г.Д.** Развитие представлений о явлениях дифракции (к 130-летию со дня смерти Томаса Юнга) // Успехи физических наук, 1959, № 69(10). С. 321–334.
6. **Леонтович М.А.** Об одном методе решения задач о распространении электромагнитных волн вдоль поверхности земли // Изв. АН СССР. Сер. Физ, 1944, т. 8, № 1. С. 16–22.
7. **Леонтович М.А., Фок В.А.** Решение задачи о распространении электромагнитных волн вдоль поверхности Земли по методу параболического уравнения // Журн. эксперим. и теор. физики, 1946, №. 16. С. 557–573.
8. **Фок В.А.** Проблемы дифракции и распространения электромагнитных волн. – М.: Сов. радио, 1970. – 517 с.
9. **Загрядская Н.Н.** Применение метода параболического приближения в задачах дифракции поверхностных волн // Журнал технической физики, 1995, № 65(8). С. 25–37.
10. **Загрядская Н.Н.** Морские волны на акваториях и у сооружений вертикального типа. –С.-П.: Изд-во Политехн. ун-та, 2006. – 224 с.
11. **Крылов Ю.М. и др.** Ветер, волны и морские порты. – Л.: Гидрометиздат, 1986. – 263 с.
12. **Penney W.G. et al.** Part I. The diffraction theory of sea waves and the shelter afforded by breakwaters // Philos. Trans. R. Soc. London. Ser. A, Math. Phys. Sci. The Royal Society London, 1952, No. 244(882), pp. 236–253.
13. **Sommerfeld A.** Mathematische theorie der diffraction // Math. Ann. Springer, 1896, No. 2(47), pp. 317–374.
14. **Крылов Ю.М.** Спектральные методы исследования и расчета ветровых волн. – Л.: Гидрометеоиздат, 1966. – 255 с.
15. **Галенин Б.Г.** Методы расчета защищенности акватории морских портов от волн: автореф. дис. канд. техн. наук: 05.22.18. М., 1988, 23 с.
16. **Завьялов В.К.** Исследования и расчеты волнового режима на огражденных акваториях портов и аванпортов: автореф. дис. канд. техн. наук: 05.22.18. ЛПИ им. М.И. Калинина, 1976, 20 с.
17. **Berkhoff J.C.W.** Computation of combined refraction—diffraction // Coastal Engineering, 1973, pp. 471–490.
18. **Berkhoff J.C.W.** Mathematical models for simple harmonic linear water waves: wave diffraction and refraction: Ph. D. Thesis, 1976.
19. **Шелушинин Ю.А.** Достоверность физического моделирования гидротехнических сооружений на примере объектов имеретинской низменности // Олимпийское наследие и крупномасштабные мероприятия: влияние на экономику, экологию и социокультурную сферу принимающих дестинаций, 2019. С. 260–264.
20. **Кантаржи И.Г., Мордвинцев К.П.** Численное и физическое моделирование в МГСУ морских портовых гидротехнических сооружений // Наука и безопасность, 2015, № 2. С. 2–16.
21. **Kantarzhi I., Anshakov A., Gogin A.** Composite modelling of wind waves in designing of port hydraulic structures // Proceedings of the International Offshore and Polar Engineering Conference. OnePetro, 2021, pp. 2254–2261.
22. **Афанасьев К.Е. и др.** Численное моделирование работы опытового волнопродуктора одиночных волн // Прикладные технологии гидроакустики и гидрофизики, 2012. С. 201–203.
23. **Железняк М.И. и др.** Численное моделирование резонансных свойств гаваней с помощью нелинейной негидростатической модели SWASH //

Математические машины и системы, 2014, № 3. С. 78–87.
24. **Komen G.J. et al.** Dynamics and modelling of ocean waves, 1996.
25. **Lavidas G., Venugopal V.** Application of numerical wave models at European coastlines: A review // Renew. Sustain. Energy Rev. Elsevier, 2018, vol. 92, pp. 489–500.
26. **Holthuijsen L.H., Herman A., Booij N.** Phase-decoupled refraction–diffraction for spectral wave models // Coastal Engineering, 2003, vol. 49, No. 4, pp. 291–305.
27. **Borsboom M.J.A.** A Boussinesq-type wave model with improved linear and nonlinear behaviour // Rep. H3203, 1998, vol. 51, Paper No. X0231.
28. **DHI Water Environment**. Boussinesq Waves Module. User Guide. Denmark: DHI Water Environment, 2017, 196 pages.
29. **Larsen J., Dancy H.** Open boundaries in short wave simulations—a new approach // Coastal Engineering, 1983, vol. 7, No. 3, pp. 285–297.

Kantarzhi Izmail Grigorievich, Professor, Doctor of Technical Sciences; Professor of Department of Hydraulics and Hydraulic Engineering, Moscow State University of Civil Engineering (MSUCE), Russia, Moscow, Yaroslavl highway 26; E-mail: kantardgi@yandex.ru

Gogin Alexander Grigorievich, PhD, Laboratory Assistant of Department of Hydraulics and Hydraulic Engineering, Moscow State University of Civil Engineering (MSUCE), Russia, Moscow, Yaroslavl highway 26; E-mail: ag.gogin@yandex.ru

Кантаржи Измаил Григорьевич, профессор, доктор технических наук; профессор кафедры Гидравлики и гидротехнического строительства Московского государственного строительного университета (НИУ МГСУ), Россия, Москва, Ярославское ш., 26; E-mail: kantardgi@yandex.ru

Гогин Александр Григорьевич, кандидат технических наук; лаборант кафедры Гидравлики и гидротехнического строительства Московского государственного строительного университета (НИУ МГСУ), Россия, Москва, Ярославское ш., 26; E-mail: ag.gogin@yandex.ru

International Journal for Computational Civil and Structural Engineering, 19(1) 69–84 (2023)

DOI:10.22337/2587-9618-2023-19-1-69-84

THE PROBLEM OF CRACK OPENING WIDTH AND STIFFNESS OF REINFORCED CONCRETE STRUCTURES, BUILDINGS AND CONSTRUCTIONS

Vladimir I. Kolchunov

Research Institute of Building Physics of Russian Academy of Architecture and Construction Sciences, Moscow, RUSSIA
Southwestern State University, Kursk, RUSSIA

Abstract. The article defines the main results for the development of reinforced concrete mechanics. In the isotropic medium between the cracks is used "first object - flows-blocks", "second object - main cracks" and the effect of reinforced concrete, the physical essence of which is the non-uniformity of concrete and continuous reinforcement. Reactions arise in the concrete for deformation of the reinforcement from the bonding of the compressed concrete in the tensile region. The average resistance of the tensile concrete and the "average total force of the working reinforcement," the third object, are transmitted through the effect of reinforced concrete and the "dowel" effect. The crack opening widths are the relative mutual displacements of reinforcement and concrete, determined from the boundary conditions and the Thomas-Author hypothesis. A new classification of cracks has been developed: regular cracks (anisotropic medium of reinforced concrete) and main cracks based on the effect of reinforced concrete (origins - concentrations) and maximum opening in the closed equations of mechanics of reinforced concrete from the Lagrange function. The author has proposed hypotheses, theorems of linear and angular deformations, functionals for deplanation of cross section of reinforced concrete element from elastic-plastic stage, jumps - cracks and stiffness matrix in a single compound strip which allow to reduce the order of differential equations. The resistance design model method for reinforced concrete mechanics is used for the rod, wall, and slab of the "envelope" of cracks. Hybrid from Lira (finite element method of reinforced concrete from anisotropy) developed in the form of two finite element effect of reinforced concrete of "flat and spatial cantilever" for external and internal displacements. The general principle from Loleith to the "opening - closing" of cracks, the stiffness of the mechanics of reinforced concrete is obtained in the form of the method of the computational model of resistance.

Keywords: reinforced concrete effect, crack classification, source-concentrations, single stripes, resistance models, crack opening-closing

ПРОБЛЕМА ШИРИНЫ РАСКРЫТИЯ ТРЕЩИН И ЖЕСТКОСТИ ЖЕЛЕЗОБЕТОННЫХ КОНСТРУКЦИЙ, ЗДАНИЙ И СООРУЖЕНИЙ

Вл.И. Колчунов

Научно-исследовательский институт строительной физики РААСН, г. Москва, РОССИЯ
Юго-Западный государственный университет, г. Курск, РОССИЯ

Аннотация. В статье определены основные результаты для развития механики железобетона. В изотропной среде между трещинами используется «первый объект – потоки-блоки», «второй объект - магистральные трещины» и эффект железобетона, физическая суть которого заключается в несплошности бетона и сплошной арматуре. В бетоне возникают реакции для деформации арматуры от сцепления сжатого бетона в растянутой области. Среднее сопротивления растянутого бетона и «средне суммарное усилие рабочей арматуры», - третий объект, - передаются через эффект железобетона и «нагельный» эффект (главный вектор в трещине). При этом ширина раскрытия трещин - относительные взаимные смещения арматуры и бетона, определяемые из граничных условий и гипотезы Томаса – автора. Разработана новая классификация трещин: регулярные трещины (анизотропная среда железобетона) и магистральные трещины на основе эффекта железобетона (истоки - концентрации) и максимальной раскрытия в замкнутых уравнениях механики железобетона из функции Лагранжа. Автором предложены гипотезы, теоремы линейных и угловых деформаций, функционалы для

депланации поперечного сечения железобетонного элемента из упругопластической стадии, скачки - трещины и матрица жесткости в единичной составной полоске, позволяющие сократить порядок дифференциальных уравнений. Метод расчетной модели сопротивления для механики железобетона используется для стержня, стены, плиты из «конверта» из спиралеобразной, иксообразной и гармошкообразной трещины. Гибрид из Лира (метод конечных элементов железобетона из анизотропии) разработан в форме эффекта железобетона из двух конечных элементов в виде «плоская и пространственная консоль» для внешних и внутренних перемещений. Общий принцип от Лолейта до «раскрытия – закрытия» трещин, жесткости механики железобетона получен в виде метода расчетной модели сопротивления.

Ключевые слова: эффект железобетона, классификация трещин, истоки-концентрации, единичные полоски, модели сопротивления, раскрытие-закрытие

The mechanics of reinforced concrete is the basis for the safety of the system of buildings and structures under new challenges of man-made natural and terrorist nature. The solutions to these problems are obtained at a new scientific level due to modern technologies of experimental research of structures and convergence of physical phenomena in reinforced concrete on the basis of fracture mechanics.

THE MAIN RESULTS FOR THE ACADEMY'S BUILDING SCIENCES ARE FORM:

I. Development of the mechanics of reinforced concrete, - result I.

1) Let's look at the main premises

● The reinforced concrete environment includes force flows from concrete blocks for isotropic environment between cracks "first object - flows (blocks)" in the local region near the fracture bank in fracture mechanics of reinforced concrete.

● The second object is the main cracks from the fracture mechanics of reinforced concrete and the effect of discontinuity of concrete developed by the author. Its essence is the discontinuity of concrete and solid reinforcement, where there are shear reactions ΔT (deformations between reinforcement and concrete), taking into account the compression force for tensile concrete $\sigma_{bt,c}$, the relative deformations of reinforcement $\varepsilon_S = \varepsilon_{S,j} - \varepsilon_э$ and other parameters to solve the problem of resistance near the reinforcement zone of a reinforced concrete element. Experimental strain diagrams were obtained in experiments of J.M. Nemirovsky, B.Sh. Shamuradov, works of the author [1-4] and others.

● In a reinforced concrete structure, the resistance of the tensile concrete is obtained for a transversal-isotropic material. The force for the tensile concrete in the working reinforcement can be transferred through the general parameter ψ_s (or $\psi_{s,sw}$) by Prof. V.I. Murashev [5]. For the average longitudinal force N_{sm} $(N_{s,m} = \varepsilon_s \cdot \psi_s \cdot E_s \cdot A_s)$ and transverse force $Q_{s,m}$ $(Q_{s,m} = \varepsilon_s \cdot \psi_{Q,s} \cdot E_s \cdot A_s)$ we can talk about the connection of a special third object - the "total average force $N_{s,m,sum}$ of the working reinforcement" ($N_{s,m,sum} = \sqrt{N_{s,m}^2 + Q_{s,m}^2}$) using the reinforced concrete effect and the dowel forses (Fig. 1). The author has developed a second level building mechanics model for a rebar, crack opening, bank shear and buckling.

● The following results were obtained on the basis of fracture mechanics. The author developed a special dual-console element (DCE) and discovered the effect of its physical essence, which consists in the reaction between the discontinuity of concrete and the continuity of the working reinforcement (Fig. 1).

● Using the pliability of structural mechanics, a canonical system of equations is derived from classical methods (method of forces, method of displacements, mixed method, finite element method) (Fig. 1):

$$\zeta_{cu} = \lim_{\delta A \to 0}\left(\frac{\delta W - \delta V}{\delta A}\right) = C_I \cdot \Delta T \frac{\partial \Delta T}{\partial h_{crc}} - C_{II} P_1 \cdot \frac{\partial P_1}{\partial h_{crc}} - C_{III} P_2 \cdot \frac{\partial P_2}{\partial h_{crc}} - C_0 M_{con} \cdot \frac{\partial M_{con}}{\partial h_{crc}}; \quad (1)$$

Here δV is the decrease of the body's potential energy when the crack advances by a small increment δa; δW is the additional work performed on the body when the crack advances by a small increment δa.

$$\left.\begin{aligned} &X_1\delta_{11} + X_2\delta_{12} + X_3\delta_{13} + \Delta_{1p} - (-\Delta_3 + \Delta_2) + \Delta_2 + h_{crc} \cdot (\phi_1 + \Delta\phi) = 0; \\ &X_1\delta_{21} + X_2\delta_{22} + X_3\delta_{23} + \Delta_{2p} - (\Delta_6 + \Delta_2) + \Delta_2 + (h_{crc} - t_b) \cdot (\phi_1 + \Delta\phi) = 0; \\ &X_1\delta_{31} + X_2\delta_{32} + X_3\delta_{33} + \Delta_{3p} + (\phi_2 - \Delta\phi) + (\phi_1 + \Delta\phi) = 0; \\ &X_4\delta_{44} = 1 \cdot (-\Delta\Gamma_1) - 1 \cdot \Delta_2 + (x_{crc} - h_{b,1}) \cdot \Delta\phi\ . \end{aligned}\right\} \quad (2)$$

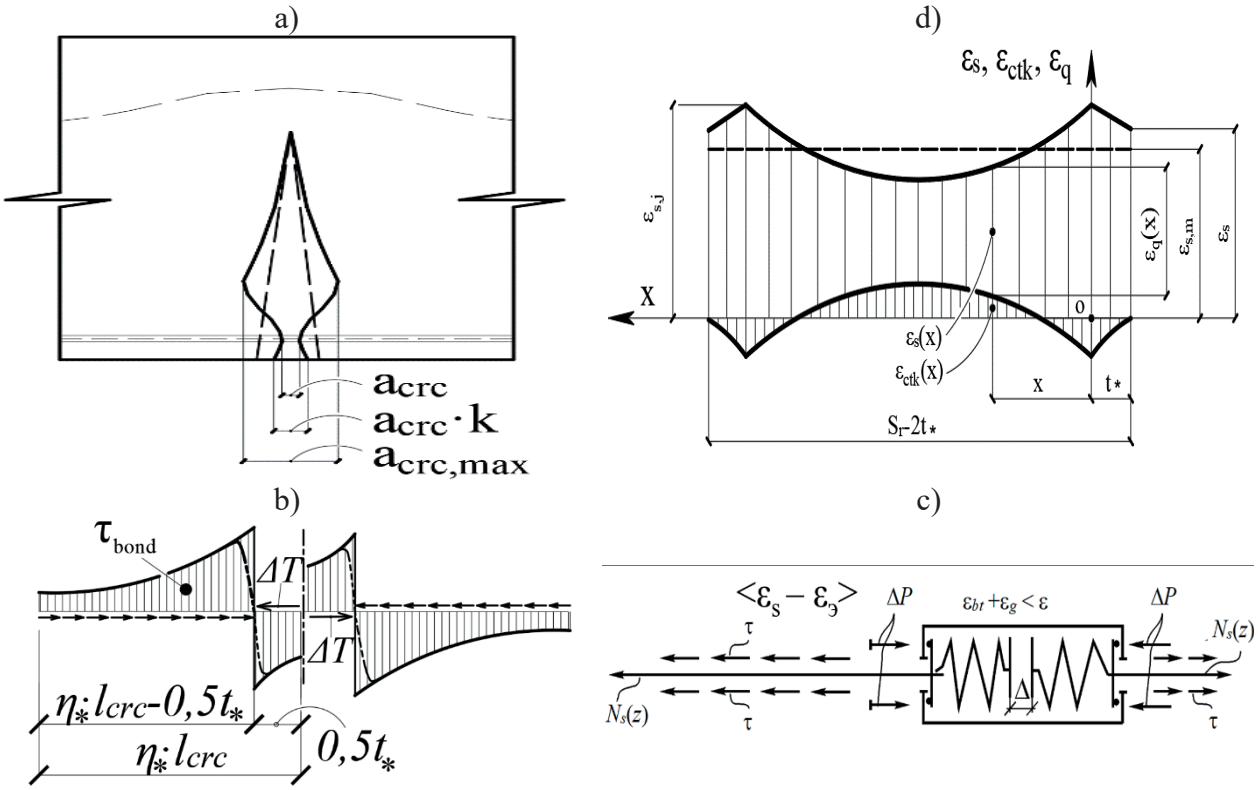

Figure 1. Effect of reinforced concrete: the shape of the crack from triangle to ellipsoid (a); the response from the continuous concrete and continuous reinforcement (b); the mechanical model (c); the relative deformations of the reinforcement and the stretched concrete (d)

Prof. V.I. Murashev has developed formulas for transverse cracks and stiffness, distance between cracks l_{crc}, resistance coefficient of tensile concrete ψ_s and crack opening width a_{crc}. This was later developed to the effect of discontinuity in concrete (Fig. 1 and Fig. 2a). The crack opening width is determined using the Thomas-author hypothesis, and the relative mutual displacements of the reinforcement and concrete are determined from the dependence:

$$\varepsilon_g(x) = \varepsilon_s(x) - \varepsilon_{bt}(x). \quad (3)$$

$\varepsilon_s(x)$ - relative deformations of reinforcement;

$\varepsilon_{bt}(x)$ - relative deformations of concrete in section x.

The definition problem is reduced to finding the relative deformations of concrete from dependence (3) and the equilibrium of the reinforcing bar.

$$\frac{d\varepsilon_g(x)}{dx} + B\varepsilon_g(x) = 0. \quad (4)$$

The solution of the homogeneous first-order differential equation has the form:

$$\varepsilon_g(x) = C \cdot e^{-Bx}. \quad (5)$$

The integration constant C is found from the boundary condition, according to which at $x = 0,\ \varepsilon_{bt,c}(x) = -\sigma_{bt,c} / (v_b E_b)$:

$$C = \frac{B_3}{B} + \frac{1}{B(1-K)}\left(-\frac{\sigma_{bt,c}}{v_b E_b}\right). \quad (6)$$

The distance between cracks is determined from the ratio:

$$l_{crc} = \frac{2\left(\ln B_4 - Bt_*\right)}{-B}. \quad (7)$$

The coefficient that takes into account the uneven distribution of the relative strains of the tensile reinforcement between the cracks:

$$\psi_S = \frac{2 \cdot K \cdot B_3}{\varepsilon_S \cdot l_{crc} \cdot B}\cdot\left[1 - e^{-B\cdot(0.5 l_{crc} - t_*)}\right] + \frac{2}{\varepsilon_S \cdot l_{crc}}\left(\varepsilon_S + \frac{\Delta T}{E_S A_S} - K \cdot B_3\right)\cdot\left(0,5 l_{crc} - t_*\right) + \\ + \frac{\delta Q \cdot K}{\varepsilon_S \cdot l_{crc} \cdot B \cdot t_*}\left(0,5 l_{crc} - t_*\right)^2 + \frac{2 \cdot \varepsilon_S \cdot E_S \cdot A_S + \Delta T}{\varepsilon_S \cdot l_{crc} \cdot E_S \cdot A_S} \cdot t_*; \quad (8)$$

and the crack opening width has the form:

$$a_{crc} = -\frac{2\Delta T}{G} + \frac{2}{B}\left(\frac{q_{sw} S}{A_{sw} E_{sw}} + B_{a,1}\right)\left(1 - e^{\ln B_4}\right) - \frac{2B_2}{B}\ln B_4 = \\ = -\frac{2\Delta T}{G} - \frac{2B_{a,2}}{B} - \frac{2B_2}{B}\ln\left(1 + \frac{B_{a,2} \cdot A_{sw} E_{sw}}{q_{sw} S + B_{a,1} A_{sw} E_{sw}}\right); \quad (9)$$

Here in equations (7)-(9): $B = \frac{S \cdot G}{A_{sw} E_{sw} K}$; $B_{a,1} = \frac{\Delta T}{E_{sw} A_{sw}} - \frac{\sigma_{bt,c}}{v_b E_b} - B_2$; $\frac{1}{K} = 1 + \frac{A_s E_s}{\omega_{bt}(x) A_{bt}(x) E_b \cdot v_{bt}(x)} =$

$= 1 + \delta\frac{\mu_s \cdot n\left(h_0 + x\cdot(\gamma - 1)\right)}{0.32 \cdot h_0 \cdot (\gamma - \xi)(\gamma + 0.03\xi)}$; $B_2 = \frac{\delta Q}{t\, B}$; $B_3 = \varepsilon_s + \frac{\Delta T}{E_s A_s} - \frac{\sigma_{bt,s}}{v_b E_b} - B_2$; $B_4 = 1 + \frac{\sigma_{bt,c}}{(K-1) B_{3,*} v_b E_b} +$

$+ \frac{\varepsilon_{bt,u}}{B_{3,*}(K-1)}$.

The new level of fracturing corresponds to the fulfillment of the following inequality:

$$l_{crc,i} \le \eta_* \cdot l_{crc,i-1}. \quad (10)$$

Cracking continues up to the moment of fracture. There are several levels of cracking:

$$\left.\begin{array}{l} l_{crc} > l_{crc,1} - \text{no cracks;} \\ l_{crc,1} \ge l_{crc} \ge l_{crc,2} - \text{first level;} \\ l_{crc,2} \ge l_{crc} \ge l_{crc,3} - \text{second level;} \\ \ldots\ldots\ldots\ldots\ldots\ldots\ldots\ldots\ldots\ldots \\ l_{crc} \ge 6t_* \end{array}\right\}. \quad (11)$$

● The dowel effect of the author of the second level model [9,10] is developed for a beam with two pinched ends at turns of the pinched ends as well as crack opening $\Delta_{crc,s}$, shifting of the crack-track banks Δ_{crc} and concrete buckling. The longitudinal axis of the reinforcing bar has a sinusoidal shape when displaced with a maximum amplitude of $0.5\Delta_1$, from the longitudinal force $N_s(x)$ and eccentricities in the vertical and horizontal directions (Fig. 2).

The unknowns X_2, X_3, $X_{3,t}$, X_4, X_5 are found from the calculation of statically indeterminate systems by the method of forces from coupled systems of equations (systems (12) and (13)):

$$\left.\begin{array}{l} X_1\delta_{11} + X_3\delta_{13} + \Delta_{1,P} = 0 \\ X_1\delta_{31} + X_3\delta_{33} + \Delta_{3,P} = 0 \end{array}\right\}; \quad (12)$$

$$\left.\begin{array}{l} X_{3,t}\delta_{43t} + X_4\delta_{44} + \Delta_{4,P} = 0 \\ X_{3,t}\delta_{53t} + X_5\delta_{55} + \Delta_{5,P} = 0 \end{array}\right\}. \quad (13)$$

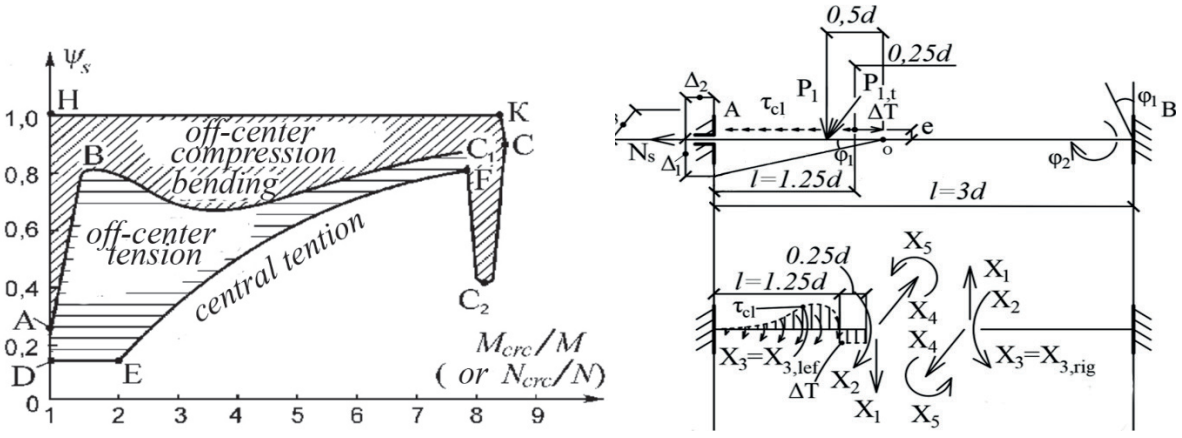

a) *b)*

Figure 2 - The nature of the coefficient change under various influences (a), the calculation scheme of the dowel effect (b)

After solving the coupled system, the values are obtained:

$$X_4 = X_3 \cdot \frac{E(\lambda)I_z}{G(\lambda)I_{tor}} \cdot \eta \cdot 0,25 \cdot N_{s,1} -$$

$$-(0.25 \cdot d \cdot P_{l,t} + 0.16 \cdot \frac{\Delta_3}{d} \cdot \left(N_{s,1} + N_{s,2}\right)$$

$$-0.44 \cdot \frac{\Delta_3}{d^3} \cdot E(\lambda)I_z + 0.59 \cdot \frac{\varphi_2}{d^2} \cdot E(\lambda)I_z); \quad (14)$$

$$X_5 = X_3 \cdot \eta \cdot N_{s,1} \cdot e - 0.17 \cdot d \cdot P_{l,t}. \quad (15)$$

Here $X_{3,t}$ are the torsional forces $P_{l,t}$ in Fig. 1 and Fig. 2 b, c).

The main vector u of forces in the reinforcement is characterized by two values u_{gi}, υ_{gi} and is related to the normal stresses $\sigma_{s,i}$ of the reinforcement in the cracks and the tangential stresses $\tau_{s,i}$. (Fig. 3).

The relationships between υ_{gi} and angle β from the experiments are of the form:

$$\upsilon_{gi} = k_{\text{sup}} \cdot R_{\text{sup}} = k_{\text{sup}} (Q_{\text{s}} + N_{\text{s}} \cdot tg\beta + P_i)\zeta; \quad (16)$$

Here are the rod yield functions for the distance l_{crc} (using the area and perimeter of the rod) at some small segment u_{gi} and υ_{gi}, ζ is coefficient for the generalized reaction R_{sup}

The components of the main vector along some orthogonal directions are related to each other:

$$0.5 \cdot a_{crc} = u_{gz} \cdot \cos\alpha + u_{gx} \cdot \sin\alpha \quad (i \neq x, z); \quad (17)$$

$$u_{gz} = \frac{0.5 \cdot a_{crc} - u_{gx} \cdot \sin\alpha}{\cos\alpha}; \quad (18)$$

$$\upsilon_{gi} = u_{gy} \cdot \cos\beta_i - u_{gx} \cdot \sin\beta_i; \quad (19)$$

$$\upsilon_{gi} = u_{gz} \cdot \cos\beta_i - u_{gx} \cdot \sin\beta_i; \quad (20)$$

Then (Fig. 3) we get:

$$\cos\beta = 0,5A_\beta \pm \sqrt{(0,5A_\beta)^2 - B_\beta}; \quad (21)$$

Here $A_\beta = \frac{2 \cdot \upsilon_{gi} \cdot u_{gz}}{\left(u_{gx}^{\ 2} + u_{gz}^{\ 2}\right)}$; $B_\beta = \frac{\upsilon_{gi}^{\ 2} - u_{gx}^{\ 2}}{\left(u_{gx}^{\ 2} + u_{gz}^{\ 2}\right)}$.

After that we get the dependence

$$u_{gi} = u_{gx} \cdot \cos\beta_i + u_{gy} \cdot \sin\beta_i. \quad (22)$$

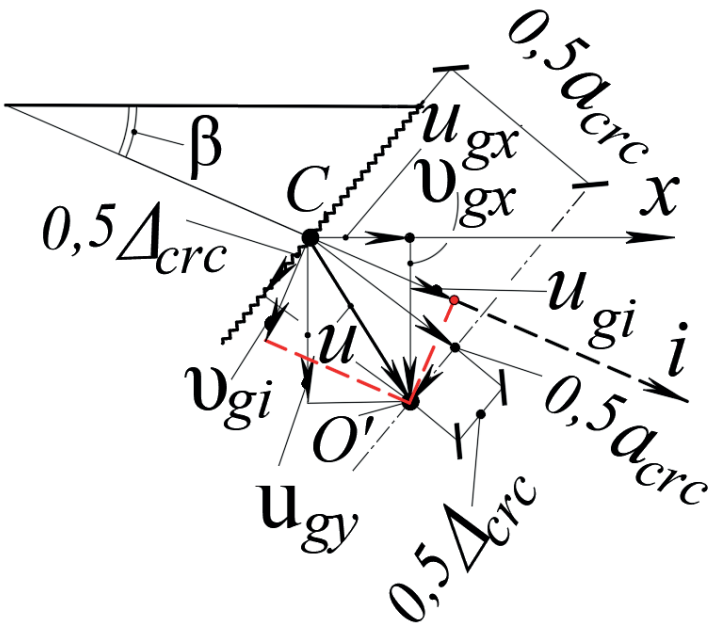

Figure 3. Connected displacements of reinforcing bars u_{gi} and υ_{gi} (for crumpled concrete) in the crack with crack bank opening a_{crc} and shear Δ_{crc}, taking into account the main vector u and the angle β of forces in the reinforcement crossing the crack

2) The classification of trunk cracks has the form (Fig. 4):

- regular cracks Prof. N.I. Karpenko [19] (anisotropic medium of reinforced concrete and finite element method, no effect of reinforced concrete, no width of "opening - closing");
- main cracks of the author (Fig. 4) based on the effect of disruption of the continuity of reinforced concrete.

Basic cracks (geometric force and inter-medium concentrations for the augmented and internal displacements Δ_1, Δ_2, φ_1, φ_2, $\Delta\varphi_{crc}$.

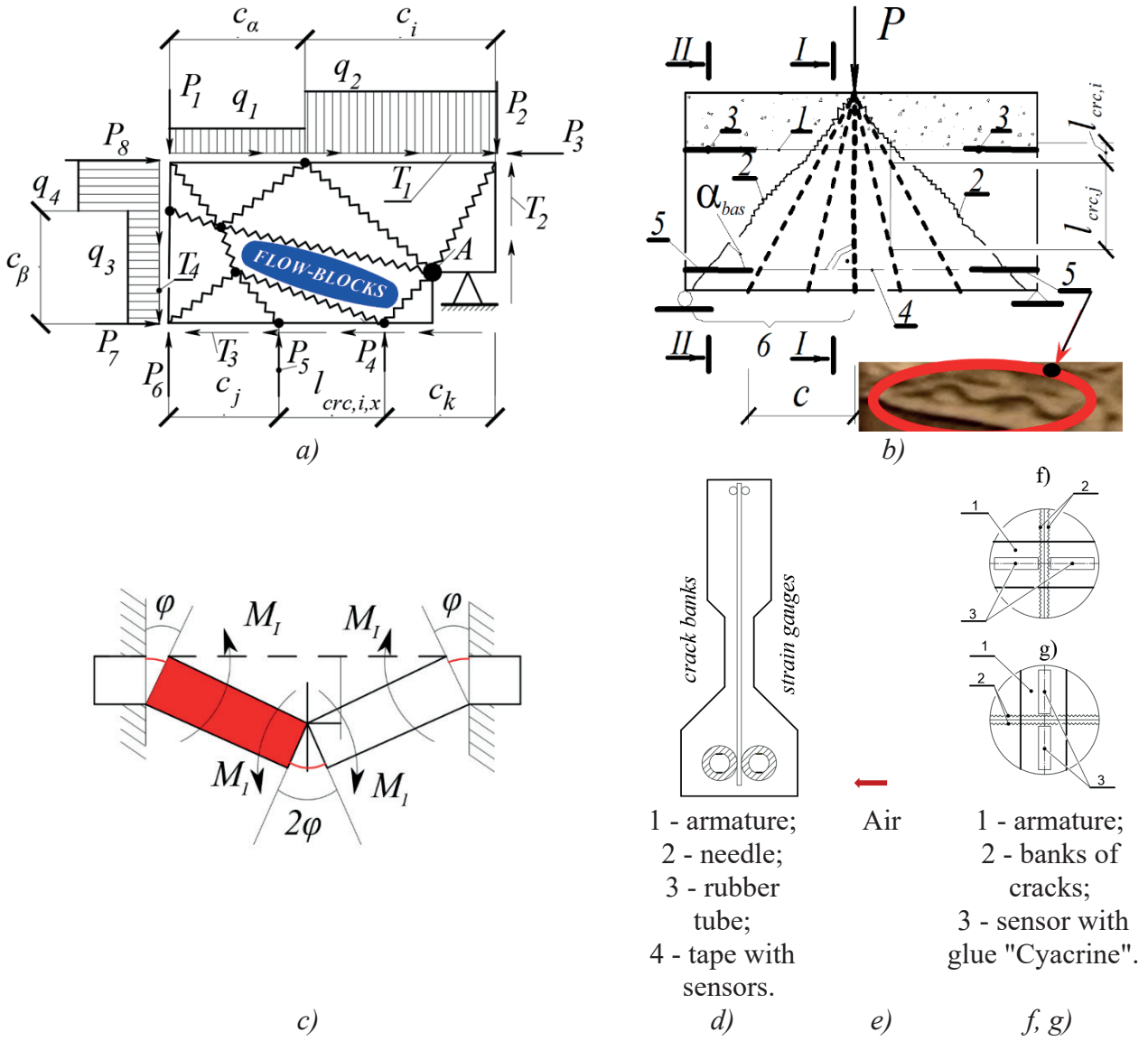

Figure 4. Classification of trunk cracks: a - calculation model of resistance 4 for a wall with trunk oblique cracks; b - baseline crack origins - concentrations: geometric, force concentrations for external and internal displacements Δ_1, Δ_2, φ_1, φ_2, $\Delta\varphi_{crc}$); c - computational model of resistance 4a - slab with trunk cracks; d - shape of cross-section for types of cracks and technology of experiments for punches in the reinforcement (e), gauges with glue "Zyakrin" for the banks of cracks (f, g)

The general model is proposed for the analysis of systems partitioning into physical and computational models of resistance of reinforced concrete (RRC) in cracks rod for RRC 1 - 3, flat cracks RRC4, 4 * and spatial RRC5, 5 * for system "opening-closing" width.

Here types I-III of area cracks M >Mcrc, Mt < Mt,crc and Q ≥ Qcrc; M < Mcrc, Mt > Mt,crc or Mt < Mt,crc, Q > Qcrc; type IV - crack development from fracture mechanics; type V - cracks from compressed concrete ε_3 (top) and ε_1 (wall); type VI - cracks from anchoring

The Lagrange function is constructed for the maximum crack opening width in the closed equations of reinforced concrete mechanics

(Fig. 4) $F_i = f\left(q_{sw}, x_B, \sigma_s, x, \sigma_c, \sigma_{s,1}, \sigma_{c,1}, C_2, \lambda_1, \lambda_2, \lambda_3, \lambda_4, \lambda_5, \lambda_6, \lambda_7\right)$:

$$\left.\begin{array}{l} \dfrac{\partial f}{\partial x_1} + \lambda_1 \dfrac{\partial \theta_1}{\partial x_1} + \lambda_2 \dfrac{\partial \theta_2}{\partial x_1} + ... + \lambda_m \dfrac{\partial \theta_m}{\partial x_1} = 0; \\ ..... \\ \dfrac{\partial f}{\partial x_n} + \lambda_1 \dfrac{\partial \theta_1}{\partial x_n} + \lambda_2 \dfrac{\partial \theta_2}{\partial x_n} + ... + \lambda_m \dfrac{\partial \theta_m}{\partial x_n} = 0. \end{array}\right\} \quad (23)$$

3) The author proposed new hypotheses and theorems:
- The first one is about the distribution of relative linear deformations $\varepsilon_{x,b}$ and $\varepsilon_{x,s}$ using a special geometric volumetric figure for the deplanation of the cross-section of a reinforced concree element from elastic-plastic stages I-III and in jumps - cracks [14-18];
The second hypothesis on the distribution of relative angular deformations of concrete and reinforcement ($\gamma_{sum,b}$ and $\gamma_{sum,s}$) using a special geometric volume figure for the deplanation of the cross-section of a reinforced concrete element from elastic-plastic stages I-III, in jumps - cracks and theorems 1-3 [14-18];
4) Analytical functionals first - fourth are developed when solving the system of proposed complex functions from the grids method families in the compressed and stretched zones with the help of small squares. Linear and angular deformations are determined at all stages I-III for a complex-stressed reinforced concrete element and in the jumps-cracks. The first functional $f_{5,*}(y,z)$ is a function of two functions along the y-axis and z-axis; the second functional $f_{***}(x,z,y)$ is a function of three functions along the x-axis, z-axis, and y-axis. The bending and torsional moments are determined using the third uncertain function $f_{\varepsilon,\text{int,vol}}(x,y,z)$ (a special function of subtraction from the triangle in the calculated cross sections of the element when it is approximated by rectangles), and the torsional moments are determined using the fourth uncertain function $f_{5,**,\iint}(z,y)$.

5) Stiffness due to intersecting cracks for a unit strip uses the hypothesis, which allowed for reinforced concrete to reduce the differential equations of composite structures by an order of magnitude A.R. Rzhanitsyn [11, 18]. The stiffness matrix is constructed for rectangular cross-sections using small squares for physical characteristics: static equations (equilibria), geometric equations (deformations), and physical equations (Fig. 5).

$$\left.\begin{array}{l} \dfrac{T_1'}{\xi_{\text{m},1}} - \Delta_{11}T_1 - \Delta_{12}T_1 - ... - \Delta_{in}T_n = \Delta_{10}; \\ \dfrac{T_2'}{\xi_{m,2}} - \Delta_{21}T_1 - \Delta_{22}T_2 - ... - \Delta_{2n}T_n = \Delta_{20}; \\ \dfrac{T_n'}{\xi_{m,n}} - \Delta_{ni}T_i - \Delta_{n2}T_2 - ... - \Delta_{nn}T_n = \Delta_{n0}. \end{array}\right\} \quad (24)$$

$$\Delta = -\frac{N_{0.1}}{(E_{b,1}A_{b,1})_{ekv}} + \frac{N_{0.2}}{(E_{b,2}A_{b,2})_{ekv}} - \frac{f(x_{crc})}{r_y}; \quad (25)$$

$$\lambda = \sqrt{\xi\gamma} = \sqrt{\xi\left[\frac{1}{(E_{b,1}A_{b,1})_{ekv}} + \frac{1}{(E_{b,2}A_{b,2})_{ekv}} + \frac{f^2(x_{crc})}{M \times r_y}\right]}; \quad (26)$$

Here T_1, T_2, T_n - shear forces accumulated along the length of the rod to the section; $\xi_{\text{m},1}$, $\xi_{\text{m},2}$, $\xi_{\text{m,n}}$ - modulus in a single shear band of the joint; Δ - displacements along a given direction; - difference of average relative linear and angular deformations in the joint point; ε_{qm}, $\gamma_{b,m}$ - equivalent stiffness; $f(x_{crc})$ - function of height of concrete compressed zone, averaged between cracks; $1/r_y = \chi$ - curvature of reinforced concrete composite rod.

II. RESISTANCE CALCULATION MODEL METHOD FOR STRUCTURAL MECHANICS, - RESULT II.

Calculated models of resistance (Fig. 5) fully meet the modern trend of deformation models of the theory of reinforced concrete, denoted today by the conceptual hierarchy (section - element - system) for the following levels: rod, flat and volumetric.

The analysis of the first model is performed. This is the rod with main normal cracks for the analytical fracture mechanics functional. The analysis of the second model for trunk oblique cracks is also performed using closed equations, which are included in the Lagrange function to determine the dangerous crack.

The third model of resistance has diagonal and other cracks for pliable units, as opposed to rigid units from structural mechanics (Fig. 5). Model 4 is a wall with trunk oblique cracks as well as diagonal (seismic) cracks, and 4a is a slab with trunk cracks (Fig. 4c and Fig. 5). Model 5 uses volumetric spatial blocks in torsion with bending. 5a are volumetric spatial blocks under the action of torsion with bending and shear force.

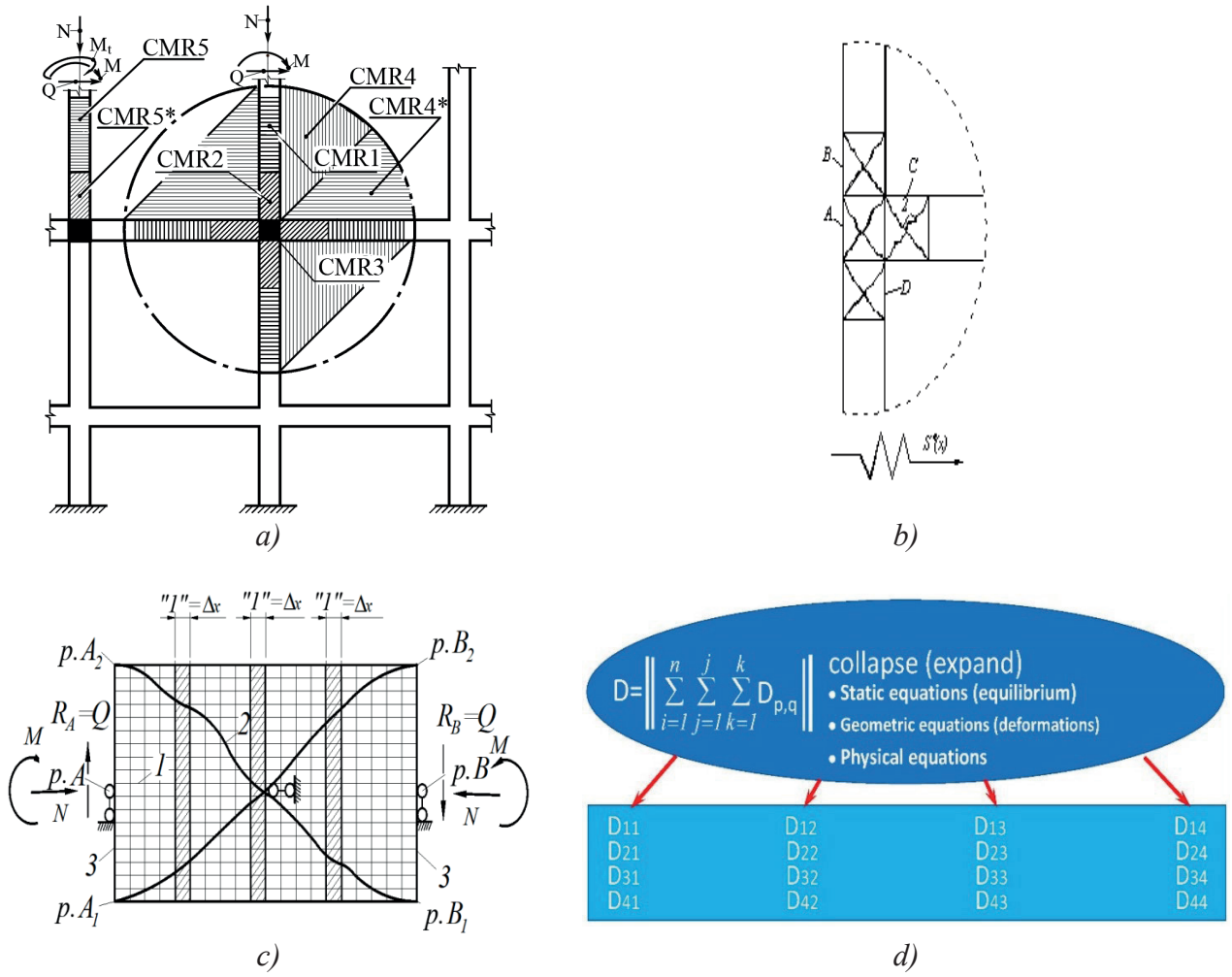

Figure 5. Calculation models of resistance (CMR) of buildings and structures (a) and stiffness for intersecting cracks of reinforced concrete for a single strip of composite rods (b, c), stiffness matrix scheme (d)

In the spatial design model of resistance in bending with torsion, two-console elements in models A and B [6], as well as a universal dual console element in reinforced concrete [8, 15] are used.

Applying the method of initial parameters [7 9] for a compressed-curved axis in the form of a spline is a general solution of the differential equation for displacements, - external (a_{crc} and $\delta(\Delta_{crc})$, φ_i, Θ_i) and internal (jump-crack: Δ_1, Δ_2, φ_1, φ_2, $\Delta\varphi_{crc}$). The construction mechanics classification for active or passive parameters is used for equal [7]

$$\frac{\mathrm{d}^4 y}{dx^4} = 0. \qquad (27)$$

The general solution of equation (27) is expressed as a linear combination of the four functions:

$$y(x) = C_1 \cdot K_1(\beta x) + C_2 \cdot K_2(\beta x) + \\ + C_3 \cdot K_3(\beta x) + C_4 \cdot K_4(\beta x), \qquad (28)$$

where $\beta = \sqrt[4]{a}$; $\mathrm{K}_1(x) = \frac{1}{2}(\mathrm{ch}\, x + \cos x)$, $\mathrm{K}_2(x) = \frac{1}{2}(\mathrm{sh}\, x + \sin x)$, $\mathrm{K}_3(x) = \frac{1}{2}(\mathrm{ch}\, x - \cos x)$, $\mathrm{K}_4(x) = \frac{1}{2}(\mathrm{sh}\, x - \sin x)$ or we can use the Krylov-Vlasov functions: $\Phi_1(\mathrm{x}) = \mathrm{chx} \cdot \mathrm{cosx}$; $\Phi_2(\mathrm{x}) = \mathrm{shx} \cdot \mathrm{sinx}$; $\Phi_3(\mathrm{x}) = \mathrm{shx} \cdot \mathrm{cosx}$; $\Phi_4(\mathrm{x}) = \mathrm{chx} \cdot \mathrm{sinx}$.

The method of initial parameters for displacements allows us to obtain expressions for deformations and rotation angles under the action of bending moment and shear force on the deformable base:

$$y_i = \varphi_1 L \frac{i-1}{n} - \frac{L^2}{n^2}\left(\frac{(3i-4)\chi_1 + \chi_i}{6} \sum_{j=2}^{i-1} (i-j)\chi_j\right) + \delta_i. \qquad (29)$$

$$\varphi_i = \varphi_1 - M_1 \frac{L}{n} \times \left(\frac{\chi_1 + \chi_i}{2} + \sum_{j=2}^{i-1} \chi_j\right) + \Theta_i. \qquad (30)$$

$$\chi(z) = \chi_i + \left(\frac{\chi_{i+1} - \chi_i}{2}(z - b_i)\right) \qquad (31)$$

$$R_i = k_i y_i a. \qquad (32)$$

Here R_i, k_i and y_i are the force, stiffness and displacement, respectively, in the i-th bond of the base.

The bending moment is described by the following relationship:

$$M_i = M_1 + Q_1 L \frac{i-1}{n} + \left(\frac{L}{n}\right)^2 \sum_{j=1}^{i-1} (i-j) y_j k_j - q_l \bar{M}_{0i}, \qquad (33)$$

where M_1 is the moment in the console at i = 1; M_i - the moment in the i-th cross-section from a given unit vector of external forces.

We obtain a system of n equations ($2 \le k \le n + 1$) in the form of the method of initial parameters:

$$\Phi_k \left[y_1, \varphi_1, M_1, Q_1, M_{n+1}, y_i, q_l(q_d)\right] = 0.$$

Here $q_l(q_d)$ is the modulus of the force (deformation) impact vector,

Experimental studies are important (about a hundred experiments of the author) for full-scale structures, buildings and constructions. New technologies are used: glue "Cyacrine" (Cyanocrylate), sensors to measure 80% of the destructive load, punches for the inside of the working reinforcement, installation for displacements.

III. HYBRID calculations in the software package by means two elements in the form of "flat and spatial console", - RESULT III for internal and external displacements $S_i, \Delta_1, \Delta_2, \Delta_3, \delta\Delta_{crc}, \varphi_1, \varphi_2, \varphi_{crc}$.

IV. GENERAL PRINCIPLE - from the works of A.F. Loleit to the "opening - closing" of cracks in the working reinforcement and stiffness of reinforced concrete structures, buildings and structures taking into account the development of mechanics of reinforced concrete, - RESULT IV. There is also an economical expenditure of

material (steel) in beams (ξ=0.3-0.4; μ=1%-2%); in slabs (ξ=0.10-0.15; μ=0.3%-0.6%) and in columns (ξ=0.4; μ= up to 3.0%)). The calculation must take into account that if a_m > a_R , then:

- 1) increase the cross-section of the elements and the shape of the cross-section;
- 2) increase the class of concrete to B100;
- 3) introduce reinforcement of compressed concrete;
- 4) use a diagram of materials (steel);
- 5) consider the criteria of fragmentation of the compressed concrete (ultimate deformations $\varepsilon_{b,u}$, as well as in the violation of the force equilibrium and $\varepsilon_{3,ult,t}$, ε_1 - top and , - wall), the development of cracks $d\zeta_{bu} / dh_{crc} = 0$ from fracture mechanics, and cracks from the anchoring ($l_x / l_{an} = m_{a33}$) for tensile working reinforcement.

6) consider the main (basic and adjacent) cracks for levels, stiffness and "opening-closing" of the crack using design models of resistance of reinforced concrete (rod 1-3, flat-tensioned 4 and 4*, spatial 5 and 5*.

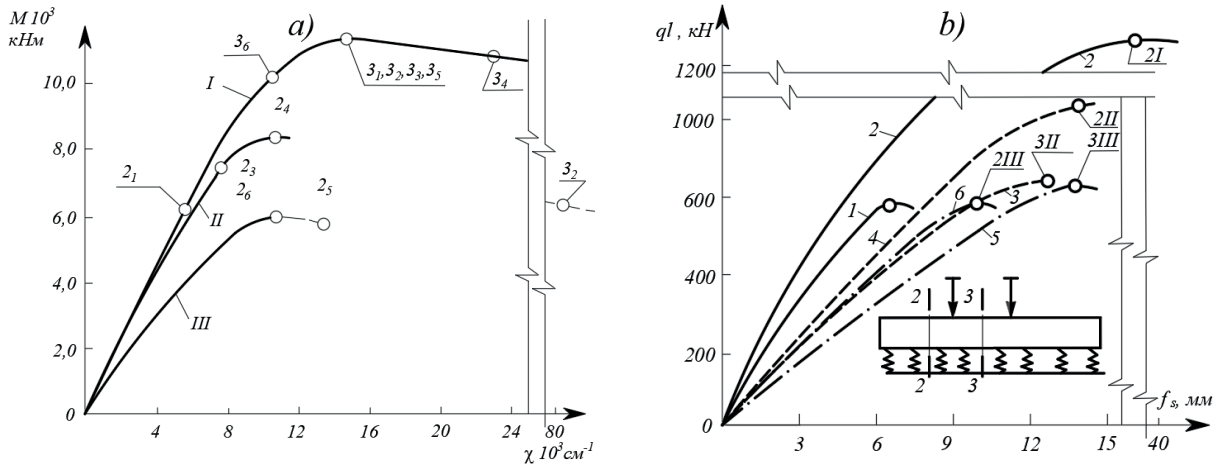

Figure 6. Diagrams of M-χ (a) and ql-fs dependences (b): I, II, III - M-χ dependences for clean zone, transverse bending zone in the absence of inclined cracks and transverse bending zone in the presence of inclined cracks, respectively; 1, 2, 3, 4, 5, 6 - ql-fs dependences at s = 3 and dependences I in section 2; at s = 2 and dependence I in section 2; at s = 3 and dependence II in section 2; at s = 2 and dependence II in section 2; at s = 3 and dependence III in section 2; at s = 2 and dependence III in section 2, respectively

CONCLUSION

1. The development of the mechanics of reinforced concrete and the basic prerequisites, - result I:

● The environment of reinforced concrete includes the force flows of solid deformable body mechanics of concrete blocks for isotropic medium between cracks, - " first object - flows (blocks). "Second object, - trunk cracks" using the functional, two-concrete element and the effect of reinforced concrete. The physical essence is the discontinuity of concrete and solid reinforcement, where there are reactions between the reinforcement and concrete in the form of relative deformations of the reinforcement $\varepsilon_S = \varepsilon_{S,j} - \varepsilon_э$, adhesion ΔT, the stress $\sigma_{bt,c}$ of compressed concrete, the pliability of structural mechanics and other parameters. The resistance of the tensile concrete in the transversal-isotropic medium is

transferred to the working reinforcement through the general parameter (ψ_s or $\psi_{s,sw}$ by Prof. V.I. Murashev. The average longitudinal force N_{sm} and transverse force $Q_{s,m}$ are related using a special third object, the "total average force of the working reinforcement". Models of the second level of structural mechanics have been developed for a rebar with two pinched ends at cantilever rotations as well as crack opening $a_{crc,s}$, shear of crack banks Δ_{crc}. The longitudinal axis of the rebar is sinusoidal when moved with a maximum amplitude of $0.5a_{crc}$ and $0.5\Delta_{crc}$. The unknown X_2, X_3, $X_{3,t}$, X_4, X_5 quantities are determined from the calculation of statically indeterminate systems by the method of forces from coupled systems of equations. The main vector of reinforcement displacement in the crack is characterized by two values ugi, υgi in orthogonal directions and the angle β. Distances between cracks l_{crc}, resistance parameter of tensile concrete ψ_s and crack opening width a_{crc} use the effect of discontinuity of concrete from Thomas-author hypothesis, where the relative mutual displacements of reinforcement and concrete are found from the equilibrium of the cut reinforcement bar and the homogeneous differential equation with boundary conditions. The perimeter, diameter and area of the reinforcement, B_i, $1/K$, ΔT, $\sigma_{bt,c}$, modulus of elasticity and shear of concrete, reinforcement factor, boundary linear deformations of concrete, several levels, etc. are used for this purpose.

● Classification of main cracks has the form:

- regular cracks of Prof. N.I. Karpenko (anisotropic medium of reinforced concrete, without the effect of reinforced concrete and the width of "opening - closing");
- the author's main cracks on the basis of the effect of reinforced concrete discontinuity;
- base cracks for geometric (undercutting), force and inter-medium concentration, as well as external and internal displacements.

Consider the first - third types of cracks for the bending moment, torsional moment and shear force area. The fourth type is obtained in the development of cracks from the fracture mechanics condition $d\zeta_{bu}/dh_{crc}=0$, the fifth type - cracks from compressed concrete, the sixth type - cracks from anchoring ($l_x/l_{an}=m_{az3}$).

The calculated models of resistance of reinforced concrete for their analysis of rod, plane and spatial cracks have been developed. The Lagrange function $F_i=f\left(q_{sw},x_B,\sigma_s,x,\sigma_c,\sigma_{s,I},\sigma_{c,I},C_2,\lambda_1,\lambda_2,\lambda_3,\lambda_4,\lambda_5,\lambda_6,\lambda_7\right)$ is used for the maximum crack opening width in the closed equations of reinforced concrete mechanics.

The author proposed new hypotheses and theorems:

The first of these is about the distribution of linear deformations and for the deplanation of the cross-section of a reinforced concrete element.

The second hypothesis about the distribution of total relative deformations of concrete and reinforcement shear ($\gamma_{sum,b}$ and $\gamma_{sum,s}$) for the deplanation of the cross-section of a reinforced concrete element.

● Analytical functionals are developed when solving the system of the proposed complex functions from the families of the mesh method in the compressed and stretched zones using small squares. The first functional $f_{5,*}(y,z)$ is a function of two functions along the y-axis and z-axis. The second functional $f_{***}(x,z,y)$ is a function of three functions on the x-axis, z-axis, and y-axis. The bending and torsional moments are determined using the third undefined functional $f_{\varepsilon,\text{int,vol}}(x,y,z)$ as well as the fourth undefined functional $f_{5,**,\iint}(z,y)$.

● Stiffness hypothesis allowed for reinforced concrete by an order of magnitude reduced differential equations of composite structures by A.R. Rzhanitsyn. The stiffness matrix of

rectangular cross-sections uses static equations (equilibria), geometric equations (deformations) and physical equations.

2. The method of computational model of resistance for structural mechanics, - result II:

● Analysis of the first model (rod with main normal cracks) and the second model (main inclined cracks between the links of reinforcement and concrete blocks) was performed. The third model of resistance has diagonal and other cracks for pliable units as opposed to rigid units from structural mechanics. The fourth model is a wall with mainline oblique cracks, and model 4a is a slab with mainline "envelope" cracks. Model 5 (5a under the action of torsion with bending and transverse force) uses volumetric spatial blocks.

● The general solution of the Krylov-Vlasov function equation is a system of a linear combination of four functions, for the general solution of a differential equation.

● The basic solutions in the boundary parameters for compressed-bent and stretched-bent prismatic rods (frames with rigid units) are defined by means of active and passive parameters.

● Applying the initial parameter method for a compressed-curved axis is a general solution of the differential equation for external (a_{crc}, φ_i, Θ_i) and internal (Δ_1, Δ_2, φ_1, φ_2, $\Delta\varphi_{crc}$) displacements.

● The method of initial parameters for displacements allows us to obtain, in the i-th cross section, the deformations and angles of rotation under the action of bending moment and transverse force on the deformable base from a given unit module of the force vector ql (deformation qd) impact of external forces in the form of an equation $\Phi_k\left[y_1, \varphi_1, M_1, Q_1, M_{n+1}, y_i, q_l(q_d)\right] = 0$.

● Experimental research for structures, buildings and constructions is important. New technologies are used: glue "Cyacrine" (cyanocrylate), sensors, punches for the inside of the working armature, installation for determining displacements.

3. Hybrid calculations in the software package and by means of the finite element method, - result III for internal and external displacements $S_i, \Delta_1, \Delta_2, \Delta_3, \delta\Delta_{crc}, \varphi_1, \varphi_2, \varphi_{crc}$

4. The general principle from A.F. Loleit's works to "opening - closing" of cracks in working reinforcement and stiffness of reinforced concrete structures taking into account development of mechanics of reinforced concrete (MRMS method), - result IV. The economical consumption of material (steel) in beams (ξ=0,3-0,4; μ=1%-2%), in slabs (ξ=0,10-0,15; μ=0,3%-0,6%), in columns (ξ=0,4; μ= up to 3,0%) is obtained. If $a_m > a_R$, then increase the cross-section of elements $b\,x\,h_0$ and the form of cross-section; increase the class of concrete from B to B100; introduce reinforcement of compressed concrete A_s'.

REFERENCE

1. **Golyshev A.B., Kolchunov. V.I.** Soprotivlenie zhelezobetona [Resistance of Reinforced Concrete]. –K.: Osnova. 2009. – 432 c.
2. **Golyshev A.B., Kolchunov V.I., Klyueva N.V., Lisitsin B.M., Mashkov I.L., Yakovenko I.A.** Reference Manual on Structural Mechanics. In two volumes – Moscow: Publishing house ASV, 2014. – 432 c.
3. **Bondarenko V. M., Kolchunov. V. I.** Raschetnye modeli silovogo soprotivleniya zhelezobetona [Calculation Models of Strength Resistance of Reinforced Concrete]. – M.: ASV, 2004. – 472 c.
4. **Bashirov, H. Z., Kolchunov, V. I., Fedorov, V. S., Yakovenko, I. A.** ZHelezobetonnye sostavnye konstrukcii zdanij i sooruzhenij [Reinforced concrete composite structures of buildings and

structures], – Moscow: ASV Publishing House, 2017. – 248 c.
5. **Murashev V. I.** Treshchinoustojchivost', zhestkost' i prochnost' zhelezobetona [Crack resistance, rigidity and strength of reinforced concrete]. – M: Mashstroyizdat, 1950. – 268 p.
6. **Kolchunov V. I., Demyanov A. I., Yakovenko I. A.** Razrabotka universal'nogo korotkogo dvuhkonsol'nogo elementa k soprotivleniyu zhelezobetonnyh konstrukcij pri kruchenii s izgibom [Development of a universal short dualconsol element to the resistance of reinforced concrete structures in torsion with bending] // Proceedings of higher educational institutions. Technology of textile industry, 2017, № 4(370). c. 246-251.
7. **Kornoukhov N. V.** Izbrannye trudy po stroitel'noj mekhanike [Selected Works on Structural Mechanics] // Acad. Institute of Mechanics. – Kyiv: Acad. of Sciences of USSR, 1963. – 324 c.
8. **Iakovenko I. A., Kolchunov V. I.** The development of fracture mechanics hypotheses applicable to the calculation of reinforced concrete structures for the second group of limit states // Journal of Applied Engineering Science, 2017, Vol. 15. No 3. p. 371-380.
9. **Kolchunov V., Dem'yanov A., Naumov N.** Analysis of the "nagel effect" in reinforced concrete structures under torsion with bending // IOP Conference Series: Materials Science and Engineering. 2020. p. 953.
10. **Kolchunov V., Naumov N. , Smirnov B.** Physical essence of the "nagel effect" for main reinforcement in an inclined crack of reinforced concrete structures // IOP Conference Series: Materials Science and Engineering, Vladimir, 2020. p. 012055.
11. **Kolchunov V. I., Karpenko S. N.** Rigidity of reinforced concrete structures under complex resistance // Russian Journal of Building Construction and Architecture, 2022, No 1(53). p. 7-20. – DOI 10.36622/VSTU.2022.53.1.001.
12. **Kolchunov V. I., Dem'yanov A. I.** The modeling method of discrete cracks and rigidity in reinforced concrete // Magazine of Civil Engineering, 2019, No 4(88). p. 60-69.
13. **Kolchunov, V. I., Dem'yanov A. I.** The modeling method of discrete cracks in reinforced concrete under the torsion with bending // Magazine of Civil Engineering, 2018, No 5(81). p. 160-173.
14. **Kolchunov V., Demyanov A., Grichishnikov S., Shankov V.** The New Linear Deformations Hypothesis of Reinforced Concrete Under Combined Torsion and Bending // Lecture Notes in Civil Engineering, 2022, Vol. 182. – p. 109-121.
15. **Kolchunov Vl., Dem'yanov A., Protchenko M.** The new hypothesis angular deformation and filling of diagrams in bending with torsion in reinforced concrete structures // Journal of Applied Engineering Science, 2022, Vol.19(4). p. 972-979.
16. **Kolchunov V.I., Demyanov A.I., Protchenko M.V.** Moments in reinforced concrete structures under bending with torsion // Building and Reconstruction, 2021, № 3(95). p. 27-46.
17. **Kolchunov V.I.** Deplanation hypotheses for angulardeformations in reinforced concrete structures under combined torsion and bending // Building and Reconstruction, 2022, №2. p. 3-12.
18. **Kolchunov V.I., Al-Hashimi O., Protchenko M.V.** Stiffness of reinforced concrete structures under bending with transverse and longitudinal forces // Building and Reconstruction, 2021, №6. p. 5-19.
19. **Karpenko N.I.** Obshchie modeli mekhaniki zhelezobetona [General models of reinforced concrete mechanics]. Moscow: Strojizdat, 1996. 410 p. (in Russian).

СПИСОК ЛИТЕРАТУРЫ

1. **Голышев А. Б., Колчунов. Вл.И.** Сопротивление железобетона. – К.: Основа. 2009. – 432 с.
2. **Верюжский Ю. В., Голышев А. Б., Колчунов Вл. И., Клюева Н. В., Лисицин Б. М., Машков И. Л., Яковенко И. А.** Справочное пособие по строительной механике. В двух томах.: Учебное пособие. – М.: Изд-во АСВ, 2014. – 432 с.
3. **Бондаренко В. М., Колчунов. Вл. И.** Расчетные модели силового сопротивления железобетона. – М.: АСВ, 2004. – 472 с.
4. **Баширов, Х. З., Колчунов, Вл. И., Федоров, В. С., Яковенко, И. А.** Железобетонные составные конструкции зданий и сооружений, – М.: Издательство АСВ, 2017. – 248 с.
5. **Мурашев В. И.** Трещиноустойчивость, жесткость и прочность железобетона. – М: Машстройиздат, 1950. – 268 с.
6. **Колчунов Вл. И., Демьянов, А. И., Яковенко И. А.** Разработка универсального короткого двухконсольного элемента к сопротивлению железобетонных конструкций при кручении с изгибом // Известия высших учебных заведений. Технология текстильной промышленности, 2017, № 4(370). с. 246-251.
7. **Корноухов Н. В.** Избранные труды по строительной механике // Акад. наук УССР. Ин-т механики. – Киев : Изд-во Акад. наук УССР, 1963. – 324 с.
8. **Iakovenko I. A., Kolchunov V. I.** The development of fracture mechanics hypotheses applicable to the calculation of reinforced concrete structures for the second group of limit states // Journal of Applied Engineering Science, 2017, Vol. 15. No 3. p. 371-380.
9. **Kolchunov V., Dem'yanov A., Naumov N.** Analysis of the "nagel effect" in reinforced concrete structures under torsion with bending // IOP Conference Series: Materials Science and Engineering. 2020. p. 953.
10. **Kolchunov V., Naumov N. , Smirnov B.** Physical essence of the "nagel effect" for main reinforcement in an inclined crack of reinforced concrete structures // IOP Conference Series: Materials Science and Engineering, Vladimir, 2020. p. 012055.
11. **Kolchunov V. I., Karpenko S. N.** Rigidity of reinforced concrete structures under complex resistance // Russian Journal of Building Construction and Architecture, 2022, No 1(53). p. 7-20. – DOI 10.36622/VSTU.2022.53.1.001.
12. **Kolchunov V. I., Dem'yanov A. I.** The modeling method of discrete cracks and rigidity in reinforced concrete // Magazine of Civil Engineering, 2019, No 4(88). p. 60-69.
13. **Kolchunov, V. I., Dem'yanov A. I.** The modeling method of discrete cracks in reinforced concrete under the torsion with bending // Magazine of Civil Engineering, 2018, No 5(81). p. 160-173.
14. **Kolchunov V., Demyanov A., Grichishnikov S., Shankov V.** The New Linear Deformations Hypothesis of Reinforced Concrete Under Combined Torsion and Bending // Lecture Notes in Civil Engineering, 2022, Vol. 182. – p. 109-121.
15. **Kolchunov Vl., Dem'yanov A., Protchenko M.** The new hypothesis angular deformation and filling of diagrams in bending with torsion in reinforced concrete structures // Journal of Applied Engineering Science, 2022, Vol.19(4). p. 972-979.
16. **Колчунов Вл. И., Демьянов А. И., Протченко М. В.** Моменты в железобетонных конструкциях при изгибе с кручением // Строительство и реконструкция, 2021, № 3(95). с. 27-46.
17. **Колчунов Вл. И.** Гипотезы о депланации сечения от деформаций

сдвига в железобетонных конструкциях, испытывающих кручение с изгибом // Строительство и реконструкция, 2022, № 2(100). с. 3-12.
18. **Колчунов Вл. И. Аль-Хашими О. И., Протченко М. В.** Жесткость железобетонных конструкций при изгибе поперечной и продольной силами // Строительство и реконструкция, 2021, № 6(98). с. 5-19.
19. **Карпенко Н.И.** Общие модели механики железобетона. – М.: Стройиздат, 1996. 410 с.

Kolchunov Vladimir Ivanovich, Southwestern state university, Kursk, Russia, corresponding member of the Russian Academy of Architecture and Construction Sciences, doctor of Technical Sciences, Professor of the Department of Unique Buildings and Structures. E-mail: vlik52@mail.ru

Колчунов Владимир Иванович, ФГБОУ ВО «Юго-Западный государственный университет», г. Курск, Россия, член-корреспондент РААСН, доктор технических наук, профессор кафедры уникальных зданий и сооружений. E-mail: vlik52@mail.ru

DOI:10.22337/2587-9618-2023-19-1-85-96

CONTROL SYSTEM OF PARAMETERS OF ELECTRICAL CURING OF CAST-IN-SITU REINFORCED CONCRETE STRUCTURES

Stepan V.Leontev, Andrey A. Taleyko

Perm National Research Polytechnic University, Perm, RUSSIA

Abstract: At the moment in house-building industry cases of increase of efficiency of cast-in-situ concrete structures electrical curing are insufficiently studied. Development and implementation of control systems of parameters of electrical curing can be solve of current concerns. Development sequence of this control system included: collection of initial data; development of virtual model of considered structures, using ELCUT; analysis of rate of simulation parameters, depend on ambient conditions; fixation of values of simulation parameters; development of mathematical model of correlation between transformer voltage and temperatures of concrete, ambient air and time of electrical curing; development and description of circuit diagram of proposed control system.

The control system, developed by the authors, can be the basis for creation of automated complex of electrical curing of cast-in-situ reinforced concrete structures. Application of this system will significantly allow to decrease electricity consumption and labor costs, connected with electrical curing of structures

Keywords: parameters of electrical curing, control of parameters of curing, winter concreting, cast-in-situ reinforced concrete structures, simulation of curing conditions

СИСТЕМА УПРАВЛЕНИЯ ПАРАМЕТРАМИ ЭЛЕКТРОПРОГРЕВА ЖЕЛЕЗОБЕТОННЫХ МОНОЛИТНЫХ КОНСТРУКЦИЙ

С.В. Леонтьев, А.А. Талейко

Пермский национальный исследовательский политехнический университет, г. Пермь, РОССИЯ

Аннотация: В статье представлены результаты разработки системы управления параметрами электропрогрева монолитных железобетонных конструкций. Последовательность разработки включала в себя следующие этапы: сбор исходных данных; построение виртуальной модели конструкций в программе Elcut; анализ динамики изменения параметров модели в зависимости от внешних факторов; фиксация числовых значений параметров модели; построение математической модели зависимости выходного напряжения трансформатора от температур бетона, окружающей среды и времени электропрогрева; разработка и описание принципиальной схемы функционирования предложенной системы управления.

Разработанная авторами система управления может послужить основой при создании автоматизированного комплекса электропрогрева монолитных железобетонных конструкций, применение которого позволит значительно снизить энергопотребление и трудозатраты связанные с их электропрогревом.

Ключевые слова: электропрогрев бетона, управление параметрами тепловой обработки, зимнее бетонирование, монолитные железобетонные конструкции, моделирование условий прогрева

INTRODUCTION

At present the main technology, used in the construction of buildings and structures, is cast-in-situ construction technology. One of the undeniable advantages of this technology is the high pace of construction-and-assembling operations [1-3].
But, also the rate of concrete strength gain is the main constraint for construction activities rate, that's why it is impossible to do without the intensification of this process at the construction site, especially in conditions of cold weather. This concern is too relevant for Russia, so cold weather conditions are in the most area of country from 3 to 10 month. It is established by normative documents, that cold weather concreting can be applied at temperature up to -40 °C. However, in practice the rational field of application of cold weather concreting is not lower temperature than (-15) – (-20) °C [4-7].
In case of erection of cast-in-situ structures of residential and public buildings (slabs, walls, column etc., which have module of cooling surface about 4-10) electrical curing with heating wires is one of the most widespread methods of temperature and humidity intensification of concrete strength gain. Insulated heating wires with constant step are installed to mesh reinforcement, and stay subsequently inside the structure body [8, 9].
However, advantages of this method of electrical curing have some concerns, solve of which is so important for striving for quality improvement and increase of rate of construction [10, 11]. One of these is problem of concrete strength gain in conditions of cold weather and also rational use of energy consumed [12-15].
Regardless of apparent simplicity and efficiency of concrete electrical curing, there are concerns in practice such as: significant unjustified overspending of electricity consumed for heating of reinforce concrete structures in winter, associated with constant parameters of electrical curing, that is independent of ambient conditions; lack of a unified methodology of calculation of transformer voltage according to variable curing factors. Existing solutions of electrical heating are standard and do not take into account a lot of factors such as: structure type, temperature of ambient air, curing time [16, 17].
The solve of this concern is development of efficient control system of parameters of electrical curing of reinforce cast-in-situ structure, which would consider the factors mentioned above. Control system were developed by the example of standard elements of cast-in-situ framework such as walls, columns and slabs. These structures are thin-walled, therefore, special attention is required for thermal regime in the cold weather condition [18-20].

MATERIALS AND METHODS

Mathematical model of correlation of transformer voltage on concrete temperature, ambient air temperature and curing time were based on considered control system. Sequence of development of control system of electrical curing parameters for thin-walled reinforced concrete structures can be presented as follows:
1. Collection of initial data for developing of model (geometric size of structure and formwork, thermal parameters of materials, parameters of ambient conditions, parameters of concrete curing);
2. Development of virtual model of considered structures with variable parameters of ambient conditions and concrete electrical curing, using ELCUT software package, which is used for temperature field creating for different physical processes. ELCUT is universal domestic software product of two-dimensional simulation. The field development is realized with finite element method [21, 22];
A lot of studies of Russian researchers [21-23] were devoted to the use of ELCUT software package for simulation of concrete curing. Tuo Shi et al. [11-14] investigated the correlation of computer model of concrete curing, created with ANSYS software package, and experimental data of temperature distribution. The authors found that simulation data was in good agreement with the measured results;

3. Analysis of concrete rate of temperature across cross-section of explored cast-in-situ structures (temperature of ambient conditions, parameters of transformer work, scheme of heating wires layout, time). Determination of structures temperature at the different periods of time. Collecting temperature data for developing of mathematical model;
4. The mathematical model development of considered process for each type of structures, using temperature data of computer simulation. Mathematical model was created with use of mathematical methods of complex experiment planning and statistical data manipulation, using STATISTICA software package.
5. Transition from temperature of reinforced concrete structure in current time to transformer voltage. Development and description of control system of reinforced concrete structure curing parameters.
6. Development and description of principal scheme of the proposed control system.

In the first phase data was collected for each type of structures, used during development of virtual model of concrete curing. Initial data for considered structures are presented in table 1.

"ПНСВ" wires with diameter of current carrying 1,2 mm were chosen as the heat source.

In the second phase virtual models of heating of structures of wall, column and slab were created with ELCUT, based on initial data.

ELCUT is an integrated interactive system of programs, which allows to solve different field problems, including temperature fields

Table 1. Initial data

No.	Parameter	Unit	Value
1	Size of concrete structures	mm	
1.1	Column section		600x300
1.2	Wall thickness		200
1.3	Slab thickness		200
2	Concrete grade	-	B25
3	Cement content (use for evaluation of concrete liberation of heat during hydration)	kg/m^3	350
4	Range of ambient temperature	˚C	-30…-10
5	Wind speed	m/s	5
6	Temperature of as-placed concrete	˚C	10
7	Temperature of isothermal concrete curing	˚C	50
8	Curing period	days	3
9	Thermal conductivity of materials	W/(m·°C)	
9.1	Concrete		1.51
9.2	"Dornit" (insulating cover)		0.029
9.3	Form plywood		0.12
9.4	Steel reinforcement		58
10	Specific heat capacity of materials	J/(kg·K)	
10.1	Concrete		840
10.2	"Dornit" (insulating cover)		1340
10.3	Form plywood		2300
10.4	Steel reinforcement		482
11	Density of materials	kg/m^3	
11.1	Concrete		2400
11.2	"Dornit" (insulating cover)		29
11.3	Form plywood		600
11.4	Steel reinforcement		7850

(stationary and nonstationary heat transfer problem).

ELCUT allows to solve two-dimensional boundary-value problem of mathematical physics, which described by partial differential equation of elliptic type regarding the scalar or single-component vector function (potential), and also analysis problem of strain-stress state of solid (plane-stresses, plane-deformations, axially symmetric loads), including problems of building of temperature fields. [22].

At this study stationary and nonstationary heat transfer problems in linear statement have been solved. Following heat conduction equation is used during solving of heat transfer problem in described statement (1):

$$\frac{\partial}{\partial x}\left(\lambda_x \frac{\partial T}{\partial x}\right) + \frac{\partial}{\partial y}\left(\lambda_y \frac{\partial T}{\partial y}\right) = -q - c\rho \frac{\partial T}{\partial t} \qquad (1)$$

where, T – temperature; t – time; λ_{xy} – components of the thermal conductivity tensor; q – specific power of heat liberation, in the linear formulation of problem - constant; c – specific heat capacity, in the linear formulation of problem – constant; ρ – density.

In stationary problem the last addend at the right is zero. All parameters of equation in the linear statement are constant within each of blocks of model.

The solution of problem can be divided into following phases.

- Building of geometrical models of structures (Fig. 1), using CAD program, uploading to DXF and import to ELCUT.

Assigning of materials blocks markers and setting of their properties according to initial data.

- Assigning of edges markers to set boundary conditions of convections (in the interface of structure and ambient air) and to set initial temperature of concrete, surface of reinforcement and hard concrete of existed structures (only for stationary problem).
- Assigning of apexes markers to set specific electrical loading on the wire.

During development of model liberation of heat of concrete was considered with setting of bulk thermal-power density as follows (2) [8]:

$$Q = Z \cdot qmax \cdot (1 - (0.04 * (t/3600) + 1) * \exp(-0.04 * (t/3600)))/((t+1)/3600)/36 \qquad (2)$$

where, Z – cement content, kg/m^3; q_{max} – maximal heat liberation of cement, kJ/kg (for PC400 the value is 335 kJ/kg); t – ELCUT variable of time.

After setting of all markers and their properties stationary heat transfer problem was solved to set initial conditions of heating. Next, on the base of previous result the main nonstationary

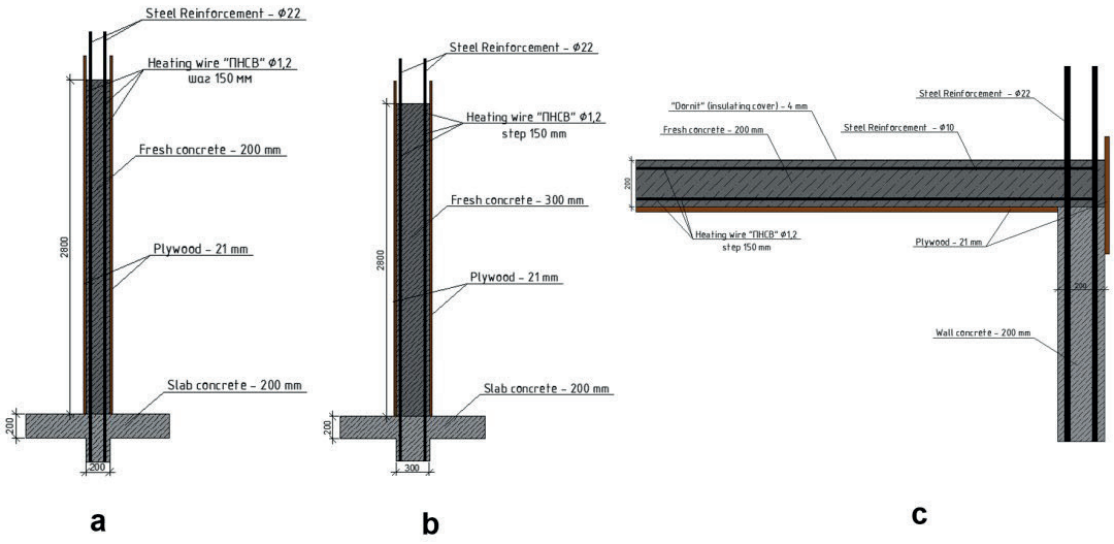

Figure 1. Geometric models of explored structures: a) wall; b) column; c) slab

heat transfer problem was solved for the 48th hours period of time with integration step of 2 hours.

Described problems were solved for different temperatures of ambient air (-10, -20, -30 °C) and different specific electrical loadings on the wire (30, 40, 50 W/m) [23].

Additionally, nonstationary heat transfer problem was solved, which simulate structure cooling under the condition, that supply voltage was stopped after 48 hours of heating. Initial conditions for this problem were result of previous nonstationary problem at the time of 48 hours.

RESULTS AND DISCUSSIONS

Based on obtained solution the rate of change of average temperature of concrete was analyzed, and also temperature values were determined in different times. The results for wall are presented in tables 2.

Then, based on the temperature data mathematical model of concrete heating was built, using STATISTICA. In result, following equations were found, relating temperature of structure with specific electrical loading on the wire and temperature of ambient air, of form (3):

Table 2. Average temperature of wall

No.	Specific electrical loading, W/m	Temperature of ambient air, °C	Temperature of concrete structure, °C												
			Heating, h									Cooling, h			
			0	6	12	18	24	30	36	42	48	54	60	66	72
1	30	-10	10.0	14.9	18.8	21.9	24.4	26.3	27.9	29.0	29.9	16.5	7.6	2.4	-0.6
2	40	-10	10.0	19.1	25.8	30.7	34.4	37.0	39.0	40.6	41.6	24.0	12.5	5.6	1.5
3	50	-10	10.0	23.1	32.6	39.2	44.0	47.4	49.9	51.8	53.0	31.4	17.3	8.7	3.5
4	30	-20	10.0	11.8	13.5	15.0	16.5	17.8	18.9	19.9	20.5	6.6	-2.3	-7.5	-10.5
5	40	-20	10.0	15.9	20.2	23.6	26.2	28.3	29.9	31.1	31.9	14.2	2.7	-4.3	-8.4
6	50	-20	10.0	19.9	27.0	32.1	35.9	38.7	40.7	42.3	43.3	21.6	7.4	-1.2	-6.4
7	30	-30	10.0	8.6	7.9	7.9	8.4	9.0	9.8	10.4	10.9	-3.1	-12.1	-17.4	-20.5
8	40	-30	10.0	12.7	14.6	16.4	18.0	19.5	20.6	21.6	22.3	4.5	-7.2	-14.2	-18.3
9	50	-30	10.0	16.7	21.4	24.9	27.7	29.9	31.5	32.8	33.7	11.9	-2.3	-11.1	-16.3

Table 3. Coefficients of the equations for model of wall heating

t, час	a_0	a_1	a_{11}	a_2	a_{22}	a_{12}	a_{122}	a_{112}	a_{1122}
0-6	4.68	0.46	-0.007	0.3	-0.0002	0.0002	0	0	0
6-12	-3.8	1.04	-0.004	0	0	0	0.0007	-0.0004	-0.000008
12-18	-2.3	1.12	-0.003	0.34	-0.006	0.016	0	0	-0.000003
18-24	-6	1.435	-0.006	0.007	-0.013	0.04	0.0006	-0.004	-0.000008
24-30	-3	1.36	-0.04	0.0355	-0.01	0.02	0.0005	-0.003	-0.000005
30-36	4.1	1.07	0.0005	1.17	0.01	-0.016	-0.0006	0.0002	0.000008
36-42	-6.7	1.7	-0.06	-0.05	-0.02	0.05	0.0009	-0.005	-0.00001
42-48	-3.2	1.54	-0.004	0.24	-0.01	0.03	0.0007	-0.0004	-0.000007
48-54	5.3	0.7	0.0005	1.24	0.005	-0.01	-0.0002	0.0001	0.000002
54-60	7.4	0.25	0.03	1.7	0.02	-0.04	-0.001	0.0005	0.00001
60-66	2.1	0.35	-0.0005	0.99	0	0	0	0	0
66-72	1.4	0.29	-0.001	0.84	-0.005	0.007	0.0002	-0.00007	-0.000002

$$T_{str} = a_0 + a_1 p + a_{11} p^2 + a_2 T_{ext} + a_{22} T_{ext}^2 + a_{12} p T_{ext} + a_{122} p T_{ext}^2 + a_{112} p^2 T_{ext} + a_{1122} p^2 T_{ext}^2 \quad (3)$$

where, Tstr – temperature of structure, °C; p – specific electrical loading, W/m; Text – temperature of ambient air, °C.

Coefficients of these equations for structure of wall are presented in table 3.

To use obtained equations for determination of necessary electrical loading, it is needed to find temperature of ambient air and specified temperature of structure at a given time. For this purpose, determination of thermal regime for each type of structure is further found.

Based on data from МДС 12-48.2009 rates of heating and cooling of cast-in-situ reinforced concrete structures depend on module of surface (Ms). For columns and walls with module of surface 4-6 m^{-1} the rate of heating must not exceed 6 °C per hour and rate of cooling – 3 °C per hour. But for slabs with module of surface 7-10 m-1 the rate of heating must not exceed 10 °C per hour and rate of cooling – 5 °C per hour.

According to МДС 12-48.2009 temperature of isothermal concrete curing was 50 °C. Thermal regime was chosen based on data of rate of heating and cooling and also that concrete would gain 70% of project strength at the end of isothermal curing [24, 25]. According to this, thermal regime can be presented as follows (Fig. 2).

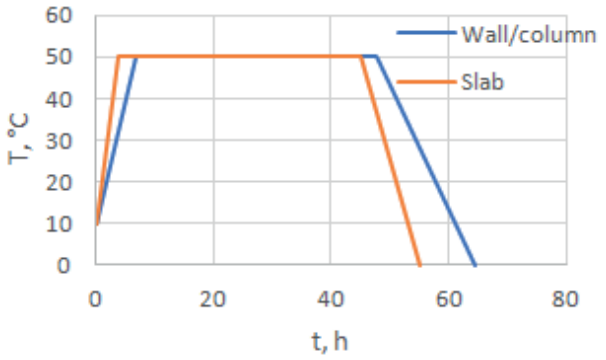

Figure 2. Operation of structure heating

According to the above, to find specified electrical loading on the wire, it needs to solve the equation with specified temperature of structure (according to the graph) and with current temperature of ambient air. Herewith, it is necessary to select equation, which meet the current period of time.

For example, it needs to find electrical loading on the wire at the time of 10 h with temperature of ambient air -15 °C for heating of wall. Specified temperature of structure at this time will be 50 °C. Then, solving the equation (4):

$$T_{str} = -3.8 + 1.04p - 0.004p^2 + 0.0007pT_{ext}^2 - 0.0004p^2 T_{ext} - 0.000008p^2 T_{ext}^2 \quad (4)$$

for p, we find p=45 W/m.

In the Fig. 3 the data of specified electrical loading on the wire are shown for temperature of ambient air -15 °C for heating of wall.

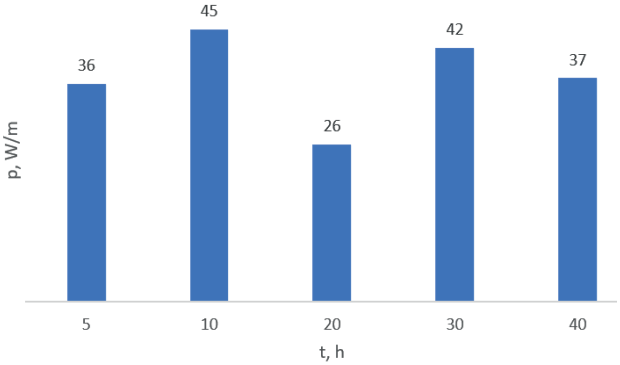

Figure 3. Specific electrical loading during heating of wall

Mathematical model of described control system of electrical heating of reinforced concrete structures based on algorithm noted above. Control of thermal regime of structure is realized with voltage variation on the wire, that's why it needs to transit from electrical loading on the wire to transformer voltage.

In the Fig. 4 the circuit diagram of control system of electrical curing of cast-in-situ reinforced concrete structures is shown.

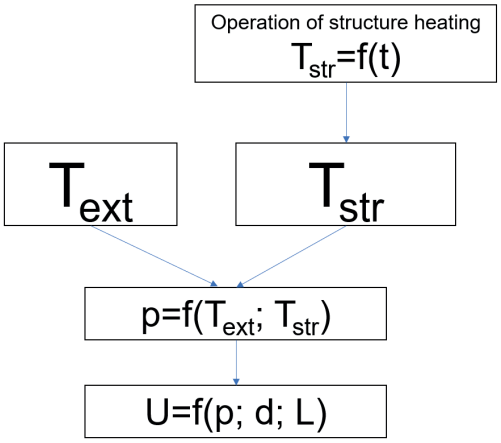

Figure 4. Circuit diagram of governing system of voltage on the wire (T_{ext} – temperature of ambient air, °C; T_{str} – permissible temperature of structure, °C; t - time, h; p – specific electrical loading, W/m; U – voltage on the wire, V; d – diameter of current carrying wire, mm; L – length of wire, m)

Transition from calculated specific electrical loading on the wire to voltage is realized with well-known equation [10] (5):

$$P = \frac{U^2 S}{L\rho_t} \quad (5)$$

from which it follows (6):

$$U = \frac{2L}{d}\sqrt{\frac{p\rho_t}{\pi}} \quad (6)$$

where P – effective power, realized by the wire, W; U – voltage, V; S – cross sectional area of current carrying wire, m^2; L – length of wire, m; ρ_t – electrical resistivity of the current carrying wire at a given temperature, Ω·м; d – diameter of current carrying wire, mm; p – specific electrical loading, W/m.

For calculations it was accepted: L= 30 m, $\rho_t = 10 \cdot 10^{-8}$ Ω·m (for steel), d = 1.2 mm

Thus, the transformer voltage at the different time for heating of wall is presented in Fig. 5.

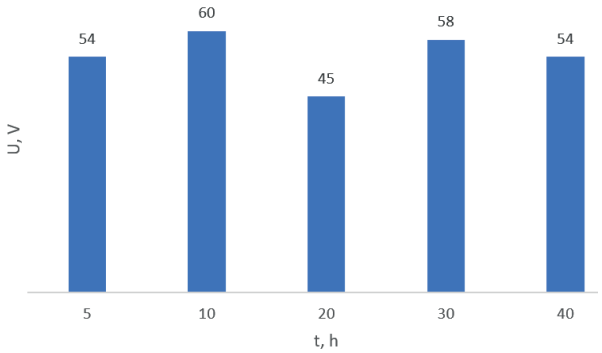

Figure 5. Voltage on the wire from different curing period

This voltage values will be set on the transformer, after the system, based on temperature detector data, has performed operation described above and transfer data to control assembly. The temperature detectors are installed inside structure and on the surface of structure.

The control system of cast-in-situ reinforced concrete structure heating with heating wire can be presented as “black box” model (Fig. 6). Input parameter is transformer voltage (U) and output parameters are divided into uncontrollable (temperature of ambient air (T_{ext}), wind speed (v_{wind})) and controllable (temperature of concrete of structure (T_{str}), time of isothermal curing (t_{isoth})).

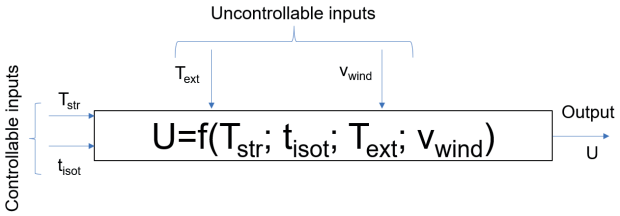

Figure 6. Circuit diagram of governing system of concrete heating

Content and type of cement, having accelerator admixtures and whether or not thermal insulation of structure during concrete curing, diameter, resistance and length of wire can also be attributed to input parameters. However, described parameters with their constant values can be considered into the numerical model, because construction method for each of building company is constant. That's why the controlled input can be considered only that was described above.

It is also necessary to point out natural limitations of parameters values (table 4).

Thus, finding equations together with thermal regime of concrete curing can be used for building of automated control system of heating of reinforced concrete structure with heating wire. And in doing so, thermal regime can be presented as equation, witch correlate specified concrete temperature with curing time, considering noted limits.

CONCLUSION

Thus, it needs to note that at this time there are some unsolved problems of electrical curing of cast-in-situ reinforced concrete structures and it needs optimization and improvement. Development and implementation of control system of parameters of electrical curing can be solves of this concern.

The control system developed by the authors can be basis for creation of automated system of electrical heating of cast-in-situ reinforced concrete structures. Maintenance of optimal thermal regime of concrete curing will be task of developed system depending on different internal factors such as temperature of ambient air, rate of surface cooling, time of concrete curing, type and parameters of heating wire etc.

Application of such automated control systems of electrical curing will facilitate reduction of labor cost and provide optimal curing conditions for concrete strength gain. It also will facilitate to save electricity through reduction of wire voltage depending on time of concrete curing and temperature of ambient air.

ACKNOWLEDGMENTS

The authors would like to thank LLC "TOR" for provision of software and technical support.

REFERENCES

1. **Ryazanova G.N., Popova, D.M.** Analiz sushchestvuyushchih metodov vozvedeniya konstrukcij iz monolitnogo betona i zhelezobetona v zimnih usloviyah **[**Analysis of existing methods of construction of monolithic concrete and reinforced concrete structures in winter conditions] // Urban construction and architecture, 2018, 30(1), pp. 16-23. (in Russian). DOI: 10.17673/Vestnik.2018.01.3
2. **Bofang Z.** Construction of mass concrete in winter. In: thermal stresses and temperature control of mass concrete // Butterworth-Heinemann: Tshingua University Press, 2014, pp. 431-438.

Table 4. Limits of some concrete curing parameters

Parameters	Limits	Limit definitions
p	≤40 W/m	Temperature of wire exceeds 100°C during high loading, that leads to structural damage of concrete and decrease of its strength. In addition, insulation of wire can be damaged, and short circuit on reinforcement will able to occur
U	{55, 65, 75, 85, 95}, V	Discrete voltage level (depends on transformer type)
T_{str}	≤ (70-80) °C	It due to structurization and strength gain processes of concrete

3. **Fedorova G., Mestnikov V., Matveeva O., Nikolayev, E.** Features of High-Strength Concrete Creation for Concreting of Monolithic Constructions in the Far North Conditions // Procedia Engineering, 2013, No. 57, pp. 264-269.
4. **Gnam P.A., Kiviharju R.K.** Tekhnologii zimnego betonirovaniya v Rossii **[**Technologies of winter concreting in Russia] // Construction of Unique Buildings and Structures, 2016, 9 (48), pp. 7-25, (in Russian). DOI: 10.18720/CUBS.48.1.3.
5. **Nassif, A.Y., Petrou, M.F.:** Influence of cold weather during casting and curing on the stiffness and strength of concrete // Construction and Building Materials, 2013, Vol. 44. pp. 161–167. https://doi.org/10.1016/j.conbuildmat.2013.03.016
6. **Zhang G., Yu H.Y., Li H.M., Yingzi Y.** Experimental study of deformation of early age concrete suffering from frost damage // Construction and Building Materials, 2019, Vol. 215. pp. 410–421. https://doi.org/10.1016/j.conbuildmat.2019.04.187
7. **Ortiz J., Aguado A., Agulló L., García T.** Influence of environmental temperatures on the concrete compressive strength: simulation of hot and cold weather conditions // Cement and Concrete Research, 2005, № 35(10), pp.1970-1979. DOI:10.1016/j.cemconres.2005.01.004.
8. **Zach J., Sedlmajer M., Hroudova J. Nevaril A.** Technology of concrete with low generation of hydration heat // Procedia Engineering, 2013, No. 65, pp. 296-301. https://doi.org/10.1016/j.proeng.2013.09.046
9. **Dudin M.O., Barabanshchikov Y.G.** Specifika montazha elektricheskogo provoda v tekhnologii progreva betona **[**Specifity of wiring into technology of heating concrete] // Construction of Unique Buildings and Structures, 2015, № 6(33), pp. 47-61, (in Russian). DOI: 10.18720/CUBS.33.4
10. **Shishkin V.V.** Covershenstvovanie metoda zimnego betonirovaniya s primeneniem nagrevatel'nyh provodov [Improvement of the method of winter concreting with the use of heating wires] // Industrial and Civil Engineering, 2019, №6, pp. 51-58, (in Russian). DOI: 10.33622/0869-7019.2019.06.51-58.
11. **Tuo S., Chunlin D., Jiaqi Z., Pingxiang D., Zhihong F.** Temperature field of concrete cured in winter conditions using thermal control measures // Advances in Materials Science and Engineering, 2022, vol. 2022, pp. 1-12. DOI: https://doi.org/10.1155/2022/7255601.
12. **Barna L.A., Seman P.M., Korhonen C.J.** Energy-efficient approach to cold-weather concreting // Journal of Materials in Civil Engineering, 2011, Vol. 23, №11, pp. 1544–1551.
13. **Varuna M., Raikar D., Sunil S.** Studies on temperature differential for different types of overlay over cement concrete pavement // Proceedings of 5th International Conference of Transportation Research Group of India. Bhopal, 2019, pp 365-376. DOI: 10.1007/978-981-16-9921-4_27.
14. **Kumar S.S., Ravindraraj B.J.** Study of temperature differential in different concrete slabs of varying slab thickness in different regions // International journal of Civil Engineering and Technology, 2018, № 9(4), pp. 1008 – 1013.
15. **Le Q.X., Dao V.TN., Torero J.L., Maluk C., Bisby L.** Effects of temperature and temperature gradient on concrete performance at elevated temperatures // Advances in Structural Engineering, 2018, № 21(8), pp. 1223–1233. https://doi.org/10.1177/1369433217746347.
16. **Marzouk H., Hussein A.** Effect of curing age on high-strength concrete at low temperatures // Journal of Materials in Civil Engineering, 1995, Vol. 7, No. 3, pp. 161–167. DOI:10.1061/(ASCE)0899-1561(1995)7:3(161).

17. **Zhurov N.N., Komissarov S.V.** Sistema temperaturno-prochnostnogo kontrolya betona v rannem vozraste [System temperature-strength concrete control at early age] // Vestnik MGSU, 2010, № 4(5), pp. 296-301. (in Russian).
18. **Korobkov S. Gnyrya A., Kuznetsov S.** Computer Simulation of Electric Heating of Concrete Column // Lecture Notes in Networks and Systems, 2022, Vol. 403, pp. 349-357. DOI: 10.1007/978-3-030-96383-5_39.
19. **Dhananjay M., Abhilash K.** Study of thermal gradient in concrete slabs through experimental approach // Global Journal of Reserches in Engineering: E Civil and Structural Engineering, 2014, №14(5), pp. 1–17.
20. **Khoa H.N., Cong V.C.** Analyzing temperature field and thermal stress in massive concrete by finite element method // Journal of Construction Science and Technology. Buildings, 2012, №14(12), pp. 17–27.
21. **Zinevich L.V.** Primenenie chislennogo modelirovaniya pri proektirovanii tekhnologii obogreva i vyderzhivaniya betona monolitnyh konstrukcij [Application of numerical modeling in the design of heating technology and concrete curing of monolithic structures] // Magazine of Civil Engineering, 2011, No. 2. pp. 24-28. (in Russian).
22. **Dudin M.O., Vatin N.I., Barabanshchikov Yu.G.** Modelirovanie nabora prochnosti betona v programme elcut pri progreve monolitnyh konstrukcij provodom [Modeling a set of concrete strength in the program ELCUT at warming of monolithic structures by wire] // Magazine of Civil Engineering, 2015, №2, pp. 33-45. (in Russian). DOI 10.5862/MCE.54.4.
23. **Gnyrya A., Korobkov S., Gaag I.** Numerical solution of the thermal problem for electric heating of concrete structures in winter // Proceedings of Ural Environmental Science Forum “Sustainable Development of Industrial Region” (UESF-2021). Chelyabinsk, 2021, pp. 1-10. DOI 10.1051/e3sconf/202125809048.
24. **Zhang G., Yang Y.Z., Li H.M.** Calcium-silicate-hydrate seeds as an accelerator for saving energy in cold weather concreting // Construction and building materials, 2020, Vol. 264, pp.1-15. DOI:10.1016/j.conbuildmat.2020.120191.
25. **Alzaza A., Ohenoja K., Langas I., Arntsen B., Poikelispaa M., Illikainen M.** Low-temperature (−10°C) curing of Portland cement paste – Synergetic effects of chloride-free antifreeze admixture, C–S–H seeds, and room-temperature pre-curing // Cement and Concrete Composites, 2022, Vol 125, pp. 1-13.

СПИСОК ЛИТЕРАТУРЫ

1. **Рязанова Г.Н., Попова Д.М.** Анализ существующих методов возведения конструкций из монолитного бетона и железобетона в зимних условиях // Градостроительство и архитектура, 2018, №1(30), с. 16-23. DOI: 10.17673/Vestnik.2018.01.3
2. **Bofang Z.** Construction of mass concrete in winter. In: thermal stresses and temperature control of mass concrete // Butterworth-Heinemann: Tshingua University Press, 2014, pp. 431-438.
3. **Fedorova G., Mestnikov V., Matveeva O., Nikolayev, E.** Features of High-Strength Concrete Creation for Concreting of Monolithic Constructions in the Far North Conditions // Procedia Engineering, 2013, No. 57, pp. 264-269.
4. **Гнам П.А., Кивихарью Р.К.** Технологии зимнего бетонирования в России // Строительство уникальных зданий и сооружений, 2016, №9(48), с. 7-25. DOI: 10.18720/CUBS.48.1.3.
5. **Nassif, A.Y., Petrou, M.F.** Influence of cold weather during casting and curing on the stiffness and strength of concrete //

Construction and Building Materials, 2013, Vol. 44. pp. 161–167. https://doi.org/10.1016/j.conbuildmat.2013.03.016

6. **Zhang G., Yu H.Y., Li H.M., Yingzi Y.** Experimental study of deformation of early age concrete suffering from frost damage // Construction and Building Materials, 2019, Vol. 215. pp. 410–421. https://doi.org/10.1016/j.conbuildmat.2019.04.187
7. **Ortiz J., Aguado A., Agulló L., García T.** Influence of environmental temperatures on the concrete compressive strength: simulation of hot and cold weather conditions // Cement and Concrete Research, 2005, № 35(10), pp.1970-1979. DOI:10.1016/j.cemconres.2005.01.004.
8. **Zach J., Sedlmajer M., Hroudova J. Nevaril A.** Technology of concrete with low generation of hydration heat // Procedia Engineering, 2013, No. 65, pp. 296-301. https://doi.org/10.1016/j.proeng.2013.09.046
9. **Дудин М.О., Барабанщиков Ю.Г.** Специфика монтажа электрического провода в технологии прогрева бетона // Строительство уникальных зданий и сооружений, 2015, № 6(33), pp. 47-61. DOI: 10.18720/CUBS.33.4
10. **Шишкин В.В.** Совершенствование метода зимнего бетонирования с применением нагревательных проводов // Промышленное и гражданское строительство, 2019, №6, pp. 51-58. DOI: 10.33622/0869-7019.2019.06.51-58.
11. **Tuo S., Chunlin D., Jiaqi Z., Pingxiang D., Zhihong F.** Temperature field of concrete cured in winter conditions using thermal control measures // Advances in Materials Science and Engineering, 2022, vol. 2022, pp. 1-12. DOI: https://doi.org/10.1155/2022/7255601.
12. **Barna L.A., Seman P.M., Korhonen C.J.** Energy-efficient approach to cold-weather concreting // Journal of Materials in Civil Engineering, 2011, Vol. 23, №11, pp. 1544–1551.
13. **Varuna M., Raikar D., Sunil S.** Studies on temperature differential for different types of overlay over cement concrete pavement // Proceedings of 5th International Conference of Transportation Research Group of India. Bhopal, 2019, pp 365-376. DOI: 10.1007/978-981-16-9921-4_27.
14. **Kumar S.S., Ravindraraj B.J.** Study of temperature differential in different concrete slabs of varying slab thickness in different regions // International journal of Civil Engineering and Technology, 2018, № 9(4). pp. 1008 – 1013.
15. **Le Q.X., Dao V.TN., Torero J.L., Maluk C., Bisby L.** Effects of temperature and temperature gradient on concrete performance at elevated temperatures // Advances in Structural Engineering, 2018, № 21(8), pp. 1223–1233. https://doi.org/10.1177/1369433217746347
16. **Marzouk H., Hussein A.** Effect of curing age on high-strength concrete at low temperatures // Journal of Materials in Civil Engineering, 1995, Vol. 7, No. 3, pp. 161–167. DOI:10.1061/(ASCE)0899-1561(1995)7:3(161).
17. **Журов Н.Н., Комиссаров С.В.** Система температурно-прочностного контроля бетона в раннем возрасте // Вестник МГСУ, 2010, № 4-5, с. 296-300.
18. **Korobkov S. Gnyrya A., Kuznetsov S.** Computer Simulation of Electric Heating of Concrete Column // Lecture Notes in Networks and Systems, 2022, Vol. 403, pp. 349-357. DOI: 10.1007/978-3-030-96383-5_39.
19. **Dhananjay M., Abhilash K.** Study of thermal gradient in concrete slabs through experimental approach // Global Journal of Reserches in Engineering: E Civil and Structural Engineering, 2014, №14(5), pp. 1–17.
20. **Khoa H.N., Cong V.C.** Analyzing temperature field and thermal stress in massive concrete by finite element method

// Journal of Construction Science and Technology. Buildings, 2012, №14(12), pp. 17–27.
21. **Зиневич Л.В.** Применение численного моделирования при проектировании технологии обогрева и выдерживания бетона монолитных конструкций // Инженерно-строительный журнал, 2011, № 2(20), с. 24-28.
22. **Дудин М.О., Ватин Н.И., Барабанщиков Ю.Г.** Моделирование набора прочности бетона в программе ELCUT при прогреве монолитных конструкций проводом // Инженерно-строительный журнал, 2015, № 2(54), с. 33-45. DOI: 10.5862/MCE.54.4
23. **Gnyrya A., Korobkov S., Gaag I.** Numerical solution of the thermal problem for electric heating of concrete structures in winter // Proceedings of Ural Environmental Science Forum "Sustainable Development of Industrial Region" (UESF-2021). Chelyabinsk, 2021, pp. 1-10. DOI 10.1051/e3sconf/202125809048.
24. **Zhang G., Yang Y.Z., Li H.M.** Calcium-silicate-hydrate seeds as an accelerator for saving energy in cold weather concreting // Construction and building materials, 2020, Vol. 264, pp.1-15. DOI:10.1016/j.conbuildmat.2020.120191.
25. **Alzaza A., Ohenoja K., Langas I., Arntsen B., Poikelispaa M., Illikainen M.** Low-temperature (−10°C) curing of Portland cement paste – Synergetic effects of chloride-free antifreeze admixture, C–S–H seeds, and room-temperature pre-curing // Cement and Concrete Composites, 2022, Vol 125, pp. 1-13.

Stepan V. Leontev - Ph.D. in Engineering Science, senior lecturer of department of Construction Engineering and Materials Science, Perm National Research Polytechnic University; Russia, 614010, Perm, ul. Kuibyshev, 109; phone +73422198352, e-mail: n1306cl@yandex.ru.

Andrey A. Taleyko - student of department of Construction Engineering and Materials Science, Perm National Research Polytechnic University; Russia, 614010, Perm, ul. Kuibyshev, 109; phone +73422198352, e-mail: taleyko.99@mail.ru

Леонтьев Степан Васильевич - к.т.н., доцент кафедры «Строительный инжиниринг и материаловедение» Пермского национального исследовательского политехнического университета; Россия, 614010, г. Пермь, ул. Куйбышева, 109; тел. +73422198352, e-mail: n1306cl@yandex.ru

Талейко Андрей Алексеевич - студент (магистрант) кафедры «Строительный инжиниринг и материаловедение» Пермского национального исследовательского политехнического университета; Россия 614010, г. Пермь, ул. Куйбышева, 109; тел. +73422198352, e-mail: taleyko.99@mail.ru

International Journal for Computational Civil and Structural Engineering, 19(1) 97–111 (2023)

DOI:10.22337/2587-9618-2023-19-1-97-111

MATHEMATICAL MODELING OF UNDRAINED BEHAVIOR OF SOILS

Rashid A. Mangushev, Ivan B. Bashmakov, Daria A. Paskacheva, Alina V. Kvashuk

St. Petersburg State University of Architecture and Civil Engineering, St. Petersburg, RUSSIA

Abstract: Mathematical modeling of the undrained behavior of soils is carried out on the basis of theoretical paths of effective stresses under undrained deviatory loading in a triaxial compression chamber. The recommendations of normative sources and scientific papers on the application of undrained calculations in practice are analyzed. The basic laws of soil mechanics are considered in calculations taking into account the formation of excess pore pressures in the base. Theoretical calculations obtained by A. Skempton for the law of effective stresses of C. Terzaghi are applied for mathematical modeling of paths. Based on the results of mathematical modeling of an ideal elastic-plastic body it is shown that an accurate description of the paths of effective soil stresses using the elastic theory does not correspond to real soil tests. The influence of the law of volumetric plastic deformation on the paths of effective stresses and on the undrained shear strength is analyzed. The formula for determining the undrained strength parameter for the Modified Cam Clay model is presented. Attention is drawn to the fact that in addition to volumetric plastic deformation which affects the undrained calculation it is necessary to take into account the shear component of plastic deformation which is decisive for the calculations of excavations. Simulation of laboratory tests of soils in the Soil Test for the Mohr-Coulomb, Modified Cam Clay and Hardening Soil Models was carried out. A comparison of the obtained results with the data of laboratory tests is presented. The influence of the choice of soil model on the value of resistance to undrained shear is shown. Recommendations are given for choosing a soil model for numerical simulation based on the results of laboratory triaxial consolidated undrained tests.

Keywords: undrained behavior, Skempton's parameters, effective stress path, soft soil, soil model, cup loading surface

МАТЕМАТИЧЕСКОЕ МОДЕЛИРОВАНИЕ НЕДРЕНИРОВАННОГО ПОВЕДЕНИЯ ГРУНТОВ

Р.А. Мангушев, И.Б. Башмаков, Д.А. Паскачева, А.В. Квашук

Санкт-Петербургский Государственный Архитектурно-Строительный Университет, г. Санкт-Петербург, РОССИЯ

Аннотация: Выполнено математическое моделирование недренированного поведения грунтов на основе теоретических траекторий эффективных напряжений при недренированном девиаторном загружении в камере трехосного сжатия. Проанализированы рекомендации нормативных источников и научных трудов о применении недренированных расчетов в практике. Рассмотрены основные законы механики грунтов при расчетах с учетом образования избыточных поровых давлений в основании. Для математического моделирования траекторий применены теоретические выкладки, полученные А. Скемптоном для закона эффективных напряжений К. Терцаги. На основе результатов математического моделирования идеально-упруго-пластического тела показано, что точное описание траектории эффективных напряжений грунта с помощью теории упругости не соответствует реальным испытаниям грунтов. Проанализировано влияние закона объемного пластического деформирования на траекторию эффективных напряжений и на сопротивление недренированному сдвигу. Представлена формула определения параметра недренированной прочности для модели Modified Cam Clay. Обращается внимание на то, что кроме объемного пластического деформирования, влияющего на недренированный расчет, необходимо учитывать сдвиговую составляющую пластических деформаций, являющуюся определяющей для расчетов котлованов. Выполнено моделирование лабораторных испытаний грунтов в ПК «Soil Test» для моделей Мора-Кулона, Modified Cam Clay и Hardening Soil Model. Представлено сравнение полученных

результатов с данными лабораторных испытаний. Показано влияние выбора модели грунта на значение сопротивления недренированному сдвигу. Даны рекомендации для выбора модели грунта для численного моделирования на основании результатов лабораторных трехосных консолидированно-недренированных испытаний.

Ключевые слова: недренированное поведение, параметры Скемптона, траектория эффективных напряжений, слабый грунт, модель грунта, шатровая поверхность нагружения

1. INTRODUCTION

The construction of deep pits in cities has become widespread over the past twenty years. To avoid significant margins occurring in assessment of the bearing capacity of the foundation, it is necessary to increase the accuracy of the geotechnical forecast.

First of all, this problem arises at the construction of underground structures on a large thickness of soft soils, which are typical for such a metropolis as St. Petersburg [1].

The geological section of St. Petersburg is represented by a large stratum of Quaternary deposits in the form of water-saturated, ribbon, silty-clay soils and water-saturated sands overlying a variable stratum of moraine deposits underlain by Upper Kotlin and Lower Cambrian clays as Fig. 1 presents [2].

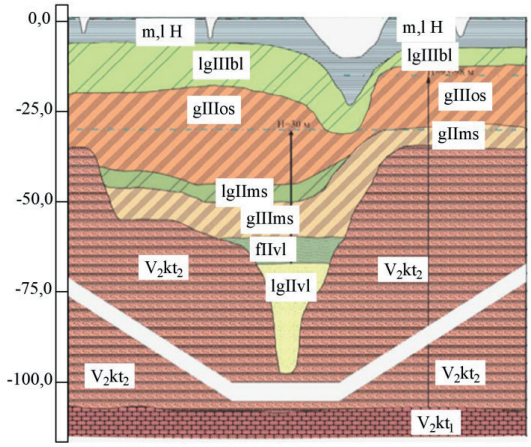

Figure 1. Geological section of the central part of St. Petersburg [2]

Therefore, "soft" glaciolacustrine deposits (lg III) widespread in this area requires a special approach to analysis of foundation pits in St. Petersburg. These deposits have low strength and deformation characteristics. At the same time, they are the main part of the active zone of the base of foundations and structures under construction. This circumstance entails the need to use expensive solutions in the construction of pits and their enclosures.

Figure 2 presents a typical design scheme for the construction of a pit in St. Petersburg. Since lacustrine-glacial deposits, as a rule, are in the active zone of the foundation, the choice of a soil model significantly affects to determination of the forces and displacements of the enclosing structures and additional deformations of the foundation foundations of the surrounding buildings.

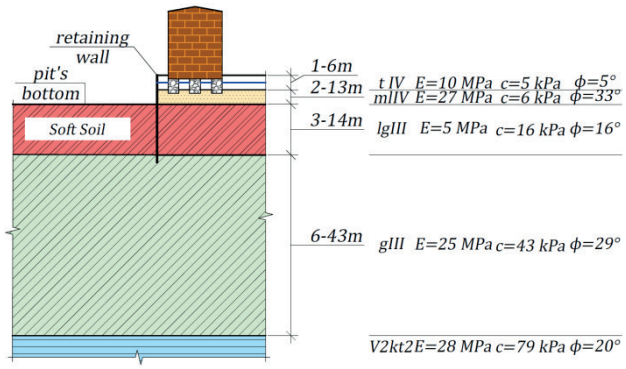

Figure 2. Design scheme for the construction of a pit in St. Petersburg

In modern practice of designing excavation enclosures, the Hardening Soil model is usually used for simulation. However, the mathematical description of this model contains many empirical relations, the validity of which for soft glaciolacustrine deposits of St. Petersburg is practically not confirmed.

On another hand, Models of the Cam-Clay family (Cam-Clay, Modified Cam Clay, Soft Soil, etc.) are widely used in world practice. However, the laws embedded in these models were originally obtained for volumetric

compression, which can greatly distort the results for shear deformation. Thus, it is important to pay attention to the limits of its applicability [3], when using any model.

As initial data for models, mechanical characteristics obtained from test schemes that do not correspond to the actual work of the soil or the requirements of the model are often assigned. So, the Hardening Soil model requires triaxial compression tests, and if it is necessary to take into account excess pore pressures. Besides, test results in an undrained mode are required.

Since the process of excavation and installation of underground structures is limited in time, and soft clay soils have rather low filtration coefficients, it makes sense to consider the work of clay soils, considering the possibility of excessive pore pressure.

This study was aimed to develop a computational method for determining the parameters of undrained behavior of soil that is required for numerical simulation of pits in conditions of soft water-saturated soils.

Studies of the undrained behavior of clay soils began with consideration of the behavior of the soil as an ideal elastic-plastic body [4]. This description of the behavior of the soil was based only on the theory of elasticity and did not correlate with the test results. Then models were introduced to take into account the nonlinear deformation and "hardening" of soils, which directly affects the behavior of the pore fluid [5], [6], [7], [8]. Mathematical relations embedded in these models were built on the basis of a series of soil tests.

Proving of the applicability of models for specific soil conditions requires an assessment of the influence of the input soil parameters on the mathematical relations embedded in different models. In the case under consideration, the applicability criterion can be the path of effective stresses under undrained loading or the intersection of the path with the line of the limiting state (the value of undrained shear strength).

In foreign practice, analysis of pits in clay soils is allowed to be carried out both in drained and undrained settings [9]. At the analysis of excavations in clay soils, the decision to calculate excess pore pressures can be made based on the time factor, which depends on the degree of soil consolidation and construction time [10]:

$$T = \frac{c_v}{D^2} t = \frac{k_f \cdot E_{oed}}{\gamma_w \cdot D^2} t \qquad (1)$$

where c_v is the factor of primary (filtration) consolidation;

D is the filtration path,

t is the construction time;

k_f is the filtration coefficient;

E_{oed} is the odometric modulus of deformation;

γ_w is the specific gravity of water.

For the values of the time factor $T \geq 0.4$, it is recommended not consider excess pore pressures and to carry out a drained analysis in effective stresses. If $T \leq 0.01$, then it is recommended to take into account excess pore pressures and conduct an undrained analysis. For intermediate values of the time factor, it is necessary to analyze both the drained and undrained behavior of the soil mass during the excavation.

A number of literary sources recommend do not dwell on only the analysis of the undrained behavior, since in this case results can be obtained that do not consider the filtration and consolidation processes occurring in the base over time [11], [12].

Based on the previously stated in this paper, the following tasks were considered during the analysis of mathematical modeling of the undrained behavior of soils:

- study of the path of effective stresses under undrained deviatoric loading for an ideal-elastic-plastic body;
- determination of the influence of the shape of the loading surface on the path of effective stresses;
- study of the path of effective stresses for the most common non-linear soil models;
- determination of criteria for applicability of models in geotechnical calculations.

2. METHODS

2.1. Basic laws of soil mechanics in undrained analysis

In classical soil mechanics, it is customary to consider soil as a multiphase dispersed system.

In the simplest setting, the soil consists of solid particles and a liquid that fills the pores. Such a formulation can be represented as the Terzaghi law of effective stresses:

$$\sigma = \sigma' + p_{active} \quad (2)$$

where σ is the total stresses in the soil mass;

σ' is the stress in the soil skeleton (effective);

p_{active} is the stress in the pore fluid (pore pressure).

In turn, the pore pressure can be separated into hydrostatic one, which is determined by the position of the groundwater level, and excess one, which is formed under loading in the absence of drainage:

$$p_{active} = p_{steady} + p_{excess} \quad (3)$$

where p_{steady} is the steady pore pressure;

p_{excess} – избыточное поровое давление.

Since the main strength criterion for soils as materials subject to plastic flow is shear strength, it is important to consider the effect of excess pore pressure on the stress distribution in the soil. In accordance with (2), the effect of pore pressure on soil shear strength can be shown using Coulomb's law for the failure site, denoted by *n*:

$$\tau_n = \sigma'_n \cdot \tan(\phi') + c' = (\sigma_n - p_{active}) \tan(\phi') + c' \quad (4)$$

where τ_n is the tangent stress acting on fracture area;

σ_n is the normal stress acting on the fracture area.

It is convenient to analyze the soil behavior for different stress-strain states using principal stresses.

In principal stresses, Coulomb's law can be represented as follows:

$$\sin(\phi') = \frac{\sigma'_1 - \sigma'_3}{\sigma'_1 + \sigma'_3 + 2 \cdot c' \cdot \cot(\phi')} \quad (5)$$

where σ_1' is the largest principal effective stress;

σ_3' is the least principal effective stress.

An analysis is carried out in total stresses, when it is not possible to assess the effect of pore pressure on soil stresses.

When analyzed in total stresses, the law of shear resistance looks like this:

$$\tau_{\max} = C_u \quad (6)$$

where $\tau_{\max} = \frac{\sigma_1 - \sigma_3}{2}$ is the maximum tangent stress;

C_u is the undrained shear resistance (strength).

Figure 3 presents graphs illustrating the law of soil shear resistance. Stress components σ_n', τ_n, presented in formula (5), correspond to the combination of effective principal stresses at the failure site (on the Mohr-Coulomb line). For total stresses, based on formula (6), only the value C_u is known, which is independent of the level of stresses in the soil.

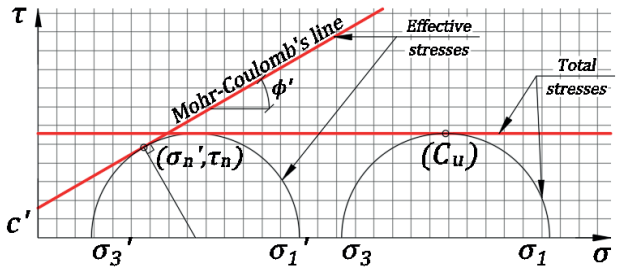

Figure 3. Coulomb's law for soils in effective and total stresses in $\sigma - \tau$ axes

In foreign practice, analysis in "p-q" coordinates is used to assess the stress state of the soil. This allows visually evaluate the "path" of effective and total stresses in the soil sample.

The mean effective stress p` and the stress deviator q are expressed in terms of the principal stresses in triaxial compression as follows:

$$p' = p - p_{active} = \frac{\sigma_1' + 2\sigma_3'}{3} \quad (7)$$

$$q = q' = \sigma_1' - \sigma_3' \quad (8)$$

Representation the Mohr-Coulomb law (5) in "p-q" coordinates:

$$q = \frac{6\sin(\phi')}{3-\sin(\phi')} p' + \frac{6 \cdot c' \cos(\phi')}{3-\sin(\phi')} = Mp' + a \quad (9)$$

where $M = \frac{6\sin(\phi')}{3-\sin(\phi')}$ and $a = \frac{6c'\cos(\phi')}{3-\sin(\phi')}$ are the parameters of the critical state line, depending on the angle of internal friction and specific cohesion.

Figure 4 presents a graph illustrating the Mohr-Coulomb law in "p-q" coordinates.

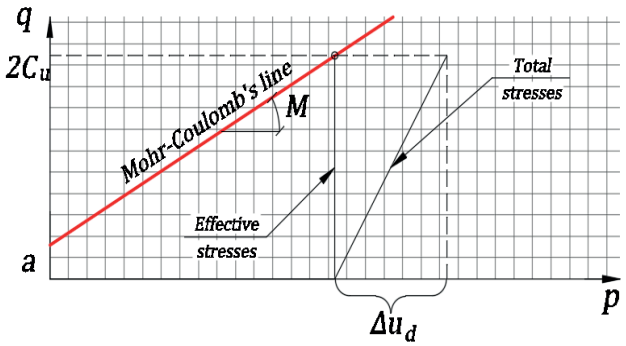

Figure 4. Coulomb's law for soils in effective and total stresses in coordinates $p-q$

2.2. Theoretical path of undrained deviatoric loading for an ideal elastic-plastic body

The path of undrained loading for an ideal elastic-plastic body was described by Skempton [4].

To take into account the distribution of the load between the pore fluid and the soil skeleton in the space of principal stresses during tests of triaxial isotropic compression, Terzaghi's law can be represented as:

$$\Delta p_{active} = B(\Delta\sigma_3 + A(\Delta\sigma_1 - \Delta\sigma_3)) \quad (10)$$

where A and B are the Skempton coefficients, the derivation of which is presented below.

Figure 5 provides the scheme of an idealized triaxial test.

The change in pore pressure at the stage of all-round compression is denoted as Δu_a, at the stage of deviatoric loading as Δu_d.

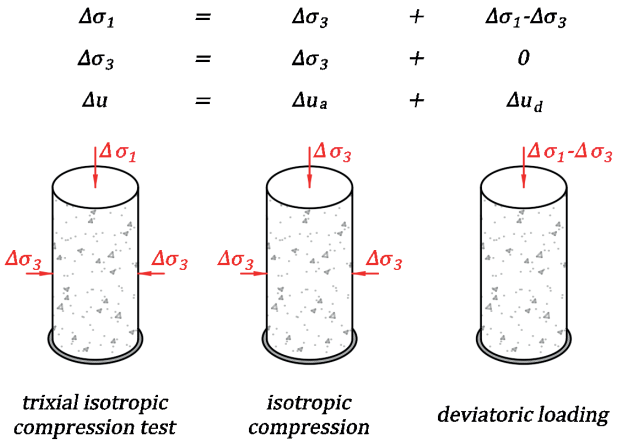

Figure 5. Schemes of idealized triaxial tests

The stage of comprehensive compression is characterized by hydrostatic uniform compression of the soil sample by pressure to restore natural stresses in the soil sample. Let us express the effective stresses in terms of Terzaghi's law:

$$\Delta\sigma_1' = \Delta\sigma_3' = \Delta\sigma_3 - \Delta u_a \quad (11)$$

In accordance with Hooke's law, the relative volumetric deformations of the soil skeleton can be obtained from the following relationship:

$$\varepsilon_V{}^c = \frac{\Delta V}{V} = C_c \cdot \Delta p' \quad (12)$$

where ΔV is the change in sample volume;

V is the initial sample volume;

C_c is the compressibility of the soil skeleton;

Let us represent Hooke's law for the volumetric compression of the pore fluid:

$$\varepsilon_V^{\ w} = \frac{\Delta V}{V} = C_w \cdot n \cdot \Delta u_a \qquad (13)$$

where C_w is the compressibility of the pore fluid; n is the porosity of soil.

For the stage of comprehensive compression of the soil, taking into account expressions (11) and (12), it was obtained:

$$\Delta V = C_c \cdot V(\Delta\sigma_3 - \Delta u_a) \qquad (14)$$

Assuming that the change in the volume of the soil sample occurs only due to the change in the volume of its pores, expressions (13) and (14) can be equated:

$$\frac{\Delta u_a}{\Delta\sigma_3} = \frac{1}{1+\frac{C_w \cdot n}{C_c}} = B \qquad (15)$$

For a completely water-saturated soil, in which there are no gas inclusions in the pore space, the Skempton parameter is $B = 1$.

The Skempton coefficient B depends on the degree of soil consolidation. The coefficient is close to 1, when evaluating the instantaneous strength, i.e., for time 0. This means that the entire mean stress was accepted up by the pore fluid. For a fully drained analysis, the B factor is 0.

At the stage of deviatoric loading, the sample is destroyed due to the development of shear deformations. Using Terzaghi's law, the effective principal stresses are expressed as follows:

$$\Delta\sigma_1' = \Delta q - \Delta u_d \qquad (16)$$

$$\Delta\sigma_3' = -\Delta u_d \qquad (17)$$

Taking into account expressions (16) and (17), the Hooke's law for the stage of deviatoric loading has the form:

$$\Delta V = C_c \cdot V \cdot \frac{1}{3} \cdot (\Delta q - 3\Delta u_d) \qquad (18)$$

Let us represent Hooke's law for volumetric deformations of the pore fluid at the stage of deviatoric loading:

$$\Delta V = C_w \cdot n \cdot V \cdot \Delta u_d \qquad (19)$$

Assuming that the change in the volume of the soil sample occurs only due to the change in the volume of its pores, expressions (18) and (19) can be equated:

$$\frac{\Delta u_d}{\Delta q} = B \cdot \frac{1}{3} = B \cdot A \qquad (20)$$

Then the change in pore pressure at the stage of deviatoric loading can be represented as follows:

$$\Delta u_d = B \cdot A \cdot \Delta q \qquad (21)$$

The Skempton coefficient A determines the excess pore pressure under undrained deviatoric loading.

Since the change in pore pressure during testing is the sum of the change at the stage of all-round compression and at the stage of deviatoric loading, it is possible to obtain the effective stress law of Terzagi, substituting expressions (15) and (21), and considering the Skempton coefficients for principal stresses (10).

The Skempton coefficient A shows what part of the load during deviatoric loading (shear) is transferred to the pore fluid. Since soil destruction occurs precisely at the stage of deviatoric loading, for an undrained state it is possible to determine the value of the Skempton coefficient A at which destruction will occur. This value of the coefficient is denoted as A_f. This coefficient is fundamental in assessing the momentary stability of prefabricated structures (for example, road embankments) [13].

From expression (20), it follows that for the ideal elastic-plastic behavior of the soil, the value of the coefficient $A_f = \frac{1}{3}$.

Figure 6 presents the stress paths for a triaxial consolidated undrained test. For loading

presented in fig. 5, the path of effective stresses should first represent segment OA (comprehensive compression). Then segment AC (deviator loading). The path of total stresses under deviatoric loading is segment AD.

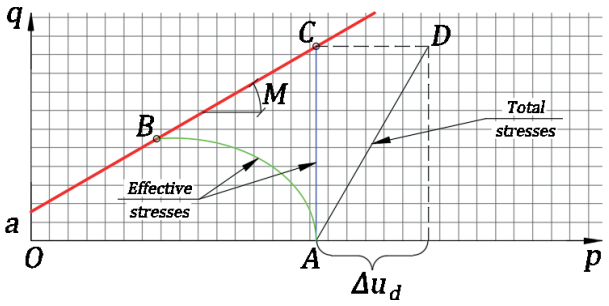

Figure 6. Stress paths: OA - path at the stage of all-round compression; AD - path in full stresses at the stage of deviatoric loading; AC is the theoretical path of effective stresses for an ideal-elastic-plastic body; AB - path obtained from experimental data for normally consolidated soils

2.3. Simulation of Volumetric Plastic Deformation Functions

As noted above, the volumetric deformation of a completely water-saturated soil is due solely to the compressibility of the liquid when it is impossible to squeeze out water from the pores. Thus, it is acceptable to assume that in an undrained triaxial test, the volume of the soil sample remains constant.

In this case, the curve q(p') of the path of undrained deviatoric loading should be an isoline of zero volumetric strains.

Volumetric deformations of the soil mass can be decomposed into two components:

$$\varepsilon_V = \varepsilon_V^e + \varepsilon_V^p \qquad (22)$$

where ε_v^e is the elastic component of volumetric deformations;

ε_v^p is the plastic component of volumetric deformations.

With a consolidated undrained test, it is true:

$$\varepsilon_V = \varepsilon_V^e + \varepsilon_V^p \cong 0 \qquad (23)$$

The isoline of equal plastic volumetric deformations in accordance with the concept of critical state (CSSM - critical state soil mechanics) can be represented as a loading surface or a “cup” (a surface that limits the zone of a quasi-elastic state under loading) [14].

To analyze the undrained behavior in different soil models, consider the load surfaces in the Cam Clay, Modified Cam Clay, Hardening Soil models. All these models look like cup. The description of the functions of the "cup" is presented in Table. 1.

Table 1. Functions of the loading surface under volume compression

Model	Yield surface for triaxial compression
Cam Clay	$f(p',q) = q + M \cdot p' \cdot \ln(p' / p_p)$
Modified Cam Clay	$f(p',q) = q^2 / M^2 + p' \cdot (p' - p_p)$
Hardening Soil	$f(p',q) = q^2 / \alpha^2 + p'^2 - p_p^2$

where p_p is the pre-consolidation pressure (represented on the graphs as the point of intersection of the cup and the abscissa axis);

α is the internal parameter of the Hardening Soil model, which is responsible for the shape of the "cup".

Figure 7 presents graphical view of the cup loading surfaces according to the dependencies from Table 1 obtained by the authors in the PC "MathCAD 15".

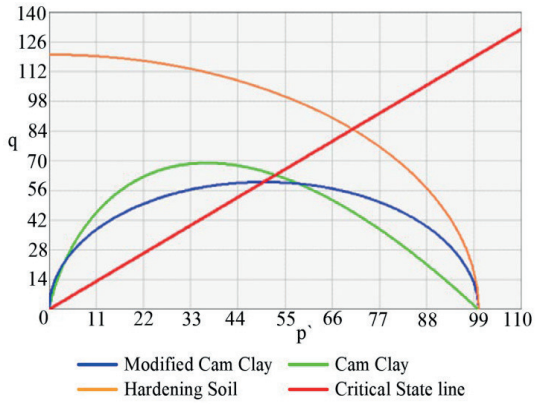

Figure 7. Cup loading surfaces.

2.4. Simulation of the path of undrained deviatoric loading for the Modified Cam Clay model

The Modified Cam Clay model was developed based on the Cam Clay model by Burland [7], [8]. Both models are a consequence of critical state soil mechanics, which is based on the assumption that soils continuously deform under load until a critical state occurs. Then the soil begins to behave like a fluid with a constant internal friction angle and a constant porosity coefficient. Cam Clay served as the basis for further modifications of cup models.

The basic concept of the model is the logarithmic relationship between the mean effective stress and the porosity coefficient, as well as the introduced yield surface, which limits the elastic deformation of the soil.

Figure 8 shows a graphical display of the change in the loading surface with a change in the porosity coefficient in coordinates obtained by the authors in the MathCAD 15 PC.

To determine the path of the effective stresses of the "cup" model, it is necessary to obtain the point of intersection of the path with the line of the critical state. The following mathematical transformations are required for this purpose.

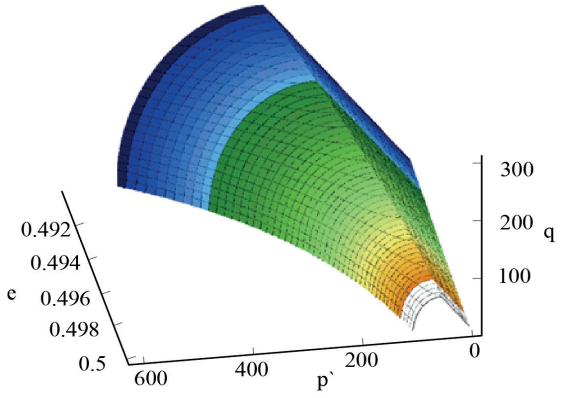

Figure 8. Load Surface for Modified Cam Clay Model

The equation of the cup loading surface is as follows:

$$(\frac{q}{M \cdot p'})^2 - \frac{p_p}{p'} + 1 = 0 \qquad (24)$$

The Coulomb-Mohr fracture surface is represented by the equation:

$$q = M \cdot p' \qquad (25)$$

Substituting expression (25) into (24), the intersection point of the "cup" and the destruction surface is found as follows:

$$(\frac{Mp'}{Mp'})^2 - \frac{p_p}{p'} + 1 = 0 \rightarrow p_p = 2p_f^{`} \qquad (26)$$

where $p_f^{`}$ is the mean effective stress at failure.

To find the path of undrained deviatoric loading, the terms in equation (23) were written. Based on the logarithmic law of model deformation, the elastic component was written as:

$$\varepsilon_v^e = \kappa^* \cdot \ln(p'/p_0) \qquad (27)$$

where p_0 is the mean effective stress in natural state.

κ^* is the modified recompression ratio:

$$\kappa^* = \frac{\kappa}{1+e_0} \qquad (28)$$

where κ is the recompression ratio;

e_0 is the soil porosity coefficient in natural state.

The plastic component is represented as the difference between the total deformation and the elastic deformation:

$$\varepsilon_v^p = (\lambda^* - \kappa^*) \cdot \ln(p_p/p_0) \qquad (29)$$

where λ^* is the modified compression ratio:

$$\lambda^* = \lambda/(1+e_0) \qquad (30)$$

where λ is the compression ratio.

Then expression (23) can be represented as:

$$\kappa \cdot \ln(\frac{p'}{p_0}) = -(\lambda - \kappa) \cdot \ln(\frac{p_p}{p_0}) \qquad (31)$$

Substituting expression (26) into expression (31) and expressing p_p, the following relation was obtained:

$$p_f^{`} = 2^{\frac{\kappa-\lambda}{\lambda}} \cdot p_0 = 2^{\Lambda} \cdot p_0 \qquad (32)$$

where $\Lambda = (\kappa - \lambda)/\lambda$ is the soil deformability parameter.

The value of the limiting stress deviator can be represented using expression (32) as:

$$q_f = C_u/2 = M \cdot p_f^{`} = M \cdot 2^{\Lambda} \cdot p_0 \qquad (33)$$

Then the path can be represented as an ellipse passing through the origin, p_p and $q(p_f^{`})$.

Figure 9 shows the path of the undrained loading of the Modified Cam Clay model, obtained by the authors in the MathCAD 15 PC.

The value of the Skempton coefficient A_f at fracture can be determined from the following relationship:

$$A_f = \frac{\Delta u_d}{\Delta q} = \frac{p_p}{M \cdot 2^{\Lambda} \cdot p_0} + \frac{1}{3} - \frac{1}{M} \qquad (34)$$

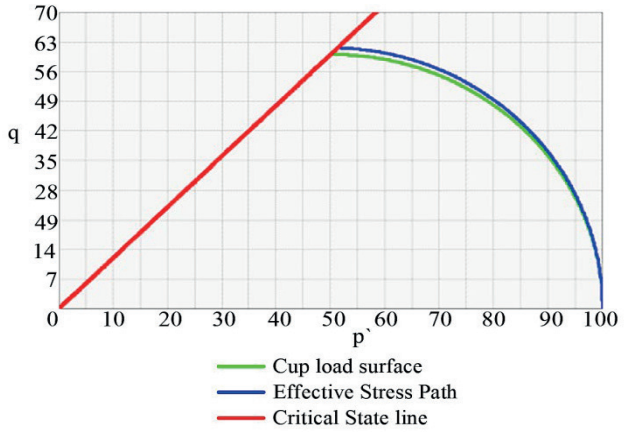

Figure 9. Path of undrained deviatoric loading in the Modified Cam Clay model

2.5. Modeling the path of undrained deviatoric loading during virtual soil testing

For a visual comparison of the work of specific soil models with laboratory experiments, the Soil Test module for the Plaxis PC was used.

Let's perform virtual consolidated-undrained triaxial soil tests in the Modified Cam Clay model. The pressure of triaxial compression has been accepted equal to $p_0 = 100kPa$.

The tests for soil with similar mechanical parameters presented in Table 2 were carried out. Triaxial compression pressure during the test was $100kPa$. The results of the comparison are shown in fig. 10.

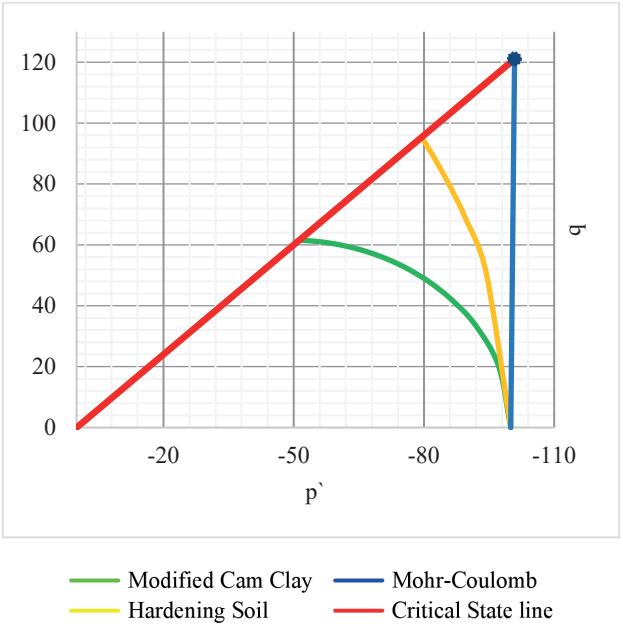

Figure 10. Paths of effective stresses under undrained loading

Table 2. Soil parameters for models

Model	Strength parameters	Deformability parameters
Mohr-Coulomb	$\phi' = 30^o, c' = 0$	$E' = 30MPa$
Modified Cam Clay	$M = 1.2$	$\lambda = 0.005, \kappa = 0.0018$
Hardening Soil	$\phi' = 30^o, c' = 0$	$E_{oed}^{ref} = 30MPa, E_{50}^{ref} = 30MPa, E_{ur}^{ref} = 150MPa, m = 0.5, p_{ref} = 0.1MPa$

3. RESULTS AND DISCUSSION

The authors performed mathematical modeling of paths of undrained deviatoric loading for:

- ideal elastic-plastic body (Mohr-Coulomb Model);
- Modified Cam Clay models.

Also, during virtual triaxial tests in the Soil Test module, paths were built for the Mohr-Coulomb, Modified Cam Clay, Hardeming Soil models.

Mathematical modeling of an ideal elastic-plastic material shows that with an undrained deviatoric loading, there is no deviation of the loading path from the vertical. In this case, one can observe a deviation of the path with a decrease in the mean effective stress [15], [16] in real samples of normally consolidated soil. For example, figure 10 presents the effective stress paths for an undrained triaxial test of kaolin clays.

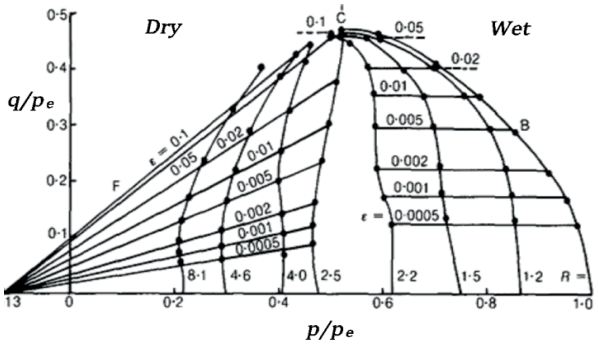

Figure 11. Effective Stress Paths for an Undrained Triaxial Test on Kaolin Clays [17]

At the same time, the graph clearly shows the relationship between the curvature of the stress path and the degree of overconsolidation of the soil.

In addition, the Modified Cam Clay model was considered. Comparison of the results of mathematical modeling with the behavior of the Modified Cam Clay model in the Soil Test shows the complete convergence of the analytical loading path with the test results. This indicates the correctness of the mathematical modeling. Figure 12 presents the results of the comparison. From the point of view of mathematical modeling, the path of undrained deviatoric loading depends on the shape of the cup and on how the elastic and plastic components of deformations were described. Thus, if the shape of the yield surface, the law of plastic deformation (associated or non-associated) and the relationship between stresses and strains are known, one can obtain the path of effective stresses.

The Modified Cam Clay model describes the relationship between volumetric strains and mean stress, using an elliptical yield surface and the associated plastic flow law. This means that the shear deformations will depend only on the calculated volumetric ones, which can greatly distort the deformation pattern when shear deformation prevails (for example, when analyzing pits).

The mathematical proven for the Cam Clay model is similar to the Modified Cam Clay model, except for the different "cup" functions. The Cam Clay model was not considered in this article due to its absence in numerical simulation software packages. This is due to the impossibility of differentiating the function of the yield surface of the model at one point.

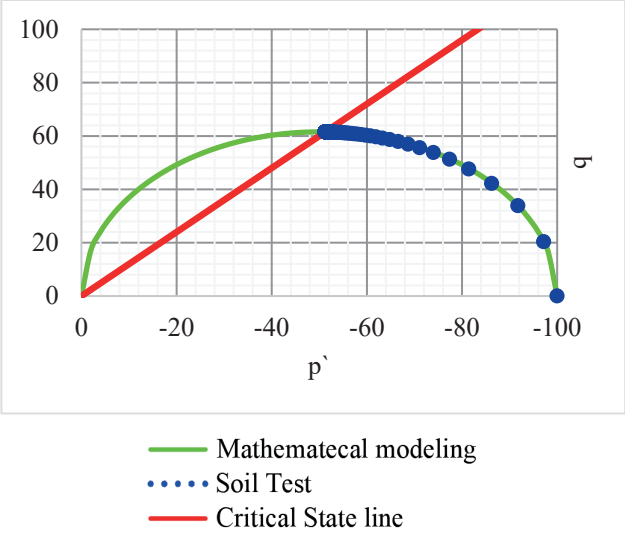

Figure 12. Comparison of analytical calculation results with Soil Test results

Mathematical modeling of the Hardening Soil model is hampered by the lack of an unambiguous definition of the parameters (H is the model hardening parameter, α is the "cup" shape parameter) [3], which do not allow to reproduce the path of undrained deviatoric loading analytically.

Virtual soil tests in the Soil Test complex allow you to evaluate the performance of various soil models with similar characteristics.

Table provides the values of the coefficients A_f calculated for different soil models.

Table 1. Coefficient Values of the coefficient A_f for different soil models

Soil model	Coefficient A_f
Mohr-Coulomb	0,33
Hardening Soil	0,55
Modified Cam Clay	1,13

Depending on the chosen model, the description of plastic deformation is fundamentally different. This affects to the path of deviatoric loading and the resulting resistance to undrained shear.

Considering the curvature of the path, the value of the coefficient A, mathematically derived by Skempton, is no longer a constant value (as for ideal elastic-plastic behavior), but a function. Specific failure values A_f for different types of soils were obtained by Skempton during a series of triaxial consolidated-undrained tests of some types of soils [4] (Table 4).

For numerical simulation of problems that consider the undrained behavior of soils, it is necessary either to introduce the resistance to undrained shear directly, or to obtain a "true" effective stress path.

After the appearance of cup models, the path of undrained deviatoric soil loading became mathematically tied to the function of the cup [18]. Numerical modeling of undrained behavior of soils requires consideration of specific soil models.

Table 2. Values of the coefficient A_f [4]

Type of clay soil	Values of the coefficient A_f
Clays with high sensitivity	*0.75 to 1.5*
Normally consolidated clays	*0.5 to 1*
Compacted sandy clays	*0.25 to 0.75*
Lightly over-consolidated clays	*0 to 0.5*
Compacted clay-gravels	*-0.25 to 0.25*
Heavily over-consolidated clays	*-0.5 to 0*

Thus, "true" path of effective stresses under undrained deviatoric loading can be obtained when conducting consolidated-undrained triaxial soil tests at the stage of engineering surveys. The designer can obtain specific values A_f for soils analyzing path data. Knowing the values of the Skempton coefficient obtained from laboratory tests and the theoretical values of A_f, one can

choose a soil model that adequately describes the undrained behavior.

The correct choice of the soil model will allow not to overestimate (which can lead to loss of stability of the excavation wall) and not to underestimate the resistance to undrained shear (which can lead to excessive reserves and, accordingly, an increase in the cost of design solutions).

In known soil models, undrained shear resistance C_u is affected by over consolidation, stiffness, and effective strength parameters. This can be represented as a dependency of the form:

$$\frac{c_u}{\sigma_{v0}^{'}} = f(\phi', OCR, C_c, C_s) \quad (35)$$

where $\sigma_{v0}^{'}$ is the effective vertical stress;

OCR is the soil consolidation factor;

C_s is the elastic component of soil skeleton compressibility.

To obtain correct data on soil compaction, stiffness and undrained strength, it is necessary to conduct laboratory and field tests using appropriate correlations and available geotechnical testing experience in the region [19], [20].

For the soil conditions of St. Petersburg, a special viscoelastic-plastic model with an independent hardening mechanism was developed. Figure 13 presents the model construction scheme.

This model does not belong to the "cup" models. The construction of the loading surfaces was carried out directly based on the results of testing the soils of St. Petersburg.

The deviation of isolines of zero volumetric plastic deformations is explained by the dilatancy phenomenon and, at the same time, it is mentioned that the isolines are approximated by a straight vertical line, referring to the lack of knowledge of the dilatancy phenomenon in soft clay soils of St. Petersburg [6].

The different behavior of soil models under undrained deviatoric loading makes the choice of the model especially important when calculating excavations in an undrained setting. For further comparison, it is advisable to consider specialized models for shale calculations in an undrained formulation under various loading paths, for example, NGI-ADP.

4. CONCLUSION

An accurate description of the path of effective soil stresses using the theory of elasticity does not correspond to real soil tests. This circumstance limits the use of ideal elastic-plastic models in undrained calculations.

Using similar initial parameters in various nonlinear soil models, one can obtain fundamentally different functions of plastic volumetric deformation and, as a result, paths of undrained deviatoric loading. This leads to completely different Skempton coefficient A_f and undrained shear strength values.

An analytical method for determining the Skempton coefficient A_f for the Modified Cam Clay model has been presented in the article;

The paper provides recommendations for assigning a soil model for undrained calculations based on the Skempton coefficient A_f, which can be obtained by processing the results of consolidated undrained triaxial soil tests;

The obtained solutions allow more accurate designing the pits of great depth in soft water-saturated soils.

REFERENCES

1. **Mangushev, R.A., Osokin, A.I.** (2020). The experience of the underground construction for the complex of buildings on a soft soil in the center of St. Petersburg. *International Journal for Computational Civil and Structural Engineering*, vol. 16, no. 3, pp. 47-53.doi:10.22337/2587-9618-2020-16-3-47-53
2. **Dashko, R.E., Aleksandrova, O.Y., Kotyukov, P.V., Shidlovskaya, A.V.** (2011). Osobennosti inzhenerno-geologicheskih uslovij Sankt-Peterburga

[Features of engineering and geological conditions of St. Petersburg], *Urban development and geotechnical construction*, vol. 1, pp. 1-47.

3. **Ulickiy, V.M., Shashkin, A.G., Shashkin, K.G., Shashkin, V.A.** (2014). Osnovy sovmestnyh raschetov zdanij i osnovanij [Fundamentals of joint calculations of buildings and foundations]. St. Petersburg: Publishing House of the Institute "Georeconstruction". (in Russian)
4. **Skempton, A. W.** (1954). The Pore-Pressure Coefficients A and B. *Geotechnique*, vol. 4, no. 4, pp. 143–147. doi:10.1680/geot.1954.4.4.143
5. **Schanz, T., Vermeer, P. A., Bonnier, P. G.** (2019). The hardening soil model: formulation and verification. *In Beyond 2000 in computational geotechnics*, Routledge, pp. 281-296.
6. **Shashkin, A.G.** (2011). Vyazko-uprugo-plasticheskaya model' povedeniya glinistogo grunta [Visco-elastic-plastic model of clay soil behavior], *Urban development and geotechnical construction*, vol. 2, pp. 1-32.
7. **Roscoe, K. H., Schofield, A. N., Wroth, C. P.** (1958). On The Yielding of Soils. *Geotechnique*, vol. 8, no. 1, pp. 22–53. doi:10.1680/geot.1958.8.1.22
8. **Burland, J. B. (1965).** The yieding and dilation of clay. *Géotechnique*, vol. 15, no. 1, pp. 211-214.
9. **Puller, M.** (2003). *Deep Excavations: A Practical Manual*, Thomas Telford Ltd.
10. **Vermeer, P. A.** (1999). Column Vermeer. *Plaxis Bulletin*, Delpth: Plaxis, pp. 2-3.
11. **Kolybin, I.V.** (2008). Uroki avarijnyh situacij pri stroitel'stve kotlovanov v gorodskih usloviyah [Lessons of emergency situations during the construction of pits in urban conditions], *Urban development and geotechnical construction*, vol. 12, pp. 90-124.
12. **Yannie, J.** (2012). *Change of shear strength in soft soil excavations*. Paper presented at the 22nd European Young Geotechnical Engineers Conference in Gothenburg, 26-29 August, 2012.
13. **Solov`yov, Y.I., Karaulov, A.M., Vaganov, P.S.** (1980). The theory of instantaneous strength and its application in the calculations of the stability of consolidating soil arrays. Proceedings of the *Design and study of the foundations of hydraulic structures: Materials of conferences and meetings on hydraulic engineering*. Leningrad: Energy, pp. 104-105.
14. **Paramonov, V.N.** (2012). *Metod konechnyh elementov pri reshenii nelinejnyh zadach geotekhniki* [Finite element method for solving nonlinear geotechnical problems]. St. Petersburg: Georeconstruction Group of Companies. (in Russian)
15. **Yang, Y., Kou, H., Li, Z., Jia, Y., Zhu, C.** (2022). Normalized Stress–Strain Behavior of Deep-Sea Soft Soils in the Northern South China Sea. *Journal of Marine Science and Engineering*, vol. 10, no. 8, pp. 1142. doi:10.3390/jmse10081142
16. **Yin, J., Zhang, K., Geng, W., Gaamom, A., Xiao, J.** (2021). Effect of initial water content on undrained shear strength of K0 consolidated clay. *Soils and Foundations,* vol. 61, no. 5, pp. 1453-1463. doi:10.1016/j.sandf.2021.08.010
17. **Wroth, C. P.** (1984). The interpretation of in situ soil tests. *Geotechnique*, vol. 34, no. 4, pp. 449–489. doi:10.1680/geot.1984.34.4.449
18. **Mayne, P. W., Coop, M. R., Springman, S. M., Huang, A. B., Zornberg, J. G.** (2009). Geomaterial behavior and testing. In Proceedings of the *17th International Conference on Soil Mechanics and Geotechnical Engineering (Volumes 1, 2, 3 and 4),* 5-9 October 2009, Alexandria: IOS Press., pp. 2777-2872.
19. **Iovlev, G.A., Piskunov, N.S., Bahvalov, E.D., Ochkurov, V.I. (2022).** Metody optimizacii parametrov nelinejnyh gruntovyh modelej dlya inzhenerno-geologicheskih uslovij Sankt-Peterburga [Methods of optimization of parameters of nonlinear soil

models for engineering and geological conditions of St. Petersburg]. *Mining Information and Analytical Bulletin (scientific and technical journal)*, vol. 7, pp. 148-163.

20. **Alekseev, A.V., Iovlev, G.A.** (2019). Adaptaciya modeli uprochnyayushchegosya grunta (hardening soil) dlya inzhenerno-geologicheskih uslovij Sankt-Peterburga [Adaptation of the hardening soil model for the engineering and geological conditions of St. Petersburg]. *Mining Information and Analytical Bulletin (scientific and technical journal)*, vol. 4, pp. 75-87.

СПИСОК ЛИТЕРАТУРЫ

1. **Мангушев Р., Осокин А.** Опыт подземного строительства для комплекса зданий на слабых грунтах в центре Санкт-Петербурга //International Journal for Computational Civil and Structural Engineering, 2020, №3(16). С. 47-53.
2. **Дашко Р. Э. и др.** Особенности инженерно-геологических условий Санкт-Петербурга //Развитие городов и геотехническое строительство, 2011, (1). С. 1-47.
3. **Улицкий В. М. и др.** Основы совместных расчетов зданий и оснований. – СПб.: Издательство института «Георекономструкция», 2014. – 328 с.
4. **Skempton A. W.** The pore-pressure coefficients A and B // Geotechnique, 1954, No. 4 (4), pp. 143-147.
5. **Schanz T., Vermeer P. A., Bonnier P. G.** The hardening soil model: formulation and verification // Beyond 2000 in computational geotechnics, Routledge, 2019, pp. 281-296.
6. **Шашкин А. Г.** Вязко-упруго-пластическая модель поведения глинистого грунта // Развитие городов и геотехническое строительство, 2011, (2). pp. 1-32.
7. **Roscoe K. H., Schofield A. N., Wroth C. P.** On the yielding of soils // Geotechnique, 1958, No. 1 (8), pp. 22-53.
8. **Burland J. B.** The yieding and dilation of clay // Géotechnique, 1965. No. 1(15), pp. 211-214.
9. **Puller M.** Deep excavations: A practical manual. – Thomas Telford, 2003, 590 pages.
10. **Vermeer P. A.** Column Vermeer // Plaxis Bulletin, 1999, pp. 2-3.
11. **Колыбин И. В.** Уроки аварийных ситуаций при строительстве котлованов в городских условиях // Развитие городов и геотехническое строительство, 2008, №. 12. С. 90-124.
12. **Yannie J.** Change of shear strength in soft soil excavations // Proceedings of 22nd European Young Geotechnical Engineers Conference. Gothenburg, 2012.
13. **Соловьев Ю. И., Караулов А. М., Ваганов П. С.** Теория мгновенной прочности и ее применение в расчетах устойчивости консолидирующихся массивов грунта // Проектирование и исследование оснований гидротехнических сооружений: М-лы конф. и совещ. по гидротехнике. Л.: Энергия, 1980. С. 104-105.
14. **Парамонов В. Н.** Метод конечных элементов при решении нелинейных задач геотехники. – СПб.: Группа компаний «Георекономструкция, 2012. 264 с.
15. **Yang Y. et al.** Normalized Stress–Strain Behavior of Deep-Sea Soft Soils in the Northern South China Sea // Journal of Marine Science and Engineering, 2022, No. 8(10). pp. 1142.
16. **Yin J. et al.** Effect of initial water content on undrained shear strength of K0 consolidated clay // Soils and Foundations, 2021, No. 5(61). pp. 1453-1463.
17. **Wroth C. P.** The interpretation of in situ soil tests // Geotechnique, 1984, No. 4(34). pp. 449-489.
18. **Mayne P. W. et al.** Geomaterial behavior and testing // Proceedings of the 17th

International Conference on Soil Mechanics and Geotechnical Engineering (Volumes 1, 2, 3 and 4). Alexandria, IOS Press, 2009, pp. 2777-2872.

19. **Иовлев Г. А. и др.** Методы оптимизации параметров нелинейных грунтовых моделей для инженерно-геологических условий Санкт-Петербурга // Горный информационно-аналитический бюллетень (научно-технический журнал), 2022, №. 7. С. 148-163.
20. **Алексеев А. В., Иовлев Г. А.** Адаптация модели упрочняющегося грунта (hardening soil) для инженерно-геологических условий Санкт-Петербурга // Горный информационно-аналитический бюллетень (научно-технический журнал), 2019, №. 4. С. 75-87.

Rashid Abdullovich Mangushev – Honorary Figure of Russian Higher Education, Laureate of Russian Government prize, Dr.Sc., professor; Department of geotechnics, St. Petersburg State University of Architecture and Civil Engineering (SPbGASU); h.5, Egorova str., St. Petersburg, 190103, Russia; +7(812)316-03-41. ramangushev@yandex.ru

Ivan Borisovich Bashmakov – Master of Engineering and Technology, assistant; Department of geotechnics, St. Petersburg State University of Architecture and Civil Engineering (SPbGASU); h.5, Egorova str., St. Petersburg, 190103, Russia; +7(911)992-82-96. 179bib@gmail.com

Daria Alekseevna Paskacheva – Bachelor of Science, Department of geotechnics, St. Petersburg State University of Architecture and Civil Engineering (SPbGASU); h.5, Egorova str., St. Petersburg, 190103, Russia; +7(950)002-25-16. dashaP17012000@yandex.ru

Alina Vitalyevna Kvashuk – Civil engineer, assistant, Department of geotechnics, St. Petersburg State University of Architecture and Civil Engineering (SPbGASU); h.5, Egorova str., St. Petersburg, 190103, Russia; +7(931)320-82-96. alina_kvashuk@mail.ru

Рашид Абдуллович Мангушев – член-корреспондент РААСН, Заслуженный работник высшего образования РФ, лауреат Премии Правительства РФ, доктор технических наук, профессор; кафедра Геотехники, Санкт-Петербургский Государственный Архитектурно-Строительный Университет (СПбГАСУ); д.5, ул. Егорова, Санкт-Петербург, 190103, Россия; +7(812)316-03-41. ramangushev@yandex.ru

Иван Борисович Башмаков – магистр техники и технологии, ассистент; кафедра Геотехники, Санкт-Петербургский Государственный Архитектурно-Строительный Университет (СПбГАСУ); д.5, ул. Егорова, Санкт-Петербург, 190103, Россия; +7(911)992-82-96. 179bib@gmail.com

Дарья Алексеевна Паскачева – бакалавр, кафедра Геотехники, Санкт-Петербургский Государственный Архитектурно-Строительный Университет (СПбГАСУ); д.5, ул. Егорова, Санкт-Петербург, 190103, Россия; +7(950)002-25-16. dashaP17012000@yandex.ru

Алина Витальевна Квашук – инженер-строитель, ассистент, кафедра Геотехники, Санкт-Петербургский Государственный Архитектурно-Строительный Университет (СПбГАСУ); д.5, ул. Егорова, Санкт-Петербург, 190103, Россия; +7(931)320-82-96. alina_kvashuk@mail.ru

International Journal for Computational Civil and Structural Engineering, 19(1) 112–123 (2023)

DOI:10.22337/2587-9618-2023-19-1-112-123

ROD BUTT BOLTS BOLT JOINTS OF TENSION RODS USING SLANTING FLANGES

Alexander S. Marutyan [1], Avetik G. Abovyan [2]

[1] Branch of the North Caucasus Federal University, Pyatigorsk, RUSSIA
[2] National Research Moscow State University of Civil Engineering, Moscow, RUSSIA

Abstract. A new technical solution for the mounting joints of metal structures in the form of bolted joints on oblique flanges located at an angle of 30 degrees relative to the longitudinal axes of the rod elements and equipped with support tables is given. In such joints, the longitudinal forces that fall on the flanges are decomposed into normal and tangential (tangential) components. Normal components are transmitted to bolted fasteners, and tangents are perceived by support tables. At the same time, in oblique flanges, the bolts are loaded two times less than in straight ones. Butt joints have the necessary and sufficient bearing capacity, provide a reduction in the consumption of structural material and are equally strong with docked rod elements. A practical method for calculating such compounds is proposed, confirmed by the results of a trial (control) series of studies of prototypes.

Keywords: mounting joints of metal structures, bolt fasteners, connections on flanges, oblique flanges, support tables, calculation method

СТЫКОВЫЕ БОЛТОВЫЕ СОЕДИНЕНИЯ СТЕРЖНЕВЫХ ЭЛЕМЕНТОВ С КОСЫМИ ФЛАНЦАМИ И ИХ РАСЧЕТ

А.С. Марутян [1], А.Г. Абовян [2]

[1] Филиал Северо-Кавказского Федерального Университета, г. Пятигорск, РОССИЯ
[2] Национальный исследовательский Московский Государственный Строительный Университет, г. Москва, РОССИЯ

Аннотация. Приведено новое техническое решение монтажных стыков металлических конструкций в виде болтовых соединений на косых фланцах, расположенных под углом 30 градусов относительно продольных осей стержневых элементов и снабженных опорными столиками. В таких стыках продольные усилия, приходящиеся на фланцы, раскладываются на нормальные и касательные (тангенциальные) составляющие. Нормальные составляющие передаются на болтовые крепления, а касательные – воспринимаются опорными столиками. При этом в косых фланцах болты нагружены в два раза меньше, чем в прямых. Стыковые соединения обладают необходимым и достаточным запасом несущей способности, обеспечивают уменьшение расхода конструкционного материала и являются равнопрочными со стыкуемыми стержневыми элементами. Предложена практическая методика расчета таких соединений, подтвержденная итогами пробной (контрольной) серии исследований опытных образцов.

Ключевые слова: монтажные стыки металлических конструкций, болтовые крепления, соединения на фланцах, косые фланцы, опорные столики, методика расчета

INTRODUCTION

Flange connections are currently among the most common and mass types of bolt fasteners, differing in the mechanisms for transmitting external forces. Here, these forces are perceived mainly due to overcoming the compression resistance of the flanges from the pre-tension of high-strength bolts. Flange joints are one of the most effective types of bolted joints, since the very significant bearing capacity of high-strength bolts is used directly

and almost completely. The field of rational and effective use of flange joints is quite large. It covers the connections of elements subject to stretching, compression, bending or their joint action. This area can also be extended for the transmission of cyclic loads, but in this case appropriate calculation and experimental checks are necessary [1].

It is known that the butt joint of the stretched elements of the closed profile is known, including the ends of the rod elements with flanges, additional ribs and tightening bolts installed along the perimeter of the closed profile in pairs symmetrically relative to the ribs [10]. The disadvantage of the connection is the large dimensions of the flange and a significant number of connecting parts, which increases the consumption of material and the complexity of the structure. The closest to the proposed technical solution is the mounting butt joint of the lower (stretched) belt of trusses from bent welded closed profiles, including the ends of the rod elements with flanges, additional ribs, tightening bolts and a sheet gasket between the flanges for attaching the rods of the truss grate and connections between the trusses [11]. The disadvantage of the connection, as in the previous case, is the material intensity and laboriousness of the mounting joint on the flanges.

The main task, the solution of which is aimed at the flange connection of the stretched elements of the closed profile, is to reduce the mass (consumption) of the structural material. The result is achieved by the fact that in the flange connection of the stretched elements of the closed profile, including the ends of the rods with flanges, tightening bolts and the sheet gasket between the flanges, the flanges are installed at an angle of 30 ° relative to the longitudinal axes of the rod elements, and the sheet gasket consists of paired support tables, rigidly fastened to the flanges and in the assembled connection mutually resting on each other [12].

The proposed flange connection has a fairly universal technical solution. So, it can be used in the mounting joints of lattice structures from pipes of round, oval, elliptical, rectangular (Fig. 1), square, pentagonal (Fig. 2) [13, 14] and other closed cross-sections. As another example of the use of the proposed connection, similar joints can be given in the installation of structural elements from paired and single corners, channels, I-beams (Fig. 3), taurus, Z-, H-, U-, V-, Λ-, X-, C-, U-shaped and other open (unclosed) profiles. The proposed flange connection of stretched closed profile elements 1 contains attached using welds are solid leaf flanges 2 mounted at an angle of 30° relative to the longitudinal axes of the stretched elements. The support tables 3 are rigidly fastened to the flanges 2 by means of welded seams. In the protruding parts 4 of the flanges 2 and the support tables 3 there are coaxial holes 5, in which, after assembling the joint, tightening bolts 6 are installed on the mount. For the attachment of the rod element of the grille 7 in the proposed flange connection, the support tables 3 are extended beyond the protruding parts 4 of the flanges 2 in such a way that additional bolts 8 can be placed in them, as is done in a typical mounting joint on the flanges. In the case of using the proposed flange connection for the stretched elements of the unclosed profile 9, the coaxial openings 5 in the flanges 2 and the support tables 3, as well as the tightening bolts 6, may be located not only outside the cross-section (transverse or oblique) of the unclosed (open) profile, but also in its internal zones. In the complete absence of tightening bolts 6 in the outer (external) areas of the open profile 9, the proposed flange connection is more compact.

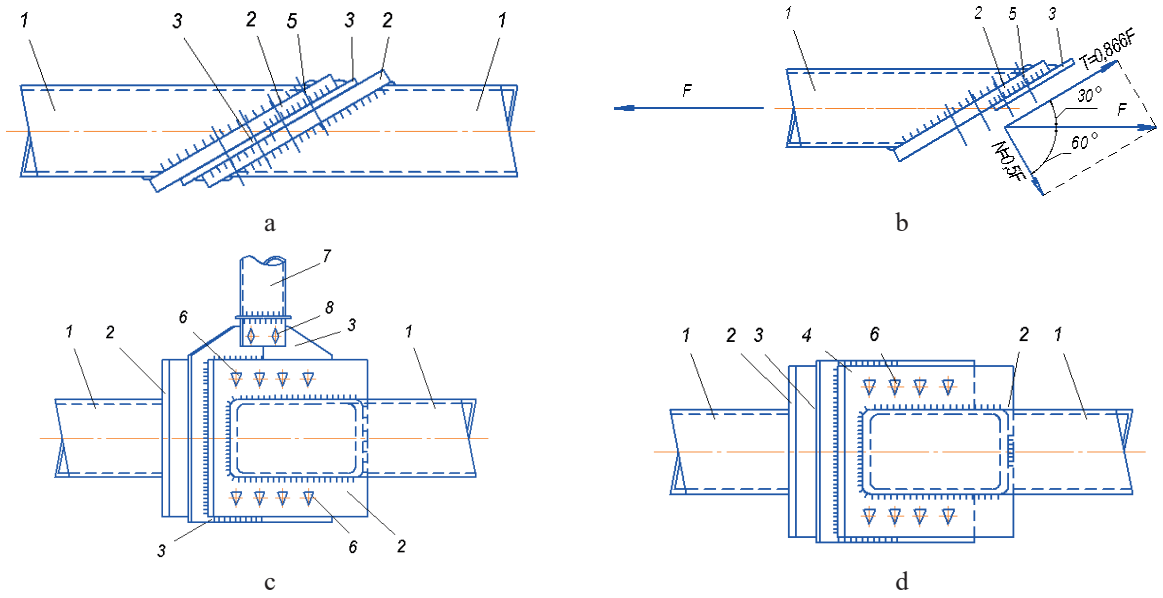

Figure 1. Schemes of flange connections of rectangular closed bent-welded profiles: a - top view; b - design diagram of an element with an oblique flange and a support table; c – side view; d – side view in the absence of lattice rod elements; 1 - lower (stretched) truss belt; 2 - oblique flange; 3 - support table; 4 - protruding part of the flange in the outer zone of the profile; 5 - bolt hole; 6 - coupling bolt; 7 - rod element of the lattice; 8 - bolted fastening of the lattice element; F is the longitudinal tensile force; N is the normal component; T - tangential (tangential) component

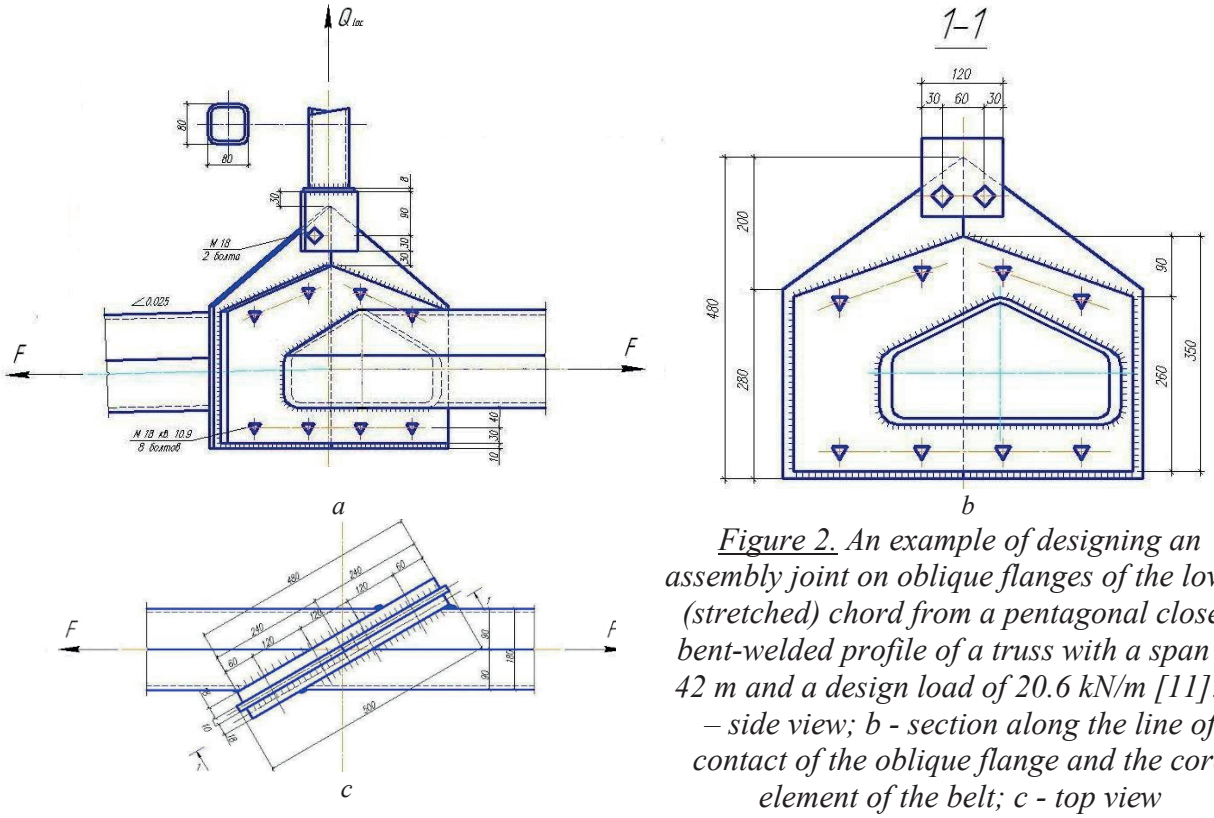

Figure 2. An example of designing an assembly joint on oblique flanges of the lower (stretched) chord from a pentagonal closed bent-welded profile of a truss with a span of 42 m and a design load of 20.6 kN/m [11]: a – side view; b - section along the line of contact of the oblique flange and the core element of the belt; c - top view

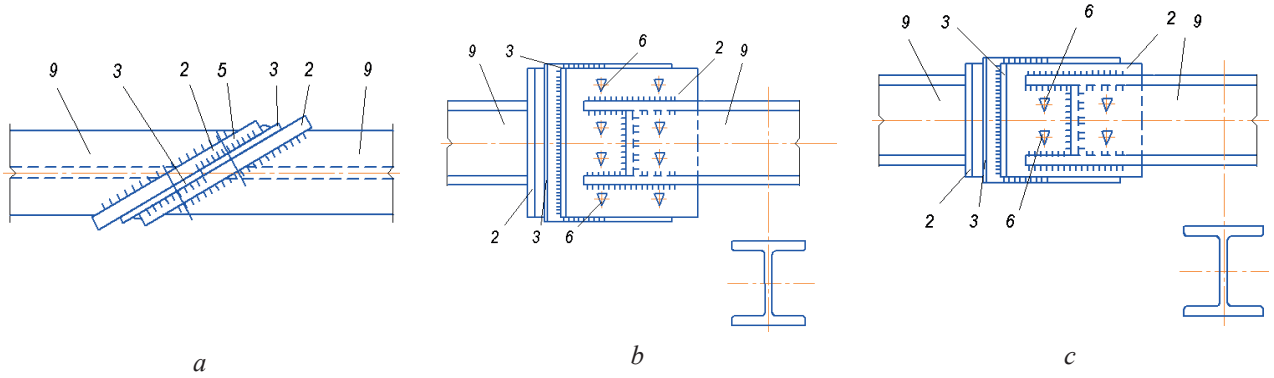

Figure 3. Schemes of flange connections of I-profiles: a - top view; b – side view; c - side view in the absence of bolts in the outer zones of the profile; 2 - oblique flange; 3 - support table; 5 - bolt hole; 6 - coupling bolt; 9 - I-profile

METHODS

In trusses of rectangular and square pipes (bent welded closed profiles), the angles of adhesion of the braces to the belt should be at least 30 ° to ensure the density of the weld section from the side of the sharp angle [15]. Therefore, in the proposed flange connection of the stretched closed profile elements 1, the flanges 2 and the support tables 3 fastened to them are mounted at an angle of 30° relative to the longitudinal axes. In this case, the longitudinal force *F*, which causes the tensile of the closed profile element 1, is decomposed into two components (Fig. 1, g):

- normal, perceived by tightening bolts [6],

$$N = Fcos60° = 0.5F \qquad (1)$$

- tangential, transmitted to the support tables 3,

$$T = Fcos30° = 0.886F. \qquad (2)$$

Reducing the bolting forces by half the same number of times reduces the moments that bend the flanges, and this allows you to use thinner sheets for them, thereby reducing the consumption of structural material. In addition, the material capacity of the proposed joint is positively affected by a possible reduction in the diameters of the tightening bolts 6, a decrease in their number or a combination of the first and second.

Here, the strength of the bolts of the flange joints of the rod elements of the closed (tubular) profile is ensured if

$$\frac{N}{0.9n_b \cdot N_{bt}} \leq 1, \qquad (3)$$

where n_b is the total number of bolts; N_{bt} is the calculated force perceived by a single bolt for the tension with which it must first be pulled (flange connection of type A), and calculated by the formula

$$N_{bt} = R_{bt} \cdot A_{bn}, \qquad (4)$$

where R_{bt} is the calculated tensile resistance of the bolted joints; *Abn* is the cross-sectional area of the "net" bolt.

The calculated bolt connection shall be positioned momentlessly (symmetrically) relative to the centre of gravity of the belt element cross-section, as close as possible to it and taking into account the minimum allowable distances from the profile to the axis of the bolt $_{bb}$ and from the axis of the bolt to the edge of the flange *cb*. In this case, each of the bolts must be equidistant from the profile. The diameter of the holes can be taken 3 mm larger than the diameter of the bolts. The bending strength of the flanges is ensured if σ

$$\frac{\sigma_{fl}}{\gamma_c R_{y,fl}} = \frac{M}{W_{fl}\gamma_c R_{y,fl}} \leq 1 \qquad (5)$$

where γ_c is the coefficient of working conditions; σ_{fl}, W_{fl} and $R_{y,fl}$ - respectively normal voltage, design resistance of steel and moment of cross-sectional resistance of the flange, $W_{fl}=b_1 t_{fl}^2/6$ (b_1 - pitch of bolts, t_{fl} - thickness of oblique flange); M is the highest value of the calculated bending moment.

In the flange joints of the rod elements of the closed (tubular) profile, as well as in the outer zone of the joints of the elements of the open (unclosed) profile, the bending moments of the flanges can be determined according to a conditional design scheme, as in a beam pinched from the side of the belt, hinged with an operte along the edge of the flange and loaded with a force in the bolt N_b [8, 9]:

$$M_1 = \frac{N_b \cdot l_1 \cdot b_b \cdot (l_1 + c_b)}{3l_1^2 - c_b^2};$$
$$M_2 = \frac{N_b \cdot b_b^2 \cdot (3l_1 - b_b)}{3l_1^2 - c_b^2}, \qquad (6)$$

where $N_b \leq 0.9 N_{bt}$; l_1 is the span of the beam, $l_1 = b_b + c_b$; b_b and c_b are the minimum allowable distances.

The same design scheme makes it possible to determine the deflections of the oblique flange [18]:

- along the axis of the bolted connection

$$f_{fl} = \frac{N_b \cdot b_b^3 \cdot c_b^2 \cdot (3b_b + 4c_b)}{12 \cdot l_1^3 \cdot EI_{f1}}; \qquad (7)$$

- highest value

$$f_{fl,max} = \frac{0.0098 \cdot N_b \cdot l_1^3}{EI_{fl}} \qquad (8)$$

where E is the modulus of elasticity of the flange material; I_{fl} is the moment of inertia of the flange cross-section, $I_{fl}=b_1 t_{fl}^3/12$.

The calculated oblique flange of the stretched joints is welded to the belt element by unilateral angular seams. They must be checked by the calculation of strength:

- on the metal of the seam

$$\frac{F}{\beta_f \cdot k_f \cdot l_w \cdot R_{wf} \cdot \gamma_{wf} \cdot \gamma_c} < 1; \qquad (9)$$

- on the metal of the fusion boundary with the belt element

$$\frac{F}{\beta_z \cdot k_f \cdot l_w \cdot R_{wz} \cdot \gamma_{wz} \cdot \gamma_c} < 1; \qquad (10)$$

- on the metal of the fusion boundary with the flange in the direction of the thickness of the rolled products

$$\frac{F}{\beta_z \cdot k_f \cdot l_w \cdot R_{th} \cdot \gamma_{wz} \cdot \gamma_c} < 1, \qquad (11)$$

where F is the load on the welds; k_f - angular seam roll, $k_f \leq 1{,}2 t_{min}$ (t_{min} - thickness of the thinnest of the welded elements); l_w - the calculated length of the seam, it is taken to be less than its full length by 1 cm; R_{th} is the calculated resistance of the oblique flange material across the rolled products, $R_{th}=0{,}5R_{y,fl}$.

Supporting slats (support tables) of oblique flanges are advisable to take in 1.5 ... 2 times thinner than flanges [19]:

$$t_{cr} = \frac{t_{fl}}{(1.5 \ldots 2)}. \qquad (12)$$

The support bar is welded to the oblique flange by one-sided angular seams along its three edges, and the fourth edge is milled to ensure a tight contact in the assembled joint for the transmission and perception of the tangent component T. Checking the welds is as follows:

- on the metal of the seam

$$\frac{T}{\beta_f \cdot k_f \cdot l_w \cdot R_{wf} \cdot \gamma_{wf} \cdot \gamma_c} < 1; \qquad (13)$$

- on metal fusion boundaries with flange

$$\frac{T}{\beta_z \cdot k_f \cdot l_w \cdot R_{wz} \cdot \gamma_{wz} \cdot \gamma_c} < 1, \qquad (14)$$

where T is the load on the welds; k_f - angular seam cathlete, $k_f \leq 1.2t_{min}$; l_w - the calculated length of the seam, is taken to be less than its full length by 1cm.

The support bars (support tables) of oblique flanges must also be checked by calculation of the crumpled strength condition:

$$\frac{T}{b_{cr} \cdot t_{cr} \cdot R_p} \leq 1, \qquad (15)$$

where b_{cr} is the width of the support bar in the contact zone (crumple); R_p is the calculated resistance of the steel to the crumpling of the end surface.

The Q_{loc} transverse force in the assembled joint is transmitted through an additional fastening between the lining of the truss lattice rod with a thickness *of* t_k *and the* support bars of the oblique flanges on two bolts, under the conditions of unification of the same flanges as the bolts. They can be installed without prior tension, so the additional bolted connection must be checked by calculation from the strength conditions:

- per slice

$$\frac{Q_{loc}}{N_{bs} \cdot n_b} \leq 1; \qquad (16)$$

- On Confusion

$$\frac{Q_{loc}}{N_{bp} \cdot n_b} \leq 1, \qquad (17)$$

wherein N_{bs} and N_{bp} are the design forces that can be perceived by a single bolt respectively per cut and crumpled; n_b is the number of bolts in the connection, n_b=2.

The necessary and sufficient reserve of bearing capacity of bolted joints of stretched rod elements with oblique flanges was confirmed by the results of a trial (control) series of studies of prototypes conducted in the construction laboratory of Pyatigorsk State Technological University (Fig. 4). The breaking forces of the prototypes exceeded the level of design loads of 1.7... 2.5 times, and the experimental and calculated deformations had a fairly acceptable convergence. Experimental deformations were determined from the readings of mechanical indicators in the direction of action of longitudinal forces in the rod elements (Fig. 5). The calculated deformations were calculated as the total deflection of two oblique flanges in the projection on the longitudinal axis of the prototype:

$$\Delta = \frac{2f_{fl,max}}{sin30^\circ} = 4f_{fl,max} \qquad (18)$$

where $f_{fl,max}$ is the deflection of one flange defined by the formula (8).

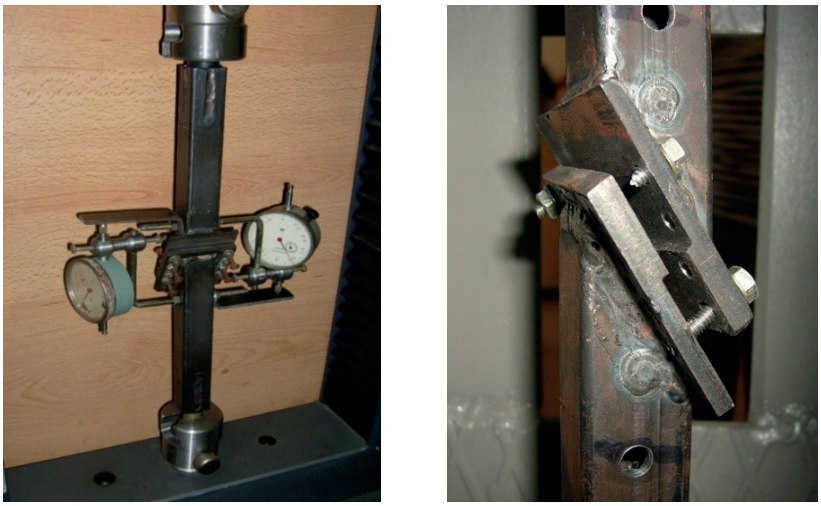

a *b*

Figure 4. Pictures of experimental studies of prototypes of mounting joints on oblique flanges: a - general view; b - type of bolted joints after rupture

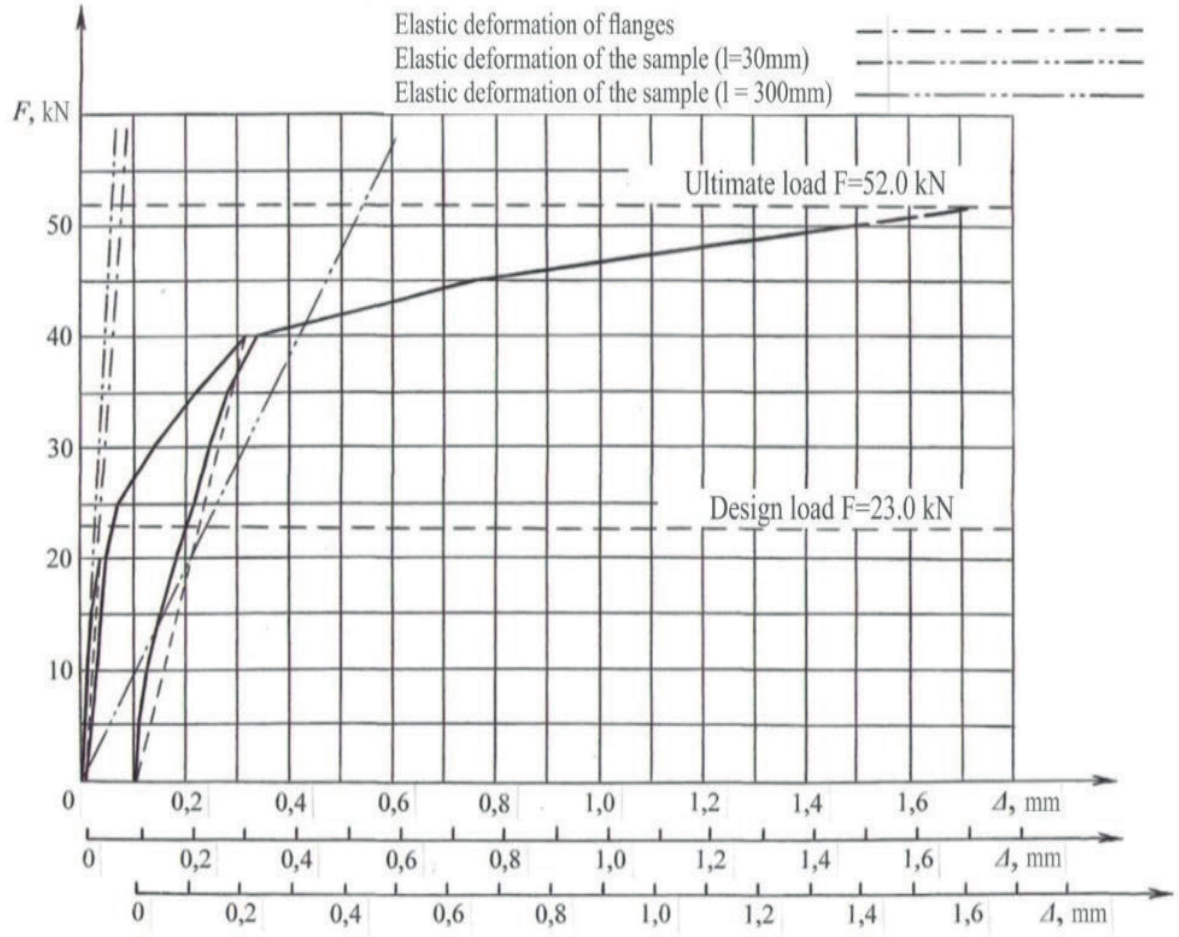

Figure 5. Stretch diagram of one of the prototypes of butt bolt joints of rod elements with oblique flanges, built on average readings of two mechanical indicators

RESULTS AND DISCUTION

Summarizing the results of the first series of tests given in Chart 1, we can conclude that butt joints on oblique flanges are not only equally strong with rod elements, but are also quite suitable for use in load-bearing structures of buildings and structures. In the future, it is planned to continue testing and experimental studies of bolted joints on oblique flanges, combining them with a laboratory workshop on metal structures as part of the educational process for the training and advanced training of civil engineers, for which a corresponding installation with a capacity (load capacity) of 50 tons has already been manufactured and tested (Figure 6).

To compare the proposed (new) technical solution with the known one, a standard assembly connection on the flanges of roof trusses from bent-welded closed profiles of the Molodechno system was taken as the base object [12]. The material consumption of the compared options is shown in Chart 2, from which it can be seen that in the new solution it decreased by 54.7 / 26.8 = 2.04 times.

In addition, here it is necessary to take into account the consumption of material for the tie bolts. In the known and proposed flange connections, the number of coupling bolts is the same and is 8 pcs. If the first of them uses M24 bolts, then the second uses M18 bolts of the same strength class. Then it is obvious that in the new solution the material consumption is reduced in proportion to the decrease in the "net" cross-sectional area of the bolt, that is, by 3.52/1.92=1.83 times.

Table 1. Results of the Pilot Test Series of Prototype Studies

Parameters of prototypes (steel C235)					
№	Cross-section of rod elements, mm	Thickness, mm		Bolted connections	
		Flanges	Tables	diameter, mm	class
1	2	3	4	5	6
1	□25×25×1,5 GOST 8369-68	4	2	M4	5.8
2	□25×25×1,5 GOST 8369-68	4	2	M4	5.8
3	□25×25×1,5 GOST 8369-68	4	2	M5	5.8

Bearing capacity, kN							
№	Calculated				Experimental		
	core elements	oblique flanges	support tables	bolted connections	the cause of the destruction of the prototype	the ultimate in case of destruction	experiment. Calculation
1	7	8	9	10	11	12	13
1	32,5	24,7	40,4	23,0	*Machine power	*40,0	*1,74
2	32,5	24,7	40,4	23,0	bolt break	52,0	2,26
3	32,5	24,7	40,4	40,2	bending of flanges	62,0	2,51

№	Deformations, mm					
	from design loads			from the maximum loads		
	Calculation	experiment.	experiment. Calculation	Calculation	experiment.	experiment. Calculation
1	14	15	16	17	18	19
1	0,035	0,044; 0,039	1,26; 1,12	0,060	1,14	19,0
2	0,035	0,052; 0,047	1,49; 1,34	0,078	1,61	20,7
3	0,037	0,061; 0,058	1,65; 1,57	0,093	2,07	22,3

Table 2. Consumption of structural material (steel)

Name	Dimensions, mm	Amount, pcs.	Weight, kg			Notes
			1 pc.	All	Joint	
Straight flange	300×300×30	2	21,2	42,4	54,7	Notable solution
Stiffening rib	140×110×8	8	0,5*	4,0		
Connecting gasket	400×300×8	1	7,5	7,5		
Welds (1.5%)				0,8		
Oblique flange	300×250×18	2	10,6	21,2	26,8	New Solution
Support table	270×150×8	2	2,6	5,2		
Welds (1.5%)				0,4		
* Triangular shape taken into account						

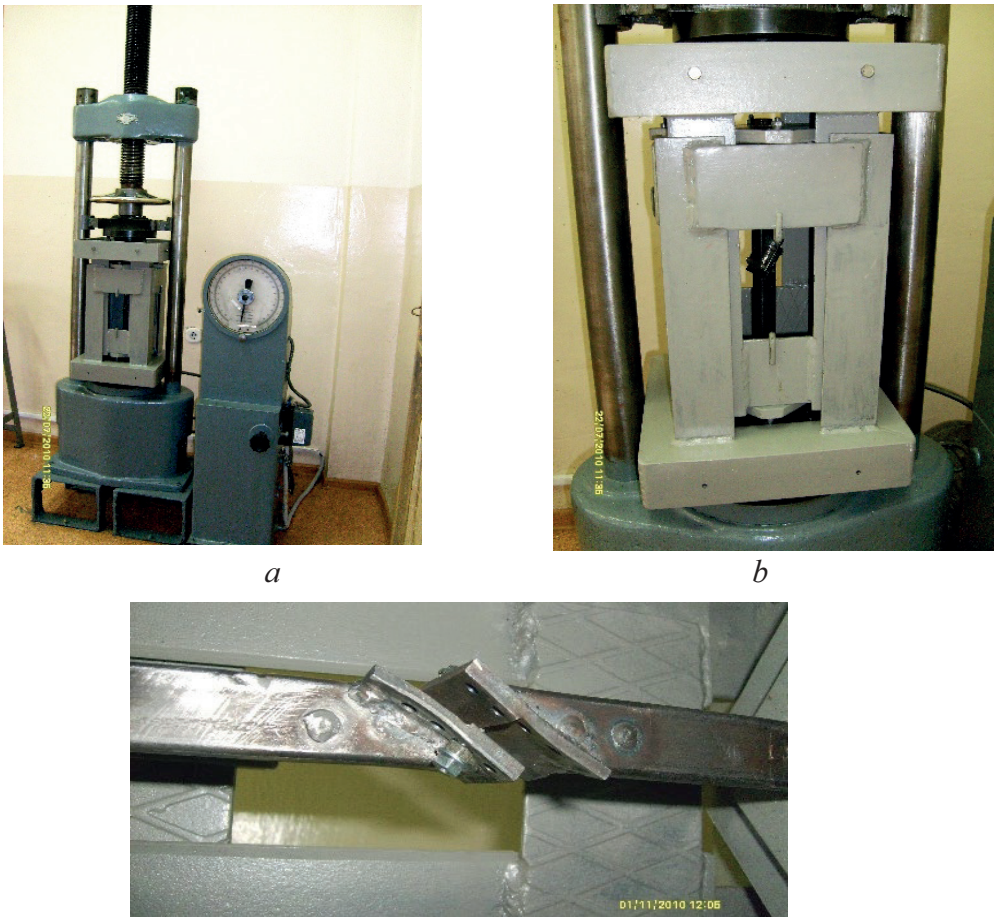

a *b* *c*

Figure 6. Pictures of a general view of the test facility (a), its reverse part (b) and a prototype after destruction due to bending of oblique flanges (c)

CONCLUSION

Thus, the development of butt bolted joints of bar elements with oblique flanges, their calculation and the results of experimental studies of the first (trial) series of prototypes make it possible to recommend for implementation in construction practice and draw a number of main conclusions.

1. Bolted joints on oblique flanges have the necessary and sufficient margin of bearing capacity, which ensures their equal strength with the connected rod elements.
2. The engineering method for calculating bolted connections on oblique flanges is quite simple and correct for use in building design.
3. Butt bolted joints of rod elements with oblique flanges under the action of tensile forces significantly reduce the consumption of structural material compared to straight flanges, which predetermines the prospects for their use in load-bearing structures of buildings and structures.
4. It is advisable to continue experimental studies of bolted joints on oblique flanges and combine them with a laboratory workshop on metal structures as part of the educational process of training and advanced training of civil engineers.

REFERENCES

1. **Kuznetsova V.V.** (1998) Soedineniya [Connections]. *Metallicheskiye konstruktsii* **[**Metal structures], In 3 vols. T. 1. General part. Moscow, Publishing office ASV, pp. 179–204. (in Russian).

2. **Kharlanov V.L., Kharlanova S.V.** (2021) Metody fiktivnych reaksiy v modelirovanii kontaktnoy poverkhtnosty na primere flantsevich soyedineniy [Method of fictitious reactions in the modeling of the contact surface on the example of flanged connections]. *Stroitelnaya mechanika i raschet sooruzheniy* (electronic journal) [Structural mechanics and calculation of structures], no 2, pp. 73–78. (in Russian).
3. **Son M.P.** (2018) Eksperimentalnye issledovaniya prochnosti flantsevykh soyedineniy [Experimental studies of the strength of flange joints]. *Stroitel'naya mekhanika inzhenernykh konstruktsiy i sooruzheniy* (electronic journal) [Structural mechanics of engineering structures and structures], no. 4, pp. 344–355. (in Russian).
4. **Kriksunov E.Z., Perelmuter A.V., Yurchenko V.V.** (2010) Raschetnye modeli flantsevykh soyedineniy ramnykh uzlov metallicheskikh konstruktsiy i ikh programmnaya realizatsiya v SCAD Office [Calculation models of flange connections of frame units of metal structures and their software implementation in SCAD Office]. *Byulleten stroitelnoy tekhniki* (electronic journal) [Bulletin of construction equipment], no. 1, pp. 56–59. (in Russian).
5. **Mohamed Elflah, Marios Theofanous, Samir Dirar, Huanxin Yuan.** (2019) Behavior of stainless steel beam-to-column joints – Part 1: Experimental investigation, *Journal of Constructional Steel Research 152*, pp. 183–193.
6. **H.X. Yuan, S. Hua, X.X. Dua, L. Yangb, X.Y. Cheng, M. Theofanous.** (2019) Experimental behavior of stainless steel bolted T-stub connections under monotonic loading, *Journal of Constructional Steel Research 152*, pp. 213–224.
7. **Tchabremane Jean de la Croix Kombate, Kıvanç Tas¸kın.** (2022) State-of-the-art review on the behaviour of T-stubs and prying action, *Journal of Constructional Steel Research 191*, 107203.
8. **Yasin Onuralp Ozkılıc.** (2021) The capacities of unstiffened T-stubs with thin plates and large bolts, *Journal of Constructional Steel Research 186*, 106908.
9. **Kuznetcova V.V.** (1998) Stalnye konstruktsii zdaniy i sooruzheniy [In Steel structures of buildings and structures]. *Metallicheskiye konstruktsii* [Metal structures]. Moscow, Publishing office ACB, pp. 157, pic. 7.6, б. (in Russian).
10. **Goreva V.V.** (2001) Elementy konstruktsiy [Structural elements]. *Metallicheskiye konstruktsii* [Metal structures], In 3 vols. T. 1. Moscow, Higher School, Page 462. (in Russian).
11. **Marutyan A.S., Pershin I.M., Pavlenko Yu.I.** (2011) Flantsevoye soyedineniye rastyanutykh elementov zamknutogo profilya [Flange connection of tensioned elements of a closed profile], Application No. 2009139553/03 (056081), 10/26/2009, Patent No. 2413820. - 10.03.2011. Bull. No. 7. (in Russian).
12. **Marutyan A.S., Kobaliya T.L., Glukhov S.A., Yanukyan G.M., Pavlenko Yu.I.** (2011) Pyatiugolniy zamknutiy gnutosvarnoy profil [Pentagonal closed bent-welded profile], Application No. 2009147247/03(067318), 12/18/2009. - Patent No. 104582. - 05/20/2011. Bull. No. 14. (in Russian).
13. **Marutyan A.S., Glukhov S.A., Pavlenko Yu.I.**(2010) Pyatiugolniy zamknutiy gnutosvarnoy profil [Pentagonal closed bend-welded profiles]. *Stroitelnaya mekhanika i raschet sooruzheniy* [Structural mechanics and calculation of structures], No. 5, pp. 53–57. (in Russian).
14. **Kudishin. Yu. I.** (2007) *Metallicheskiye konstruktsii: Uchebnik dlya vuzov* [Metal structures: textbook for universities]. Moscow, Academy, p. 296. (in Russian).
15. **Sakhnovsky M.M.** (1984) *Legkiye konstruktsii stalnykh karkasov zdaniy i sooruzheniy* [Lightweight steel frame structures for buildings and structures]. Kyiv, Budivelnik, pp. 68-70. (in Russian).

16. **Marutyan A.S.** (2006) *Proyektirovaniye stalnykh ferm pokrytiy* [Design of steel roof trusses], Pyatigorsk: PSTU, p. 60. (in Russian).
17. **Pisarenko G.S. (1988)** *Spravochnik po soprotivleniyu materialov* [Handbook of the strength of materials]. Kyiv, Naukova Dumka, pp. 346-347. CM drawings. See folio 44. (in Russian).
18. **Marutyan A.S.** (2010) *Kursovoye i eksperimentalnoye proyektirovaniye stalnykh ferm pokrytiy* [Course and experimental design of steel roof trusses], Pyatigorsk: PSTU, pp. 112. (in Russian).
19. **Stalnyye konstruktsii pokrytiy proizvodstvennykh zdaniy proletami 18, 24, 30 m** s primeneniyem zamknutykh gnutosvarnykh profiley pryamougol'nogo secheniya tipa «Molodechno» [Steel structures of the roofs of industrial buildings with spans of 18, 24, 30 m using closed bent-welded profiles of rectangular section of the Molodechno type]. Series 1.460.3-14. KM drawings. Pp. 44 (in Russian).

СПИСОК ЛИТЕРАТУРЫ

1. **В.В. Кузнецова.** Металлические конструкции. В 3 т. Т. 1. Общая часть. – М.: Изд-во АСВ, 1998. – С. 179–204.
2. **Харланов В.Л., Харланова С.В.** Метод фиктивных реакций в моделировании контактной поверхности на примере фланцевых соединений. – Строительная механика и расчет сооружений, 2021, № 2. – С. 73–78.
3. **Сон М.П.** Экспериментальные исследования прочности фланцевых соединений. – Строительная механика инженерных конструкций и сооружений, 2018, № 4. – С. 344–355.
4. **Криксунов Э.З., Перельмутер А.В., Юрченко В.В.** Расчетные модели фланцевых соединений рамных узлов металлических конструкций и их программная реализация в SCAD Office. – Бюллетень строительной техники, 2010, № 1. – С. 56–59.
5. **Mohamed Elflah, Marios Theofanous, Samir Dirar, Huanxin Yuan.** Behaviour of stainless steel beam-to-column joints – Part 1: Experimental investigation. – Journal of Constructional Steel Research 152 (2019) – Pp. 183–193.
6. **H.X. Yuan, S. Hua, X.X. Dua, L. Yangb, X.Y. Cheng, M. Theofanous.** Experimental behaviour of stainless steel bolted T-stub connections under monotonic loading. – Journal of Constructional Steel Research 152 (2019) – Pp. 213–224.
7. **Tchabremane Jean de la Croix Kombate, Kıvanç Tas¸kın.** State-of-the-art review on the behaviour of T-stubs and prying action. – Journal of Constructional Steel Research 191 (2022) 107203.
8. **Yasin Onuralp Ozkılıc.**The capacities of unstiffened T-stubs with thin plates and large bolts. – Journal of Constructional Steel Research 186 (2021) 106908.
9. **В.В. Кузнецова.** Металлические конструкции. В 3 т. Т. 2. Стальные конструкции зданий и сооружений. – М.: Изд-во АСВ, 1998. – С. 157, рис. 7.6, б
10. **В.В. Горева.** Металлические конструкции. В 3 т. Т. 1. Элементы конструкций. – М.: Высшая школа, 2001. – С. 462.
11. **Марутян А.С., Першин И.М., Павленко Ю.И.** Фланцевое соединение растянутых элементов замкнутого профиля. – Заявка № 2009139553/03 (056081), 26.10.2009. – Патент № 2413820. – 10.03.2011. Бюл. № 7.
12. **Марутян А.С., Кобалия Т.Л., Глухов С.А., Янукян Г.М., Павленко Ю.И**. Пятиугольный замкнутый гнутосварной профиль. – Заявка № 2009147247/03(067318), 18.12.2009. – Патент № 104582. – 20.05.2011. Бюл. № 14.
13. **Марутян А.С., Глухов С.А., Павленко Ю.И.** Пятиугольные замкнутые гнутосварные профили. – Строительная

механика и расчет сооружений, 2010, № 5. – С. 53–57.
14. **Ю.И. Кудишина.** Металлические конструкции: Учеб. для вузов. – М.: Академия, 2007. – С. 296.
15. **Сахновский М.М.** Легкие конструкции стальных каркасов зданий и сооружений. – Киев: Будивельник, 1984. – С. 68–70.
16. **Марутян А.С.** Проектирование стальных ферм покрытий. – Пятигорск: ПГТУ, 2006. – 60 с.
17. Справочник по сопротивлению материалов / Отв. ред. Писаренко Г.С. – Киев: Наукова думка, 1988. – С. 346-347.
18. **Марутян А.С.** Курсовое и экспериментальное проектирование стальных ферм покрытий. – Пятигорск: ПГТУ, 2010. – 112 с.
19. **Стальные конструкции покрытий производственных зданий пролетами 18, 24, 30 м** с применением замкнутых гнутосварных профилей прямоугольного сечения типа «Молодечно». Серия 1.460.3-14. Чертежи КМ. Лист 44.

Alexander Surenovich Marutyan, Candidate of Technical Sciences, Associate Professor, Leading Researcher of the Department of project and grant activities, Branch of the North Caucasus Federal University; 56, 40 years of October Avenue, Pyatigorsk, 357538, Russia; E-mail: abovyan_1958@mail.ru, 0000-0001-5464-5929.

Avetik Gurgenovich Abovyan, Candidate of Technical, Associate Professor, Department of wood and metal structures, Moscow State University of Civil Engineering (National Research University) (MGSU); 129337, 26, Yaroslavskoe shosse, Moscow, 129337, Russia; E-mail: abovyan_1958@mail.ru; 0000-0002-6005-2465.

Александр Суренович Марутян, кандидат технических наук, доцент, ведущий научный сотрудник отдела проектно-грантовой деятельности, филиал Северо-Кавказского Федерального Университета; 357538, Россия, г. Пятигорск, ул. 40 лет Октября, д. 56; E-mail: abovyan_1958@mail.ru; 0000-0001-5464-5929.

Аветик Гургенович Абовян, кандидат Технических Наук, доцент, кафедра металлических и деревянных конструкций Национального исследовательского Московского государственного строительного университета (НИУ МГСУ); 129337, Россия, г. Москва, Ярославское шоссе д. 26; E-mail: abovyan_1958@mail.ru; 0000-0002-6005-2465.

International Journal for Computational Civil and Structural Engineering, 19(1) 124–134 (2023)

DOI:10.22337/2587-9618-2023-19-1-124-134

NUMERICAL SIMULATION OF OSCILLATIONS OF A PLATE IN RESTING FLUID

Irina Yu. Negrozova, Oleg S. Goryachevsky

National Research Moscow State University of Civil Engineering, Moscow, RUSSIA
Scientific Research Center StaDyO, Moscow, RUSSIA

Abstract: This paper presents a numerical solution of the problem of oscillations of a flexible plate placed in a viscous incompressible fluid done with ANSYS. In constructing a finite element model of the plate, both volumetric and shell finite elements, which are more commonly used in engineering applications, are considered. By way of example it is shown that it is possible to transition from a volumetric mesh to a shell mesh without loss of accuracy in solving this problem and similar problems. The considered coupled approach to solving the problem for the shell plate mesh has an important practical application in solving real-world problems of aeroelasticity, because in engineering practice it is much more convenient to represent structures and constructions in the form of beam and shell models. The solution of this problem is of particular importance for the verification of techniques of numerical modelling of coupled aeroelasticity problems.

Keywords: numerical simulation, coupled problem, FSI, contact, numerical damping

ЧИСЛЕННОЕ МОДЕЛИРОВАНИЕ ЗАДАЧИ О СВОБОДНЫХ КОЛЕБАНИЯХ ГИБКОЙ ПЛАСТИНЫ, ПОМЕЩЕННОЙ В ВЯЗКУЮ НЕСЖИМАЕМУЮ ЖИДКОСТЬ

И.Ю. Негрозова, О.С. Горячевский

Национальный исследовательский Московский государственный строительный университет, г. Москва, РОССИЯ
Научно-исследовательский центр СтаДиО, г. Москва, РОССИЯ

Аннотация: В настоящей работе представлено численное решение задачи о свободных колебаниях гибкой пластины, помещенной в вязкую несжимаемую жидкость, с использованием программного комплекса ANSYS. При построении конечноэлементной модели пластины рассматривались как объемные, так и чаще применяемые в инженерных приложениях оболочечные типы конечных элементов. На примере показана возможность перехода от объемной модели к оболочечной без потери точности при решении подобных задач. Рассмотренный подход при решении задачи в связанной постановке для оболочечной модели пластины имеет практически важное применение к решению реальных задач аэроупругости, так как в инженерной практике конструкции и сооружения существенно удобнее представлять в виде оболочечно-стержневых моделей. Решение данной задачи имеет отдельную значимость для верификации методик численного решения связанных задач аэроупругости.

Ключевые слова: численное моделирование, связанная задача, FSI, контактное взаимодействие, численное демпфирование

1. INTRODUCTION

The interaction of structures with fluid or gas plays an important role in many construction problems. Besides suspension bridges, aeroelasticity has to be considered in wind impact analysis for structures of high-rise buildings, towers, oil platforms, and lightweight membrane coverings used in large-span structures.

The fluid-structure interaction analysis has been implemented in ANSYS since version 10.0. The CFD part can be solved with either ANSYS CFX or ANSYS Fluent, and ANSYS

Mechanical is used for stress-strain analysis. The coupling between codes is configured in ANSYS Workbench using System Coupling module. This tool is convenient for solving coupled aeroelasticity problems, but there are some limitations. At the contact between fluid and structure an interface is specified to transfer data from one module to another. In order to set such an interface, both the geometry must match and a shared surface between fluid and structure must exist. Therefore, Solid type volumetric finite elements are commonly used for aeroelasticity problems in ANSYS. However, in practical applications, most building structures are calculated using beam and shell models. Such models have smaller dimensionality and are considerably easier to create than volumetric models. For these reasons, a technique needs to be developed and verified that will allow solving the aeroelasticity problems with any type of finite elements in ANSYS.

The problem of oscillations of a plate referenced in [1] was chosen for the verification. In that paper, the problem was solved using the authors' own code. The problem is also presented in [2-4]. In [2-3] it is solved with authors' own code, too, and in [4] it is solved with ANSYS using volumetric finite elements.

In this paper, the problem is solved with ANSYS Workbench (Mechanical + Fluent).

2. PROBLEM STATEMENT

A thin flexible plate of length L = 1.0 m and width W = 0.4 m with the fixed bottom edge is considered [1]. A load in form of evenly distributed pressure p = 75 Pa is applied on the plate for 0.5 s, then removed in 0.01 s so that the plate starts to vibrate (Fig. 1).

The thickness of flexible plate d_s = 0.06 m, modulus of elasticity E = 2.5 MPa, Poisson's ratio ν = 0.35, material density ρ_s = 2550 kg/m^3. The density of the fluid is assumed to be ρ ρ_f = 1 kg/m^3. In [1] 3 values of dynamic viscosity were considered: $\mu_{f,1}$ = 0.2 Pa·s, $\mu_{f,2}$ = 1.0 Pa·s, $\mu_{f,3}$ = 5.0 Pa·s. In this paper, only one value of the dynamic viscosity $\mu_{f,1}$ will be considered.

The computational domain is 20.06 × 6 × 0.4 m.

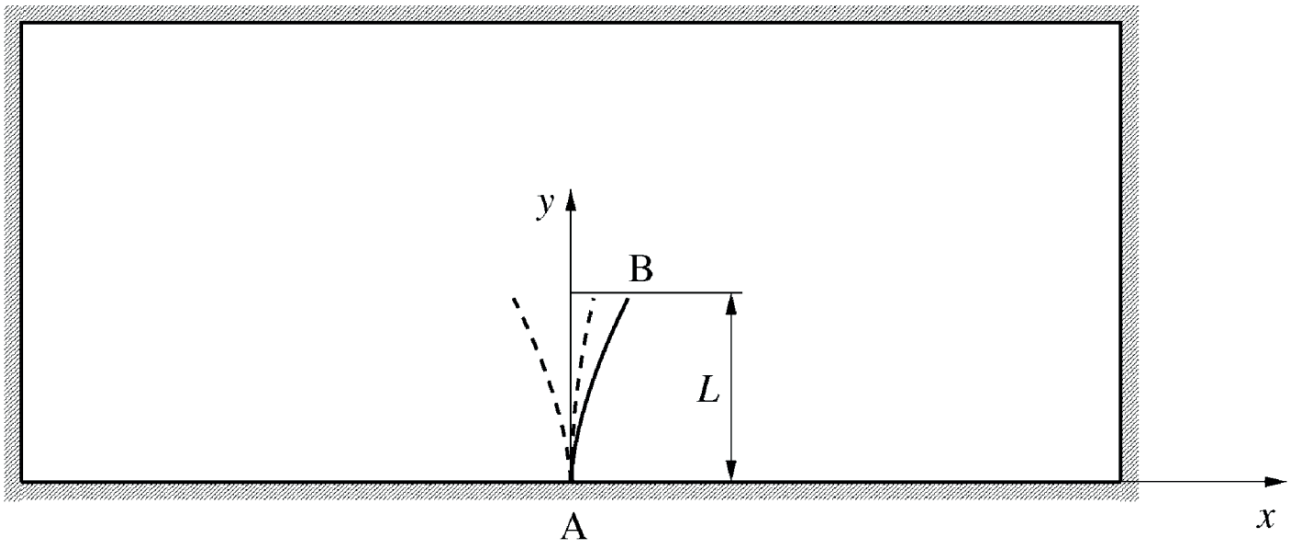

Figure 1. Oscillations of a plate problem geometry

3. COMPUTATIONAL MODELS

3.1. Computational models of the flexible plate

In this example, a volumetric and a shell type of the plate geometry will be considered (Fig. 2).
For the volumetric geometry, 3 types of grids will be considered to evaluate mesh convergence and select the optimum mesh. For the shell geometry, 1 type will be considered (Table 1, Fig. 3).

Table 1. Finite-element meshes parameters

	Nodes	Elements	FE type
Model 1	15 777	3 000	SOLID186
Model 2	826 665	192 000	SOLID186
Model 3	7 353	1 000	SOLID186
Model 4	1 071	1 000	SHELL181

3.2. Computational model of viscous incompressible fluid

The computational domain has been partitioned into a structured computational mesh with inflation on the walls (Fig. 4).
Since the Reynolds number for the problem is $Re \ll 100$, the flow is laminar, and turbulence models are not used in the calculations.
Due to weakly pronounced three-dimensional effects occurring along the plate ends, the problem was solved in the quasi-dimensional formulation (one FE in the ***Z*** direction), as in [1].

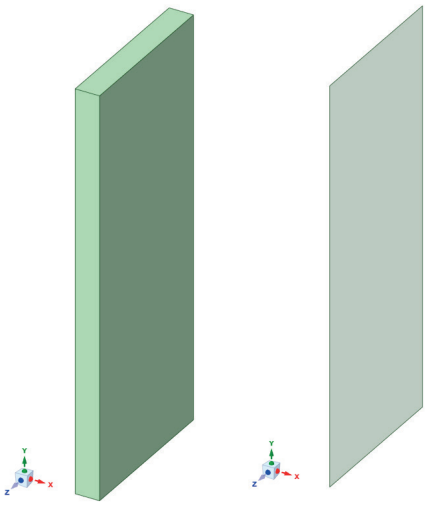

Volumetric type *Shell type*

Figure 2. Geometry types of the plate

Boundary conditions

On the side faces, parallel to the plane ***xy***, the *Symmetry* conditions were set. The *No-Slip Wall* condition (***U***=***V***=***W***=0 m/s) was specified for the rest of the faces.

Initial conditions

Zero velocity (***U***=***V***=***W***=0 m/s) and zero relative pressure were set as initial conditions.

4. RESULTS OF MODAL ANALYSIS

The first 6 eigenfrequencies and eigenmodes were determined for all computational models. The obtained results are presented in Table 2.

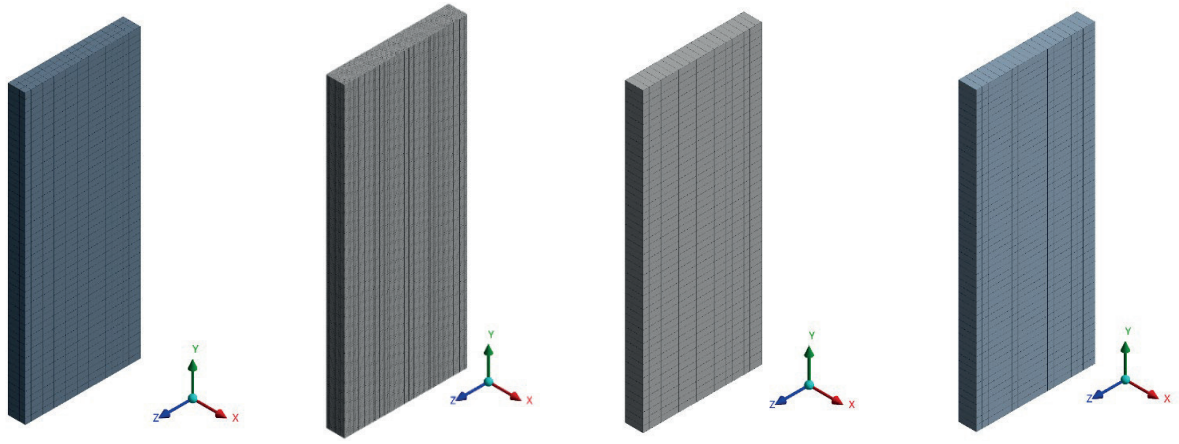

Model 1 *Model 2* *Model 3* *Model 4*

Figure 3. Finite-element meshes of the flexible plate

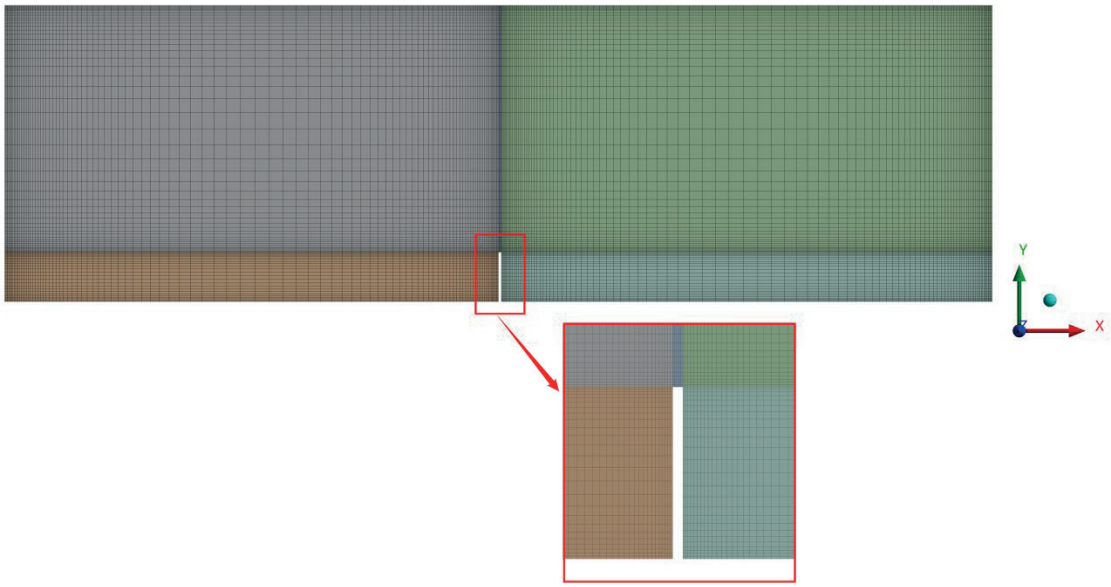

Figure 4. Finite-volume mesh of the viscous incompressible fluid (32 632 cells)

Table 2. Computed eigenfrequencies (Hz) for all models in comparison with the reference (Ref. [1])

Mode of vibration	*Ref. []*	*Model 1*		*Model 2*		*Model 3*		*Model 4*	
		f_i, Hz	$\varepsilon(f_i)$, %	f_i, Hz	$\varepsilon(f_i)$, %	f_i, Hz	$\varepsilon(f_i)$, %	f_i, Hz	$\varepsilon(f_i)$, %
1. Bending (*xy*)	0.31	0.3108	0.26	0.3106	0.19	0.3112	0.39	0.31	0.01
2. Torsional	-	1.4947	-	1.4939	-	1.5035	-	1.4952	-
3. Bending (*yz*)	-	1.8243	-	1.8233	-	1.8242	-	1.8191	-
4. Bending (*xy*)	1.85	1.9071	3.09	1.9056	3.01	1.9124	3.37	1.9032	2.28
5. Torsional	-	4.7159	-	4.7131	-	4.7493	-	4.7179	-
6. Bending (*xy*)	4.93	5.2162	5.81	5.2116	5.71	5.2430	6.35	5.2101	5.68

As can be seen from Table 2, the discrepancy between current results and [1] does not exceed 6.35% (*Model 3*). For further related calculations using the volumetric plate model, *Model 1* will be used since the error between this model and *Model 2* is at most 0.1%, with *Model 1* containing less nodes.

5. SOLVING A PROBLEM IN A COUPLED FORMULATION

To ensure convergence and stability of solution at each timestep, it is necessary to specify the maximum number of iterations at each timestep and the convergence criterion for loads and displacements. For this problem, 5 maximum iterations at each coupled FSI timestep were set and the convergence criterion for the loads and displacements was set to 10^{-3}. The equations of motion of the plate are solved with the Newmark method, and the total physical time is 50 s.

5.1. Coupled solution using a volumetric plate model

Results of the coupled analysis in comparison with the results of [1] are shown in figures 5 to 6. The timesteps are $\Delta t_1 = 0.1$s and $\Delta t_2 = 0.01$s.

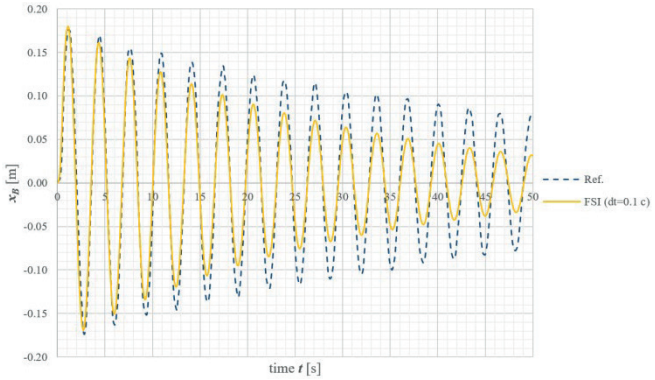

Displacement of the free edge of the oscillating plate in x direction [m]

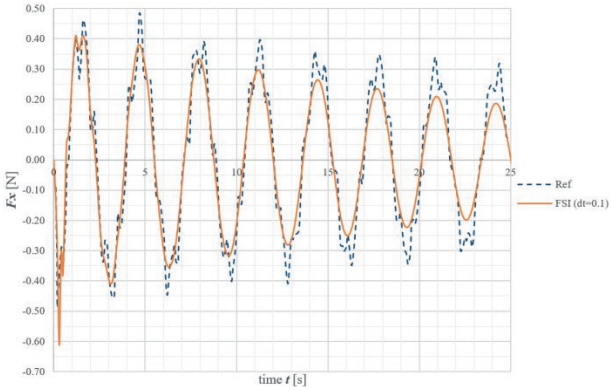

Drag force F_x [N]

Figure 5. Comparison of the simulation results (Δt_1 =0.1 s) with the reference [1]

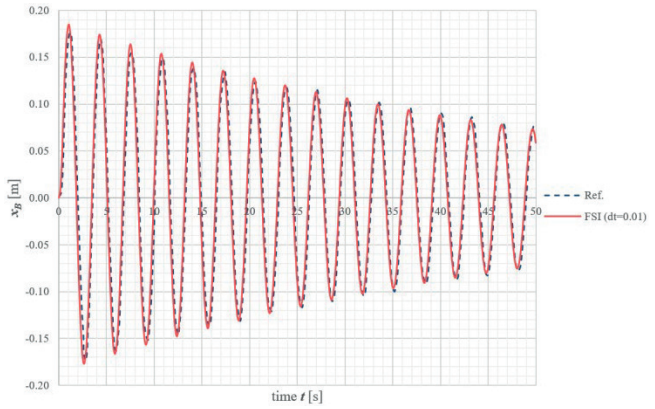

Displacement of the free edge of the oscillating plate in x direction [m]

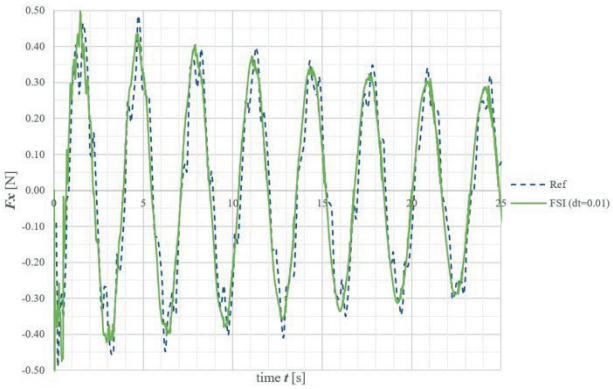

Drag force F_x [N]

Figure 6. Comparison of the simulation results (Δt_2 =0.01 c) with the reference [1]

In the ANSYS Workbench Transient Structural module a numerical damping value is utilized to stabilize the scheme of numerical integration of equations of motion by damping high-frequency modes [5]. By default, it equals 0.1.

For the Newmark's method, if the parameters α, δ satisfy the conditions:

$$\delta \geq \frac{1}{2} \tag{1}$$

$$\alpha \geq \frac{1}{4}\left(\frac{1}{2} + \delta\right)^2 \tag{2}$$

then it can be unconditionally stable [5]. If the above conditions are not satisfied, the additional amplitude damping ratio γ is introduced into the equations:

$$\delta = \frac{1}{2} + \gamma \tag{3}$$

$$\alpha = \frac{1}{4}(1 + \gamma)^2 \tag{4}$$

$$\gamma \geq 0 \tag{5}$$

While the amplitude damping ratio γ allows to make the integration procedure stable, it affects the resulting solution.

The results of the calculations are presented below. It can be seen that for Δt_1 =0.1 c a rapid damping of the plate vibration is obtained, but the reduction of the timestep (Δt_2 =0.01 c) gets rid of it.

Since reducing the timestep increases the computation time, it is necessary to minimize

the effect of numerical damping. In order to achieve that, calculations at Δt_1 =0.1 with different numerical damping values (*ND1* = 0.05, *ND2* = 0.01, *ND3* = 0.005) were performed. The results of the coupled analysis in comparison with the results of [1] are shown in Fig 7. As it can be seen, reducing the numerical damping value allows to approach the solution referenced in [1].

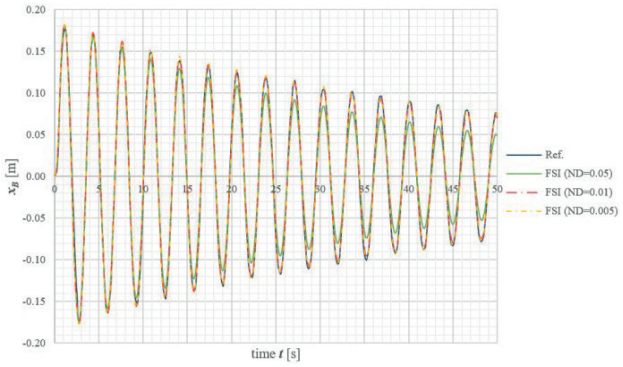

Displacement of the free edge of the oscillating plate in x direction [m]

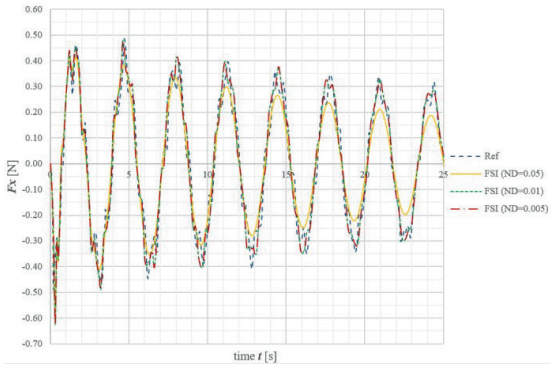

Drag force F_x [N]

Figure 7. Comparison of the simulation results at Δt_1 =0.1 s for different numerical damping values (ND_1=0.05, ND_2=0.01, ND_3=0.005) with the reference [1]

5.2. Coupled solution using a shell plate model

The next step in solving this problem was the transition from the volumetric plate model to the shell model. However, a problem arises in the assignment of the interface between the fluid and the plate due to some limitations: as pointed out before, the geometries where contact occurs must coincide. To circumvent this, a dummy surface was created at the fluid-structure boundary (Fig. 8), which served as an interface to transfer data from one module to another.

In order for the flexible plate and the dummy surface to work together, a Bonded type contact was established between them, in which no separation or sliding between the faces was allowed. This type of contact is linear and is calculated in one iteration. Multi-point constraints were used for the interface which is a form of Lagrange multipliers method. The algorithms used did not significantly increase the number of iterations and the counting time.

Model 4 was chosen for the plate.

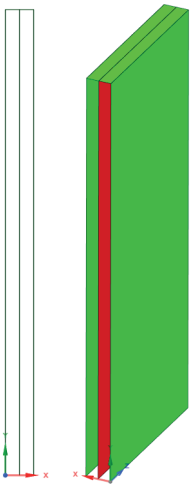

Figure 8. Geometry of the flexible plate (red) with the dummy surfaces (green) acting as interfaces to the fluid domain

The dummy surface was modelled with a *Shell181* FE. Three models of a flexible plate with the dummy surface were considered with differing thickness:

- *Model A*: 1 mm;
- *Model B*: 0.1 mm;
- *Model C*: 0.01 mm.

The material of the dummy surface corresponds to that of the flexible plate.
In order to ensure similar behaviour of the flexible plate with and without the dummy surface, a modal analysis was performed for *Models A, B, C.*

Results of the modal analysis

The results of calculations versus the results of modal analysis for *Model 4* are presented in Table 3 and Figs. 9-14.
It can be seen from the results that *Model A* shows a different behaviour from *Model 4*. A significant difference is seen not only in the eigenfrequencies (up to 21.47% for mode 2), but also in the eigenmodes (2 and 3). For *Model B* and *Model C* the eigenmodes correspond to *Model 4*, and the maximum error in the eigenfrequencies is observed in the mode 2 (3.14% for *Model B*, 0.33% for *Model C*). Therefore, *Model B* and *Model C* have been chosen for the coupled calculations.
Fig. 15 shows the results of the coupled analysis compared to the results of [1] for *Model B*. The time step size is Δt = 0.1 s and the numerical damping coefficient is 0.005.
No results were obtained for *Model C* due to the strong distortion of the dummy surface grid caused by the small thickness of the shell.

Table 3. Computed eigenfrequencies (Hz) for all models

Mode of vibration	*Model 4*	*Model A*		*Model B*		*Model C*	
		f_i, Hz	$\varepsilon(f_i)$, %	f_i, Hz	$\varepsilon(f_i)$, %	f_i, Hz	$\varepsilon(f_i)$, %
1	0.31	0.3049	1.65	0.3095	0.16	0.31	0
2	1.495	1.816	21.47	1.542	3.14	1.5	0.33
3	1.819	1.8482	1.61	1.8188	0.01	1.8191	0.01
4	1.903	1.8701	1.73	1.8997	0.17	1.9029	0.01
5	4.718	4.8284	2.34	4.7298	0.25	4.7191	0.02
6	5.210	5.1205	1.72	5.2009	0.17	5.2092	0.02

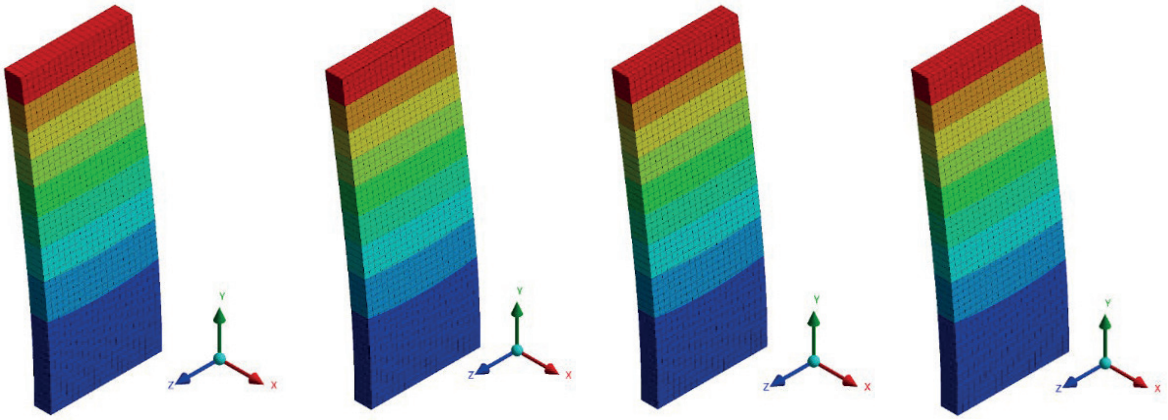

Model 4 (f_1 = 0.31 Hz) | *Model A* (f_1 = 0.3049 Hz) | *Model B* (f_1 = 0.3095 Hz) | *Model C* (f_1 = 0.31 Hz)

Figure 9. Eigenmodes and eigenfrequencies (mode 1)

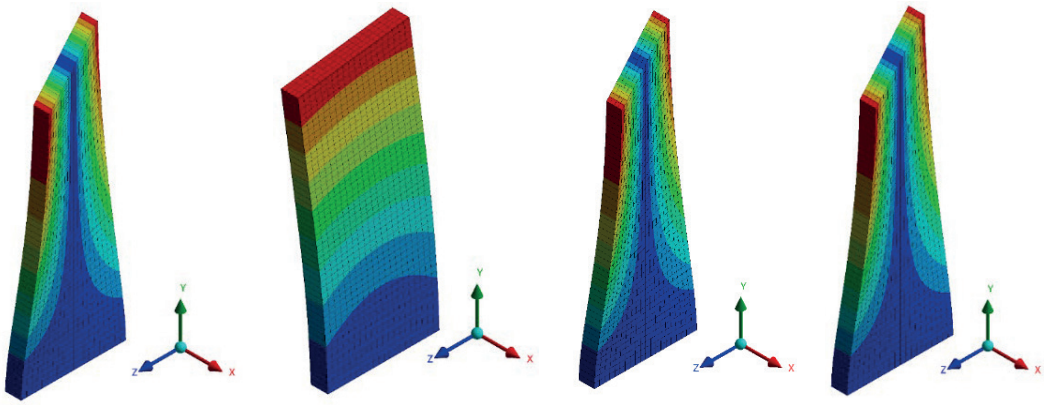

Model 4 (f_2 = 1.4952 Hz) *Model A* (f_2 = 1.816 Hz) *Model B* (f_2 = 1.542 Hz) *Model C* (f_2 = 1.5 Hz)

Figure 10. Eigenmodes and eigenfrequencies (mode 2)

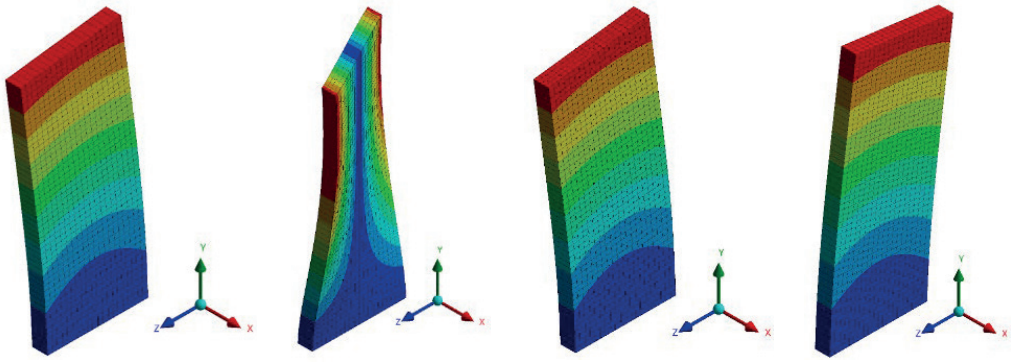

Model 4 (f_3 = 1.8191 Hz) *Model A* (f_3 = 1.8482 Hz) *Model B* (f_3 = 1.8188 Hz) *Model C* (f_3 = 1.8191 Hz)

Figure 11. Eigenmodes and eigenfrequencies (mode 3)

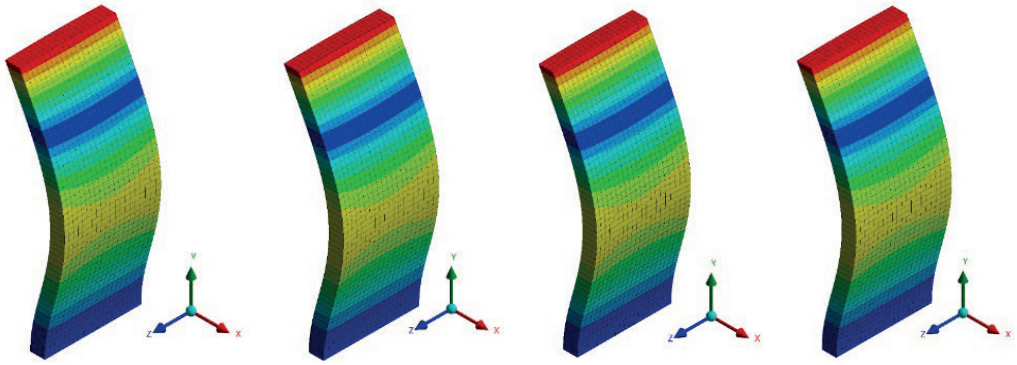

Model 4 (f_4 = 1.9032 Hz) *Model A* (f_4 = 1.8701 Hz) *Model B* (f_4 = 1.8997 Hz) *Model C* (f_4 = 1.9029 Hz)

Figure 12. Eigenmodes and eigenfrequencies (mode 4)

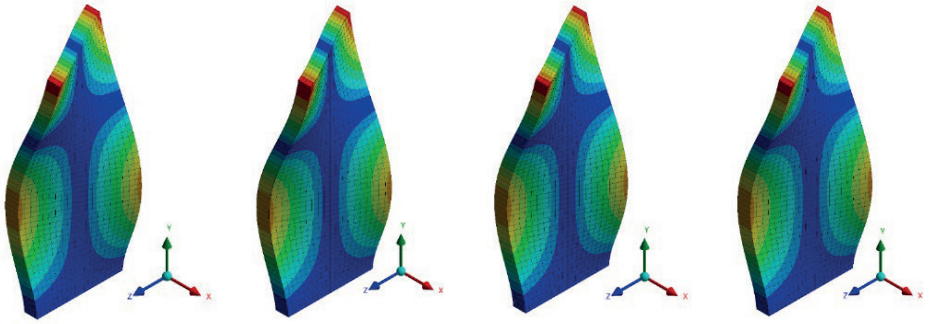

Model 4 (f_5 = 4.7179 Hz) *Model A* (f_5 = 4.8284 Hz) *Model B* (f_5 = 4.7298 Hz) *Model C* (f_5 = 4.7191 Hz)

Figure 13. Eigenmodes and eigenfrequencies (mode 5)

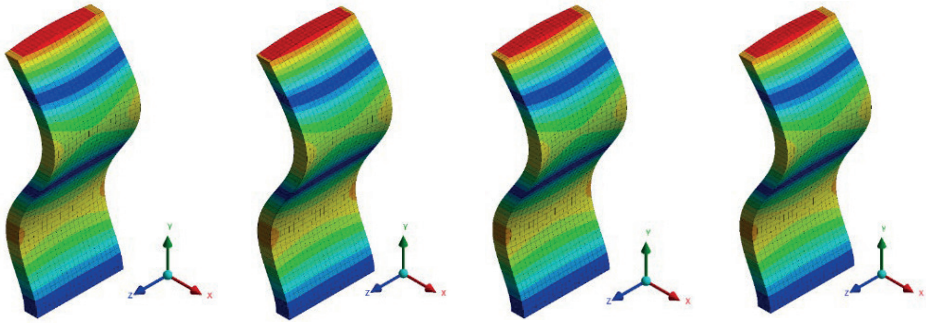

Model 4 (f_6 = 5.2101 Hz) *Model A* (f_6 = 5.1205 Hz) *Model B* (f_6 = 5.2009 Hz) *Model C* (f_6 = 5.2092 Hz)

Figure 14. Eigenmodes and eigenfrequencies (mode 6)

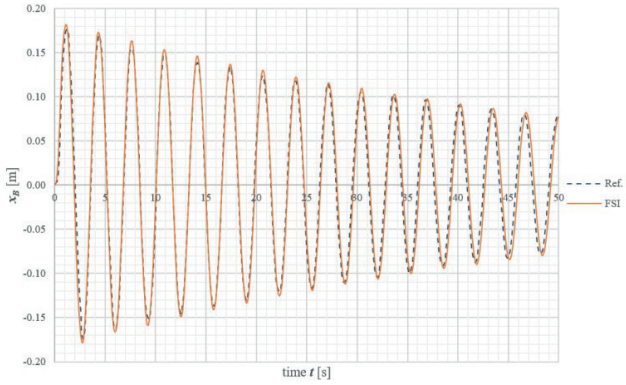

Displacement of the free edge of the oscillating plate in x direction [m]

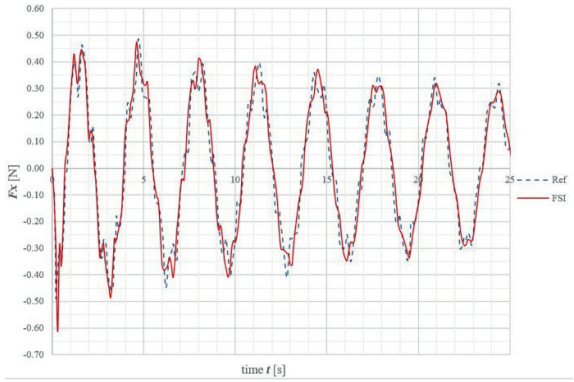

Drag force F_x [N]

Figure 15. Model B: Comparison of the simulation results with the reference [1]

6. CONCLUSION

The considered problem is included in the development of technique for estimating the aeroelastic instability of building structures ([6-7]) as a verification problem. This example shows the possibility of transition from a volumetric model to a shell model. The results obtained for both types of the flexible plate models showed good agreement with the

reference. The considered coupled approach, which utilizes a shell model of the plate, has practically important application to the real-world problems of aeroelasticity, since in engineering practice the building structures are most often modeled by beam and shell models.

ACKNOWLEDGMENTS

This work was financially supported by the Ministry of Science and Higher Education of the Russian Federation (Project: Theoretical and experimental design of new composite materials to ensure safety during the operation of buildings and structures under conditions of technogenic and biogenic threats #FSWG-2020-0007).

REFERENCES

1. **Glück M., Breuer M., Durst F., Halfmann A., Rank E.** Computation of fluid–structure interaction on lightweight structures //Journal of Wind Engineering and Industrial Aerodynamics, 2001, T.89, №. 14-15, 1351-1368. DOI: 10.1016/S0167-6105(01)00150-7
2. **Lee J. S., Shin J. H., Lee S. H.** Fluid–structure interaction of a flapping flexible plate in quiescent fluid //Computers & Fluid, 2012, T. 57, 124-137. DOI: 10.1016/j.compfluid.2011.12.015
3. **Namkoong K., Choi H. G., Yoo J. Y.** Computation of dynamic fluid–structure interaction in two-dimensional laminar flows using combined formulation //Journal of fluids and structures, 2005, T. 20, №. 1, C. 51-69. DOI: 10.1016/j.jfluidstructs.2004.06.008
4. **Chimakurthi S. K., Reuss S., Tooley M., Scampoli S**. ANSYS Workbench System Coupling: a state-of-the-art computational framework for analyzing multiphysics problems //Engineering with Computers, 2018, T. 34, № 2, 385-411. DOI: 10.1007/s00366-017-0548-4
5. ANSYS 21R2 User's Guide. Canonsburg, 2021.
6. **Lantsova I.** Numerical simulation of fluid-structure interaction by the example of a flow past a cylinder with a flexible thin structure //IOP Conference Series: Materials Science and Engineering. – IOP Publishing, 2021. – T. 1030. – №. 1. – C. 012084. DOI: 10.1088/1757-899X/1030/1/012084
7. **Belostotsky A.M., Afanasyeva, I.N., Lantsova, I.Yu. Goryachevsky O.S.** Simulation of aerodynamic instability of building structures on the example of a bridge section. Part 2: Solution of the problem in a coupled aeroelastic formulation and comparison with engineering estimates //International Journal for Computational Civil and Structural Engineering. – 2021. – T. 17. – №. 3. – C. 24-38. DOI: 10.22337/2587-9618-2021-17-3-24-38

СПИСОК ЛИТЕРАТУРЫ

1. **Glück M., Breuer M., Durst F., Halfmann A., Rank E.** Computation of fluid–structure interaction on lightweight structures //Journal of Wind Engineering and Industrial Aerodynamics, 2001, T.89, №. 14-15, 1351-1368. DOI: 10.1016/S0167-6105(01)00150-7
2. **Lee J. S., Shin J. H., Lee S. H.** Fluid–structure interaction of a flapping flexible plate in quiescent fluid //Computers & Fluid, 2012, T. 57, 124-137. DOI: 10.1016/j.compfluid.2011.12.015
3. **Namkoong K., Choi H. G., Yoo J. Y.** Computation of dynamic fluid–structure interaction in two-dimensional laminar flows using combined formulation //Journal of fluids and structures, 2005, T. 20, №. 1, C. 51-69. DOI: 10.1016/j.jfluidstructs.2004.06.008
4. **Chimakurthi S. K., Reuss S., Tooley M., Scampoli S**. ANSYS Workbench System Coupling: a state-of-the-art computational framework for analyzing multiphysics problems //Engineering with Computers,

2018, T. 34, № 2, 385-411. DOI: 10.1007/s00366-017-0548-4
5. ANSYS 21R2 User's Guide. Canonsburg, 2021.
6. **Lantsova I.** Numerical simulation of fluid-structure interaction by the example of a flow past a cylinder with a flexible thin structure //IOP Conference Series: Materials Science and Engineering. – IOP Publishing, 2021. – T. 1030. – №. 1. – C. 012084. DOI: 10.1088/1757-899X/1030/1/012084
7. **Белостоцкий А. Афанасьева И., Негрозова И., Горячевский О.** Simulation of aerodynamic instability of building structures on the example of a bridge section. Part 2: Solution of the problem in a coupled aeroelastic formulation and comparison with engineering estimates // International Journal for Computational Civil and Structural Engineering. – 2021. – T. 17. – №. 3. – C. 24-38. DOI: 10.22337/2587-9618-2021-17-3-24-38

Irina Yu. Negrozova, Structural Engineer, CJSC Research Center StaDiO; Junior Researcher, REC KM named after V.I. A.B. Zolotova and Senior Lecturer of the Department of Informatics and Applied Mathematics of the National Research Moscow State University of Civil Engineering; 129337, Russia, Moscow, Yaroslavskoe shosse, 26. E-mail: irina-lanzova@mail.ru.

Oleg S. Goryachevsky, Lead Structural Engineer, CJSC Research Center StaDiO; Deputy Director of REC KM named after A.B. Zolotov of the National Research Moscow State University of Civil Engineering; 129337, Russia, Moscow, Yaroslavskoe shosse, 26. E-mail: osgoryachevskij@mail.ru

Негрозова Ирина Юрьевна, инженер-расчетчик АО Научно-исследовательский центр СтаДиО; младший научный сотрудник НОЦ КМ им. А.Б. Золотова, старший преподаватель кафедры Информатики и прикладной математики Национального исследовательского Московского государственного строительного университета; 129337, Россия, г. Москва, Ярославское шоссе, д. 26. E-mail: irina-lanzova@mail.ru.

Горячевский Олег Сергеевич, ведущий инженер-расчетчик АО Научно-исследовательский центр СтаДиО; заместитель директора НОЦ КМ им. А.Б. Золотова Национального исследовательского Московского государственного строительного университета; 129337, Россия, г. Москва, Ярославское шоссе, д. 26. E-mail: osgoryachevskij@mail.ru

International Journal for Computational Civil and Structural Engineering, 19(1) 135–146 (2023)

DOI:10.22337/2587-9618-2023-19-1-135-146

TIME ANALYSIS OF A CONSTRUCTIVELY NONLINEAR SYSTEM WITH ONE-WAY CONNECTIONS

Alexander N. Potapov, Nail T. Tazeev

South Ural State University, Chelyabinsk, RUSSIA

Annotation: An active method of suppressing wind auto-oscillations of an overground gas pipeline model is considered, which allows the system to be tuned from the resonant frequency by changing its design scheme with the help of a vibration damping device operating on the principle of one-way connection (OWC). A new mathematical model of vibrations with a symmetric form of natural vibrations of the system is proposed. Variants of vibration models with one and two OWC, located in the central span of the design scheme of the gas pipeline, are considered. The implementation of a non-stationary dynamic process is carried out within the framework of the theory of temporal analysis for a model of an overground gas pipeline in the form of a multi-span continuous beam with point masses located in the design sections of the model. The equation of motion is presented in the matrix form of the Duhamel integral, taking into account internal friction, which follows the disproportionate damping model. Computer simulation of the problem for a system with 39 degrees of freedom is carried out. The kinematic and force parameters of the dynamic response of the dissipative system are obtained, a comparative analysis of the proposed oscillation model for the design models with one and two OWC is given, and the efficiency of the model with two OWC is shown.

Keywords: overground gas pipeline, auto-oscillations, vibration damping device, connection, natural mode of vibration, stiffness matrix, displacement

ВРЕМЕННОЙ АНАЛИЗ КОНСТРУКТИВНО НЕЛИНЕЙНОЙ СИСТЕМЫ С ОДНОСТОРОННИМИ СВЯЗЯМИ

А.Н. Потапов, Н.Т. Тазеев

ФГАОУ ВО «Южно-Уральский государственный университет» (НИУ), г. Челябинск, РОССИЯ

Аннотация: Рассмотрен активный способ гашения ветровых автоколебаний модели надземного газопровода, позволяющий отстраивать систему от резонансной частоты путем изменения ее расчетной схемы с помощью устройства гашения колебаний, работающего по принципу односторонней связи (ОС). Предложена новая математическая модель колебаний с симметричной формой собственных колебаний системы. Рассмотрены варианты моделей колебаний с одной и двумя ОС, размещенными в центральном пролете расчетной схемы газопровода. Реализация нестационарного динамического процесса выполнена в рамках теории временного анализа для модели надземного газопровода в виде многопролетной неразрезной балки с точечными массами, расположенными в расчетных сечениях модели. Уравнение движения представлено в матричной форме интеграла Дюамеля с учетом внутреннего трения, подчиняющегося модели непропорционального демпфирования. Проведено компьютерное моделирование задачи для системы с 39 степенями свободы. Получены кинематические и силовые параметры динамической реакции диссипативной системы, дан сравнительный анализ предложенной модели колебаний для расчетных моделей с одной и двумя ОС и показана эффективность модели с двумя ОС.

Ключевые слова: надземный газопровод, автоколебания, устройство гашения колебаний, односторонняя связь, форма собственных колебаний, матрица жесткости, перемещение

INTRODUCTION

In operational practice overground gas pipelines, the phenomenon of wind self-oscillations caused by the nature of the laminar wind flow around the pipe is often found. At certain Reynolds numbers, on the leeward side of the pipe, the so-called Karman's track [1] is formed, consisting of vortices alternately breaking off from the upper and lower sides of the cylindrical surface of the pipe. These vortices transmit to the pipeline significant in magnitude sign-alternating pulses, which cause oscillations in the vertical plane, the frequency of which is equal to the vortex separation frequency. If this frequency coincides with the frequency of natural vibrations of the gas line, a resonance will occur, representing a serious danger to any structure. A rapid increase in the amplitude of vibrations leads to various damages: loosening of the supports, destruction of clamps at the points of attachment of the pipe with supports, the appearance of longitudinal and transverse cracks on the surface of the pipe at the support points, dropping the gas pipeline from the supports, etc.

The main conditions for the occurrence of wind self-oscillations are the laminar nature of the wind flow, the exclusion of local turbulence and the relatively high flexibility of the pipeline. It is known that for pipelines of medium (300-500 mm) and large (over 500 mm) diameters, the occurrence of wind self-oscillations is practically excluded, but for pipelines of smaller diameter this phenomenon can be destructive [2].

The existing methods for solving this problem are divided into two directions: changing the nature of the flow around a structure or the nature of the oscillatory process (active methods) and constructive limitation of the level of oscillations by changing the frequency of natural oscillations (passive) [3]. Active aerodynamic methods use various devices to change the nature of the flow around the structure (turbulators, perforated casings, etc.). Active mechanical dampers change dynamic characteristics without changing static ones (dampers, shock absorbers, etc.). Currently, active research is being conducted in both directions, but aerodynamic methods are more widespread.

Various methods of calculating systems with vibration damping devices are known in the literature [3, 4]. The article [5] examines the existing methods of calculating cylindrical structures for wind vibrations with mechanical damping devices.

In works [6, 7], the authors have studied the devices for active aerodynamic damping of wind self-oscillations of cylindrical structures. The obtained results of experiments in a wind tunnel show high efficiency of the devices. Similar studies are carried out by methods of numerical simulation [8]. In this case, in the formulation of problems, usually design dynamic models with a small number of degrees of freedom are considered, in which the internal friction of the material is taken into account on the basis of proportional damping models [9, 10].

This article analyzes the dynamic response of the gas pipeline design model in a non-stationary process. To limit the resonance amplitudes in the design model, a device is used that operates on the principle of one-way connection (OWC) and contains a cable with a zero bending stiffness as the main element [11]. Within the framework of the theory of temporal analysis, a mathematical model of oscillations of a system with one and two OWC is built. This model makes it possible to take into account the behavior of the system, both in the state of the base model (BM), when the OWC is turned off from work, and in the state of models with additional connection (MAC), when the OWC is turned on.

When analyzing the fluctuations of the design model, the influence of a number of factors on the parameters of the dynamic response of the design model was studied. In particular, the influence of the cable stiffness and the influence of the OWC location in the span relative to the supports were taken into account.

1. MODELS AND ALGORITHMS

The equation of motion of an elastic discrete dissipative system (DDS) in the framework of the linear model of viscous resistance (1) and the initial conditions (2) of the dynamic problem are represented in the form:

$$M\ddot{Y}(t)+C\dot{Y}(t)+KY(t)=P(t) \quad (1)$$

$$Y_0=Y(t_i),\ \dot{Y}_0=\dot{Y}(t_i), \quad (2)$$

where M = diag (m_1, ..., m_n), $C_j = C_j^{\mathrm{T}}$, $K_j = K_j^{\mathrm{T}} \in M_n(\mathrm{R})$ – mass matrix, damping matrix and stiffness matrix; $Y(t)$, $P(t)$ – displacement vectors and external load vectors. The index j = 0, 1, … takes into account the state of the design model over the time interval $t \in [t_i, t_{i+1}]$, at that, the zero index j of the corresponding matrices is omitted. Here t_i – is the OWC on / off time.

The construction of fundamental solutions of the homogeneous differential equation following from (1) is related to the matrix function $\Phi_j(t) = e^{S_j t}$ in which $S_j \in M_n(\mathrm{C})$ satisfies the characteristic matrix quadratic equation (MQE) – the equation of motion of natural forms:

$$MS_j^2+C_jS_j+K_j=0. \quad (3)$$

The matrices S_j play an exceptional role in the analysis of a dynamic system, because the spectra of these matrices contain the internal dynamic characteristics of the DDS (damping coefficients, frequencies and forms of natural vibrations). The MQE solution (3) has an analytical representation in the form of a root pair:

$$S_{j(1,2)}=M^{-1}(-C_j+V_j\pm U_j)/2 \quad (3)$$

where $V_j = -V_j^{\mathrm{T}}$, $U_j = U_j^{\mathrm{T}}$ – skew-symmetric and symmetric matrices.

For an elastic DDS with low dissipation, the elements of the matrices V_j, U_j are real and imaginary, respectively, and therefore the matrix roots $S_{j(1,2)}$ are complex conjugate ($S_{j,1} = S_j$, $S_{j,2} = \overline{S}_j$) [12]:

$$\begin{aligned} S_j&=M^{-1}(-C_j+V_j+U_j)/2,\\ \overline{S}_j&=M^{-1}(-C_j+V_j-U_j)/2. \end{aligned} \quad (4)$$

The system response (vectors of displacements and velocities of DDS nodes) is written in the matrix form of the Duhamel integral [13]:

$$Y(t)=2\,\mathrm{Re}\{Z(t)\},\ \dot{Y}(t)=2\,\mathrm{Re}\{S_jZ(t)\}, \quad (5)$$

$$\begin{aligned} Z(t)&=\Phi_j(t-t_i)U_j^{-1}M(-\overline{S}_jY_0+\dot{Y}_0)+\\ &+U_j^{-1}\int_{t_i}^{t}\Phi_j(t-\tau)^{\mathrm{T}}P(\tau)d\tau. \end{aligned} \quad (6)$$

The first term in (6) expresses the reaction of the design model with free vibrations, the second term is the Duhamel integral, the reaction with forced vibrations.

The aerodynamic effect of the wind load is determined by the sine law:

$$P(t)=P_0\sin(\theta t). \quad (7)$$

The amplitude value of the disturbing load acting in the node is calculated as the force of the frontal resistance to the static action of the wind of the calculated speed. The number of vortices escaping from the pipe surface in 2π seconds is the circular frequency of the disturbing load and is calculated using the following formula:

$$\theta=\frac{0,2v}{d}\cdot 2\pi. \quad (7)$$

Then the dynamic reaction (6) under the condition of constant velocity head (θ = const along the entire length of the design model) takes the form on the interval $t \in [t_i, t_{i+1}]$ [12]:

$$\left.\begin{aligned} Z(t)&=\Phi_j(t-t_i)U_j^{-1}M[-\overline{S}_jY_0+\dot{Y}_0]+\\ &+U_j^{-1}\left[(S_j^{\mathrm{T}})^2+\theta^2\right]^{-1}F(t)P_0,\\ F(t)&=S_j^{\mathrm{T}}\left[\Phi_j(t-t_i)^{\mathrm{T}}\sin(\theta t_i)-E\sin(\theta t_i)\right]+\\ &+\left[\Phi_j(t-t_i)^{\mathrm{T}}\cos(\theta t_i)-E\cos(\theta t_i)\right]\theta, \end{aligned}\right\} \quad (8)$$

where E – identity matrix.

The design scheme (Fig. 1) of the gas pipeline has the form of a continuous beam, all spans of which (except for the central one) are modeled by the same number of nodes containing point masses. In the central span, the number of nodes has been increased in order to improve the positioning accuracy of the OWC. The number of degrees of freedom of the system is equal to the number of masses.

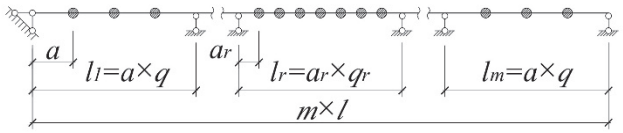

Figure 1. Design model

Activation and deactivation of connections is realized by changing the external (C_j, K_j) and internal (S_j, U_j) dynamic parameters of the system and changing the initial conditions (Y_0, $\dot{Y}_0$). In addition, when moving from interval $t \in [t_{i-1}, t_i]$ to interval $t \in [t_i, t_{i+1}]$, the time is changed from t_{i-1} to t_i.

In the case of a design dynamic model with one OWC in a span (DDM-1), Fig. 2 shows two possible states of the system (for j = 0, 1): BM and MAC. For a model with two OWC in a span (DDM-2), four possible states are considered (j = 0, 1, 2, 3): BM, MAC-1, MAC-2 and MAC-3 (Fig. 3).

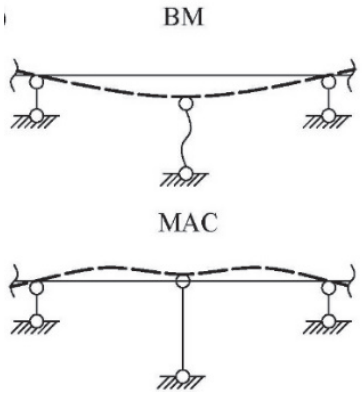

Figure 2. Schemes of possible states of the design model with one OWC (DDM-1)

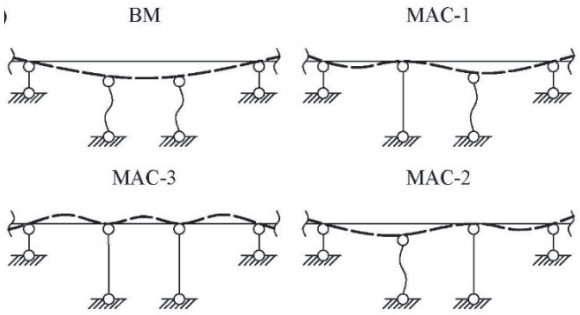

Figure 3. Schemes of possible states of the design model with two OWC (DDM-2)

Variants of the MAC-1, MAC-2 models (within the framework of the DDM-2) are possible with an arbitrary arrangement of the OWC in the central span and a velocity flow that is not constant along the length of the design model.

Initial data for calculation: outer and inner diameters of the pipe, respectively D = 219 мм, d = 209 мм, elastic modulus $E = 2{,}1\times10^8$ kN/m^2, span length l = 15 m, number of spans m = 9, the number of elementary sections in the central span q_1 = 16, in other spans q = 4. Accordingly, the number of masses in the central span is 15, in other spans – 3, the number of degrees of freedom n = 39. The tensile compliance of the cable takes values in the range $\delta_R \in [0.001, 0.1]$ m/kN. Logarithmic decrement δ = 0,07. The wind speed at which the resonance occurs is v = 2.951 m/s.

2. EXPERIMENTAL STUDIES OF THE "BEAM - CABLE" MODEL

Note that in Fig. 2, 3 show schemes of possible states of the system during vibrations only with a symmetrical arrangement of the deformed axis of the design model relative to the attachment point of the working (active) OWC, i.e. displacements of the elastic line when passing through the attachment point, where the OWC entered into operation, do not change sign. This is due to the fact that in the transient modes of the design model, when the BM is in one (any) of the states associated with the MAC, the stay in this state, as experimental studies show, lasts

a fraction of a second and does not exceed 1/10 of the time the system is in condition BM.

The experiment was carried out on a flexible beam with one OWC. The aerodynamic effect was simulated using a vibration load from a light electric motor located in the center of the beam (Fig. 4). The parameters of the design dynamic model: the cross-section of the beam is 50 × 4 mm, the length is 2 m, one-way connection in the form of a cable, within the framework of the experiment, is assumed to be inextensible. Motor weight 0.36 kg, motor angular frequency causing resonance θ = 9 rad/s, amplitude of the active component of the vertical centrifugal force P_0 = 5.3 kg. The purpose of the experiment: to determine the form of vibration of the deformed axis of the beam at the moment of activation of the OWC (cable); to show that the form of natural vibrations of the model in the MAC state is symmetric due to the absence of turns of the central section at the point of attachment of the OWC to the beam.

In Fig. 4 shows a photo of the experimental setup at the moment of OWC tension (a) and OWC deactivation (b). In both Figures, it can be seen that the elastic line of the beam at the point of attachment of the cable retains its symmetry about the center of the span, and the tangent to the elastic line at this point does not rotate relative to the horizontal. It can be stated that due to the inertia of motion and because of the short duration of the stay of the design model in the MAC state, the model does not have time to change the type of symmetry of the form of natural vibrations.

Figure 5 shows the frequency characteristics of the vibrations of the BM (Fig.5a) and the model with a cable (Fig.5b), recorded using a special application «Vibration analysis». The vibration frequency of the BM is 1.62 Hz, the maximum value of the vibration displacement amplitude is 62.94 mm – 6.06 mm/s^2. The vibration frequency of the model with a cable is 4.94 Hz, the amplitude of vibration displacements is 2.27 mm, amplitude of accelerations is 23.59 mm/s^2.

a)

b)

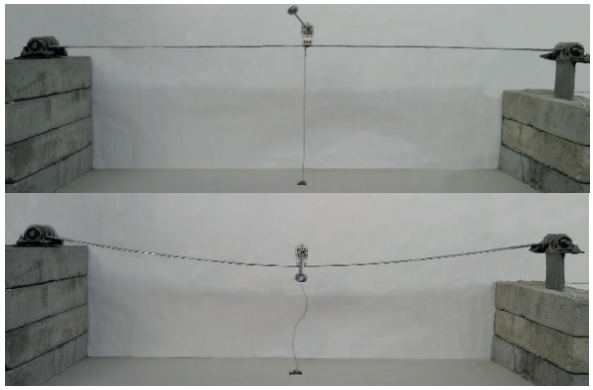

Figure 4. Design model "beam – cable": a – in a state of tension on the cable; b – when the cable is off

a)

b)

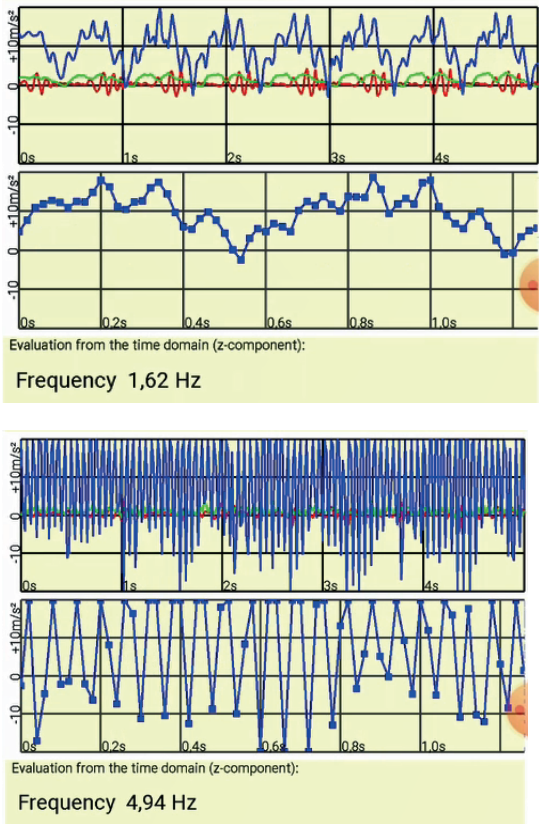

Figure 5. Characteristics of system oscillations: a) BM; b) model with a cable

It is important to note that when the beam is deformed in symmetric mode of vibration (Fig. 2, state of MAC-1), its displacements will be less than the corresponding displacements of the beam in the case of its deformation along the skew-symmetric mode of vibration. This is due to the fact that the central section of the beam in the MAC-1 state corresponds to the design scheme with a rigidly

fixed support, and when deformed according to a skew-symmetric vibration mode, it corresponds to the design scheme with a hinged support.

Turning to the design model of a gas pipeline in the form of a multi-span beam, we can conclude that the use of a symmetric vibration mode reduces deflections not only in the central span where the OWC is installed, but also in adjacent spans of the design model. Here, the gas pipeline design behaves like a living organism, showing the "instinct of self-preservation" and choosing the most optimal way out of a critical situation. Indeed, in order to resist the wind resonance, the gas pipeline construct makes the most of its external and internal reserves. The OWC acts as an external reserve, the activation of which leads to a change in the calculation scheme, and the internal reserve is the symmetric form of the system's oscillations in a new state. This transformation of the system provides more effective resistance to wind resonance than in a system with a skew-symmetric vibration mode.

3. RESULTS OF THE STUDY

In the case of a design model with two OWC in a span (DDM-2), their symmetrical arrangement relative to the center of the span at the attachment points is considered: 19-21, 18-22 and 17-23 (Fig. 6). The results of computer simulation of the problem are graphs (oscillograms) of the parameters of the dynamic reaction of a constructively nonlinear dissipative system at a given time interval. These parameters include: displacement, velocity, acceleration, restoring (elastic), dissipative and inertial forces calculated in the design sections of the model, as well as the forces in the cables. The most indicative is the graph in which the kinematic and power parameters are combined. Figure 7 shows a fragment of an oscillogram of displacements, restoring forces and forces in the cable, built for the 19th node, where the left OWC is mounted in the DDM-2 (19-21) system. As can be seen from the graph, on time intervals corresponding to the OWC tension, displacements $y_{19}(t)$ of this node (due to the compliance of the connection) become higher than the position of static equilibrium. At this moment, the activation of elastic forces occurs due to a sharp transformation of kinetic energy into potential.

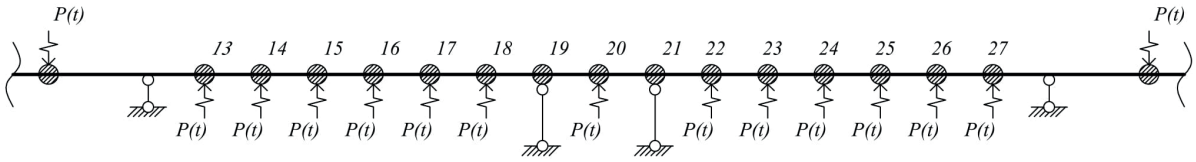

Figure 6. Scheme of application of loads in the central span of DDM-2 (19-21)

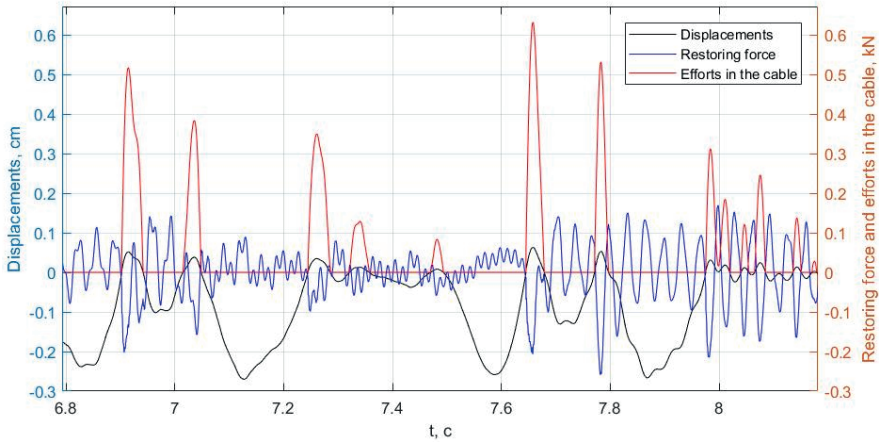

Figure 7. Fragment of the oscillogram of displacements, restoring force and efforts in the cable at the attachment point of the left OWC

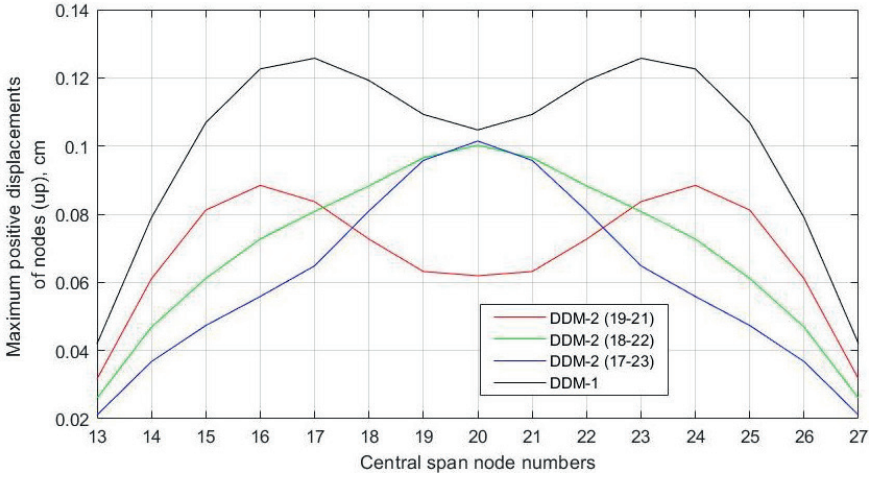

Figure 8. Graph of the maximum positive vibration displacements of the nodes of the central span

To compare the effectiveness of the ways of positioning the OWC in the span, a comparative calculation of DDM-1 and DDM-2 was carried out with the minimum cable complience (0.001 m / kN). The maximum developed displacements of the masses of the central span were estimated for the entire period of oscillations, for which the graphs of the maximum positive (upward) displacements were constructed, which, in fact, represent the enveloping diagrams of displacements (Fig. 8). The resulting graph shows that the level of fluctuations of the central span is most effectively suppressed in the DDM-2 with the OWC 19-21 location, that is, the closest to the center.

Fig. 9 shows oscillograms of the maximum displacements of the base model, DDM-1 and DDM-2 (19-21) with a cable compliance of 0.01 m/kN at a 10-second interval. As can be seen from the graph, in DDM-2 the maximum displacement values are less than in DDM-1, and the maximum is also reached earlier. Moreover, at the beginning of the process, the displacement in both models is higher than in the BM.

The maximum displacements develop at the central points of the extreme spans. Oscillograms of vibration displacements of DDM-1 and DDM-2 (19-21) for these points are shown in Fig. 10.

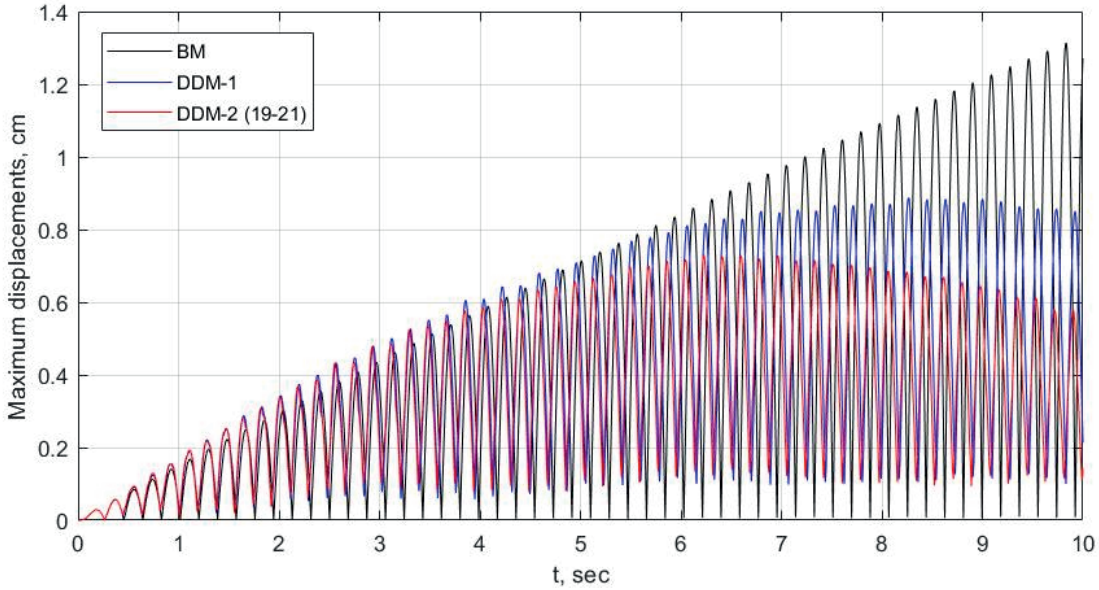

Figure 9. Oscillograms of maximum modulus displacements BM, DDM-1, DDM-2 (19-21)

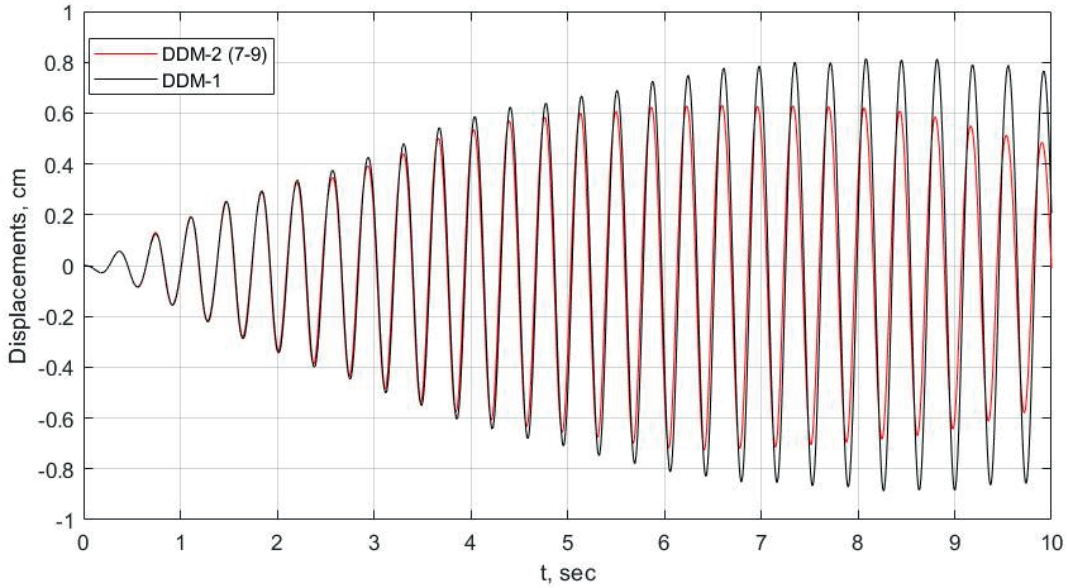

Figure 10. Oscillograms of movements of the central node of extreme span in DDM-1 and DDM-2 (19-21)

Fig. 11 shows a graph of the maximum vibration displacements max| $y_i(t)$ | for models DDM-1, DDM-2 at different values of cable compliance (from 0.001 to 0.1 m/kN).

According to the graph, the DDM-2 model (19-21) shows the maximum efficiency in almost the entire range of cable compliance values. The variant with the DDM-1 model shows the worst results in all cases. Moreover, a twofold increase in the rigidity (decrease in compliance) of the cable in DDM-1 does not give an advantage over DDM-2 in the effective range of rigidity (compliance range from 10^{-3} to $5 \cdot 10^{-2}$ m/kN). In other words, a single double-stiffness cable is not more efficient than two single-stiffness cable.

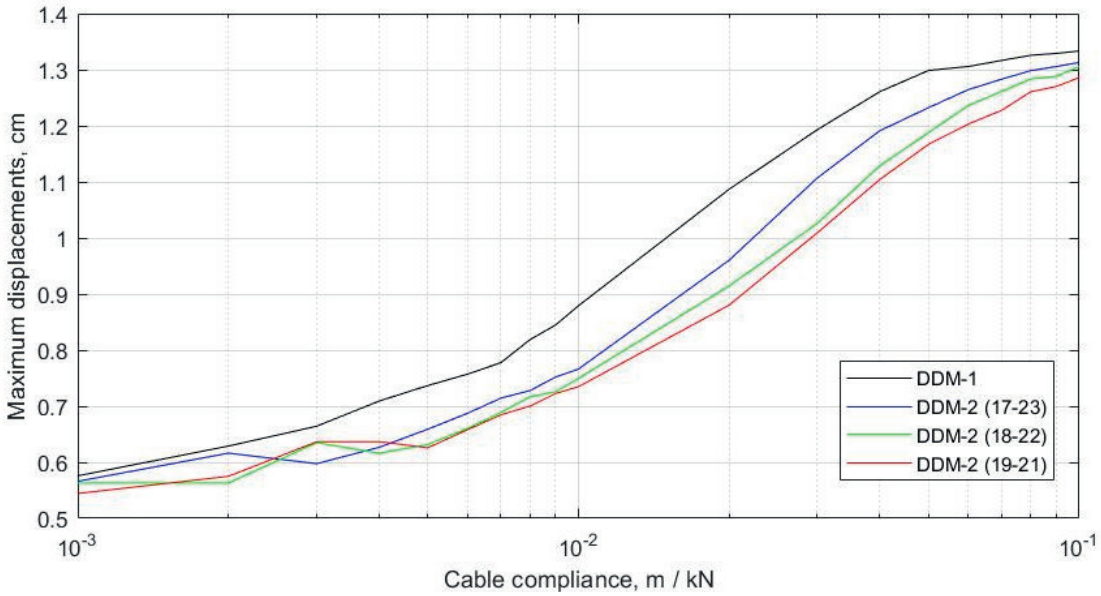

Figure 11. Graph of the dependence of the maximum vibration displacements on the cable compliance in various models

The phase diagrams $y_i(t) - \dot{y}_i(t)$ shown in Fig. 12, built for the case of the lowest cable compliance (0,001 м/кН) in the first two seconds of the system operation, demonstrate the differences in the nature of the nonlinear operation of the system. Here the *i* numbers correspond to the central nodes of the corresponding spans.

In BM, the phase trajectory of the central node of the 4th span is characterized by a uniform proportional increase in the form of a spiral. (Fig. 12 a). The same dependences constructed for DDM-1 and DDM-2 (Fig. 12 b, c), not only differ from BM, but also significantly differ from each other. For DDM-2, in comparison with DDM-1, sharper and more frequent changes in the direction of speed are characteristic, which is a reflection of the higher energy impact on the constructive nonlinear model from the side of the two OWCs when they are switched on / off. Phase diagrams of off-center (extreme) nodes of the 4th span have a similar look. In the first span operation character DDM-2 is aligned, it becomes more similar to the operation of BM (Fig. 12 g).

For the computational model with two OWC, an estimate of the accuracy of solving the differential equation of motion using the residual vector $\Delta\varphi(t) = f(t) - P(t)$, where $f(t) = M\ddot{Y}(t) + C\dot{Y}(t) + KY(t)$ is the sum of inertial, dissipative and restoring forces on the left side of the equation; $P(t) = [p_j(t)]$ – vector of external forces. Value $\Delta\varphi(t)$, expressing the difference between the left and right sides of the equation, is built for DDM-2 over the entire response interval, including the states of BM and MAC-2. The nature of the convergence of the solution (functions $f_j(t)$) to the given functions $p_j(t)$ of the right-hand side of the equation is shown on the oscillogram $\Delta\varphi_j(t)$ for the cable attachment point ($j = 7$) in Fig. 13. The accuracy of solving the differential equation of motion does not go beyond the error limits $\varepsilon \le 8{,}5\times10^{-13}$ кН.

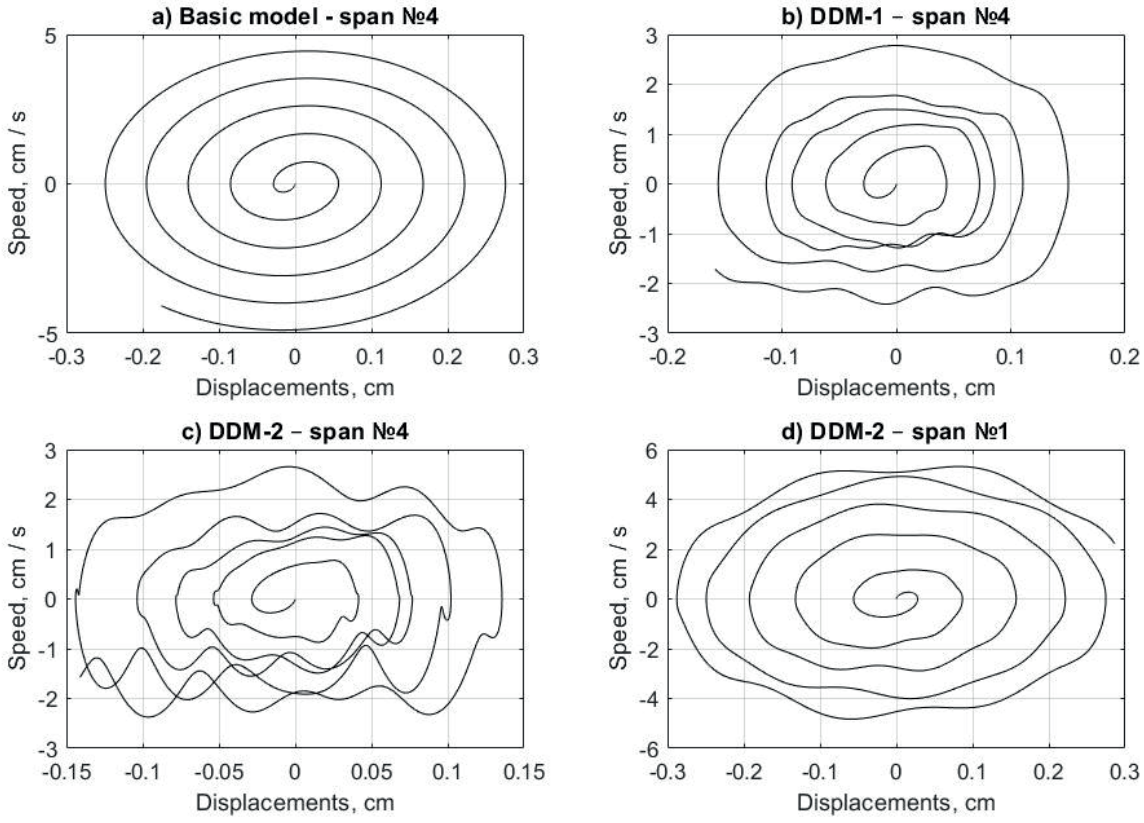

Figure 12. Phase trajectories in coordinates $y_i(t) - \dot{y}_i(t)$ for BM, DDM-1 and DDM-2 in the first two seconds of operation with cable compliance 0.001 m / kN

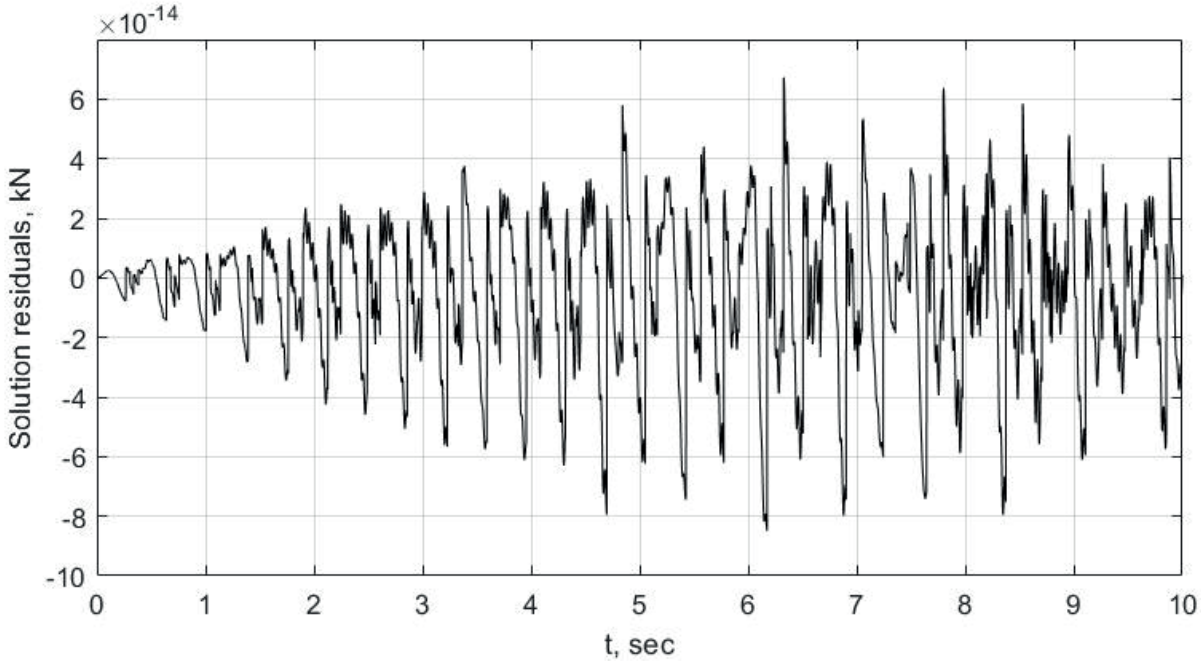

Figure 13. Oscillogram of residuals $\Delta\varphi_7(t)$ of the solution of the equation of motion (1)

CONCLUSION

Based on the results of the study, the following conclusions can be drawn.

1. On the basis of experimental data, a more perfect model with a symmetric natural vibration mode was adopted. Computer simulation of the problem with one and two OWC also showed a high efficiency of the damping device for the proposed oscillation model. This result is of great practical importance. The use of this model (within the framework of DDM-1 and DDM-2) will increase (optimize) the spacing of vibration damping devices along the elevated gas pipeline route and, thereby, reduce the number of these devices per one kilometer of the route compared to the model of vibrations with a skew-symmetric shape.
2. For DDM-2 with a symmetrical arrangement of the OWC, the optimal arrangement of connections (19-21 – in the local numbering of the central span) was obtained practically over the entire range of values of the cable compliance. With this arrangement of connections, the DDM-2 shows a more active limitation of the amplitudes of the parameters of the dynamic response in comparison with the same model with other arrangements of the OWC, and also in comparison with the DDM-1 model.
3. It is shown that all the considered variants of the DDM-2 models lead to much lower amplitudes of the response parameters in comparison with the DDM-1 model. Even a doubling of stiffness of the cable in the DDM-1 model did not reveal any advantages over the DDM-2 model in terms of maximum vibration displacements.

REFERENCES

1. **Bisplinghoff, R.L.** Aeroelasticity: monograph [Aerouprugost': monografiya] / R.L. Bisplinghoff, H. Eshli, R.L. Halfman. – Moscow.: IL, 1958. 799 p.
2. **Tartakovsky, G.A.** Pipeline structural mechanics [Stroitel'naya mekhanika truboprovoda] / G.A. Tartakovsky. -– Moscow.: «Nedra» Publ., 1967. 312 p.
3. **Kazakevich, M.I.** Aerodynamic stability of overground and overhead pipelines [Aerodinamicheskaya ustojchivost' nadzemnyh i visyachih truboprovodov] / M.I. Kazakevich. – Moscow.: «Nedra» Publ., 1977. 200 p.

4. Dynamic calculation of buildings and structures [Dinamicheskij raschet zdanij i sooruzhenij] / M.F. Bernshtejn, V.A. Il'ichev, B.G. Korenev [et al.]; edited by B.G. Korenev, I.M. Rabinovich. – 2-nd edition revised and enlarged – Moscow.: Strojizdat, 1984. – 303 p.
5. **Gabbai, R.D., Benaroya, H.** An overview of modeling and experiments of vortex-induced vibration of circular cylinders // Journal of Sound and Vibration. – 2005. – Vol. 282. – P. 575–616.
6. **Wen-Li Chen, Guan-Bin Chen, Feng Xu, Ye-wei Huang, Dong-Lai Gao, Hui Li.** Suppression of vortex-induced vibration of a circular cylinder by a passive-jet flow control // Journal of Wind Engineering & Industrial Aerodynamics. – 2020. – Vol. 199. P. – 1-13.
7. **Wang L., Jiang T.L., Dai H.L., Ni Q.** Three-dimensional vortex-induced vibrations of supported pipes conveying fluid based on wake oscillator models // Journal of Sound and Vibration. – 2018. – Vol. 422. – P. 590-612.
8. **Muddadaa S., Patnaik B.S.V.** Active flow control of vortex induced vibrations of a circular cylinder subjected to non-harmonic forcing // Ocean Engineering. – 2017. – Vol. 142. – P. 62-77.
9. **Lupi F., Niemann H-J., Hoffer R.** Aerodynamic damping model in vortex-induced vibrations for wind engineering applications // Journal of Wind Engineering & Industrial Aerodynamics. – 2018. – Vol. 174. – P. 281-295.
10. **Lei Wang, Xing-Yan Fan, Shu-Guo Liang, Jie Song, Ze-Kang Wang**. Improved expression for across-wind aerodynamic damping ratios of super high-rise buildings // Journal of Wind Engineering & Industrial Aerodynamics. – 2018. – Vol. 176. – P. 263-272.
11. Patent RF №2007109081/12.03.2007 Pipeline resonance damping device [Ustrojstvo dlya gasheniya rezonansnyh kolebanij truboprovoda] // Patent, Russia №66000.2019. Bulletin № 25. / Potapov A.N., Degtyareva N.V. [et al.].
12. **Potapov A.N.** Dynamic analysis of discrete dissipative systems under nonstationary influences [Dinamicheskij analiz diskretnyh dissipativnyh sistem pri nestacionarnyh vozdejstviyah] / A.N. Potapov. – Chelyabinsk: SUSU Publ., 2003. 167 p.
13. **Potapov, A.N.** Analysis of vibrations of structures with switching off connections [Analiz kolebanij konstrukcij s vyklyuchayushchimisya svyazyami] / A.N. Potapov // Bulletin of SUSU. Series: Construction and architecture. 2017. – Vol.17, №1. pp. 38-48. DOI: 10.14529/build170105

СПИСОК ЛИТЕРАТУРЫ

1. **Бисплингхофф, Р.Л.** Аэроупругость: монография / Р.Л. Бисплингхофф, Х. Эшли, Р.Л. Халфман. – М.: ИЛ, 1958. – 799 с.
2. **Тартаковский, Г.А.** Строительная механика трубопровода / Г. А. Тартаковский. - М.: «Недра», 1967. – 312 с.
3. **Казакевич, М.И.** Аэродинамическая устойчивость надземных и висячих трубопроводов / М.И. Казакевич. – М.: «Недра», 1977. – 200 с.
4. Динамический расчет зданий и сооружений / М.Ф. Бернштейн, В.А. Ильичев, Б.Г. Коренев [и др.]; под ред. Б.Г. Коренева, И.М. Рабиновича. – 2-е изд., перераб. И доп. – М.: Стройиздат, 1984. – 303 с.
5. **Gabbai, R.D., Benaroya, H.** An overview of modeling and experiments of vortex-induced vibration of circular cylinders // Journal of Sound and Vibration. – 2005. – Vol. 282. – P. 575–616.
6. **Wen-Li Chen, Guan-Bin Chen, Feng Xu, Ye-wei Huang, Dong-Lai Gao, Hui Li**. Suppression of vortex-induced vibration of a circular cylinder by a passive-jet flow control // Journal of Wind Engineering & Industrial Aerodynamics. – 2020. – Vol. 199. P. – 1-13.

7. **Wang L., Jiang T.L., Dai H.L., Ni Q**. Three-dimensional vortex-induced vibrations of supported pipes conveying fluid based on wake oscillator models // Journal of Sound and Vibration. – 2018. – Vol. 422. – P. 590-612.
8. **Muddadaa S., Patnaik B.S.V**. Active flow control of vortex induced vibrations of a circular cylinder subjected to non-harmonic forcing // Ocean Engineering. – 2017. – Vol. 142. – P. 62-77.
9. **Lupi F., Niemann H-J., Hoffer R.** Aerodynamic damping model in vortex-induced vibrations for wind engineering applications // Journal of Wind Engineering & Industrial Aerodynamics. – 2018. – Vol. 174. – P. 281-295.
10. **Lei Wang, Xing-Yan Fan, Shu-Guo Liang, Jie Song, Ze-Kang Wang**. Improved expression for across-wind aerodynamic damping ratios of super high-rise buildings // Journal of Wind Engineering & Industrial Aerodynamics. – 2018. – Vol. 176. – P. 263-272.
11. Патент РФ №2007109081/ 12.03.2007 Устройство для гашения резонансных колебаний трубопровода // Патент России №66000.2019. Бюл. № 25. / Потапов А.Н., Дегтярева Н.В. [и др.].
12. **Потапов А.Н.** Динамический анализ искретных диссипативных систем при нестационарных воздействиях / А.Н. Потапов. – Челябинск: Изд-во ЮУр-ГУ, 2003. – 167 с.
13. **Потапов, А.Н.** Анализ колебаний конструкций с выключающимися связями / А.Н. Потапов // Вестник ЮУрГУ. Серия «Строительство и архитектура». – 2017. – Т. 17, № 1. – С. 38–48. DOI: 10.14529/build170105

Alexander N. Potapov, South-Ural State University (National Research University), Department of Building Technologies and Structural Engineering, Doctor of Technical Sciences, Professor of the Department, Professor, Corresponding Member RAASN, 76, Lenin Prospect, Chelyabinsk, 454080, Russia. phone: +7(351)267-91-83, 8-9193437129. E-mail: potapov.alni@gmail.com.

Nail T. Tazeev, South-Ural State University (National Research University), Department of Building Technologies and Structural Engineering, graduate student, 76, Lenin Prospect, Chelyabinsk, 454080, Russia. phone: 8-951-253-16-85. E-mail: tazeev.nail@gmail.com

Потапов Александр Николаевич, ФГАОУ ВО «Южно-Уральский государственный университет» (Национальный исследовательский университет), кафедра «Строительное производство и теория сооружений», д.т.н., проф. каф., профессор, член-корреспондент РААСН, 454080, Россия, г. Челябинск, пр. Ленина, дом 76, тел.: +7(351) 267-91-83, 8-9193437129. E-mail: potapov.alni@gmail.com.

Тазеев Наиль Тимурович, ФГАОУ ВО «Южно-Уральский государственный университет» (НИУ), кафедра «Строительное производство и теория сооружений», аспирант, 454080, Россия, г. Челябинск, пр. Ленина, дом 76, тел.: 8-951-253-16-85. E-mail: tazeev.nail@gmail.com

International Journal for Computational Civil and Structural Engineering, 19(1) 147–154 (2023)

DOI:10.22337/2587-9618-2023-19-1-147-154

NUMERICAL SIMULATION OF GAS ATOM COORDINATE DISPERSION IN A MATHEMATICAL MODEL OF DEEP BLAST COMPACTION FOR SUBSIDENCE SOILS

Elena O. Tarasenko

North Caucasus Federal University, Stavropol, RUSSIA

Abstract: within the framework of mathematical modeling of geological systems, applied inverse problems arise that require solutions. This paper presents approaches to constructing solutions (approximate and explicitly analytical) of boundary value problems describing the compaction of subsidence soils by the method of deep explosions. Numerical simulation of the dispersion of the coordinates of the gas atoms formed in the subsidence soil as a result of a deep explosion of a concentrated charge is carried out. Approximate solutions of the problem are constructed for soils with characteristic properties of isotropy and anisotropy for cases of complete absorption of gas atoms by the surrounding soil and complete reflection from it.

Keywords: subsidence soil, loess, soil compaction, deep explosion, mathematical modeling, numerical modeling, dispersion of atomic coordinates

ЧИСЛЕННОЕ МОДЕЛИРОВАНИЕ ДИСПЕРСИИ КООРДИНАТ АТОМОВ ГАЗА В МАТЕМАТИЧЕСКОЙ МОДЕЛИ УПЛОТНЕНИЯ ПРОСАДОЧНЫХ ГРУНТОВ ГЛУБИННЫМИ ВЗРЫВАМИ

Е.О. Тарасенко

Северо-Кавказский федеральный университет, г. Ставрополь, РОССИЯ

Аннотация. В рамках математического моделирования геологических систем возникают прикладные обратные задачи, требующие решения. В настоящей работе представлены подходы построения решений (приближенных и в явном аналитическом виде) краевых задач, описывающих уплотнение просадочных грунтов методом глубинных взрывов. Проведено численное моделирование дисперсии координат атомов газа, образующегося в просадочном грунте, в результате глубинного взрыва сосредоточенного заряда. Построены приближённые решения поставленной задачи для грунтов с характерными свойствами изотропности и анизотропности для случаев полного поглощения атомов газа окружающим его грунтом и полного отражения от него.

Ключевые слова: просадочный грунт, лёсс, уплотнение грунта, глубинный взрыв, математическое моделирование, численное моделирование, дисперсия координат атомов

INTRODUCTION

Engineering-geological design of buildings and structures requires rational and time-consuming numerical calculations of the density and deformation characteristics of soil. This is especially relevant on subsidence loess soils, which are rather mysterious and debatable by origin Quaternary rocks. Subsidence soil strata are widespread (more than 17%) on the territory of Russia. Their greatest concentration (about 80%) is fixed in the North Caucasus, the South of Russia, Siberia, Yakutia, etc. [1, 2]. There are different methods of soil compaction [3]. Here we shall consider a method of soil compaction by means of deep explosions of the concentrated charges. This method of compaction of subsidence soils in its practical implementation demonstrates low production costs and economic efficiency [4].

A DIRECT PROBLEM

Changes in values of the average density of the compacted soil skeleton q per unit time t at a point (x_1, x_2, x_3) in a given space from a concentrated source of explosive charge is described as an initial boundary problem, typical for the case of complete absorption of gas atoms by the surrounding soil (compaction of subsiding soil is realized) [5].

$$\frac{\partial q}{\partial t} + U\frac{\partial q}{\partial x} = \frac{\partial}{\partial x}K_x\frac{\partial q}{\partial x} + \\ + \frac{\partial}{\partial y}K_y\frac{\partial q}{\partial y} + \frac{\partial}{\partial z}K_z\frac{\partial q}{\partial z} + f, \\ t \in [t_0, T] \tag{1}$$

with initial conditions

$$q(t_0, x, y, z) = \\ = Q\delta(x - x^0)\delta(y - y^0)\delta(z - z^0), \tag{2}$$

and boundary conditions

$$q(t, x, y, z)\big|_{z=z^0} = 0,\ t > t_0. \tag{3}$$

In the case of complete reflection of the gas atoms from the surrounding ground, when the ground ejection to the surface is realized, the changes of mean ground density values q are described by the initial-boundary problem (1), (2),

$$K_{zz}\frac{\partial q}{\partial z}\bigg|_{z=z^0} = 0,\ t > t_0, \tag{4}$$

where $Q = const > 0$, $\delta(x)$ is the Dirac δ-function, $z^0 = H$ is the depth of the concentrated explosive charge, $U = const$ is the horizontal transfer rate (along the axis Ox), K_x, K_y, K_z is the diffusion coefficients.

The explosive gas source function is represented as

$$f(t, x, y, z) = Q \cdot R(t, x, y, z) = \\ = Q\delta(t - t_0)\delta(x - x^0)\times \\ \times\delta(y - y^0)\delta(z - H). \tag{5}$$

Suppose that U, K_x, K_y, K_z are continuous functions of the argument z:

$$U = U(z), \\ K_x = K_x(z),\ K_y = K_y(z),\ K_z = K_z(z)$$

In addition to equation (1) to calculate the average values of the compacted soil skeleton density, it is also possible to use the function [6, 7]

$$q'(t, x, y, z) = \frac{Q}{(2\pi)^{3/2}\sigma_x(t)\sigma_y(t)\sigma_y(t)}\times \\ \times\exp\left\{-\left[\frac{(x - \overline{U}t)^2}{2\sigma_x^2(t)} + \frac{y^2}{2\sigma_y^2(t)} + \right.\right. \\ \left.\left. + \frac{(z - H)^2}{2\sigma_z^2(t)}\right]\right\}, \tag{6}$$

which is a Gaussian function of the density distributions of the soil skeleton, where $\sigma_x^2(t)$, $\sigma_y^2(t)$, $\sigma_z^2(t)$ are the dispersion coordinate changes of the gas atoms in the compacted soil, respectively along the axes Ox, Oy, Oz at the time t; $\sigma_x^2(t)$, $\sigma_y^2(t)$, $\sigma_z^2(t)$ are functions continuously differentiable by the argument t, $t \geq 0$.

According to [8], for $t \to \infty$

$$\frac{\sigma_x^2(t)}{t} \to \sigma_x^2,\ \frac{\sigma_y^2(t)}{t} \to \sigma_y^2,\ \frac{\sigma_z^2(t)}{t} \to \sigma_z^2,$$

where $\sigma_x^2 > 0$, $\sigma_y^2 > 0$, $\sigma_z^2 > 0$ are certain constants. Consequently, the following approximations are valid for $t \to \infty$:

$$\sigma_x^2(t)=\sigma_x^2 t,\ \sigma_y^2(t)=\sigma_y^2 t,\ \sigma_z^2(t)=\sigma_z^2 t. \quad (7)$$

The density of the compacted soil skeleton $q'(t,x,y,z)$, given by the Gaussian (6), when the approximate equations (7) are fulfilled, satisfies the equation

$$\frac{\partial q'}{\partial t}+\overline{U}\frac{\partial q'}{\partial x}-\frac{1}{2}\sigma_x^2\frac{\partial^2 q'}{\partial x^2}-$$
$$-\frac{1}{2}\sigma_y^2\frac{\partial^2 q'}{\partial y^2}-\frac{1}{2}\sigma_z^2\frac{\partial^2 q'}{\partial z^2}=0$$

and the initial condition (2). Let us rewrite equation (1) as

$$\frac{\partial q}{\partial t}+\overline{U}\frac{\partial q}{\partial x}-\frac{1}{2}\sigma_x^2\frac{\partial^2 q}{\partial x^2}-\frac{1}{2}\sigma_y^2\frac{\partial^2 q}{\partial y^2}-$$
$$-\frac{1}{2}\sigma_z^2\frac{\partial^2 q}{\partial z^2}+\left(U(z)-\overline{U}\right)\frac{\partial q}{\partial x}=$$
$$=\frac{\partial}{\partial x}\left(K_x(z)-\frac{1}{2}\sigma_x^2\right)\frac{\partial q}{\partial x}+ \quad (8)$$
$$+\frac{\partial}{\partial y}\left(K_y(z)-\frac{1}{2}\sigma_y^2\right)\frac{\partial q}{\partial y}+$$
$$+\frac{\partial}{\partial z}\left(K_z(z)-\frac{1}{2}\sigma_z^2\right)\frac{\partial q}{\partial z}+f.$$

Obviously, the smaller the difference

$$\left(U(z)-\overline{U}\right),\ \left(K_x(z)-\frac{1}{2}\sigma_x^2\right),$$
$$\left(K_y(z)-\frac{1}{2}\sigma_y^2\right),\ \left(K_z(z)-\frac{1}{2}\sigma_z^2\right)$$

differs from 0, the less q', given by the Gaussian (6), will differ from the exact solution q (if only q continuously depends on the coefficients of equation (1)). In order to $\overline{U}$, σ_x^2, σ_y^2, σ_z^2 have the smallest scattering on the interval of $[0,h]$ from $U(z)$, $K_x(z)$, $K_y(z)$, $K_z(z)$, where h is the depth of penetration of the gas atoms into the surrounding ground, it is sufficient to fulfill the conditions:

$$\int_0^h\left(U(z)-\overline{U}\right)^2 dz\to\min_{\overline{U}},$$
$$\int_0^h\left(K_x(z)-\frac{1}{2}\sigma_x^2\right)^2 dz\to\min_{\sigma_x^2},$$
$$\int_0^h\left(K_y(z)-\frac{1}{2}\sigma_y^2\right)^2 dz\to\min_{\sigma_y^2},$$
$$\int_0^h\left(K_z(z)-\frac{1}{2}\sigma_z^2\right)^2 dz\to\min_{\sigma_z^2}, \quad (9)$$

then $\overline{U}$, σ_x^2, σ_y^2, σ_z^2, from the conditions (9), will take the form:

$$\overline{U}=\frac{1}{2}\int_0^h U(z)dz,\ \sigma_x^2=\frac{2}{h}\int_0^h K_x(z)dz,$$
$$\sigma_y^2=\frac{2}{h}\int_0^h K_y(z)dz,\ \sigma_z^2=\frac{2}{h}\int_0^h K_z(z)dz. \quad (10)$$

Consequently, the Gaussians $q'(t,x,y,z)$, given by expression (6), where $\sigma_x(t)$, $\sigma_y(t)$, $\sigma_z(t)$ are described by relations (7), (10), can be taken as an approximate solution of problems (1), (2), (3) and (1), (2), (4).

INVERSE PROBLEM FORMULATION

According to the known average values of the skeleton density $q_1(t,x,y,z)$ of the soil compacted by the method of deep explosion of the concentrated explosive source under the condition of complete gas atom reflection from the surrounding ground (release to the surface), or the average values of the skeleton density $q_2(t,x,y,z)$ of the compacted soil under the condition of complete gas absorption by the surrounding ground (compacting of the sagging soil), as well as by the given depth of placement of explosive H and the known values of explosive

charge power Q, $\sigma_x^2(t)$, $\sigma_y^2(t)$ are the dispersions of coordinates of gas atoms in the surrounding soil, respectively along the axes Ox, Oy, to determine the unknown values $\sigma_z^2(t)$ dispersions of coordinates of gas atoms in the compacted soil along the axis Oz at the time of t.

NUMERICAL SIMULATION

Build an approximate solution of the inverse problem on the basis of the apparatus of numerical methods for solving transcendental equations. Let us apply the method of simple iteration [9, 10]. Consider two cases, according to the statement of the problem, for $q_1(t,x,y,z)$ and $q_2(t,x,y,z)$.

1) numerical solution of the applied problem by the simple iteration method (under the assumption that there is a complete reflection of the gas atoms by the surrounding ground, the surface emission is realized). Assuming that the interval $[a,b]$ is separated (a and b estimated, e.g., by selection or graphical method), which contains the sought root σ_z of the equation

$$q_1(t,x,y,z)=\frac{Q}{(2\pi)^{3/2}\sigma_x\sigma_y\sigma_z t^3}\times \times\exp\left\{-\left(\frac{\left(x-\overline{U}t\right)^2}{2\sigma_x^2 t}+\frac{y^2}{2\sigma_y^2 t}\right)\right\}\times \times\left[\begin{array}{l}\exp\left\{-\frac{(z-H)^2}{2\sigma_z^2 t}\right\}+\\ +\exp\left\{-\frac{(z+H)^2}{2\sigma_z^2 t}\right\}\end{array}\right]=0. \quad (11)$$

If the investigated geological medium has characteristic properties of anisotropy, the equation (11) is rewritten in the following form

$$\sigma_z=\frac{Q}{q_1(t,x,y,z)(2\pi)^{3/2}\sigma_x\sigma_y t^3}\times \times\exp\left\{-\left(\frac{\left(x-\overline{U}t\right)^2}{2\sigma_x^2 t}+\frac{y^2}{2\sigma_y^2 t}\right)\right\}\times \times\left[\begin{array}{l}\exp\left\{-\frac{(z-H)^2}{2\sigma_z^2 t}\right\}+\\ +\exp\left\{-\frac{(z+H)^2}{2\sigma_z^2 t}\right\}\end{array}\right],$$

Iterative successive approximations to the desired root will be defined according to representation:

$$\sigma_z^{(n+1)}=\frac{Q}{q_1(t,x,y,z)(2\pi)^{3/2}\sigma_x\sigma_y t^3}\times \times\exp\left\{-\left(\frac{\left(x-\overline{U}t\right)^2}{2\sigma_x^2 t}+\frac{y^2}{2\sigma_y^2 t}\right)\right\}\times \times\left[\begin{array}{l}\exp\left\{-\frac{(z-H)^2}{2\left(\sigma_z^{(n)}\right)^2 t}\right\}+\\ +\exp\left\{-\frac{(z+H)^2}{2\left(\sigma_z^{(n)}\right)^2 t}\right\}\end{array}\right]. \quad (12)$$

If the investigated geological medium has isotropic properties, then $\sigma_z=\sigma_y=\sigma_x$. Therefore, the equation (11) can be represented as follows

$$\sigma_z=\sqrt[3]{\frac{Q}{q_1(t,x,y,z)(2\pi)^{3/2}\sigma_z^2 t^3}}\times \times\sqrt[3]{\exp\left\{-\left(\frac{\left(x-\overline{U}t\right)^2}{2\sigma_z^2 t}+\frac{y^2}{2\sigma_z^2 t}\right)\right\}}\times$$

$$\times\sqrt[3]{\left[\exp\left\{-\frac{(z-H)^2}{2\sigma_z^2 t}\right\}+\exp\left\{-\frac{(z+H)^2}{2\sigma_z^2 t}\right\}\right]}.$$

The iterative successive approximations to the desired root in this case will be determined instead of formula (12) by the following representation:

$$\sigma_z^{(n+1)}=\sqrt[3]{\frac{Q}{q_1(t,x,y,z)(2\pi)^{3/2}\left(\sigma_z^{(n)}\right)^2 t^3}}\times$$
$$\times\sqrt[3]{\exp\left\{-\left(\frac{\left(x-\overline{U}t\right)^2}{2\left(\sigma_z^{(n)}\right)^2 t}+\frac{y^2}{2\left(\sigma_z^{(n)}\right)^2 t}\right)\right\}}\times$$
$$\times\sqrt[3]{\left[\begin{array}{l}\exp\left\{-\dfrac{(z-H)^2}{2\left(\sigma_z^{(n)}\right)^2 t}\right\}+\\ +\exp\left\{-\dfrac{(z+H)^2}{2\left(\sigma_z^{(n)}\right)^2 t}\right\}\end{array}\right]}. \qquad (13)$$

From the segment of the root separation $[a,b]$, we arbitrarily determine the first approximation $\sigma_z^{(1)}$ to the desired root (the first iteration).

The criterion for the end of the computational search for the solution of the equation is the fulfillment of the inequality

$$\left|\sigma_z^{(n)}-\sigma_z^{(n-1)}\right|<\varepsilon, \qquad (14)$$

where ε is the desired accuracy of calculations.

2) numerical construction of the solution of the set problem by the method of simple iteration for the case of complete absorption of gas atoms by the surrounding soil (realization of compaction of subsidence thickness). Assuming that the interval $[a,b]$ (as above, a andи b estimated by fitting method or graphical method) containing the required root of the equation

$$q_2(t,x,y,z)=\frac{Q}{(2\pi)^{3/2}\sigma_x\sigma_y\sigma_z t^3}\times$$
$$\times\exp\left\{-\left(\frac{\left(x-\overline{U}t\right)^2}{2\sigma_x^2 t}+\frac{y^2}{2\sigma_y^2 t}\right)\right\}\times$$
$$\times\left[\begin{array}{l}\exp\left\{-\dfrac{(z-H)^2}{2\sigma_z^2 t}\right\}-\\ -\exp\left\{-\dfrac{(z+H)^2}{2\sigma_z^2 t}\right\}\end{array}\right]=0. \qquad (15)$$

Given that the studied geological medium has characteristic properties of anisotropy, let us transform equation (15) to the form:

$$\sigma_z=\frac{Q}{q_2(t,x,y,z)(2\pi)^{3/2}\sigma_x\sigma_y t^3}\times$$
$$\times\exp\left\{-\left(\frac{\left(x-\overline{U}t\right)^2}{2\sigma_x^2 t}+\frac{y^2}{2\sigma_y^2 t}\right)\right\}\times$$
$$\times\left[\exp\left\{-\frac{(z-H)^2}{2\sigma_z^2 t}\right\}-\exp\left\{-\frac{(z+H)^2}{2\sigma_z^2 t}\right\}\right].$$

The iterative process of successive approximations to the desired root will be numerically determined by the formula

$$\sigma_z^{(n+1)}=\frac{Q}{q_2(t,x,y,z)(2\pi)^{3/2}\sigma_x\sigma_y t^3}\times$$
$$\times\exp\left\{-\left(\frac{\left(x-\overline{U}t\right)^2}{2\sigma_x^2 t}+\frac{y^2}{2\sigma_y^2 t}\right)\right\}\times$$
$$\times\left[\begin{array}{l}\exp\left\{-\dfrac{(z-H)^2}{2\left(\sigma_z^{(n)}\right)^2 t}\right\}-\\ -\exp\left\{-\dfrac{(z+H)^2}{2\left(\sigma_z^{(n)}\right)^2 t}\right\}\end{array}\right]. \qquad (16)$$

If the investigated geological medium has characteristic properties of isotropy, then $\sigma_z = \sigma_y = \sigma_x$. Consequently, the equation (15) is transformed to the form

$$\sigma_z = \sqrt[3]{\frac{Q}{q_2(t,x,y,z)(2\pi)^{3/2}\sigma_z^2 t^3}} \times \sqrt[3]{\exp\left\{-\left(\frac{\left(x-\overline{U}t\right)^2}{2\sigma_z^2 t}+\frac{y^2}{2\sigma_z^2 t}\right)\right\}} \times \sqrt[3]{\left[\exp\left\{-\frac{(z-H)^2}{2\sigma_z^2 t}\right\}-\exp\left\{-\frac{(z+H)^2}{2\sigma_z^2 t}\right\}\right]}.$$

The iterative sequence of approximations to the required root instead of (16) will be constructed according to the formula

$$\sigma_z^{(n+1)} = \sqrt[3]{\frac{Q}{q_2(t,x,y,z)(2\pi)^{3/2}\left(\sigma_z^{(n)}\right)^2 t^3}} \times \sqrt[3]{\exp\left\{-\left(\frac{\left(x-\overline{U}t\right)^2}{2\left(\sigma_z^{(n)}\right)^2 t}+\frac{y^2}{2\left(\sigma_z^{(n)}\right)^2 t}\right)\right\}} \times \sqrt[3]{\left[\exp\left\{-\frac{(z-H)^2}{2\left(\sigma_z^{(n)}\right)^2 t}\right\}-\exp\left\{-\frac{(z+H)^2}{2\left(\sigma_z^{(n)}\right)^2 t}\right\}\right]}. \quad (17)$$

The first approximation $\sigma_z^{(1)}$ to the required root (first iteration) is any σ_z value, which belongs to the root separation interval $[a,b]$.

The criterion for ending the computational process of finding a numerical solution to equation (15) is the fulfillment of the inequality

$$\left|\sigma_z^{(n)} - \sigma_z^{(n-1)}\right| < \varepsilon,$$

where ε is the desired accuracy of calculations.

CONCLUSIONS

The results of this study are analytical and numerical (iterative) representations of dispersion changes in the coordinates of gas atoms $\sigma_z^2(t)$ in the ground compacted by the deep blast method. The cases of complete absorption of gas atoms by the surrounding ground and the surface ejection of the ground during the explosion have been described. Isotropic and anisotropic properties of the compacted soil have been considered. The obtained expressions allow to perform computational experiments with a given accuracy.

The author thanks Boris F. Galay, Doctor of Geological and Mineralogical Sciences, Professor, Professor of the North Caucasus Federal University Construction Department, for his assistance in conducting this scientific research.

REFERENCES

1. Loess rocks of the USSR. V. 1. Engineering-geological features and problems of rational use / Ed. Sergeeva E.M., Larionova A.K., Komissarova N.N. Moscow. Nauka, 1986. 273 p.
2. Loess rocks of the USSR. T. 2. Regional features / Ed. Sergeeva E.M., Bykova V.S., Komissarova N.N. Moscow. Nauka, 1986. 276 p.
3. **Pantyushina E. V.** Loess soils and engineering methods for eliminating their subsidence properties // Polzunovsky vestnik. 2011. № 1. P. 127-130.
4. **Galay B. F.** Manual on compaction of subsident loess soils by deep explosions

in the conditions of the North Caucasus (research, design, production of works) / B. F. Galay. Ed. 3rd, add. Stavropol, Serviceshkola, NCFU. 2016. 142 p.
5. **Tarasenko E. O., Tarasenko V. S., Gladkov A.V.** Mathematical modeling of compaction of subsident loess soils of the North Caucasus by deep explosions // Bulletin of the Tomsk Polytechnic University. Geo Assets Engineering. 2019. vol. 330, №. 11, P. 94-101. DOI: 10.18799/24131830/2019/11/2352.
6. **Tarasenko E.O., Gladkov A.V.** Numerical solution of inverse problems in mathematical modeling of geological systems // Bulletin of the Tomsk Polytechnic University. Engineering of georesources. 2022. V. 333. №. 1. P. 105-112. DOI: 10.18799/24131830/2022/1/3208
7. **Tarasenko E.O., Gladkov A.V., Gladkova N.A.** Solution for Inverse Boundary Value Problems on the Power of a Concentrated Charge in a Mathematical Model of Subsidence Soils Compaction // Mathematics and its Applications in New Computer Systems. MANCS 2021. Lecture Notes in Networks and Systems, Springer. 2022. Vol 424. P. 537–545. DOI: 10.1007/978-3-030-97020-8_49
8. **Semenchin E.A.** Analytical solutions of boundary value problems in the mathematical model of atmospheric diffusion / E.A. Semenchin. Stavropol. Publishing house SKIUU. 1993. 141 p. ISBN 5-900429-45-8
9. **Bakhvalov N.S.** Numerical methods / N.S. Bakhvalov. Moscow. Nauka. 1973. 614 p.
10. **Verzhbitsky V. M.** Numerical methods: (mathematical analysis and ordinary differential equations) / V.M. Verzhbitsky. Moscow. Direct-Media. 2013. 400 p. ISBN 978-5-4458-3876-0.

СПИСОК ЛИТЕРАТУРЫ

1. Лёссовые породы СССР. Т. 1. Инженерно-геологические особенности и проблемы рационального использования / Под ред. Сергеева Е.М., Ларионова А.К., Комиссаровой Н.Н. Москва: Наука, 1986. 273 с.
2. Лёссовые породы СССР. Т. 2. Региональные особенности / Под ред. Сергеева Е.М., Быковой В.С., Комиссаровой Н.Н. Москва: Наука, 1986. 276 с.
3. **Пантюшина Е.В.** Лёссовые грунты и инженерные методы устранения их просадочных свойств // Ползуновский вестник. 2011. № 1. С. 127-130.
4. **Галай Б.Ф.** Пособие по уплотнению просадочных лессовых грунтов глубинными взрывами в условиях Северного Кавказа (изыскания, проектирование, производство работ). Ставрополь, 2016. 142 с.
5. **Тарасенко Е.О., Тарасенко В.С., Гладков А.В.** Математическое моделирование уплотнения просадочных лёссовых грунтов Северного Кавказа глубинными взрывами // Известия Томского политехнического университета. Инжиниринг георесурсов . 2019. Т. 330. № 11. С. 94-101. DOI: 10.18799/24131830/2019/11/2352
6. **Тарасенко Е.О., Гладков А.В.** Численное решение обратных задач при математическом моделировании геологических систем // Известия Томского политехнического университета. Инжиниринг георесурсов. 2022. Т. 333. № 1. С. 105-112. DOI: 10.18799/24131830/2022/1/3208
7. **Tarasenko E.O., Gladkov A.V., Gladkova N.A.** Solution for Inverse Boundary Value Problems on the Power of a Concentrated Charge in a Mathematical Model of Subsidence Soils Compaction // Mathematics and its

Applications in New Computer Systems. MANCS 2021. Lecture Notes in Networks and Systems, Springer. 2022. Vol 424. P. 537–545. DOI: 10.1007/978-3-030-97020-8_49

8. **Семенчин Е.А.** Аналитические решения краевых задач в математической модели атмосферной диффузии. – Ставрополь: Издательство СКИУУ, 1993. 141 с. ISBN 5-900429-45-8
9. **Бахвалов Н.С.** Численные методы. Москва: Наука, 1973. 614 с.
10. **Вержбицкий В.М.** Численные методы: (математический анализ и обыкновенные дифференциальные уравнения). – Москва: Директ-Медиа, 2013. – 400 с. – ISBN 978-5-4458-3876-0.

Tarasenko Elena Olegovna, Associate Professor of the Department of Computational Mathematics and Cybernetics of the Faculty of Mathematics and Computer Sciences named after Professor N.I. Chervyakov, North Caucasus Federal University, Candidate of Physical and Mathematical Sciences, Russia, 355009, Stavropol, Pushkin str., 1, building 2, auditorium 308. Tel. +7-905-443-68-24, e-mail: galail@mail.ru

Тарасенко Елена Олеговна, доцент кафедры Вычислительной математики и кибернетики факультета Математики и компьютерных наук имени профессора Н.И. Червякова, Северокавказский федеральный университет, кандидат физико-математических наук, доцент, Россия, 355009, г. Ставрополь, ул. Пушкина, д. 1, корпус 2, аудитория 308. Тел. +7-905-443-68-24, e-mail: galail@mail.ru

International Journal for Computational Civil and Structural Engineering, 19(1) 155–167 (2023)

DOI:10.22337/2587-9618-2023-19-1-155-167

NUMERICAL ANALYSIS OF THERMAL EFFICIENCY OF EXTERNAL WALLS WITH HEAT-CONDUCTING INCLUSIONS

Valentina M. Tusnina

National Research Moscow State University of Civil Engineering, Moscow, RUSSIA

Abstract. In the practice of design and construction, methods of numerical calculations using modern software package are widely used, which make it possible to effectively solve the problems of designing, erecting and operating buildings and structures of various functional purposes. A comparative analysis of numerical, theoretical and experimental studies in the field of building structures, buildings and structures shows that accurate calculation methods provide reliable data on the subject of research. This article presents the results of numerical studies of the thermal efficiency of inhomogeneous vertical fences on the example of several options for constructive solutions for the outer walls of a building. The studies were carried out using the TEPL software package, developed for calculating three-dimensional temperature fields based on the control volume method. The results of the analysis of the temperature distribution on the heat exchange surfaces are presented, which made it possible to determine the zones of excessive heat losses in the structures under study. Significant heat losses on the slopes of window openings are revealed, which should be taken into account when calculating the reduced resistance to heat transfer of the fence. The TEPL software package allows not only to correctly estimate heat losses, but also automatically obtain the value of the reduced heat transfer resistance of the fence structure, taking into account all the features of its design solution.

Keywords: 3D numerical method, reduced heat transfer resistance, external walls, heat losses, thermal efficiency

ЧИСЛЕННЫЙ АНАЛИЗ ТЕПЛОВОЙ ЭФФЕКТИВНОСТИ НАРУЖНЫХ СТЕН С ТЕПЛОПРОВОДНЫМИ ВКЛЮЧЕНИЯМИ

В.М. Туснина

Национальный исследовательский Московский государственный строительный университет, г. Москва, РОССИЯ

Аннотация. В практике проектирования и строительства широко применяются численные расчеты с использованием современных вычислительных комплексов, позволяющие эффективно решать задачи по проектированию, возведению и эксплуатации зданий и сооружений различного функционального назначения. Сравнительный анализ численных, теоретических и экспериментальных исследований в области строительных конструкций, зданий и сооружений показывает, что точные методы расчета дают достоверные данные о предмете исследования. В настоящей статье приводятся результаты численных исследований тепловой эффективности неоднородных вертикальных ограждений на примере нескольких вариантов конструктивного решения наружных стен здания. Исследования проводились с использованием вычислительного комплекса TEPL, разработанного для расчета трехмерных температурных полей на основе метода контрольного объема. Приведены результаты анализа распределения температур на поверхностях теплообмена, позволившие определить зоны излишних тепловых потерь в исследуемых конструкциях. Выявлены значительные тепловые потери на откосах оконных проемов, которые следует учитывать при расчете приведенного сопротивления теплопередаче ограждения. Вычислительный комплекс TEPL позволяет не только корректно оценить тепловые потери, но и автоматически получить величину приведенного сопротивления теплопередаче конструкции ограждения с учетом всех особенностей её конструктивного решения.

Ключевые слова: трехмерный численный расчет, приведенное сопротивление теплопередаче, наружные стены, тепловые потери, тепловая эффективность

1. INTRODUCTION

The parameter that characterizes the thermal qualities of the envelope is the total heat transfer resistance. For multilayer structures, this parameter is defined as the sum of thermal resistance to heat transfer of all layers of the structure and the resistance to heat perception and heat dissipation of its internal and external surfaces, respectively. The thermal transmission resistance of a multilayer structure without thermal conductive inclusions is determined by the formula:

$$R = \frac{1}{\propto_{int}} + \sum_1^n \frac{\delta_i}{\lambda_i} + \frac{1}{\propto_{ext}} \quad , \qquad (1)$$

where α_{int} is the heat transfer coefficient of the internal surface of the structure, W/ m^2·°C;
α_{ext} is the heat transfer coefficient of the external surface of the structure, W/ m^2·°C;
δ_i is the depth of the i^{th} structure's layer, m;
λ_i is the heat transfer coefficient of the i^{th} layer of the structure, W/ m·°C.
Design solutions of external vertical enclosures of modern buildings are quite diverse. Most of them are complex heterogeneous systems with heat-conducting inclusions. It is not possible to determine correctly the heat transfer resistance of such structures by the formula (1). Therefore, approximate methods are used in design practice to account heat-conductive inclusions in a structure by means of application of coefficient of thermo-technical homogeneity *r*. This coefficient characterizes the effectiveness of insulation of the structure. It is determined by the formula:

$$r = \frac{R_{red}}{R},$$

where R_{red} is the reduced heat transfer resistance of a fragment of the building's thermal envelope, m^2·°C/W;
R is the conditional resistance to heat transfer of the building envelope averaged over area or a dedicated enclosing structure, m^2·°C/W.

Thermal analysis according to the regulatory methodology is based on the representation of a fragment of the thermal protection envelope of the building as a set of independent elements affecting the heat losses. The specific heat losses through the linear thermal heterogeneity are determined as analysis result of the two-dimensional temperature field in the enclosing structure. Determination of the reduced heat transfer resistance R_{red} by the proposed methodology leads to significant errors in assessing the thermal efficiency of complex heterogeneous structures of enclosures that does not allow to take into account the influence of local thermal inclusions in the form of brackets, anchors, etc. elements available in the facade systems of modern buildings
The reduced heat transfer resistance of an inhomogeneous structure with thermal inclusions [1] can be determined correctly using the results of the analysis of the three-dimensional temperature field:

$$R_{red} = (t_{int} - t_{\text{ext}})/\, \text{q}\,,$$

where t_{int} is the temperature of internal air, °C ;
t_{ext} is the temperature of external air, °C;
q is the heat flow's density related to the design surface of the enclosure, W/m^2.
The reliability of the thermal efficiency assessment of inhomogeneous structures with thermal inclusions based on the numerical analysis of spatial temperature fields has been confirmed by numerous studies. The numerical calculation efficiency of the reduced heat transfer resistance of enclosing structures has been established by the authors of studies [2], who developed a calculation model of visual programming for building design. Work [3, 4] was devoted to the numerical analysis of increasing the thermal protection of a building with passive solar heat supply through the integration of elements of active solar units in the absorbing layer of the accumulating envelope structure. The calculation results for the three-dimensional temperature field of the curtain facade system given in [5] showed good

convergence with the experimental data, while the calculation results according to the normative methodology differed significantly from the experimental values. The authors of work [6] conducted a numerical analysis of the thermal efficiency of exterior walls, which allowed to choose the most optimal structures for the reconstruction of buildings. The authors of [7, 8] performed a 3D numerical simulation using the ANSYS Fluent computing complex to study the effect of heat losses through "cold bridges" in the areas of adjoining floor structures to the exterior walls of the building. Studies of the dynamic process of heat transfer through the enclosing structures of buildings in various climatic conditions using numerical simulation are devoted to the works [9, 10]. Using computer simulation [11], the effect of the mortar joint thickness on the thermal efficiency of buildings with heterogeneous walls with insulation is studied. Work [12] presents the numerical research results for the thermal efficiency of composite wall structures with an air gap. Those study was based on a calculation module developed by the authors using the MATLAB, which solves a one-dimensional heat flow diffusion equation with convective periodic boundary conditions. Significant heat losses through exterior walls with windows were revealed by the authors of [13, 14] by the results of numerical calculation of three-dimensional temperature fields. The index of thermal comfort of a room taking into account radiator heating was determined on the basis of numerical analysis [14]. Studies [15] are devoted to creating energy three-dimensional models of buildings on the basis of computer modeling. The issue of accuracy of numerical thermal calculations is dedicated to the work [16], which provides a comparative analysis of the results of numerical and experimental methods for research of heat transfer in enclosing structures for compliance with the calculated and experimental models.

This study was aimed at investigating the heat transfer through exterior building envelopes and evaluating their thermal efficiency based on the calculation of a three-dimensional temperature field using the TEPL computational complex [17].

2. METHODS

The TEPL computational complex [17] allow calculation of three-dimensional steady-state fields in order to analyze the temperature distribution in a building envelope and determine its reduced resistance. The computational program allows: entering and correcting initial data; performing graphical control of the computational scheme; performing numerical calculation of three-dimensional temperature fields of complex facade systems containing thermal inclusions in the form of bars; performing graphical analysis of temperature distribution in the structure; calculating the reduced heat transfer resistance of a multi-layer heterogeneous structure.

The numerical method has been developed on the basis of the control volume method for three-dimensional temperature fields under steady-state thermal conductivity conditions. The differential equation of three-dimensional steady-state thermal conductivity has the following form:

$$\frac{\partial}{\partial x}\left(\lambda\frac{\partial T}{\partial x}\right)+\frac{\partial}{\partial y}\left(\lambda\frac{\partial T}{\partial y}\right)+\frac{\partial}{\partial z}\left(\lambda\frac{\partial T}{\partial z}\right)+S=0, \quad (2)$$

where x, y, z are the coordinates;
T is the temperature;
λ is thermal conductivity coefficient;
S is the power of thermal emission per unit volume.

Numerical integration of differential equation (2) is applied to calculate temperature distribution in the structure. One of the variants of the numerical solution can be a variation of the weighted discrepancy method in the form of the control volume method [18]. The essence of the method is that the differential equation is integrated over the elementary control volumes into which the structure under consideration is separated (Figure 1).

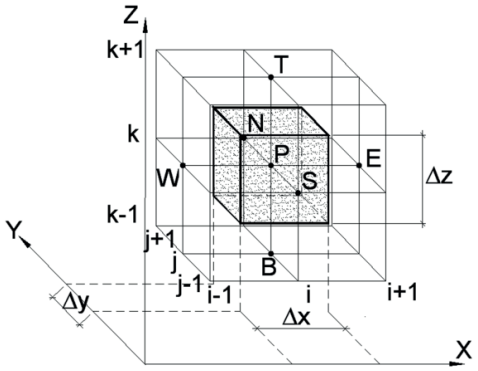

Figure 1. Calculation scheme

A nodal point P is located in the center of the control volume (highlighted with shading lines in Fig. 1). The mesh is divided into control volumes so that one material is located within each control volume, and the boundary of the control volume is in the middle between the nodal points. Neighboring node points B, E, N, S, T, W should be located in the centers of neighboring control volumes. The exceptions are the node points on the boundary planes of the structure partition. These points are located on the outer boundaries of the structure, i.e. the outermost control volumes have node points located on the outer boundaries of the volume and not inside it.

In the numerical simulation, the temperature within each control volume is assumed to be constant and equal to the temperature at the corresponding node point. The peculiarity of the control volume method is that the law of conservation of energy is observed regardless of the mesh partition of the computational model. That is, the heat flow through any surfaces does not depend on the partition mesh. However, the mesh should be thickened in order to obtain an accurate value of temperature in places of its high gradient, since the temperature at the node points depends on the division mesh.

For the three-dimensional problem, the discrete analogue of equation (2), which is expressed by the energy conservation law, according to the recommendations [18], has the form:

$$a_p T_p = a_E T_E + a_W T_W + a_N T_N + a_S T_S + a_T T_T + a_B T_B + b, \quad (3)$$

where T_E, T_W, T_N, T_S, T_T, T_B are the temperature at the nodal points;

the coefficients at temperatures:

$$a_p = a_E + a_W + a_N + a_S + a_T + a_B;$$

$$a_E = \frac{\lambda_e \Delta y \Delta z}{(\delta x)_e}; \qquad a_S = \frac{\lambda_s \Delta x \Delta z}{(\delta y)_s};$$

$$a_W = \frac{\lambda_w \Delta y \Delta z}{(\delta x)_w}; \qquad a_T = \frac{\lambda_t \Delta x \Delta y}{(\delta z)_t};$$

$$a_N = \frac{\lambda_n \Delta x \Delta z}{(\delta y)_n}; \qquad a_B = \frac{\lambda_b \Delta x \Delta y}{(\delta z)_b}.$$

The thermal conductivity coefficients at the boundaries of the control volume λ_b, λ_e, λ_n, λ_s, λ_t, λ_w are determined using the thermal conductivity coefficients of materials of the control volumes. As the test analyses have shown, the most exact correspondence of heat flows at the boundary of the test volumes is obtained if the thermal conductivity coefficients at the boundaries of the test volumes are determined by the formulas:

$$\lambda_b = \frac{2\lambda_P \lambda_B}{\lambda_P + \lambda_B}; \qquad \lambda_e = \frac{2\lambda_P \lambda_E}{\lambda_P + \lambda_E};$$

$$\lambda_n = \frac{2\lambda_P \lambda_N}{\lambda_P + \lambda_N};$$

$$\lambda_s = \frac{2\lambda_P \lambda_S}{\lambda_P + \lambda_S}; \qquad \lambda_t = \frac{2\lambda_P \lambda_T}{\lambda_P + \lambda_T};$$

$$\lambda_w = \frac{2\lambda_P \lambda_W}{\lambda_P + \lambda_W}.$$

The following dimensions are used when constructing the discrete equation:

Δx, Δy, Δz are the dimensions of the control volume in which the node point P is located;

$(\delta x)_e$ is the distance along the X axis from point P to point E;

$(\delta x)_w$ is the distance along the X-axis from point P to point W;

$(\delta y)_n$ is the distance along the Y axis from point P to point N;

$(\delta y)_s$ is the distance along the Y axis from point P to point S;

$(\delta z)_t$ is the distance along the Z axis from point P to point T;

$(\delta z)_b$ is the distance along the Z axis from point P to point B;

If there are thermal inclusions between node points, for example in the form of rod elements,

in equation (2) the coefficients a_B, a_E, a_W, a_N, a_S, a_T are calculated as follows:

$$a_E = \frac{\lambda_e \Delta y \Delta z + \lambda_s A}{(\delta x)_e}; \qquad a_W = \frac{\lambda_w \Delta y \Delta z + + \lambda_s A}{(\delta x)_w};$$

$$a_N = \frac{\lambda_n \Delta x \Delta z + \lambda_s A}{(\delta y)_n}; \qquad a_S = \frac{\lambda_s \Delta x \Delta z + \lambda_s A}{(\delta y)_s};$$

$$a_T = \frac{\lambda_t \Delta x \Delta y + \lambda_s A}{(\delta z)_t}; \qquad a_B = \frac{\lambda_b \Delta x \Delta y + \lambda_s A}{(\delta z)_b},$$

where λ_s is the thermal conductivity coefficient of the rod, A is the area of the bar.

$b = S_c \Delta x \Delta y \Delta z$, where S_c is the power of heat emission in the control volume.

To calculate the temperature distribution in the structure, in addition to assigning the geometry and material distribution, it is necessary to set the boundary conditions. Three variants of boundary conditions are possible:

- the temperature at the point is set, then in the calculation the temperature at the node point is taken equal to the set temperature;
- the heat flux density is given, then:

$$b = q_x \Delta y \Delta z + q_y \Delta x \Delta z + q_z \Delta x \Delta y + S_c \Delta x \Delta y \Delta z,$$

where q_x, q_y, q_z are the heat flux density in the direction of the X, Y, Z axes, respectively;

- there is heat exchange with the medium having a given temperature at the point, then at the heat exchange coefficient α and the temperature of the medium T_f:

$$a_p = a_E + a_W + a_N + a_S + a_T + a_B + \alpha$$

$b = S_c \Delta x \Delta y \Delta z + \alpha T_f \Delta y \Delta z$ is the heat exchange at the surface with the normal along the X-axis,

$b = S_c \Delta x \Delta y \Delta z + \alpha T_f \Delta x \Delta z$ is the heat exchange at the surface with the normal along the Y-axis,

$b = S_c \Delta x \Delta y \Delta z + \alpha T_f \Delta x \Delta y$ is the heat exchange at the surface with the normal along the Z-axis.

Equation (3) is formed for all N nodal points. This equation takes into account the presence of areas of different materials in the structure, thermal inclusions, boundary conditions. Aggregate of equations for all nodal points forms a system of N linear equations with N unknown temperatures. The solution to this system of equations allows defining the temperature at the nodal points.

Systems of linear equations can be solved using the Gaussian method or the iterative method. The computational complex for calculating three-dimensional temperature fields TEPL [17] implements the iterative method. As shown in [18], the iterative process converges taking into account the boundary conditions. To accelerate the convergence along the lines of node points in the direction of the Y axis, a direct solution of the system of order N_y (N_y is the number of partition points along the Y axis) is performed, which is then iteratively refined by running along all axes. The solution process continues until, at the next iteration step, the temperature refinement for all points does not exceed the specified error. In this case, for an error of 0.01 ºC, in most cases the temperature distribution is close to the actual one. In case of significant temperature gradients, e.g. due to the presence of thermal inclusions, the error should be reduced to 0.001-0.0001 ºC.

The TEPL computational complex [17] allows to reliably investigate heat losses through multi-layer heterogeneous enclosures with the identification of areas where condensation may occur due to thermal inclusions, as well as to determine the value of the reduced heat transfer resistance of the structure under study. The automation of determining the heat transfer resistance in the TEPL calculation complex makes it possible to take into account the temperature at all points on the heat transfer surfaces and the surface area, while ensuring a high accuracy of determining the heat loss through the enclosure.

3. RESULTS AND DISCUSSION

The thermal efficiency of multi-layer exterior walls with different structural solutions was evaluated using the TEPL computational complex. There were considered designs of walls with inner layers made of bricks and gas concrete blocks, insulation and curtain facade systems, as well as brick walls with different arrangement of insulation layer and finishing made of facing gypsum boards and brick walls without insulation layer. The design schemes included wall fragments with windows, reinforced concrete slabs, and partitions adjacent to the walls.

It is necessary to note, that approximate analysis does not allow estimating heat losses through window linings and thermal conductive inclusions, which should be considered in thermal-technical calculations of heterogeneous structures of enclosures. Because of the presence of materials with different coefficients of thermal conductivity such as thermal inclusions, air gaps associated with the outside or inside air, windows are formed areas with increased heat losses, reducing the thermal efficiency of fencing. Increased heat losses on individual wall surfaces arise due to the presence in the construction of areas with low thermal resistance, which are the so-called "cold bridges", through which heat flows outward, bypassing the thermal insulation of the wall.

For exterior wall structures, such areas are the surfaces of the window opening slopes, which, depending on the design solution, may include elements with thermal conductivity coefficients several times lower than the thermal conductivity coefficient of the main walls of the building. Such elements can be reinforced concrete lintels or metal profiles framing the window openings.

Figure 1 shows the temperature distribution in the wall of aerated concrete blocks with windows, clearly demonstrating the areas of low temperatures on the surface of the window jambs.

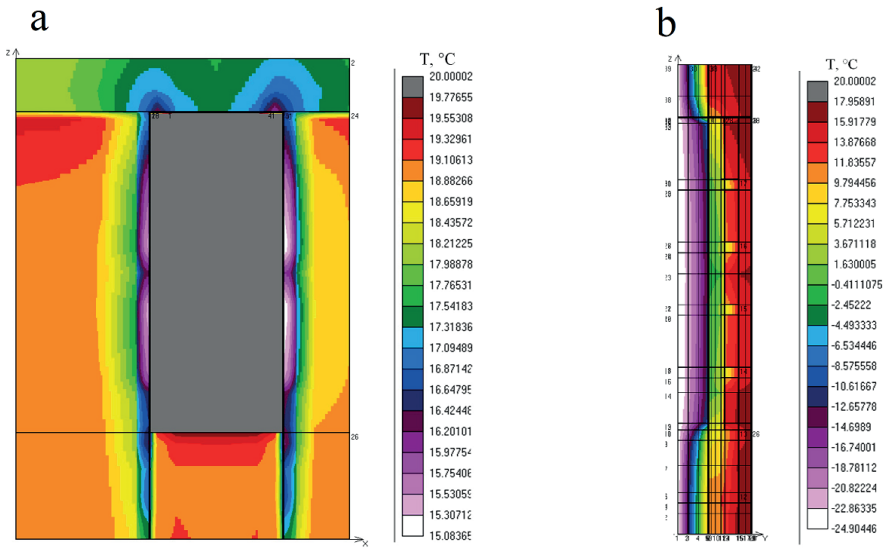

Figure 1. Temperature distribution in the wall structure made of aerated concrete blocks with a window: a - on the inner surface of the wall along the Y axis; b - on the inner surface of the window slope along the X axis

According to the calculation results, the temperature on the inner surface of the wall does not decrease below the dew point temperature everywhere. For living quarters it is 10.2°C with a normal humidity level of 55% and an interior air temperature of +20°C, which corresponds to the regulatory requirements for housing design. However the calculation shows

that the temperature on some parts of the window lining surfaces is between 5.71 - 9.79 °C, which indicates a possible condensation of water vapor on these wall surfaces. This can lead to the appearance of mold and mildew, which will negatively affect the operational reliability of the structure of the outer walls of the building.

As a result of numerical analysis of the thermal efficiency of aerated concrete block walls, it was found that half of the total heat loss through the structure of such a wall accounts for its inner surface and window soffits. At the same time, the heat losses occurring through the slopes of the window openings accounted for almost half of the heat losses through the inner surface of the wall (Table 1).

Table 1. Heat loss through the walls of aerated concrete blocks with windows

Потери тепла в различных областях стены, W/ %		
На внутренней поверхности	На оконных откосах	На окнах
38,49/24	39,57/26	79,02/50

The thermal transmittance of exterior walls made of gas concrete blocks without windows and thermal conductive inclusions R determined by the formula (1) is 2.108 m2-°C/W, and obtained by numerical calculation taking into account all inhomogeneities of the wall structure - R_{red} = 1.538 m^2°C/W. This is the thermal transmittance value that must be accounted for to evaluate the thermal efficiency of the building envelope, which correctly evaluates all heat loss (Q) through the envelope. As can be seen from Table 1, the value of total heat loss through the wall structure is 157.08 W, and the value of heat loss obtained from the calculation of heat transfer resistance according to the formula (1) is 103.37 W, which is 1.52 times lower than that determined by the numerical calculation, which takes into account all the heterogeneities existing in the fence.

The temperature distribution patterns on the heat transfer surfaces show that large heat losses occurred mainly through the surfaces of the window soffits, where there is no thermal insulation layer (Figure 2, a). As evidenced from the calculation of a wall with additional insulation made of material with a thermal conductivity coefficient of λ = 0.05 W/m°C, placed on all vertical and horizontal window opening soffits (Figure 2, b), a more favorable temperature distribution was observed in the wall structure (Figure 3). All wall surfaces recorded a temperature of at least 15.91 °C, which eliminates condensation and does not impair the performance of the exterior envelope.

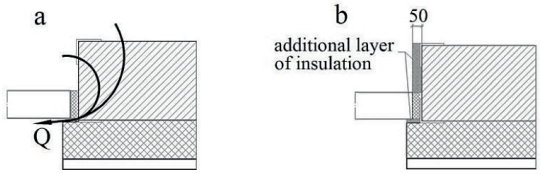

Figure 2. Window slopes surfaces: a - without thermal insulation; b - with thermal insulation

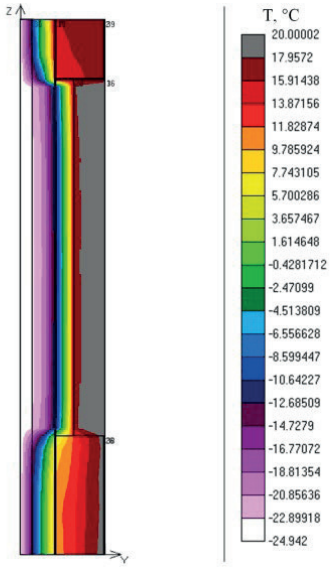

Figure 3. Temperature distribution on the inner surface of the insulated window lining along the X axis

As can be seen from Table 2, the value of total heat loss through the walls of aerated concrete blocks with insulated window soffits is 113.55 W, which is 72% of the heat loss in the wall without additional insulation of window soffits.

The heat losses through the window and the inner surface of the wall are reduced by 5-12%.

Table 2. Heat loss through the walls of aerated concrete blocks with insulated slopes of window openings

Heat loss in different areas of the wall, W/ %		
On the inside surface	On window jambs	On windows
36,41/32	7,52/7	69,62/61

It should be noted that the total heat losses through the enclosure, obtained by numerical calculation, exceed the heat losses determined by the approximate method by only 10%, which makes it possible to use an approximate method of assessing the thermal efficiency of the enclosing structure, provided that the areas with higher heat losses are insulated.

The TEPL computational complex allows to estimate correctly the heat losses through the enclosing structures and to obtain the reduced heat transfer resistance R_{red}, considering the heat flows through all surfaces of the structure, including the presence of "cold bridges".

The results of three-dimensional calculations of temperature fields of hinged ventilated facades have shown that the elements of fastening contained in their structures in the form of steel brackets and anchors, which are "cold bridges", significantly reduce the coefficient of thermal homogeneity of such systems. The study of the effect of the structural solution of hinged facades on their thermal efficiency, in terms of the material of the substructure fastening elements and their location in the outer enclosure system, was conducted on the samples of two structures: with flexible and rigid ties of cladding fastening. As a result of numerical analysis, it was found that the system on flexible links, in which the bearing brackets are installed in the floor of the building, and the insulation is attached to the wall with threaded anchor studs, has a greater heat transfer resistance (R_{red} = 1.352 m^2°C/W) than the system with rigid ties (R_{red} = 1.199 m^2°C/W).

Figure 4 shows the temperature distribution in a curtain type ventilated facade with flexible links, showing areas of reduced temperatures on the wall surface around the brackets and anchor studs. Moreover, these areas are much larger at the bracket locations than at the anchor studs. This is due to the difference in the size of the sections and the physical and mechanical properties of the fasteners

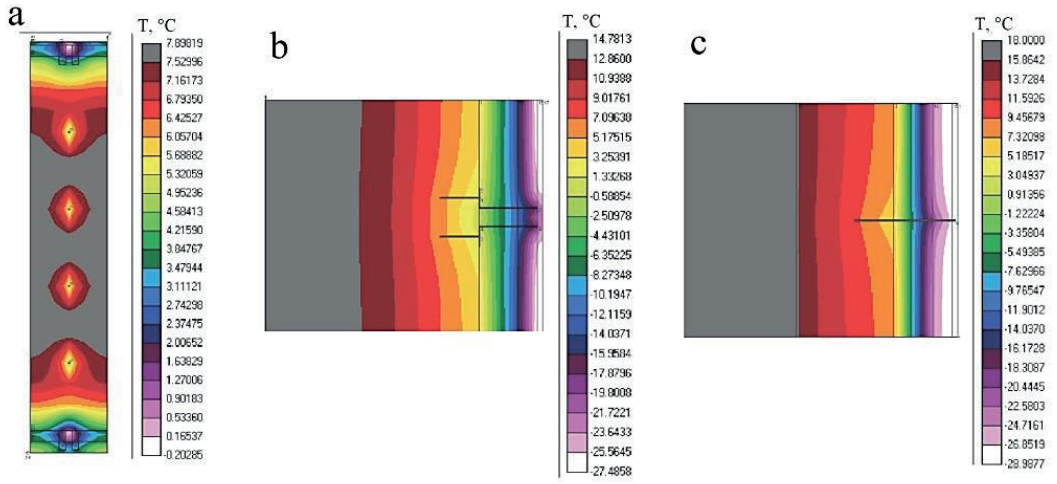

Figure 4. Temperature distribution in the structure of the curtain-type ventilated facade: a - along the facade plane; b - along the horizontal section of the wall at the attachment point of the load-bearing bracket; c - the same at the attachment point of the anchor-threaded rod

It should be noted that it is possible to increase the coefficient of thermal homogeneity of the structure of hinged facade systems, by applying the fastening elements of the substructure made of materials with a lower coefficient of thermal conductivity. For example, replacing galvanized steel load-bearing brackets (λ = 47 W/m°C) with corrosion-resistant steel brackets (λ = 20 W/m-°C) or steel anchors with fiberglass ones, thereby reducing heat loss through these elements, which are "cold bridges" in curtain type facades.

Three options for the structural solution of the exterior walls of a residential building with precast reinforced concrete floor slabs and brick partitions were investigated using the TEPL computational complex. Three types of walls were considered:

- with a 0.51 m thick inner brick layer, insulated with 0.1 m thick polystyrene foam boards and clad with 0.08 m thick gypsum boards (type 1);
- with 0.51 m thick outer brick layer, 0.05 m thick polystyrene foam insulation and 0.08 m thick gypsum boards inside (type 2);
- 0.51 m thick solid brick walls (type 3).

The heat losses in such buildings occur on all internal surfaces of the enclosure: walls, window jambs, windows, and partitions and floors adjacent to the walls.

The heat losses through the listed surfaces of the three types of walls are shown in Table 3.

Table 3. Heat loss through brick walls

Type of wall	Heat loss in different areas of the wall, W/ %				Total heat losses
	On the inside surface	On window jambs	On the windows	On partitions and ceilings	
1	50,96	27,88	106,83	14,44	200,11
2	37,71	45,76	118,86	18,92	221,25
3	137,78	46,75	114,96	39,33	338,82

Analysis of the distribution of heat flows showed that on the inner surface of the wall, the maximum heat loss occurs in the wall structure of type 3, and the minimum - type 2. The minimum heat flow through the window soffits is noted in the wall structure of type 1, and these flows are almost equal for types 2 and 3. Heat fluxes through the partitions and floors differ slightly for the walls of types 1 and 2, and for the walls of type 3 it is 2.1-2.7 times more. Heat losses through windows in the walls of the considered types differ not more than by 11%. It should be noted that heat losses through the internal surface of the wall in the total heat flow amount from 17% for a wall of the 2nd type to 41% for a wall of the 3rd type. Window jambs in the walls of the 1st and 3rd types lose up to 14% of heat, and in the wall of the 2nd type these losses make up to 21% of the total heat losses. Heat losses through the partitions and ceilings are insignificant. Their share in the total heat losses is 7% for the walls of the 1st type, 9% for the walls of the 2nd type and 12% for the walls of the 3rd type. Almost a half of all the heat losses in the walls of 1st and 2nd types account for windows, and in the 3rd type wall only one third of the heat energy is lost through the window. Total heat losses in the walls of types 1 and 2 are 1.5-1.7 times less than in the wall of type 3, respectively.

For the considered brick wall structures the heat transfer resistance values were determined taking into account the heat losses on the following heat transfer surfaces: internal wall surfaces R_1; internal surfaces and window jambs R_2; internal surfaces, window jambs and adjoining partition and floor structures R_3, as well as the total resistance R_{red}.

Numerical analysis of the thermal efficiency of the brick walls considered using the TEPL computational complex showed that if we do not take into account the heat losses through the window apertures, the resistance value on the inner wall surface R1 may be greater than the conventional resistance R, as it takes place in the walls of the 2nd and 3rd types. This is explained by the effect of temperature increase on the inner surface of the wall as you approach the window. Such excess of heat transfer resistance R1 over heat transfer resistance R is 1.3 times for a wall of type 2 and 1.1 times for a wall of type 3. The walls of types 1 and 2 have

heat transfer resistance more than required, which confirms the inadmissibility of using the heat transfer resistance without taking into account the heat losses on the slopes of window apertures in the design of exterior walls with windows. According to Table 4, heat transfer resistance values R_2 and R_3 are 2.2 and 2.7 times lower than the conventional resistance value R respectively for the first type wall, and 1.7 and 2.1 times lower for the second type wall. Despite the small difference in resistance R_2 and R_3 for the walls of types 1 and 2, they differ significantly from the resistance R. At the same time, compared to the required resistance, these resistances are 1.3 and 1.7 times lower, respectively.

Table 4. The heat transfer resistance of brick walls

Wall type	Heat transfer resistance, $m^2 \cdot °C/W$				
	Nominal resistance *R*	On the inside surface R_1	On interior surfaces and window jambs R_2	On interior surfaces, soffits, partitions and slabs R_3	Total actual one R_{red}
1	3,368	2,320	1,490	1,267	0,804
2	2,368	3,134	1,414	1,154	0,717
3	0,788	0,858	1,641	0,525	0,475

4. CONCLUSIONS

According to the results of numerical analysis of exterior walls with thermal inclusions, it can be concluded that the determination of the reduced heat transfer resistance of such structures by approximate methods leads to unacceptable errors affecting their operational reliability. The actual heat transfer resistance of heterogeneous external walls with windows and thermal inclusions should be determined on the basis of a numerical calculation of the three-dimensional temperature field. Such calculation allows considering all heat losses through the enclosure: windows and their soffits, partitions and floor structures adjacent to walls, as well as heat conductive inclusions in the form of brackets, anchors and other fastening elements, which are "cold bridges" in complex facade systems, which was confirmed by the present research using the TEPL computing complex. The verification of the TEPL computational complex is confirmed by numerous studies of the thermal efficiency of various enclosure structures, the results of which were compared with experimental data and the results of numerical calculations in other computational complexes [19, 20].

REFERENCES

1. SNiP 23-02-2003 Teplovaya zashchita zdaniy [BNR 23-02-2003 Thermal protection of buildings]. Moskva: Gosstroy Rossii, 2003. (In Russian).
2. **Abass, F., Ismail, L.H., Wahab, I.A., Elgadi, A.A.** Development of a Model for OTTV and RTTV based on BIMVPL to Optimize the Envelope Thermal Performance. IOP Conference Series: Materials Science and Engineering. 2020. 713(1), 012009.
3. **Schukina, T., Kurasov, I., Drapaliuk, D., Popov, P.** Improving the energy efficiency of buildings based on the use of integrated solar wall panels. E3S Web of Conferences. 2021. 244, 05009.
4. **M'ziane, M.C., Grine, A., Younsi, Z., Touhami, M.S.K.** Modelling and Numerical Simulation of a Passive Wall Incorporating a Phase Change Material. Journal of Advanced Research in Fluid Mechanics and Thermal Sciences. 2021.79(1). Pp. 169-181.
5. **Stonkuvienė, A., Bliūdžius, R., Burlingis, A., Ramanauskas, J.** The impact of connector's thermal and geometrical

characteristics on the energy performance of facade systems. Journal of Building Engineering. 2021. 35, 102085.

6. **Zhang, F., Ju, Y., Santibanez Gonzalez, E.D.R., (...), Dong, P., Giannakis, M.** A new framework to select energy-efficient retrofit schemes of external walls: A case study. Journal of Cleaner Production. 2021. 289, 125718.
7. **Karabulut K., Buyruk E., Fertelli A.** Numerical investigation of the effect of insulation on heat transfer of thermal bridges with different types, Thermal Science. 2016. 20 (1). Pp. 185-195.
8. **Karabulut K., Buyruk E., Fertelli A.** Numerical investigation of heat transfer for thermal bridges taking into consideration location of thermal insulation with different geometries, Strojarstvo, 2009. 51 (5), 431-439.
9. **Li, H., Zhong, K., Yu, J., Kang, Y., (John) Zhai, Z.** Solar energy absorption effect of buildings in hot summer and cold winter climate zone, China. 2020. Solar Energy 198, pp. 519-528.
10. **Yu, J., Leng, K., Ye, H., (...), Yang, Q., Gang, W.** Study on thermal insulation characteristics and optimized design of pipe-embedded ventilation roof with outer-layer shape-stabilized PCM in different climate zones. 2020. Renewable Energy 147, pp. 1609-1622.
11. **Al-Sanea, Sami A., Zedan, M.F.** Effect of thermal bridges on transmission loads and thermal resistance of building walls under dynamic conditions. 2012. Applied Energy, Elsevier, vol. 98(C), pp. 584-593.
12. **Shaik, S., Nagaraju, S., Rizvan, S.M., Gorantla, K.K.** Optimizing Vertical Air Gap Location Inside the Wall for Energy Efficient Building Enclosure Design Based on Unsteady Heat Transfer Characteristics. 2020. Advances in Intelligent Systems and Computing 1048, pp. 1003-1009.
13. **Najjar, M.K., Rosa, A.C., Hammad, A.W.A., (...), Tam, V.W.Y., Haddad, A.** A regression-based framework to examine thermal loads of buildings. 2021. Journal of Cleaner Production 292, 126021.
14. **Wang, G.** Study on effect of the external wall and window's heat load ratio to the total heat load on the indoor heat comfortability. 2013. Applied Mechanics and Materials 353-354, pp.3005-3008.
15. **Dino, I.G., Sari, A.E., Iseri, O.K., (...), Kalkan, S., Alatan, A.A.** Image-based construction of building energy models using computer vision. 2020. Automation in Construction 116, 103231.
16. **Švajlenka, J., Kozlovská, M., Vranay, F., Pošiváková, T., Jámborová, M.** Comparison of laboratory and computational models of selected thermal-technical properties of constructions systems based on wood. 2020. Energies 13(12), 3127.
17. **Tusnin A.R., Tusnina O.A.** Programmnyy kompleks dlya teplotekhnicheskogo rascheta stroitel'nykh konstruktsiy [Software complex for heat engineering calculation of building structures]. Promyshlennoye i grazhdanskoye stroitel'stvo. 2014. No. 4. Pp. 76-79. (In Russian)
18. **S.V. Patankar** Numerical heat transfer and fluid flow. New York. 1980. 197 p.
19. **Tusnina V.M., Fayzov D.Sh.** K voprosu teplotekhnicheskogo rascheta neodnorodnykh ograzhdayushchikh konstruktsiy zdaniy [To the Issue of Thermo-technical Calculation of Non-uniform Enclosing Structures of Buildings]. Promyshlennoe i grazhdanskoe stroitel'stvo. 2017. No. 4. Pp. 19–24. (In Russian).
20. Tekhnicheskiy otchet «Vypolneniye naturnykh obsledovaniy i modelirovaniya metodom konechnykh elementov s tsel'yu opredeleniya veroyatnosti promerzaniya ograzhdayushchikh konstruktsiy zhilogo kompleksa, raspolozhennogo po adresu: g. Moskva, VAO, Tyumenskiy pr., vladeniye 3-5» [Technical report "Performance of field surveys and modeling by the finite

element method in order to determine the probability of freezing of the enclosing structures of a residential complex located at the address: Moscow, VAO, Tyumensky pr., possession 3-5"]. NIU MGSU, Moskva, 2020. 46 p. (In Russian).

СПИСОК ЛИТЕРАТУРЫ

1. СНиП 23-02-2003. Тепловая защита зданий. М.: Госстрой 2003.
2. **Abass, F., Ismail, L.H., Wahab, I.A., Elgadi, A.A.** Development of a Model for OTTV and RTTV based on BIMVPL to Optimize the Envelope Thermal Performance. IOP Conference Series: Materials Science and Engineering. 2020. 713(1), 012009.
3. **Schukina, T., Kurasov, I., Drapaliuk, D., Popov, P.** Improving the energy efficiency of buildings based on the use of integrated solar wall panels. E3S Web of Conferences. 2021. 244, 05009.
4. **M'ziane, M.C., Grine, A., Younsi, Z., Touhami, M.S.K.** Modelling and Numerical Simulation of a Passive Wall Incorporating a Phase Change Material. Journal of Advanced Research in Fluid Mechanics and Thermal Sciences. 2021.79(1). Pp. 169-181.
5. **Stonkuvienė, A., Bliūdžius, R., Burlingis, A., Ramanauskas, J.** The impact of connector's thermal and geometrical characteristics on the energy performance of facade systems. Journal of Building Engineering. 2021. 35, 102085.
6. **Zhang, F., Ju, Y., Santibanez Gonzalez, E.D.R., (...), Dong, P., Giannakis, M.** A new framework to select energy-efficient retrofit schemes of external walls: A case study. Journal of Cleaner Production. 2021. 289, 125718.
7. **Karabulut K., Buyruk E., Fertelli A.** Numerical investigation of the effect of insulation on heat transfer of thermal bridges with different types, Thermal Science. 2016. 20 (1). Pp. 185-195.
8. **Karabulut K., Buyruk E., Fertelli A.** Numerical investigation of heat transfer for thermal bridges taking into consideration location of thermal insulation with different geometries, Strojarstvo, 2009. 51 (5), 431-439.
9. **Li, H., Zhong, K., Yu, J., Kang, Y., (John) Zhai, Z.** Solar energy absorption effect of buildings in hot summer and cold winter climate zone, China. 2020. Solar Energy 198, pp. 519-528.
10. **Yu, J., Leng, K., Ye, H., (...), Yang, Q., Gang, W.** Study on thermal insulation characteristics and optimized design of pipe-embedded ventilation roof with outer-layer shape-stabilized PCM in different climate zones. 2020. Renewable Energy 147, pp. 1609-1622.
11. **Al-Sanea, Sami A. , Zedan, M.F.** Effect of thermal bridges on transmission loads and thermal resistance of building walls under dynamic conditions. 2012. Applied Energy, Elsevier, vol. 98(C), pp. 584-593.
12. **Shaik, S., Nagaraju, S., Rizvan, S.M., Gorantla, K.K.** Optimizing Vertical Air Gap Location Inside the Wall for Energy Efficient Building Enclosure Design Based on Unsteady Heat Transfer Characteristics. 2020. Advances in Intelligent Systems and Computing 1048, pp. 1003-1009.
13. **Najjar, M.K., Rosa, A.C., Hammad, A.W.A., (...), Tam, V.W.Y., Haddad, A.** A regression-based framework to examine thermal loads of buildings. 2021. Journal of Cleaner Production 292, 126021.
14. **Wang, G.** Study on effect of the external wall and window's heat load ratio to the total heat load on the indoor heat comfortability. 2013. Applied Mechanics and Materials 353-354, pp.3005-3008.
15. **Dino, I.G., Sari, A.E., Iseri, O.K., (...), Kalkan, S., Alatan, A.A.** Image-based construction of building energy models

using computer vision. 2020. Automation in Construction 116, 103231.
16. **Švajlenka, J., Kozlovská, M., Vranay, F., Pošiváková, T., Jámborová, M.** Comparison of laboratory and computational models of selected thermal-technical properties of constructions systems based on wood. 2020. Energies 13(12), 3127.
17. **Туснин А.Р., Туснина О.А.** Программный комплекс для теплотехнического расчета строительных конструкций // Промышленное и гражданское строительство. 2014. № 4. С. 76-79.
18. **S.V. Patankar** Numerical heat transfer and fluid flow. New York. 1980. 197 p.
19. **Туснина В.М., Файзов Д.Ш.** К вопросу теплотехнического расчета неоднородных ограждающих конструкций зданий // Промышленное и гражданское строительство. 2017. № 4. С. 19–24.
20. Технический отчет «Выполнение натурных обследований и моделирования методом конечных элементов с целью определения вероятности промерзания ограждающих конструкций жилого комплекса, расположенного по адресу: г. Москва, ВАО, Тюменский пр., владение 3-5», НИУ МГСУ, Москва, 2020. 46 с.

Valentina M. Tusnina, docent, candidate of technical sciences, associated professor of department "Architectural and construction design and physics of the environment"; National Research Moscow State University of Civil Engineering (National Research University); Russia, 129337 Moscow, Yaroslavskoe sh., 26. Tel. +7 9165107224; e-mail: valmalaz@mail.ru. Scopus ID: 56296961500; Researcher ID: AAD-8968-2022; ORCID: 0000-0003-0328-0848.

Туснина Валентина Матвеевна, доцент, кандидат технических наук, доцент кафедры «Архитектурно-строительное проектирование и физика среды»; Национальный исследовательский московский государственный строительный университет (НИУ МГСУ); Россия, 129337 Москва, Ярославское шоссе, 26. Тел. +7 9165107224; e-mail: valmalaz@mail.ru. Scopus ID: 56296961500; Researcher ID: AAD-8968-2022; ORCID: 0000-0003-0328-0848.

International Journal for Computational Civil and Structural Engineering, 19(1) 168–177 (2023)

DOI:10.22337/2587-9618-2023-19-1-168-177

BULK THEORY ELASTICITY FINITE ELEMENT BASED ON PIECEWISE CONSTANT APPROXIMATIONS OF STRESSES

Yury Y. Tyukalov

Vyatka State University, Kirov, RUSSIA

Abstract. The solution of the volume theory elasticity problem was obtained on the basis of the additional energy functional and the possible displacements principle. On the basis of the possible displacements' principle, equilibrium equations for grid nodes are compiled, which are added to the additional energy functional using Lagrange multipliers. Linear functions are taken as possible displacements. The volumetric finite element based on piecewise constant approximations of stresses is presented. The stress fields are continuous along finite element boundaries and discontinuous inside ones. The calculation results of a cantilever beam and a bending plate are presented. The obtained solutions are compared with the solutions by the finite element method in displacements. The proposed finite element makes it possible to obtain more accurate stress values.

Keywords: finite element method, piecewise-constant stress approximation, bulk theory elasticity

КОНЕЧНЫЙ ЭЛЕМЕНТ ДЛЯ ОБЪЕМНОЙ ТЕОРИИ УПРУГОСТИ НА ОСНОВЕ КУСОЧНО ПОСТОЯННЫХ АППРОКСИМАЦИЙ НАПРЯЖЕНИЙ.

Ю.Я. Тюкалов

Вятский государственный университет, г. Киров, РОССИЯ

Аннотация. Представлен объемный конечный элемент, основанный на кусочно-постоянных аппроксимациях напряжений. Решение строится на основе функционала дополнительной энергии и принципа возможных перемещений. На основе принципа возможных перемещений составлены уравнения равновесия узлов сетки, которые добавляются к функционалу дополнительной энергии при помощи множителей Лагранжа. В качестве возможных перемещений принимаются линейные функции. Поля напряжений непрерывны вдоль границ конечных элементов и разрывны внутри элементов. Приведены результаты расчета консольной балки и изгибаемой пластины. Полученные решения сравниваются с решениями методом конечных элементов в перемещениях. Предложенный конечный элемент позволяет получить более точные значения напряжений.

Ключевые слова: метод конечных элементов, приближение кусочно-постоянных напряжений, объемная теория упругости

INTRODUCTION

A large number of papers are devoted to the development of the finite element method in displacements. They present the variational principles of finite element method and solution algorithms [1]. Also, other numerical methods are being developed. In particular, the method of boundary elements [2] and collocation method [3]. The finite element method in displacements has been widely used to calculate structures for various purposes due to its versatility. This method is well researched in terms of convergence and accuracy of solutions. An alternative approach based on stress approximations is much less explored [4-5]. The papers [6-16] propose finite elements based on the approximation of stresses for solving problems of the plane elasticity theory, plates bending and rod systems. Currently, volumetric

finite elements are increasingly used to calculate such structures as slabs, shells and composite structures [17-19], [20-22]. The development of new volumetric finite elements is still relevant. The purpose of this work is to develop a volumetric finite element based on stress approximation. Obtaining another approximate solution, which alternative to the existing approximate solutions, will allow one to obtain a two-sided estimate of the exact solution.

METHODS

The solution to the bulk theory elasticity problem will be built based on the additional energy functional:

$$\Pi = \frac{1}{2}\int_V \begin{pmatrix} \frac{1}{E}\left(\sigma_x^2+\sigma_y^2+\sigma_z^2\right) \\ -\frac{\nu}{E}\left(\sigma_x\sigma_y+\sigma_x\sigma_z+\sigma_y\sigma_z\right) \\ +\frac{1}{G}\left(\tau_{xy}^2+\tau_{xz}^2+\tau_{yz}^2\right) \end{pmatrix} dV. \quad (1)$$

E is the material elastic modulus; ν is Poisson's ratio, $G = 2(1+\mu)/E$. We write the functional (1) in matrix form:

$$\Pi = \frac{1}{2}\int_V \boldsymbol{\sigma}^{\mathrm{T}}\mathbf{E}^{-1}\boldsymbol{\sigma} dV,$$

$$\boldsymbol{\sigma}^{\mathrm{T}} = \left(\sigma_x \quad \sigma_y \quad \sigma_z \quad \tau_{xy} \quad \tau_{xz} \quad \tau_{yz}\right),$$

$$\mathbf{E}^{-1} = \begin{bmatrix} 1/E & -\nu/E & -\nu/E & 0 & 0 & 0 \\ -\nu/E & 1/E & -\nu/E & 0 & 0 & 0 \\ -\nu/E & -\nu/E & 1/E & 0 & 0 & 0 \\ 0 & 0 & 0 & 1/G & 0 & 0 \\ 0 & 0 & 0 & 0 & 1/G & 0 \\ 0 & 0 & 0 & 0 & 0 & 1/G \end{bmatrix}. \quad (2)$$

To discrete the volume, we use the rectangular parallelepiped finite elements. Let's denote the vector nodal unknown stresses vector as

$$\boldsymbol{\sigma}_{node,k}^T = \left(\sigma_{x,k} \quad \sigma_{y,k} \quad \sigma_{z,k} \quad \tau_{xy,k} \quad \tau_{xz,k} \quad \tau_{yz,k}\right). \quad (3)$$

Vector of finite element unknown stresses is

$$\boldsymbol{\sigma}_{el,k}^T = \left(\boldsymbol{\sigma}_{node,1}^T \quad \boldsymbol{\sigma}_{node,2}^T \quad \text{L} \quad \boldsymbol{\sigma}_{node,8}^T\right). \quad (4)$$

To simplify the notation, let's introduce unit step functions and diagonal matrices

$$h_i(x,y,z) = \begin{Bmatrix} 1, & (x,y,z) \in V_i \\ 0, & (x,y,z) \notin V_i \end{Bmatrix}, \quad \mathbf{H}_i = \begin{bmatrix} h_i & & \\ & h_i & \\ & & h_i \end{bmatrix}. \quad (5)$$

Then the approximation matrix of stresses in the finite element volume will have the simple form (fig. 1b):

$$\mathbf{Z}_k = \left[\mathbf{H}_1 \quad \mathbf{H}_2 \quad \text{L} \quad \mathbf{H}_8\right], \quad \boldsymbol{\sigma} = \mathbf{Z}_k\boldsymbol{\sigma}_{el,k}. \quad (6)$$

Using (4-6), we express the finite element additional energy in the following form:

$$\Pi_k = \int_{V_k} \sigma_{el,k}^T (Z_k^T E_k^{-1} Z_k)\, \sigma_{el,k} \mathrm{dV}. \quad (7)$$

The pliability matrix of the finite element is

$$D_k = \int_{V_k} Z_k^T E_k^{-1} Z_k \,\mathrm{dV}. \quad (8)$$

The matrix has a simple block-diagonal form [24]. From local matrices of finite elements are formed global matrix D of whole system. The functional (1) of whole system:

$$\Pi = \frac{1}{2}\boldsymbol{\sigma}_V^T \mathbf{D}\boldsymbol{\sigma}_V. \quad (9)$$

$\boldsymbol{\sigma}_V$ is global vector of the system unknown stresses.

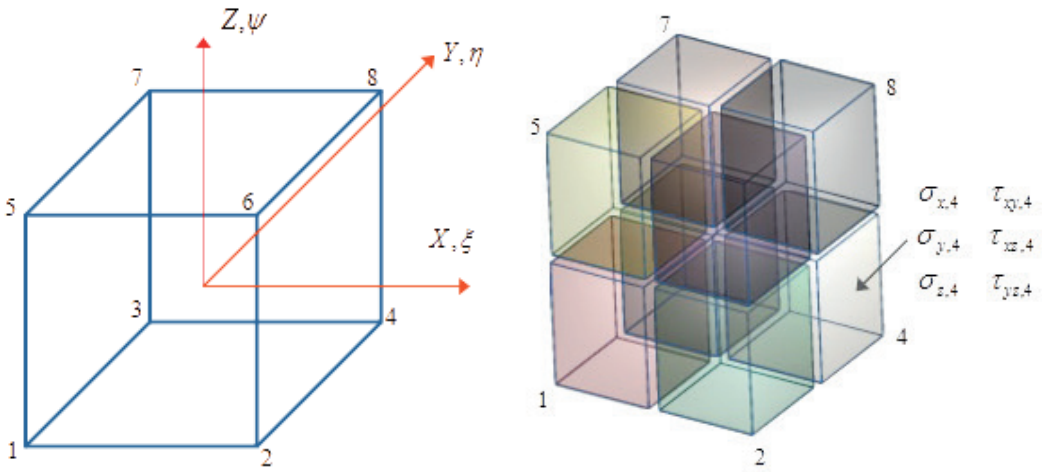

a b

Figure 1. a) global and local coordinate systems; b) division of a finite element into volumes with constant stresses

Based on the possible displacements' principle, we can compose the necessary equilibrium equations of the grid nodes. Each node of finite elements grid has three possible displacements along the OX, OY, OZ axes of the global coordinate system (Fig. 1). Approximations of the possible displacements over the finite element volume are the linear basis functions.

$$\delta u_i = \frac{1}{8}(1+\xi\xi_i)(1+\eta\eta_i)(1+\psi\psi_i),$$
$$\delta v_i = \frac{1}{8}(1+\xi\xi_i)(1+\eta\eta_i)(1+\psi\psi_i), \quad (10)$$
$$\delta w_i = \frac{1}{8}(1+\xi\xi_i)(1+\eta\eta_i)(1+\psi\psi_i).$$

In (10), the local dimensionless node i coordinates of the finite element, taking the values -1 or 1. Dimensionless coordinates are related to local coordinates x, y, z by known expressions:

$$\xi = \frac{2x}{a}, \eta = \frac{2y}{b}, \psi = \frac{2z}{c}. \quad (11)$$

Expressions (10) correspond to unit displacement of node i and zero displacements of other nodes of finite elements adjacent to the considered node. For each of these finite elements, the considered node will have different index values i in the range from 1 to 8. The index value corresponds to the ordinal node number in the description of the finite element (Fig. 1). The node i possible displacement along the X axis causes the following deformations in the finite elements adjacent to the node:

$$\delta\varepsilon_x = \frac{\partial(\delta u_i)}{\partial x} = \frac{\xi_i(1+\eta\eta_i)(1+\psi\psi_i)}{4a},$$
$$\delta\gamma_{xy} = \frac{\partial(\delta u_i)}{\partial y} = \frac{\eta_i(1+\xi\xi_i)(1+\psi\psi_i)}{4b}, \quad (12)$$
$$\delta\gamma_{xz} = \frac{\partial(\delta u_i)}{\partial z} = \frac{\psi_i(1+\xi\xi_i)(1+\eta\eta_i)}{4c}.$$

Other strains $\varepsilon_y = \varepsilon_z = \gamma_{yz} = 0$. The possible strain energy of finite element k is the integral over its volume.

$$\delta U^k_{i,x} = \iiint_{V^e} (\sigma_x\delta\varepsilon_x + \sigma_y\delta\varepsilon_y + \sigma_x\delta\varepsilon_x + \sigma_z\delta\varepsilon_z + \tau_{xy}\delta\gamma_{xy} + \tau_{yz}\delta\gamma_{yz} + \tau_{xz}\delta\gamma_{xz})dxdydz. \quad (13)$$

Taking into account expressions (8) and (12), (13) we obtain

$$\delta U_{i,x}^{k}=\frac{1}{32}\sum_{j=1}^{8}\left(\xi_i bc\left(1+\frac{\eta_i\eta_j}{2}\right)\left(1+\frac{\psi_i\psi_j}{2}\right)\sigma_{x,j}+\eta_i ac\left(1+\frac{\xi_i\xi_j}{2}\right)\left(1+\frac{\psi_i\psi_j}{2}\right)\tau_{xy,j}+\psi_i ab\left(1+\frac{\eta_i\eta_j}{2}\right)\left(1+\frac{\xi_i\xi_j}{2}\right)\tau_{xz,j}\right). \quad (14)$$

Expression (14) can be represented in vector form

$$\delta U_{i,x}^{k}=\mathbf{C}_{i,x}^{k}\boldsymbol{\sigma}_{el,k}. \quad (15)$$

Similar expressions can be written for possible displacements of nodes along the axes Y and Z:

$$\delta U_{i,y}^{k}=\mathbf{C}_{i,y}^{k}\boldsymbol{\sigma}_{el,k},\ \delta U_{i,z}^{k}=\mathbf{C}_{i,z}^{k}\boldsymbol{\sigma}_{el,k}. \quad (16)$$

From vectors $\mathbf{C}_{i,x}^{k}$, $\mathbf{C}_{i,y}^{k}$, $\mathbf{C}_{i,z}^{k}$ of all finite elements the "equilibrium" matrix $\mathbf{C}$ for all system is formed. The matrix $\mathbf{C}$ rows number is equal number of system nodes possible displacements, and the columns number is equal the total number of nodal unknown displacements. The matrix has a band structure of non-zero elements.

The work of concentrated external forces and volume-distributed loads directed along the X axis with a possible displacement δu_i is determined by the following expression:

$$\delta V_{i,x}=P_{i,x}\delta u_i+\sum_{k}\int_0^a\int_0^c\int_0^b q_x^{gr}\delta u_i dxdydz. \quad (17)$$

For the case of a uniformly distributed load

$$\delta V_{i,x}=P_{i,x}+\sum_{k}\frac{1}{8}q_x^{V}abc=\overline{P}_{i,x}. \quad (18)$$

Similarly, let's get

$$\begin{aligned}\delta V_{i,y}&=P_{i,y}+\sum_{k}\frac{1}{8}q_y^{V}abc=\overline{P}_{i,y},\\ \delta V_{i,z}&=P_{i,z}+\sum_{k}\frac{1}{8}q_z^{V}abc=\overline{P}_{i,z}.\end{aligned} \quad (19)$$

The global load vector $\mathbf{P}$ is formed from $\overline{P}_{i,x}$, $\overline{P}_{i,y}$, $\overline{P}_{i,z}$. Let's the algebraic equations system for the equilibrium of nodes in matrix form:

$$\mathbf{C}\boldsymbol{\sigma}_V+\mathbf{P}=0. \quad (20)$$

Using the Lagrange multipliers method, we add the equilibrium equations to the functional (9):

$$\Pi=\frac{1}{2}\boldsymbol{\sigma}_V^{T}\mathbf{D}\boldsymbol{\sigma}_V+\mathbf{w}^{T}(\mathbf{C}\boldsymbol{\sigma}_V+\mathbf{P})\to\min. \quad (21)$$

$\mathbf{w}$ is the nodes displacements vector. Equating to zero the functional derivatives with respect to $\boldsymbol{\sigma}_V$ and $\mathbf{w}$ we obtain the system of equations:

$$\begin{aligned}\mathbf{D}\boldsymbol{\sigma}_V+\mathbf{w}^{T}\mathbf{C}&=0,\\ \mathbf{C}\boldsymbol{\sigma}_V+\mathbf{P}&=0.\end{aligned} \quad (22)$$

We express the vector σ_V from the first matrix equation and put it into the second one. Then we get

$$\begin{aligned}\sigma_V&=-C^{T}D^{-1}w,\\ K&=-C^{T}D^{-1}C,\\ Kw&=P.\end{aligned} \quad (24)$$

$\mathbf{K}$ is the whole system stiffness matrix. That matrix also has a band structure of non-zero elements. The matrix $\mathbf{D}$ has a block-diagonal structure and is inversed analytically. When calculating the product $\mathbf{C}^{T}\mathbf{D}^{-1}\mathbf{C}$, the band structure of non-zero elements of the matrix $\mathbf{C}$ is taken into account. Solving the equations system, we determine the nodal displacements, and then calculate the nodal stresses (24). Thus, the stress fields are continuous along element boundaries and discontinuous inside ones. On the contrary, when using the finite element

method based on the displacement approximations, the stress fields are continuous inside the finite elements and discontinuous along their boundaries.

RESULTS AND DISCUSSIONS

To assess the accuracy of the proposed finite elements in stresses, the calculations of the cantilever beam and the hinged plate were performed (Fig. 2). The beam length is 6*m*, the section height and width are 1*m*. The plate length and width are 2*m*. Plate thickness is 0.1*m*. The material elasticity modulus is $1000000 kN/m^2$. Poisson's ratio is 0.25. The beam was calculated for unit force, which applied as uniformly distributed tangential stress to its end. The plate was designed for a uniformly distributed load of $10 kN/m^2$. Due to the symmetry of the plate, its quarter was calculated under the appropriate boundary conditions. For comparison, the beam and plate were also calculated by the classical finite element method based on displacement approximations. The calculation results for various finite element meshes are shown in Tables 1 and 2.

For the beam, Table 1 shows the free end displacements and the stresses of the outermost fiber in the pinch. For the plate, Table 2 shows the center displacements and the stresses in the outermost fiber in the center.

a) b)

Figure 2. a) pinched beam; b) bending hinged plate

Table 1. Bending hinged plate

FEM grid		FEM in displacements		FEM in stresses	
number of elements by thickness	number of elements by length (width)	w, *mm*	Stress, kN/m^2	w, mm	Stress, kN/m^2
2	4	2.18	148.9	9.15	830.3
2	10	6.39	447.5	9.29	934.8
4	15	7.18	751.6	8.42	1023.6
6	15	7.20	837.6	8.20	1044.9
Analytical decision in series		**7.48**	**1062**	**7.48**	**1062**

Table 2. Pinched beam

FEM grid		FEM in displacements		FEM in stresses	
number of elements by length	number of elements by high (width)	w, *mm*	Stress, kN/m^2	w, mm	Stress, kN/m^2
5	2	0.539	10.25	1.287	39.20
10	4	0.756	22.30	0.978	35.92
15	6	0.819	27.29	0.921	36.80
20	8	0.843	29.91	0.902	36.51
Analytical decision		**0.864**	**36**	**0.864**	**36**

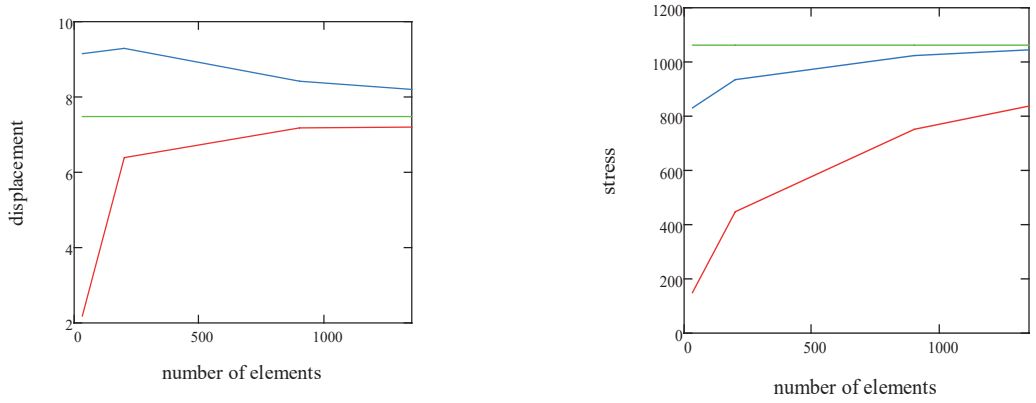

a) *b)*

Figure 3. Bending hinged plate. The red line is the solution of FEM in displacements, the blue line is the solution of FEM in stresses, the green line is the exact solution

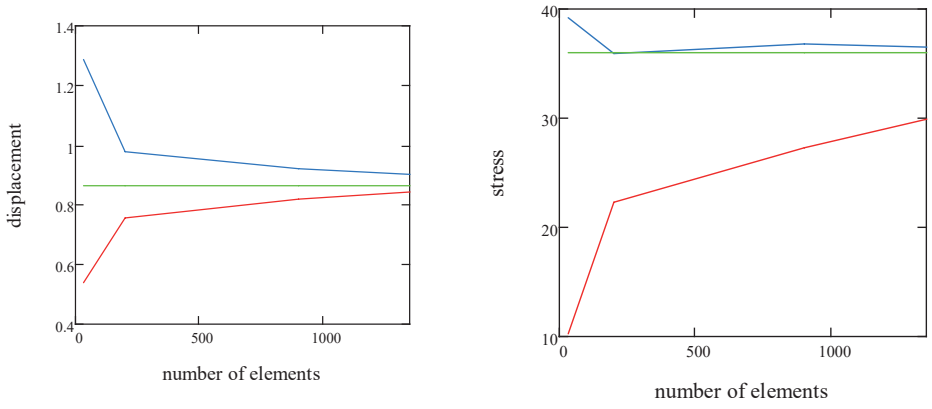

a) *b)*

Figure 4. Pinched beam. The red line is the solution of FEM in displacements, the blue line is the solution of FEM in stresses, the green line is the exact solution

The calculations results show that the proposed finite element, based on the stresses approximation, makes it possible to obtain, in comparison with the traditional finite element, more accurate stress values. In addition, the displacements obtained by the proposed method, when refining the finite elements mesh, tend to exact values from above. Quite often, the maximum stresses occur at the subject area boundary, so the proposed method is preferable in this case, since it allows us to calculate the stresses directly at the points of boundary. The above structural calculations confirm this. It is known that when the finite elements mesh is refined, the stresses in elements tend to constant values. The using the piecewise constant approximations of stresses makes it possible to ensure this condition directly.

CONCLUSION

The volumetric finite element based on piecewise constant approximations of stresses is presented. The stress fields are continuous along finite element boundaries and discontinuous inside ones. The solution of the volume theory elasticity problem was obtained on the basis of

the additional energy functional and the possible displacements principle. The proposed finite element makes it possible to obtain, in comparison with the method of finite elements in displacements, more accurate stress values. The displacements obtained by the proposed method, when refining the finite elements mesh, tend to exact values from above.

REFERENCES

1. **Abdikarimov, R., Amabili, M., Vatin, N.I., Khodzhaev, D.** Dynamic stability of orthotropic viscoelastic rectangular plate of an arbitrarily varying thickness. Applied Sciences (Switzerland). 2021. 11(13). DOI:10.3390/app11136029.
2. **Cho, J.R**. Natural element approximation of hierarchical models of plate-like elastic structures. Finite Elements in Analysis and Design. 2020. 180(September). Pp. 103439. DOI:10.1016/j.finel.2020.103439. URL: https://doi.org/10.1016/j.finel.2020.103439.
3. **Gao, X.-W., Gao, L.-F., Zhang, Y., Cui, M., Lv, J.** Free element collocation method: A new method combining advantages of finite element and mesh free methods. Computers & Structures. 2019. 215. Pp. 10–26. DOI:10.1016/j.compstruc.2019.02.002. URL: https://linkinghub.elsevier.com/retrieve/pii/S0045794918313488 (date of application: 26.03.2019).
4. **Góis, W., Proença, S.P.B.** Generalized Finite Element Method on Hybrid Stress Approach: Formulation and Numerical Performance. Buenos Aires. 2010. XXIX. Pp. 4687–4705. URL: http://www.ufabc.edu.br/%5Cnhttp://www.set.eesc.usp.br/%5Cnhttp://www.amcaonline.org.ar.
5. **Tyukalov, Y.Y.** Calculation of bending plates by finite element method in stresses. IOP Conference Series: Materials Science and Engineering. 2018. 451(1). DOI:10.1088/1757-899X/451/1/012046.
6. **Tyukalov, Y.Y.** Method of plates stability analysis based on the moments approximations. Magazine of Civil Engineering. 2020. 95(3). Pp. 90–103. DOI:10.18720/MCE.95.9. URL: http://engstroy.spbstu.ru/.
7. **Tyukalov, Y.Y.** Calculation of the circular plates ' stability in stresses. IOP Conference Series: Materials Science and Engineering. 2020. DOI:10.1088/1757-899X/962/2/022041.
8. **Tyukalov, Y.Y.** Calculation method of bending plates with assuming shear deformations. Magazine of Civil Engineering. 2019. 85(1). Pp. 107–122. DOI:10.18720/MCE.85.9.
9. **Tyukalov, Y.Y.** Stress finite element models for determining the frequencies of free oscillations. Magazine of Civil Engineering. 2016. 67(07). Pp. 39–54. DOI:10.5862/MCE.67.5. URL: http://www.engstroy.spbstu.ru/index_2016_07/05.html.
10. **Tyukalov, Y.Y.** Finite element models in stresses for plane elasticity problems. Magazine of Civil Engineering. 2018. 77(1). Pp. 23–37. DOI:10.18720/MCE.77.3.
11. **Tyukalov, Y.Y.** Finite element models in stresses for bending plates. Magazine of Civil Engineering. 2018. 82(6). Pp. 170–190. DOI:10.18720/MCE.82.16.
12. **Tyukalov, Y.Y.** Refined finite element of rods for stability calculation. Magazine of Civil Engineering. 2018. 79(3). Pp. 54–65. DOI:10.18720/MCE.79.6.
13. **Tyukalov, Y.Y**. Equilibrium finite elements for plane problems of the elasticity theory. Magazine of Civil Engineering. 2019. 91(7). Pp. 80–97. DOI:10.18720/MCE.91.8. URL: http://engstroy.spbstu.ru/.
14. **Tyukalov, Y.Y.** The functional of additional energy for stability analysis of spatial rod systems. Magazine of Civil Engineering. 2017. 70(2). Pp. 18–32. DOI:10.18720/MCE.70.3.

15. **Tyukalov, Y.Y.** Calculation of circular plates with assuming shear deformations. IOP Conference Series: Materials Science and Engineering. 2019. 687(3). DOI:10.1088/1757-899X/687/3/033004.
16. **Tyukalov, Y.Y.** Finite element model of Reisner's plates in stresses. Magazine of Civil Engineering. 2019. 5(89). Pp. 61–78. DOI:10.18720/MCE.89.6. URL: http://engstroy.spbstu.ru/.
17. **Zhou, J., Wang, K., Li, P.** A hybrid fundamental-solution-based 8-node element for axisymmetric elasticity problems. Engineering Analysis with Boundary Elements. 2019. 101. Pp. 297–309. DOI:10.1016/j.enganabound.2019.01.015. URL: https://linkinghub.elsevier.com/retrieve/pii/S0955799718305940 (date of application: 26.03.2019).
18. **Ye, J., Yan, Y., Li, J., Hong, Y., Tian, Z.** 3D explicit finite element analysis of tensile failure behavior in adhesive-bonded composite single-lap joints. Composite Structures. 2018. 201(May). Pp. 261–275. DOI:10.1016/j.compstruct.2018.05.134. URL: https://doi.org/10.1016/j.compstruct.2018.05.134.
19. **Xu, R., Bouby, C., Zahrouni, H., Ben Zineb, T., Hu, H., Potier-Ferry, M.** 3D modeling of shape memory alloy fiber reinforced composites by multiscale finite element method. Composite Structures. 2018. 200(May). Pp. 408–419. DOI:10.1016/j.compstruct.2018.05.108. URL: https://doi.org/10.1016/j.compstruct.2018.05.108.
20. **Nguyen, M.N., Bui, T.Q., Truong, T.T., Tanaka, S., Hirose, S.** Numerical analysis of 3-D solids and composite structures by an enhanced 8-node hexahedral element. Finite Elements in Analysis and Design. 2017. 131. Pp. 1–16. DOI:10.1016/j.finel.2017.04.002.
21. **Liu, B., Lu, S., Wu, Y., Xing, Y.** Three dimensional micro/macro-mechanical analysis of the interfaces of composites by a differential quadrature hierarchical finite element method. Composite Structures. 2017. 176. Pp. 654–663. DOI: 10.1016/j.compstruct.2017.05.068. URL: http://dx.doi.org/10.1016/j.compstruct.2017.05.068.
22. **Liu, B., Lu, S., Ji, J., Ferreira, A.J.M., Liu, C., Xing, Y.** Three-dimensional thermo-mechanical solutions of cross-ply laminated plates and shells by a differential quadrature hierarchical finite element method. Composite Structures. 2019. 208(May 2018). Pp. 711–724. DOI:10.1016/j.compstruct.2018.10.022.

СПИСОК ЛИТЕРАТУРЫ

1. **Abdikarimov, R., Amabili, M., Vatin, N.I., Khodzhaev, D.** Dynamic stability of orthotropic viscoelastic rectangular plate of an arbitrarily varying thickness. Applied Sciences (Switzerland). 2021. 11(13). DOI:10.3390/app11136029.
2. **Cho, J.R.** Natural element approximation of hierarchical models of plate-like elastic structures. Finite Elements in Analysis and Design. 2020. 180(September). Pp. 103439. DOI:10.1016/j.finel.2020.103439. URL: https://doi.org/10.1016/j.finel.2020.103439.
3. **Gao, X.-W., Gao, L.-F., Zhang, Y., Cui, M., Lv, J.** Free element collocation method: A new method combining advantages of finite element and mesh free methods. Computers & Structures. 2019. 215. Pp. 10–26. DOI: 10.1016/j.compstruc.2019.02.002. URL: https://linkinghub.elsevier.com/retrieve/pii/S0045794918313488 (date of application: 26.03.2019).
4. **Góis, W., Proença, S.P.B.** Generalized Finite Element Method on Hybrid Stress Approach: Formulation and Numerical Performance. Buenos Aires. 2010. XXIX. Pp. 4687–4705. URL: http://www.ufabc.edu.br/%5Cnhttp://www.s

et.eesc.usp.br/%5Cnhttp://www.amcaonline.org.ar.
5. **Tyukalov, Y.Y.** Calculation of bending plates by finite element method in stresses. IOP Conference Series: Materials Science and Engineering. 2018. 451(1). DOI:10.1088/1757-899X/451/1/012046.
6. **Tyukalov, Y.Y.** Method of plates stability analysis based on the moments approximations. Magazine of Civil Engineering. 2020. 95(3). Pp. 90–103. DOI:10.18720/MCE.95.9. URL: http://engstroy.spbstu.ru/.
7. **Tyukalov, Y.Y.** Calculation of the circular plates ' stability in stresses. IOP Conference Series: Materials Science and Engineering. 2020. DOI:10.1088/1757-899X/962/2/022041.
8. **Tyukalov, Y.Y.** Calculation method of bending plates with assuming shear deformations. Magazine of Civil Engineering. 2019. 85(1). Pp. 107–122. DOI:10.18720/MCE.85.9.
9. **Tyukalov, Y.Y.** Stress finite element models for determining the frequencies of free oscillations. Magazine of Civil Engineering. 2016. 67(07). Pp. 39–54. DOI:10.5862/MCE.67.5. URL: http://www.engstroy.spbstu.ru/index_2016_07/05.html.
10. **Tyukalov, Y.Y.** Finite element models in stresses for plane elasticity problems. Magazine of Civil Engineering. 2018. 77(1). Pp. 23–37. DOI:10.18720/MCE.77.3.
11. **Tyukalov, Y.Y.** Finite element models in stresses for bending plates. Magazine of Civil Engineering. 2018. 82(6). Pp. 170–190. DOI:10.18720/MCE.82.16.
12. **Tyukalov, Y.Y.** Refined finite element of rods for stability calculation. Magazine of Civil Engineering. 2018. 79(3). Pp. 54–65. DOI:10.18720/MCE.79.6.
13. **Tyukalov, Y.Y.** Equilibrium finite elements for plane problems of the elasticity theory. Magazine of Civil Engineering. 2019. 91(7). Pp. 80–97. DOI: 10.18720/MCE.91.8. URL: http://engstroy.spbstu.ru/.
14. **Tyukalov, Y.Y.** The functional of additional energy for stability analysis of spatial rod systems. Magazine of Civil Engineering. 2017. 70(2). Pp. 18–32. DOI:10.18720/MCE.70.3.
15. **Tyukalov, Y.Y.** Calculation of circular plates with assuming shear deformations. IOP Conference Series: Materials Science and Engineering. 2019. 687(3). DOI:10.1088/1757-899X/687/3/033004.
16. **Tyukalov, Y.Y.** Finite element model of Reisner's plates in stresses. Magazine of Civil Engineering. 2019. 5(89). Pp. 61–78. DOI:10.18720/MCE.89.6. URL: http://engstroy.spbstu.ru/.
17. **Zhou, J., Wang, K., Li, P.** A hybrid fundamental-solution-based 8-node element for axisymmetric elasticity problems. Engineering Analysis with Boundary Elements. 2019. 101. Pp. 297–309. DOI:10.1016/j.enganabound.2019.01.015. URL: https://linkinghub.elsevier.com/retrieve/pii/S0955799718305940 (date of application: 26.03.2019).
18. **Ye, J., Yan, Y., Li, J., Hong, Y., Tian, Z.** 3D explicit finite element analysis of tensile failure behavior in adhesive-bonded composite single-lap joints. Composite Structures. 2018. 201(May). Pp. 261–275. DOI:10.1016/j.compstruct.2018.05.134. URL: https://doi.org/10.1016/j.compstruct.2018.05.134.
19. **Xu, R., Bouby, C., Zahrouni, H., Ben Zineb, T., Hu, H., Potier-Ferry, M.** 3D modeling of shape memory alloy fiber reinforced composites by multiscale finite element method. Composite Structures. 2018. 200(May). Pp. 408–419. DOI: 10.1016/j.compstruct.2018.05.108. URL: https://doi.org/10.1016/j.compstruct.2018.05.108.
20. **Nguyen, M.N., Bui, T.Q., Truong, T.T., Tanaka, S., Hirose, S.** Numerical analysis of 3-D solids and composite structures by

an enhanced 8-node hexahedral element. Finite Elements in Analysis and Design. 2017. 131. Pp. 1–16. DOI:10.1016/j.finel.2017.04.002.

21. **Liu, B., Lu, S., Wu, Y., Xing, Y.** Three dimensional micro/macro-mechanical analysis of the interfaces of composites by a differential quadrature hierarchical finite element method. Composite Structures. 2017. 176. Pp. 654–663. DOI: 10.1016/j.compstruct.2017.05.068. URL: http://dx.doi.org/10.1016/j.compstruct.2017.05.068.
22. **Liu, B., Lu, S., Ji, J., Ferreira, A.J.M., Liu, C., Xing, Y.** Three-dimensional thermo-mechanical solutions of cross-ply laminated plates and shells by a differential quadrature hierarchical finite element method. Composite Structures. 2019. 208(May 2018). Pp. 711–724. DOI:10.1016/j.compstruct.2018.10.022.

Yury Y. Tyukalov, DSc, Professor of the Department «Building structures and machines», Vyatka State University, Kirov

Тюкалов Юрий Яковлевич, доктор технических наук, профессор кафедры «Строительные конструкции и машины» Вятского государственного университета, г. Киров

DOI:10.22337/2587-9618-2023-19-1-178-189

QUALITY CONTROL OF DISPERSED COMPONENTS POWDER-ACTIVATED CONCRETE WITH THE HELP OF SHUKHART'S CARDS

Sergey A. Fedosin [1], Anton N. Kuzenkov [2], Sergey S. Moiseev [3], Irina N. Maksimova [4], Irina V. Erofeeva [5], Yana A. Sanyagina [1]

[1] National Research Mordovian State University name N.P. Ogaryov, Saransk, RUSSIA
[2] Center for Nanotechnologies and Nanomaterials of the Republic of Mordovia, Saransk, RUSSIA
[3] Petersburg Cement Company, St. Petersburg, RUSSIA
[4] Penza State University of Architecture and Construction, Penza, RUSSIA
[5] National Research Moscow State University of Civil Engineering, Moscow, RUSSIA

Abstracts. In the construction industry, cement concretes are the most widely used building material. New generation materials with increased strength and durability are used in the construction of critical facilities. Special requirements are imposed on such concretes to ensure their quality. The issues of control and quality of powder-activated concretes of a new generation at the stage of preparation of their constituent components are considered. Author made in the article the analysis of the classifier data for the developed system of quality control (QC) based on Shewhart control charts. For implement an effective classification of critical situations we justified target-conformity application of support vector. We accumulated the base of possible solutions in special cases when process of cement production go out from control limits. For pro-programmatic implementation of support vector we used library application LIBSVM. We described procedures for the preparation of the accumulated data for training models of SVM. We determined optimal parameters of created models nuclei to ensure accurate classification. We created SVM models for all monitored parameters. We created HMI display effective solutions to prevent critical situations for the operator.

Keywords: Shewhart control charts, grinding of cement, statistical controllability, knowledge base, quality control, support vector machine, classification, cross-validation

КОНТРОЛЬ КАЧЕСТВА ДИСПЕРСНЫХ КОМПОНЕНТОВ ПОРОШКОВО-АКТИВИРОВАННЫХ БЕТОНОВ С ПОМОЩЬЮ КАРТ ШУХАРТА

С.А. Федосин [1], А.Н. Кузенков [2], С.С. Моисеев [3], И.Н. Максимова [4], И.В. Ерофеева [5], Я.А. Санягина [1]

[1] Национальный исследовательский Мордовский государственный университет им. Н.П. Огарёва, г. Саранск, РОССИЯ
[2] Центр нанотехнологий и наноматериалов Республики Мордовия, г. Саранск, РОССИЯ
[3] Петербургская Цементная компания, г. Санкт-Петербург, РОССИЯ
[4] Пензенский государственный университет архитектуры и строительства, г. Пенза, РОССИЯ
[5] Национальный исследовательский Московский государственный строительный университет, г. Москва, РОССИЯ

Аннотация. В строительной отрасли наиболее применяемым строительным материалом являются цементные бетоны. При возведении ответственных объектов используются материалы нового поколения, обладающие повышенными показателями прочности и долговечности. К таким бетонам предъявляются особые требования по обеспечению их качества. Рассматриваются вопросы контроля качества порошково-активированных бетонов нового поколения на стадии подготовки их составляющих компонентов. В работе выполнен анализ применимости классификатора данных для разработанной подсистемы контроля качества (КК) с использованием контрольных карт Шухарта (ККШ). Для

осуществления эффективной классификации критических ситуаций обоснована целесообразность применения метода опорных векторов – Support Vector Machine (SVM). Накоплена база возможных решений для особых случаев, соответствующих выходу показателей процесса производства цемента, приготовления наполнителей и заполнителей различных размерных уровней для порошково-активированных бетоновза контрольные пределы. Для программной реализации метода опорных векторов применена библиотека LIBSVM. Подробно описаны процедуры по подготовке накопленных данных для обучения моделей SVM. Подобраны оптимальные параметры ядер созданных моделей, обеспечивающие точность классификации. Созданы модели SVM для всех контролируемых параметров. Разработан человеко-машинный интерфейс отображения предлагаемых эффективных решений по предотвращению критических ситуаций, предназначенный для оператора.

Ключевые слова: контрольные карты Шухарта, помол цемента, статистическая управляемость, база знаний, контроль качества, метод опорных векторов, классификация, перекрестная проверка

I. INTRODUCTION

Modern high quality concretes (HDC) classify a wide range of concretes for different purposes: High-strength (HPB, Hochfester Beton - HFB) and ultra-high-strength (UHFB, Ultrahochfester Beton - UHFB), self-compacting (SVB, Selbstverdichtender Beton - SVB; Self Compacting Concrete - SCC), highly corrosion-resistant, Reaktionspulver Beton - RPB or Reactive Powder Concrete - RPC and others [1, 2, 3, 4, 5, 6, 7].

New generation concretes are used for the construction of unique buildings and structures [3, 8, 9], construction of bridges and roads [10, 11], and as a repair material [5, 12]. They are based on new generation superplasticizers in combination with new formulation of dry components. Concretes are formed by combining dispersed components of different sizes, mutually reinforcing each other [13, 14]. For example, particles of smaller size than cement granules fill in the spaces between cement particles and depending on given interaction mechanism in general polydisperse modifier structure can be crystallization centers, change plastic strength, etc. Fillers and fillers with large sizes form a framework of material with optimal packing of particles. In this case, the pores between the granules are filled with more ground particles.

Designing of multicomponent compositions of new generation concretes should be performed using the following basic formulation principles [13, 15, 16, 17]: 1) mandatory use of rock flour with micrometer particle parameters as dispersed fillers, which are rheologically active components; 2) obligatory use of very fine-grained quartz sand of fraction 0,16-0,63 mm with fineness modulus less than 1.2, supporting necessary rheological and structural condition of water-disperse mixture and increasing weighing ability of dispersion fine-grained system, which prevents settling of coarse sand and crushed stone at stratification of concrete mixture; 3) use of reactive pozzolanic additives (microsilica, dehydrated kaolin, etc.), binding hydrolysis of fluidized sand and gravel of concrete mixes. 4) the use of high-quality sand-fillers and crushed stone with specially selected granulometry, providing a high bulk density of the mixture of aggregates; 5) very low ratio of water to the sum of all the dry components in the concrete mixture, not exceeding 0,07-0,08, and an extremely high volume concentration of the solid phase (not less than 80-85%); 6) mandatory use of highly effective superplasticizers, providing the diameter of the spread (of the cone Hagerman) of cement suspensions and suspensions of mixtures of cement with rock flour (at a ratio of "cement : Stone meal" ratio 1:0,5÷1:1) in the range of 260-350 mm at В/Ц (B/T) less than 0.18 (0.2); 7) for special concretes using in the composition of the fillers nano-sized (particles whose size in one direction are at least 100 nm), polymineral composition binders, activated components, and first of all water mixing, as well as biocide additives.

Technological processing of powder-activated concrete includes the following processes:

preparation of components (cement, fillers and aggregates, mixing water, modifying additives), preparation of self-compacting concrete mixtures, product molding (shoeless or formwork method), curing of products and structures (various methods of heating, heat and humidity treatment, etc.). All operations and processes contribute to the quality of the manufactured products. The quality of the concrete constituents used is one of the most important.

Currently, it is considered that the quality of produced cement, fillers and aggregates of different size levels largely determines the place and role of the enterprise-producer in the modern building materials market. Therefore, introduction of quality control subsystems into automated control systems (ACS) for production of cement, fillers and aggregates of different types is a relevant problem. For its implementation it is necessary to solve two interrelated subtasks. The first one is the recognition (detection) of critical situations, which caused a disruption in the technological process (TP). The second one is the identification of the critical situation itself for subsequent correction of possible deviations in the TP. A well-proven method of production process control is the application of statistical methods based on control charts. In contrast to the methods using histograms and various types of diagrams (scatter, Pareto, Ishikawa), control charts allow forecasting changes in the parameters of technological process. However, the practical issues of using methods of controlling production processes with the use of control charts for the sphere of production of construction materials remain insufficiently disclosed. Therefore, in this article we attempt to comprehensively study the specifics of the application of quality control methods in the production of cement, fillers and aggregates of different dimensional level.

Purpose and objectives of the research

The research is aimed at improving the quality of manufactured powder-activated concrete by applying a virtual analyzer built on the basis of mathematical statistics methods and intelligent technologies in the technological process for the preparation of cement, fillers and aggregates of different dimensional level ARS control.

Research Objectives:

1. Create an algorithm for technology of powder-activated concrete on the basis of literature analysis in the field of creating a new generation of concrete and emphasize the importance of quality control of preparation of cement, fillers and aggregates.
2. To build a dynamic model of the technological process with the use of regression identification methods on the example of Portland cement, taking into account technological processes of concrete components preparation.
3. To develop the method of technological data preparation for statistical analysis and mathematical models for evaluation of statistical parameters of technological processes of concrete components preparation for evaluation of its statistical controllability
4. Create a virtual quality analyzer based on Support Vector Machines (SVM) method u Advanced Process Control (APC) system to monitor and control the quality of manufactured products and implement it in the APCS of cement grinding and grinding of aggregates and fillers of concrete.

II. METHODS

The technological process of concrete production consists of several stages. In the first stage, raw materials for the production of cement, fillers and aggregates are extracted. Then they are crushed in raw material mills to prepare them for the next stage. The second stage involves various types of activation of the dispersed components: co-milling with plasticizers, heat treatment, etc. The most energy-intensive process in this case is the technology of cement production. The obtained

raw components for the manufacture of cement (limestone, clay and additives) are fed into cement kilns, where the firing process takes place. At the outlet of the kilns, the so-called clinker is obtained, which in the next step is sent together with the other additives to the grinding shop. After passing through the cement mills, the finished product, Portland cement, is produced. It is the cement grinding process that is the most important in terms of quality control.
The cement grinding process is monitored in a special room equipped with several monitors, on which the mnemonic diagrams of the technological production are displayed. The operator is able to control almost every stage of the cement grinding process. He controls dosage of clinker and additives, rotational speed of separator rotor, fan speed of suction system (thus he can change air rarefaction in the whole grinding system). However, due to the large amount of information loaded from the screens, the operator is not always able to react promptly to critical situations in the grinding process, and in some cases cannot foresee the occurrence of such situations.
The quality level of fillers and aggregates preparation of different size also determines the quality of concretes based on them. Continuous planetary mills are used for preparation of aggregates up to specific surface of 3000-5000 cm^2/g. For fine-grained sand, filler sand, fine-grained aggregates jaw and cone crushers are used. Grinding of fine-grained materials is possible with the use of various mills: ball, vibratory, vario-planetary.
Practice shows that the optimal characteristics for grinding dispersed materials are achieved by grinding in a vario-planetary mill. This and the fact that the dispersed constituents of concrete have different grindability, makes the Vario Planetary Mill the most suitable one. The combinations of pressure, friction and impact are controlled in the Vario Planetary Mill.
Filler grinding in a Vario Planetary Mill promotes the formation of electron acceptor centers in the particles. This has a positive effect on the rheological characteristics of self-compacting concrete mixtures without the additional consumption of mixing water and superplasticizer.
It is effective to use for the manufacture of powder-activated concrete as fillers and fine aggregates the rock screening fractions < 5 mm, which form multi-tonnage dumps and storages, occupying large areas and disturbing the ecological balance of regions [18]. To solve the first of the problems mentioned in the introduction (recognition of critical situations), a well-proven quality control tool based on Schuchart control charts (SCC) was chosen [19]. The following is an example of research related to quality control of Portland cement. The use of SCC as part of the ACS can provide detection of changes in the TP (including the process going beyond the statistical controllability) even before it has reached a non-emergency state [20, 21].
In [22] an experimental implementation of the subsystem of monitoring and identification of critical situations in the TP on the basis of control data in JSC "Mordovcement", Republic of Mordovia is described. Six characteristics were selected for monitoring: specific surface of cement (1); cement grinding fineness, when sifting through sieve No.008 (2); mass fraction in percentage of sulfuric acid anhydride in cement (3); mass fraction of opock in cement (4); mass fraction of calcium oxide in cement (5); percentage of moisture content in cement (6).
There are allowable limits for all these parameters [23], exceeding which indicates the presence of defects in the produced cement.
As a result of the research, an ACS subsystem [22] was developed, which displays SCC in real time. With the help of this subsystem the operator can monitor graphs of change over time of quantities determining cement quality and, depending on the displayed information, perform actions, which are recorded in the use case diagram. There are several rules for detecting loss of statistical controllability. However, for the practical application of SCC it is sufficient to use the first four rules - this

reduces the probability of false positives [21]. A script was implemented in the C language that monitors the "triggering" (execution) of these four rules: one point corresponding to the TP indicator exceeds the three-sigma limits (1); at least two of three consecutive points lying on one side of the center line exceed the two-sigma limits (2); at least four of five consecutive points lying on one side of the center line exceed one sigma (3); at least eight consecutive points lie on one side of the center line (4).

During the three months of subsystem testing, about 3,000 values were processed for each monitored process parameter, i.e., a total of about 10,000 values. During this period of time, the SCC for all characteristics of parameters revealed the loss of statistical controllability for each of the above four rules. All effective decisions taken by the operator to return the TP to the state of statistical controllability, as well as parameters of the production process (temperature, separator rotation speed, etc.) were entered into the knowledge base - to form an expert evaluation for identifying the causes of deviations from the TP. Thus, it was possible to implement a classifier that links the accumulated data in the knowledge base with special events leading to the loss of statistical controllability. In this case, the values of parameters "1-6" are used as input data. A promising solution for this problem is the use of a classifier based on the SVM reference vector method. The main idea of this method is to translate the initial vectors of controlled parameters (corresponding to the actual sets of indicators for a certain moment in time) into a space of higher dimensionality and to search for a separating hyperplane with the maximum gap between it and two parallel hyperplanes built on both sides of it (Fig. 1).

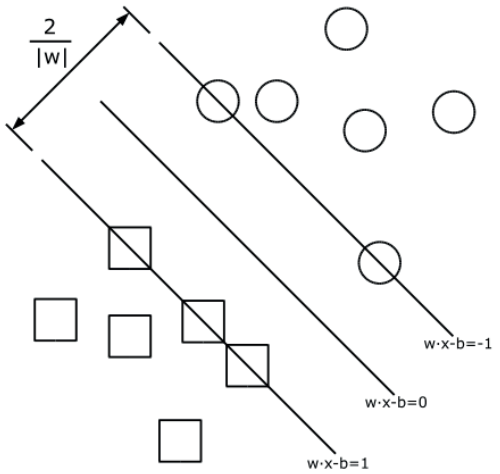

Figure 1. Geometric representation of the SVM vector reference method

Mathematically, the training sample of controlled parameters is written as $(x_1, y_1), \ldots, (x_m, y_m), x_i \in R^n, y_i \in \{-1,1\}$ [24, 25]. The reference vector method constructs a classification function in the form:

$$F(x) = sign(\langle w, x \rangle + b), \qquad (1)$$

where $\langle , \rangle$ is the scalar product, w is the perpendicular to the separating hyperplane, and b is equal modulo to the distance from the hyperplane to the origin. In this case the objects for which $F(x) = 1$, fall into one class, and the objects with $F(x) = -1$ fall into another class. This function is used because any hyperplane can be given in the form $\langle w, x \rangle + b = 0$ for some w and (Fig. 7). It is necessary to choose such and b, which maximize the distance to each class. It can be shown that this distance is equal to $1/\|w\|$. The problem of finding a $1/\|w\|$ maximum is equivalent to the problem of finding a minimum and is reduced to an optimization problem:

$$\begin{cases} arq\min\|w\|^2 \\ y_i\left(\langle w, x_i\rangle + b\right) \geq 1, i = 1,...,m. \end{cases} \quad (2)$$

It is a standard quadratic programming problem and is solved analytically using Lagrange multipliers. If there is no linear class separability [24, 25], one should resort to expanding the space by increasing its dimension by choosing to map $\varphi(x)$ vectors x into a new space. This results in a new scalar product function:

$$K(x, y) = \varphi(x) \cdot \varphi(y). \quad (3)$$

The function $K(x, y)$ is called the kernel. It is the basic parameter for tuning the SVM method. From the mathematical point of view, any positively defined symmetric function of two variables can serve as the kernel. Positive definiteness is necessary so that the corresponding Lagrange function in the optimization problem is bounded from below. Thus, the optimization problem would be correctly defined. The accuracy of the classifier depends, in particular, on the choice of the kernel. In practice, the following types of kernels are (are) used:

- Polynomial: $k(x, x') = (\langle x, x'\rangle + const)^d$;
- radial basis function (the most common type of kernel): $k(x, x') = \exp(-\gamma\|x - x'\|^2)$;
- Gaussian radial basis function: $k(x, x') = e - \|x - x'\|^2/2\sigma^2$;
- sigmoid: $k(x, x') = \tanh(k\langle x, x'\rangle + c), k > 0, c < 0$.

The software module for operation with Schuchart maps, in the absence of statistical controllability for a particular technological parameter, sets the variable corresponding to this parameter to unity. Thus, the cement grinding quality control subsystem allows you to identify for which technological characteristic a special case took place. The SVM method is then applied. First, the subsystem recognizes which of the four rules the statistical controllability was lost, i.e., it assigns the case to one of the four classes.

At the second stage SVM will determine whether the process indicator (parameter) went beyond statistical controllability by its upper or lower boundary (limit), i.e. it will separate one class from the other.

III. ALGORITHMIC AND SOFTWARE IMPLEMENTATION OF THE PROPOSED METHOD

As a tool for software implementation of this method it was decided to use the freely distributed library LIBSVM. To achieve the most effective classification it is necessary to perform actions for preparation of data sets and search for the best kernel for them, namely to do the following.

Convert the numerical data corresponding to the TP out of statistical controllability to the format of the information system using SVM:

- to perform data scaling in the range from 0 to 1;
- use the kernel RBF: $k(x, x') = \exp(-\gamma\|x - x'\|^2)$;
- use cross-validation to find the best parameters C and γ. The constant "C" is a control parameter of the method. This parameter allows to find a compromise between maximizing the distance between the two hyperplanes and minimizing the total error; to use the found values of C and γ to train the model in order to obtain a classifier for a particular technological parameter; to test the obtained classifier on a test case.

All the accumulated data on the process exiting the state of statistical controllability were reduced to the LIBSVM format and procalated in the range from 0 to 1 - to provide more accurate model training (Fig. 2).

```
11:0.3471          6:0.332117:0.3400
21:0.3465
22:0.3472     10:0.3521    18:0.3626
24:0.3621
33:0.3645          6:0.367817:0.3691
31:0.3699
42:0.3934          17:0.386522:0.3878
36:0.3812
```

Figure 2. Data fragment for training the SVM model

The data format for LIBSVM is a string of the form:: <label><index>: <value>. The parameter <label> characterizes the class to which the following values belong. At the first stage of classification it is required to identify to which of the four rules of loss of statistical controllability a particular special case belongs. Therefore the training (training) file must contain values for the four classes. It should be noted that in case of a loss of statistical controllability by several rules simultaneously, the highest priority is given to rule No.1, while the lowest is given to rule No.4. The <index> : <value> pair gives the characteristic of the value of the controlled parameter. The <index> parameter is an integer number starting with "1" and increasing with each step. The <value> parameter is a real number reflecting the value of the selected characteristic, scaled from "0" to "1".

When using the RBF kernel, at least two coefficients are selected: the regularization coefficient "C" and the kernel parameter "γ". Since it is impossible to assess a priori the optimal value of these parameters by mathematical methods, in practice we resort to an empirical procedure - cross-validation (cross-validation). The essence of this procedure is the following: the range, within which the values of parameters "C" and "γ" will vary, and the sampling step for it are set. As a result, we obtain a "grid", whose nodes specify a set of pairs of "C" and "γ" values, among which it is necessary to select the optimal one; for each pair of "C" and "γ" values, the training sample is divided into n parts. One part is used for training at given values of "C" and "γ", and another part is used for testing. This procedure is repeated n times (to get more accurate result). Finally, each of the n parts is used for testing; then the values obtained are averaged. The procedure is repeated for all values of combinations of parameters "C" and "γ". Sometimes cross-validation with large step of "C" and "γ" changes is performed at first to preliminarily localize the best solution. Then in that interval (on that subinterval), where the best results were achieved, cross-validation is carried out again, but with a smaller step.

The disadvantage of this method of parameter fitting is the high computational complexity and, consequently, the long execution time.

After cross-validation, the best parameters "C" and "γ" for each case were found for each classifier model using the LIBSVM library. Four statistical metrics are introduced as part of machine learning to evaluate the quality of the classifier performance.

All samples for which the classifier gave an answer can be divided into four groups: positive results correctly found by the classifier as positive (true positive); negative results incorrectly found by the classifier as positive (false positive); negative results correctly defined by the classifier as negative (true negative); positive results incorrectly found by the classifier as negative (false negative).

On the basis of these four statistical metrics, the LIBSVM library allocates the metric Accuracy = (true positive + true negative) / (true positive + false negative + false positive + true negative). In content terms, this corresponds to the fraction (from "1") of correct classifier responses among all responses. When testing the trained SVM models on test data, this figure did not fall below 96.875%.

In the process of grinding of cement, fillers and aggregates, in case of loss of statistical controllability by any technological parameter, the subsystem retrieves the solution from the knowledge base (formed on the basis of

opinions of experts in the field of cement production technology, preparation of fillers and aggregates of various sizes) corresponding to the choice of the classifier - this choice is made in automatic mode. After that, the operator's display shows advice on how to solve the critical situation.

For all parameters of the technological process, knowledge bases were formed in relation to the effective solutions adopted (eight solutions were entered in the base for each parameter). So, for all six process parameters, 48 possible solutions (subclasses) were identified for special cases. Five SVM models were created for each of the six process parameters. The first model determines, when a critical situation occurs, which of the four rules is triggered by the CCH. Then, depending on the rule number, the corresponding classifier (one of the four) is selected. The selected classifier determines whether the special case occurred at the upper or lower limit, and associates it with the corresponding solution in the knowledge base (proposed solutions).

CONCLUSIONS

The issues of quality control of the technological process of production of powder-activated concrete of a new generation are considered. In the course of this study, a classifier based on the method of reference vectors was introduced into the subsystem of quality control of cement grinding, filler and aggregate grinding using SCC. To implement the classifier LIBSVM library was applied. During the testing of the classifier the optimal values of the settings of the SVM models were selected. This allowed the share of correct answers to be at least 96.875%. Improved using the proposed classifier, the quality control subsystem showed sufficient accuracy in identifying critical situations and increased the efficiency of operator actions aimed at preventing such situations.

REFERENCES

1. **Aïtcin P.C.** Cements of yesterday and today – concrete of tomorrow. Cement and Concrete Research 2000. 30 (9):1349-1359. DOI:10.1016/S0008-8846(00)00365-3.
2. **Richard P., Cheyrezy M.** Composition of reactive powder concretes. Cement and Concrete Research1995; 25:1501-1511. https://doi.org/10.1016/0008-8846(95)00144-2.
3. **Wang D., Shi C., Wu Z., Xiao J., Huang Z., Fang Z.** A review on ultra high performance concrete: Part II. Hydration, microstructure and properties. Construction and Building Material 2015; 96:368-377. https://doi.org/10.1016/j.conbuildmat.2015.08.095.
4. **Matte V., Moranville M.** Durability of Reactive Powder Composites: influence of silica fume on the leaching properties of very low water/binder pastes. Cement and Concrete Composites 1999. https://doi.org/10.1016/S0958-9465(98)00025-0.
5. **Salim L.G., Al-Baghdadi H.M., Muteb H.H.** Reactive powder concrete with steel, glass and polypropylene fibers as a repair material. Civil Engineering Journal, 2019. Vol 5, No 11 (2019). https://doi.org/10.28991/cej-2019-03091422.
6. **Shubbar H. A., Alwash N. A.** The fire exposure effect on hybrid reinforced reactive powder concrete columns. Civil Engineering Journal, 2020. Vol 6, No 2 (2020). DOI: 10.28991/cej-2020-03091476.
7. **Abdelmonem A., El-Feky M.S., Nasr E., Kohail M.** Performance of high strength concrete containing recycled rubber. Construction and Building Material 2019; 227. https://doi.org/10.1016/j.conbuildmat.2019.08.041.
8. **Meleka N.N., Bashandy A.A., Arab M.A.** Economical reactive powder concrete cast using available materials in North Sinai, Egypt. Archives of Civil Engineering. 2013.

59 (2). https://doi.org/10.2478/ace-2013-0009.

9. **Sadrekarimi A.** Development of a light weight reactive powder concrete. Journal of Advanced Concrete Technology 2004, Vol. 2, No. 3, 409-417. https://doi.org/10.3151/jact.2.409.
10. **Li H., M.-hua Zhang, J.-ping Ou.** Flexural fatigue performance of concrete containing nano-particles for pavement. International Journal of Fatigue 2007. 29 (7):1292-1301. https://doi.org/10.1016/j.ijfatigue.2006.10.004.
11. **Hou X., Cao S., Rong Q., Zheng W., Li G.** Effects of steel fiber and strain rate on the dynamic compressive stress-strain relationship in reactive powder concrete. Construction and Building Material 2018; 170 (1):570-581. https://doi.org/10.1016/j.conbuildmat.2018.03.101.
12. **Erofeev V.T., Vatin N.I., Maksimova I.N., Tarakanov O.V., Sanyagina Y.A., Erofeeva I.V., Suzdaltsev O.V.** Powder-activated concrete with a granular surface texture // International journal for computational civil and structural engineering. 2022. № 4 (18). Pp. 49-61. DOI:10.22337/2587-9618-2022-18-4-49-61.
13. **Kalashnikov V.I., Erofeev V.T., Moroz M.N. [et al.]** Nanogidrosilikatnyye tekhnologii v proizvodstve betonov [Nanohydrosilicate technologies in the production of concrete] // Stroitelnye materialy. 2014. No. 5. Pp. 88-91 (In Russian).
14. **Nazerigivi A., Nejati H.R., Ghazvinian A., Najigivi A.** Effects of SiO_2 nanoparticles dispersion on concrete fracture toughness. Construction and Building Material 2018; 171: 672-679. https://doi.org/10.1016/j.conbuildmat.2018.03.224.
15. **Kalashnikov V.I., Erofeev V.T., Tarakanov O.V.** Suspenzionno-napolnennyye betonnyye smesi dlya poroshkovo-aktivirovannykh betonov novogo pokoleniya [Suspension-filled concrete mixtures for powder-activated concrete of a new generation] // Izvestiya vysshikh uchebnykh zavedeniy. Stroitel'stvo. 2016. No. 4. Pp. 38-37. (In Russian).
16. **Reches Y.** Nanoparticles as concrete additives: review and perspectives. Construction and Building Material. 175 (2018) 483-495. https://doi.org/10.1016/j.conbuildmat.2018.04.214.
17. **Aggarwal P., Singh R.P., Aggarwal Y.** Use of nano-silica in cement based materials—a review. Cogent Engineering. 2015. 2 (1):1078018. https://doi.org/10.1080/23311916.2015.1078018.
18. **Kalashnikov V.I., Erofeev V.T., Tarakanov O.V.** Tekhniko-ekonomicheskaya effektivnost' vnedreniya arkhitekturno-dekorativnykh poroshkovo-aktivirovannykh karbonatnykh peschanykh betonov **[**Technical and economic efficiency of the introduction of architectural and decorative powder-activated carbonate sand concretes] // Izvestiya vysshikh uchebnykh zavedeniy. Stroitel'stvo, 2016. No. 6 (690). Pp. 39-46. (In Russian)
19. GOST R ISO 7870-2-2015. Statisticheskiye metody. Kontrol'nyye karty. Chast' 2. Kontrol'nyye karty Shukharta [Statistical methods. Control cards. Part 2. Shewhart's Control Charts]. Moscow: Standardinform, 2016. 46 p. (In Russian)
20. **Shewart W.A.** Economic Control of Quality of Manufactured Product. Van Nordstrom, 1931. 18 c.
21. **Wheeler D., Chambers D.** (2009) Statisticheskoye upravleniye protsessami: per. s angl. **[**Statistical Process Control: translated from English]. Moscow: Alpina Business Books. 409 p. (In Russian)
22. **Kuzenkov A.N.** Avtomatizirovannaya podsistema kontrolya kachestva tsementa na osnove ispol'zovaniya kart Shukharta

[Automated subsystem for cement quality control based on the use of Shewhart maps] // Prikaspiyskiy zhurnal: upravleniye i vysokiye tekhnologii. 2014. No. 4. Pp. 134-144. (In Russian)

23. **Kanne M.M., Ivanov B.V., Koreshkov V.N., Skhirtladze A.G.** (2008) Sistemy, metody i instrument menedzhmenta kachestva [Systems, methods and tools of quality management]. St. Petersburg: Piter. 560 p. (In Russian)
24. **Ayvazyan S.A.** (1989) Prikladnaya statistika: klassifikatsiya i snizheniye razmernosti [Applied Statistics: Classification and Dimension Reduction]. M.: Finansy i statistika. 342 p. (In Russian).
25. **Bartlett P., Shawe-Taylor J.** Generalization performance of support vector machines and other pattern classifiers // Advances in Kernel Methods. – MIT Press, Cam-bridge, USA, 1998. – Pp. 43-54.

СПИСОК ЛИТЕРАТУРЫ

1. **Aïtcin P. C.** Cements of yesterday and today – concrete of tomorrow. Cement and Concrete Research 2000. 30 (9):1349-1359. DOI:10.1016/S0008-8846(00)00365-3.
2. **Richard P., Cheyrezy M.** Composition of reactive powder concretes. Cement and Concrete Research 1995; 25: 1501-1511. https://doi.org/10.1016/0008-8846(95)00144-2.
3. **Wang D., Shi C., Wu Z., Xiao J., Huang Z., Fang Z.** A review on ultra high performance concrete: Part II. Hydration, microstructure and properties. Construction and Building Material 2015; 96: 368-377. https://doi.org/10.1016/j.conbuildmat.2015.08.095.
4. **Matte V., Moranville M.** Durability of Reactive Powder Composites: influence of silica fume on the leaching properties of very low water/binder pastes. Cement and Concrete Composites 1999. https://doi.org/10.1016/S0958-9465(98)00025-0.
5. **Salim L. G., Al-Baghdadi H. M., Muteb H. H.** Reactive powder concrete with steel, glass and polypropylene fibers as a repair material. Civil Engineering Journal, 2019.Vol 5, No 11 (2019). https://doi.org/10.28991/cej-2019-03091422.
6. **Shubbar H. A., Alwash N. A.** The fire exposure effect on hybrid reinforced reactive powder concrete columns. Civil Engineering Journal, 2020.Vol6, No 2 (2020).DOI: 10.28991/cej-2020-03091476.
7. **Abdelmonem A., El-Feky M.S., Nasr E., Kohail M.** Performance of high strength concrete containing recycled rubber. Construction and Building Material 2019; 227. https://doi.org/10.1016/j.conbuildmat.2019.08.041.
8. **Meleka N.N., Bashandy A.A., Arab M.A.** Economical reactive powder concrete cast using available materials in North Sinai, Egypt. Archives of Civil Engineering. 2013. 59 (2). https://doi.org/10.2478/ace-2013-0009.
9. **Sadrekarimi A.** Development of a light weight reactive powder concrete. Journal of Advanced Concrete Technology 2004, Vol. 2, No. 3, 409-417. https://doi.org/10.3151/jact.2.409.
10. **Li H., M.-hua Zhang, J.-ping Ou.** Flexural fatigue performance of concrete containing nano-particles for pavement. International Journal of Fatigue2007. 29 (7):1292-1301. https://doi.org/10.1016/j.ijfatigue.2006.10.004.
11. **Hou X., Cao S., Rong Q., Zheng W., Li G.** Effects of steel fiber and strain rate on the dynamic compressive stress-strain relationship in reactive powder concrete. Construction and Building Material 2018; 170 (1):570-581. https://doi.org/10.1016/j.conbuildmat.2018.03.101.

12. **Erofeev V.T., Vatin N.I., Maksimova I.N., Tarakanov O.V., Sanyagina Y.A., Erofeeva I.V., Suzdaltsev O.V.** Powder-activated concrete with a granular surface texture // International journal for computational civil and structural engineering. 2022. № 4 (18). Pp. 49-61. DOI:10.22337/2587-9618-2022-18-4-49-61.
13. **Калашников В.И., Ерофеев В.Т., Мороз М.Н. [и др.]** Наногидросиликатные технологии в производстве бетонов // Строительные материалы. 2014. № 5. С. 88-91.
14. **Nazerigivi A., Nejati H.R., Ghazvinian A., Najigivi A.** Effects of SiO_2 nanoparticles dispersion on concrete fracture toughness. Construction and Building Material 2018; 171: 672-679. https://doi.org/10.1016/j.conbuildmat.2018.03.224.
15. **Калашников В.И., Ерофеев В.Т., Тараканов О.В.** Суспензионно-наполненные бетонные смеси для порошково-активированных бетонов нового поколения // Известия высших учебных заведений. Строительство. 2016. № 4. С. 38-37.
16. **Reches Y.** Nanoparticles as concrete additives: review and perspectives. Construction and Building Material. 175 (2018) 483-495. https://doi.org/10.1016/j.conbuildmat.2018.04.214.
17. **Aggarwal P., Singh R.P., Aggarwal Y.** Use of nano-silica in cement based materials—a review. Cogent Engineering. 2015. 2 (1):1078018. https://doi.org/10.1080/23311916.2015.1078018.
18. **Калашников В.И., Ерофеев В.Т., Тараканов О.В.** Технико-экономическая эффективность внедрения архитектурно-декоративных порошково-активированных карбонатных песчаных бетонов // Известия высших учебных заведений. Строительство, 2016. № 6 (690). С. 39-46.
19. ГОСТ Р ИСО 7870-2-2015. Статистические методы. Контрольные карты. Часть 2. Контрольные карты Шухарта. Москва: Стандартинформ, 2016. 46 с.
20. **Shewart W.A.** Economic Control of Quality of Manufactured Product. Van Nordstrom, 1931. 18 с.
21. **Уилер Д., Чамберс Д.** Статистическое управление процессами: пер. с англ. М.: Альпина Бизнес Букс, 2009. 409 с.
22. **Кузенков А.Н.** Автоматизированная подсистема контроля качества цемента на основе использования карт Шухарта // Прикаспийский журнал: управление и высокие технологии. 2014. № 4. С. 134-144.
23. **Канне М.М., Иванов Б.В., Корешков В.Н., Схиртладзе А.Г.** Системы, методы и инструменты менеджмента качества. СПб.: Питер, 2008. 560 с.
24. **Айвазян С.А.** Прикладная статистика: классификация и снижение размерности. М.: Финансы и статистика, 1989. 342 с.
25. **Bartlett P., Shawe-Taylor J.** Generalization performance of support vector machines and other pattern classifiers // Advances in Kernel Methods. – MIT Press, Cam-bridge, USA, 1998. – Pp. 43-54.

Sergey A. Fedosin, professor, candidate of technical sciences, head of the department «Automated information processing systems and control», National Research Mordovian State University name N.P. Ogaryov; 430005, Republic of Mordovia, Saransk, st. Bolshevik, d. 68; E-mail: fedosin@mrsu.ru

Anton N. Kuzenkov, Candidate of Technical Sciences, Senior Project Manager of the Center for Nanotechnologies and Nanomaterials of the Republic of Mordovia; 430034, Republic of Mordovia, Saransk, st. Lodygina, 3; E-mail: kuzenkov@cnnrm.ru

Sergey S. Moiseev, Candidate of Technical Sciences, CEO of LLC «Petersburg Cement Company»; 199178, St. Petersburg, Maly V.O., d. 15 a; E-mail: director@nsicem.ru

Irina N. Maksimova, Associate Professor, Candidate of Technical Sciences, Associate Professor of the Department of Quality Management and Technology of Construction Production, Penza State University of Architecture and Construction; tel. +7(903) 324-95-02; E-mail: maksimovain@mail.ru

Irina V. Erofeeva, Candidate of Technical Sciences, Senior Lecturer of the Department «Fundamentals of Architecture and Artistic Communications», National Research Moscow State University of Civil Engineering; 129337, Moscow, Yaroslavl highway, 26; E-mail: ira.erofeeva.90@mail.ru

Yana A. Sanyagina, Competitor of the Department of Building Materials and Technologies, National Research Mordovian State University name N.P. Ogaryov; 430005, Republic of Mordovia, Saransk, st. Bolshevik, d. 68; E-mail: sanyagina@mail.ru

Федосин Сергей Алексеевич, профессор, кандидат технических наук, заведующий кафедрой «Автоматизированные системы обработки информации и управление», Национальный исследовательский Мордовский государственный университет им. Н.П. Огарёва; 430005, Республика Мордовия, г. Саранск, ул. Большевистская, д. 68; E-mail: fedosin@mrsu.ru

Кузенков Антон Николаевич, кандидат технических наук, старший менеджер проектов Центра нанотехнологий и наноматериалов Республики Мордовия; 430034, Республика Мордовия, г. Саранск, ул. Лодыгина, д. 3; E-mail: kuzenkov@cnnrm.ru

Моисеев Сергей Степанович, кандидат технических наук, генеральный директор ООО «Петербургская Цементная компания»; 199178, г. Санкт-Петербург, проспект Малый В.О., д. 15 а; E-mail: director@nsicem.ru

Максимова Ирина Николаевна, доцент, кандидат технических наук, доцент кафедры «Управление качеством и технология строительного производства», Пензенский государственный университет архитектуры и строительства; тел. +7(903) 324-95-02; E-mail: maksimovain@mail.ru

Ерофеева Ирина Владимировна, кандидат технических наук, старший преподаватель кафедры «Основы архитектуры и художественных коммуникаций», Национальный исследовательский Московский государственный строительный университет; 129337, г. Москва, Ярославское шоссе, д. 26; E-mail: ira.erofeeva.90@mail.ru

Санягина Яна Андреевна, соискатель кафедры «Строительные материалы и технологии», Национальный исследовательский Мордовский государственный университет им. Н.П. Огарёва; 430005, Республика Мордовия, г. Саранск, ул. Большевистская, д. 68; E-mail: sanyagina@mail.ru

DOI:10.22337/2587-9618-2023-19-1-190-203

MATHEMATICAL MODELING AND EXPERIMENTAL INVESTIGATION OF THE PROCESS OF NON-STATIONARY HEAT TRANSFER IN A BLOCK FOAM GLASS SAMPLE AT THE ANNEALING STAGE

Sergey V. Fedosov [1], Maxim O. Bakanov [2], Ilya A. Kuznetsov [2]

[1] Moscow State University of Civil Engineering, Moscow, RUSSIA
[2] Ivanovo Fire Rescue Academy of State Firefighting Service of Ministry of Russian Federation for Civil Defense, Emergencies and Elimination of Consequences of Natural Disasters, Ivanovo, RUSSIA

Abstract. The specifics of the technology for the production of block foam glass are presented, the results of experimental studies of the properties of the material are presented, a method for improving production based on mathematical modeling of heat transfer processes is proposed. It is shown that the processes of high-temperature processing of foam glass make a key contribution to the formation of a high-quality porous structure, therefore, this area of research needs the development of adequate methods for calculating the main macrophysical parameters based on the theory of heat transfer. A technique for checking the adequacy of the mathematical model of heat transfer is presented using the example of spontaneous cooling of a foam glass block. The entire procedure for checking the adequacy of the mathematical model was carried out in three stages. At the first stage, the degree of validation of the model is assessed, functional dependencies with the results of an experimental study based on the Pearson determination coefficient. The main stage includes the evaluation of the confidence intervals of the experimental data and the discussion of the convergence of the results of the analytical calculation with the results of the experimental data. The final stage, at which a comprehensive assessment of the adequacy of the mathematical model is given, includes both the results of the preparatory and the main stages. The results of the study showed that it can be concluded that the calculated data have sufficient convergence with the experimental data and indicate the adequacy of the developed mathematical model of heat transfer.

Keywords: mathematical modeling, foam glass, raw mix, heat treatment, heat transfer, Pearson's criterion, Student's criterion

МАТЕМАТИЧЕСКОЕ МОДЕЛИРОВАНИЕ И ЭКСПЕРИМЕНТАЛЬНОЕ ИССЛЕДОВАНИЕ ПРОЦЕССА НЕСТАЦИОНАРНОГО ТЕПЛОПЕРЕНОСА В ОБРАЗЦЕ БЛОЧНОГО ПЕНОСТЕКЛА НА СТАДИИ ОТЖИГА

С.В. Федосов [1], М.О. Баканов [2], И.А. Кузнецов [2]

[1] Национальный исследовательский Московский государственный строительный университет, г. Москва, РОССИЯ
[2] Ивановская пожарно-спасательная академия ГПС МЧС России, г. Иваново, РОССИЯ

Аннотация. Представлена специфика технологии производства блочного пеностекла, приведены результаты экспериментальных исследований свойств материала, предложен способ совершенствования производства на основе математического моделирования процессов теплопереноса. Показано, что процессы высокотемпературной обработки пеностекла вносят ключевой вклад в формирование качественной пористой структуры, поэтому данная область исследования нуждается в разработке адекватных методик расчета основных макрофизических параметров на основе теории теплопереноса. Представлена методика проверки адекватности математической модели теплопереноса на примере самопроизвольного остывания блока пеностекла. Всю процедуру проверки адекватности математической модели проводили в три этапа. На первом этапе проводится оценка степени валидации модели, функциональных зависимостей с результатами экспериментального исследования на основе

коэффициента детерминации Пирсона. Основной этап включает в себя оценку доверительных интервалов экспериментальных данных и обсуждение схождения результатов аналитического расчета с результатами экспериментальных данных. Заключительный этап, на котором дается комплексная оценка адекватности математической модели, включает в себя как результаты подготовительного, так и основного этапов. Результаты исследования показали, что расчетные данные имеют достаточную сходимость с экспериментальными данными и свидетельствуют об адекватности разработанной математической модели теплопереноса.

Ключевые слова: математическое моделирование, пеностекло, сырьевая смесь, термическая обработка, теплоперенос, критерий Пирсона, критерий Стьюдента

INTRODUCTION

The technology of foam glass production is characterized by a long sequence of different technological operations often complicated by destructive factors. Therefore, the development, analysis and implementation of advanced technologies require a wide range of physico-chemical and physico-technological studies to obtain a final product with optimal operational properties.

The crucial factor that determines the processes of change in the foam glass structure is the temperature-time mode of foaming and holding (annealing) of the material, which is also called the mode of high-heat treatment [1-3]. In the process of high-heat treatment of the raw material mixture for foam glass production, structural transformations are intensified, from softening to reaching the level of glassy state of the material. The necessity of theory development in this area is caused both by the factors of development and improvement of research methodology of foam glass technology as well as by reduction of unit production cost of finished products. It should be noted that modeling of heat transfer processes as a result of high temperature effect on the material plays an important corrective role.

For production of foam glass nowadays, both domestic raw materials and domestically recycled materials are used. The use of waste glass (recyclable sheet or industrial glass) solves the problem of disposal of waste glass, which contributes to solving a number of environmental problems.

There are various technologies of foam glass production, the most effective being the two-stage powder technology [4,5] which was first proposed by I.I.Kitaygorodskiy and T.N. Keshishyan [6].

The principal process diagram of block foam glass production is presented in Figure 1 [7].

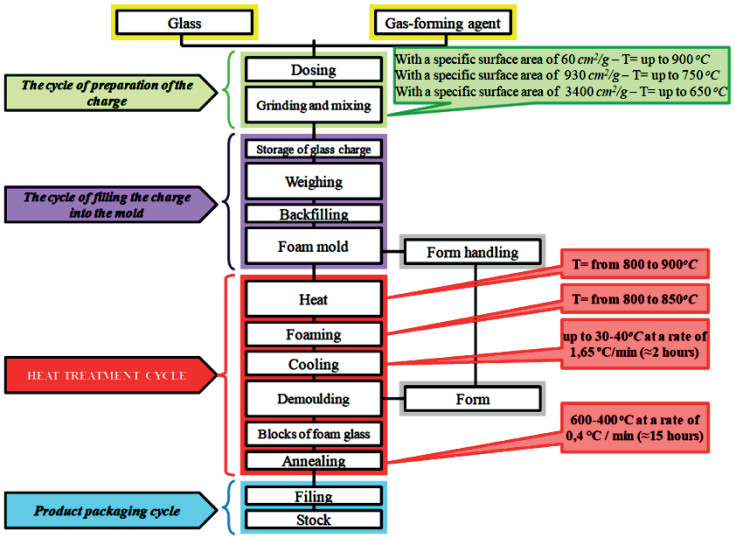

Figure 1. Process flowchart for foam glass production under two-stage powder technology

The operational sequence of the block foam glass production by means of the two-stage powder method is as follows: the feed raw material mixture being in a mold is transported into a lehr oven on ceramic rollers (Figure 2) [8,9].

In the first kiln (the section of thermal influence on the raw material mixture), the raw material mixture is heated, sintered, foamed and the foamed glass-crystalline structure is stabilized (Figure 3), then the foam glass blocks are extracted from the molds (Figure 4).

Figure 2. Loading the raw material mixture into the molds

Figure 3. Section of heating, sintering, foaming and stabilizing oven

Figure 4. Stage of extracting the finished foam glass blocks from molds

The used molds are returned on the conveyor belt to the stage of loading the raw material mixture (Figure 5), and the extracted blocks are transported to the annealing furnace (the section of thermal influence on foam glass) (Figure 6).

Figure 5. Fragment of the conveyor belt

Figure 6. Fragment of a foam glass annealing furnace

The powder method for foam glass production is as follows: crushed and milled glass and gas-forming agent (0.5-5% of glass weight) are loaded into the forms, heated to thermal decomposition temperature of gas-forming agent and annealed [9,10].

While the temperature increases, the glass particles are actively softened. For most types of glass, the active softening stage begins at temperatures of about 600°C [9,11]. The viscosity values of the milled glass remain high during this time. At further heating, thermal decomposition of the gas-forming agent occurs, and viscosity indices begin to decrease. Gases at the beginning of thermal decomposition of gas-forming agent form pores in the glass melt. Such kinetics of the process leads to growth of the pore diameter due to stretching of the glass mass shell. When the given size is reached, the heating process is stopped and the temperature is reduced to stabilize the foam glass structure [12,13].

When developing and improving the technology of foam glass production with taking into account the peculiarities of high-heat treatment and time parameters of its production, our researchers carry out their work in two main directions. The first one is the experimental determination of possible compositions of raw material mixtures for production of foam glass and selection of thermal treatment modes by means of the method of correction of quantitative parameters of raw material mixture composition [14-20]. The second research

direction is based on the development of theoretical and numerical methods of modeling of thermal processes occurring during foam glass production [21-28]. The second direction seems to be the most promising in terms of research of foam glass production technology as it allows us to reveal the regularities of material structure formation as well as to take into account the external and internal factors contributing to optimization of the process of foam glass production. However, it is worth noting that it would be practically impossible to develop any theoretical foundations without having the results obtained by the researchers applying the first experimental approach in their works, so it is necessary that theory and practice should exist in symbiotic relationship and complement and confirm the results obtained.

Modeling of heat treatment processes is based on the heat transfer theory, which allows us to take into account the influence of macro-physical parameters on each other. When developing a mathematical model being able to take into account changes in the physico-chemical properties of the raw charge, there arise some difficulties that might require the use of simplified (or approximate) mathematical models of heat transfer [29-33].

The system of differential equations worked out by A.V.Lykov and some physical concepts developed by him with respect to the moisture removal mechanism [34] constitute the theoretical basis for studying the heat and mass transfer processes occurring as a result of high-temperature effect on materials.

Application of exact analytical methods for solving nonlinear problems is practically impossible with modern methods of mathematical analysis, so numerical methods are becoming more and more popular. Solutions of partial differential equations are found using computer programs. The approaches described are applicable when the patterns of heat transfer have already been established, so it is required to obtain equations for simpler models, and, at the first stages of modeling, it is advisable to set boundary conditions and solve a plane problem for one of the coordinates (Figure 7).

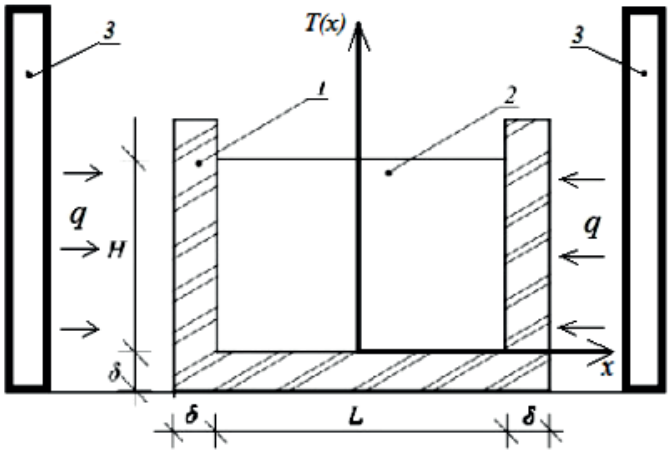

Figure 7. Geometric model used for setting up a problem: 1 - metal wall of the mold; 2 - raw material mixture; 3 - heat source; δ, L - thickness of the mold wall and raw material mixture

Under these conditions, the boundary problem of heat transfer in the raw material mixture placed in a metal mold is written as follows [35]:

$$\rho c \frac{\partial t(x,\tau)}{\partial \tau} = \lambda \frac{\partial^2 t(x,\tau)}{\partial x^2}; \tau > 0; 0 \le x \le \frac{L}{2}, \quad (1)$$

where ρ, c, λ are respectively: density, heat capacity and thermal conductivity of the raw material mixture.
- initial condition:

$$t(x,\tau)\big|_{\tau=0} = t_0(x); \quad (2)$$

- boundary conditions, respectively, of the first and second kind:

$$t(x,\tau)\big|_{x=0} = t_H\ ; \quad (3)$$

$$\frac{\partial t(x,\tau)}{\partial x}\bigg|_{x=\frac{L}{2}} = 0. \quad (4)$$

To solve a boundary value thermal conductivity problem, the Laplace transform method is used. The final solution of the boundary heat conduction problem is as follows:

$$T\left(\bar{x}, Fo\right) = 1 - \frac{4}{\pi}\sum_{n=1}^{\infty}\frac{1}{(2n-1)}\sin\left[\frac{\pi}{2}(2n-1)\bar{x}\right]\cdot\exp\left[-\frac{\pi^2}{4}(2n-1)^2 Fo\right] + 2\sum_{n=1}^{\infty}\sin\left[\frac{\pi}{2}(2n-1)\bar{x}\right]\cdot\int_0^1 T_0(\xi)\cdot$$
$$\cdot\sin\left[\frac{\pi}{2}(2n-1)\xi\right]d\xi\cdot\exp\left[-\frac{\pi^2}{4}(2n-1)^2 Fo\right]\cdot \quad (5)$$

We transform the equation (5) into a dimensional form and obtain:

$$t(x,\tau) = t_H - (t_H - t_0)\cdot\left(\frac{4}{\pi}\cdot\sum_{n=1}^{\infty}\frac{1}{(2n-1)}\sin\left[\frac{\pi}{2}(2n-1)\cdot\bar{x}\right]\cdot\exp\left[-\frac{\pi^2}{4}(2n-1)^2 Fo\right] + \right.$$
$$\left. + 2\sum_{n=1}^{\infty}\sin\left[\frac{\pi}{2}(2n-1)\cdot\bar{x}\right]\cdot\int_0^1 T_0(\xi)\cdot\sin\left[\frac{\pi}{2}(2n-1)\cdot\xi\right]d\xi\cdot\exp\left[-\frac{\pi^2}{4}(2n-1)^2 Fo\right]\right). \quad (6)$$

The main requirements for mathematical models are adequacy, universality and efficiency.
A model is considered adequate if it reflects the given properties with acceptable accuracy. Accuracy is defined as a degree of coincidence of values of output parameters of the model and the object. Model accuracy is different in different conditions of technological process functioning. These conditions are characterized by external parameters. In the space of external parameters, it is necessary to identify the area of model adequacy, where the error is less than the specified maximum permissible error. Determining the area of model adequacy is a complex procedure that requires large computational efforts that rapidly increase with increasing the dimensionality of the space of external parameters. This problem can considerably exceed by its volume the problem of parametric optimization of the model itself, so it may not be solved for newly designed processes.

During the simulation of temperature fields in a foam glass block, the task of checking the adequacy of the mathematical models developed becomes many times more complicated due to the influence of a wide range of factors both on the simulated system and on the conditions of full-scale test. The authors present a method of research of developed mathematical model of heat transfer on the surface of foam glass during spontaneous cooling (annealing).

RESEARCH METHODS

For carrying out computational and full-scale experiments, a foam glass block was removed from the conveyor belt at the stage of extraction of blocks from the molds (extraction station) and placed on a pallet (in the air).
Figure 8 shows schematically the placement of thermocouples in a foam glass block.

Thereafter, we will consider the temperature change at Points 1 and 2 that are the center and surface of the foam glass block respectively, as their location can give the closest possible description of the temperature change features on the block interaction boundary, namely, the surface of its sides and the center of the material (Fig. 9).

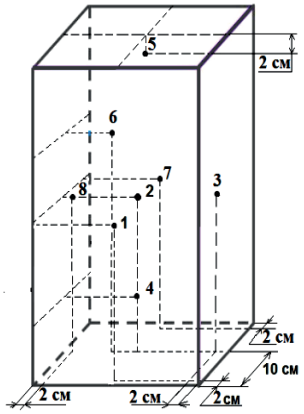

Figure 8. Distribution of thermocouples on the block under study

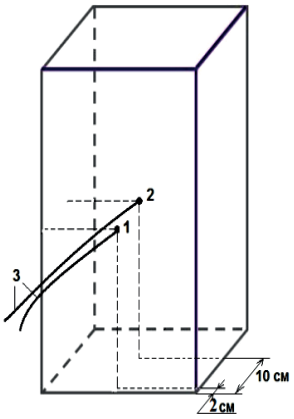

Figure 9. Distribution of thermocouples at Points No.1 and No.2 i.e. the center and the surface of the foam block respectively

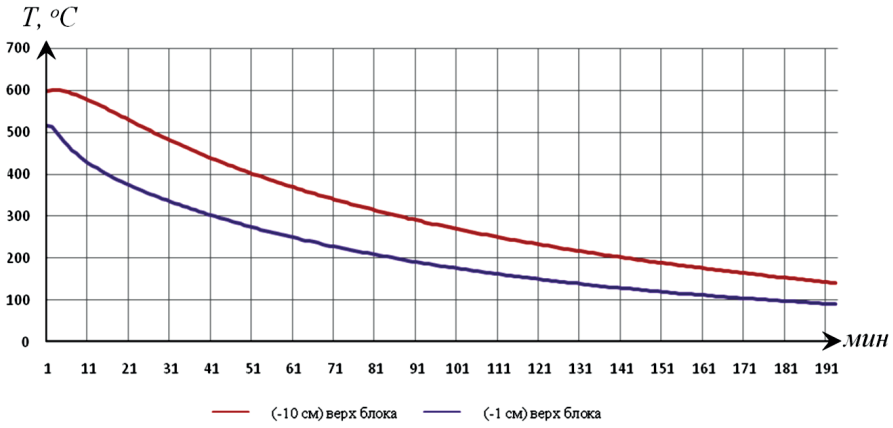

Figure 10. Temperature values in the center and on the surface of the block

As shown in the graphs (Fig. 10), in the process of spontaneous cooling of the foam glass block, the temperature values at the surface and in the center show similar dynamics with the presence of a stable difference binding. This fact indicates that there is a complex process of heat transfer. The porous structure of the material itself should also be considered as it contributes to the retention of heat within the foam glass block. The initial cooling conditions and interaction of the outer boundaries of the foam glass block with the surrounding air did not lead to a sharp decrease in temperature at its borders due to the closed pore structure, which can also be said about the temperature indicators in the center of the block.

To verify the adequacy of the mathematical model, we calculate the temperature values in the center and on the surface of the foam glass block. For calculations, we use a model (6).

For implementation of numerical modeling, we assume that the initial temperature of the foam glass block is 600±10 °C. The surface temperature (25±5°C) corresponds to the air temperature in the shop at the time of the experiment.

Calculations for the control point №1 are carried out at a time of 1 minute, the calculated value of

the Fourier number at this time is taken equal to 0.001. Based on the results of the calculations, we plot the graphical dependence of the temperature distribution in the foam glass block.

For descriptive reasons, we build a general functional dependence of the distribution of temperature fields from 1 to 90 minutes (Figure 11).

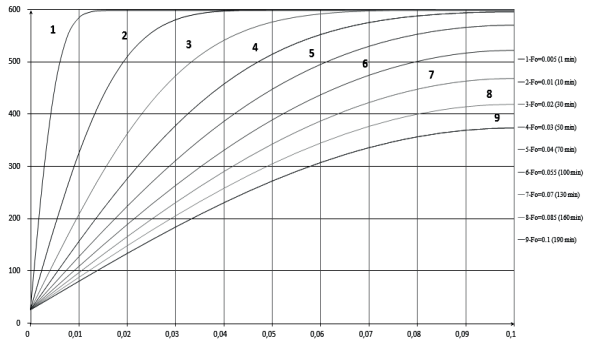

Figure 11. Graph of temperature field distribution on the surface of the foam glass at its cooling, taking into account the data obtained by a thermoelectric transducer at the Control Point No.1

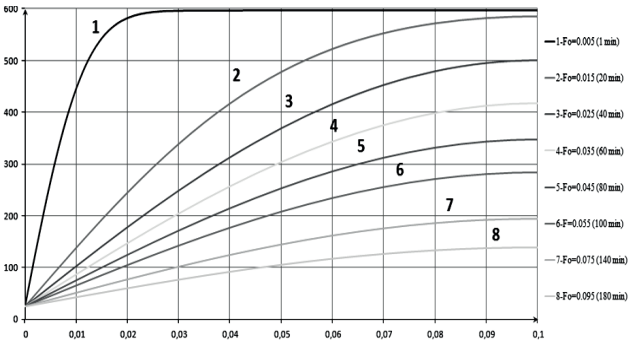

Figure 12. Graph of temperature field distribution in the center of the foam glass at its cooling, taking into account the data obtained by a thermoelectric transducer at the Control Point No. 2

Calculations for Control Point No. 2 are carried out at a time of 1 minute, the calculated value of the Fourier number at this time is 0.005. The difference of the Fourier number values compared with the values for the surface is due to the fact that the temperature gradient is directed from the center not only in the direction under consideration, but also in three other directions, so unlike the parameters on the surface, the temperature change rate at Control Point No.2 will be higher. In our calculations, we took it as being 3 times higher. Based on the results of the calculations, we plot the graph of temperature distribution indicators for the foam block (Figure 12).

As can be seen from the graphs of calculated and experimental values of temperature changes during cooling down of the block at the Control Point at 2 cm from the surface during 190 min (Fig. 13), the temperature dynamics is nonlinear, indicating the presence of an area of intense cooling and an area of temperature stabilization. The most intensive cooling is observed in the time intervals from 0 to 50 seconds, then a relative stabilization of the temperature is observed.

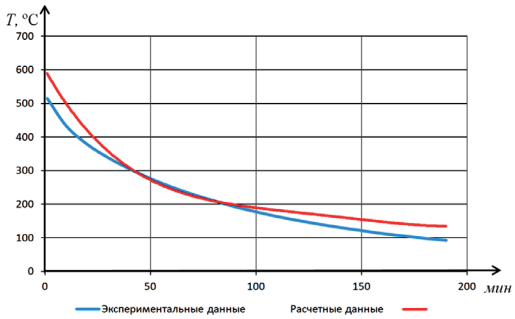

Figure 13. Diagram of changes in calculated and experimental values of temperature when cooling down the block at the Control Point for the center within 190 min.

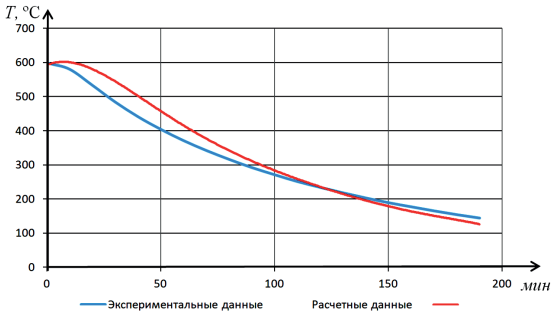

Figure 14. Diagram of changes in calculated and experimental values of temperature when cooling down the block at the Control Point for the surface within 190 min.

On the graphs of changes in calculated and experimental values of temperature when cooling down the block at the Control Point for the center for 190 min (Fig. 14), the temperature dynamics is also non-linear, indicating a complex heat transfer in the center of the foam glass block. Heat transfer by heat conduction (pore walls) as well as by convection (gas phase inside the pores) is observed. The key influence on the peculiarities of heat transfer in the center of the foam glass block is exerted by a closed pore structure inside the material.

Assessment of mathematical model adequacy includes preparatory, main and final stages.

At the preparatory stage, we evaluate the degree of validation of the model, functional relationships with the results of the experimental study on the basis of the Pearson determination coefficient.

The main stage includes the estimation of confidence intervals of experimental data and a discussion of the convergence of analytical calculation results with the results of experimental data.

The final stage which provides a comprehensive assessment of the adequacy of the mathematical model includes both the results of the preparatory and main stages.

RESEARCH RESULTS

According to the data presented in Fig. 15, we can draw the following conclusions:

- the calculated data for the model are close in value to the mean estimates of the experimental data and are contained within the confidence interval along the entire time axis;
- the maximum deviation of the calculated data is observed at the beginning and at the end of the time axis, which demonstrates the correct choice of the diffusion model of experimental data;
- the deviation of the calculated data from the experimental data is directed toward the upper exact limit, which provides the necessary margin for modeling the process of cooling the foam glass block.

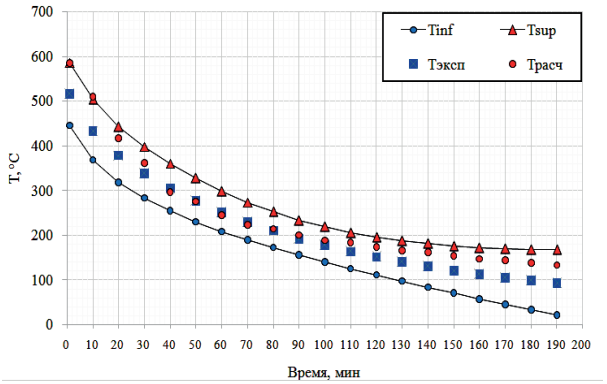

Figure 15. Comparison of calculated and experimental values of temperature when cooling down the block on the surface

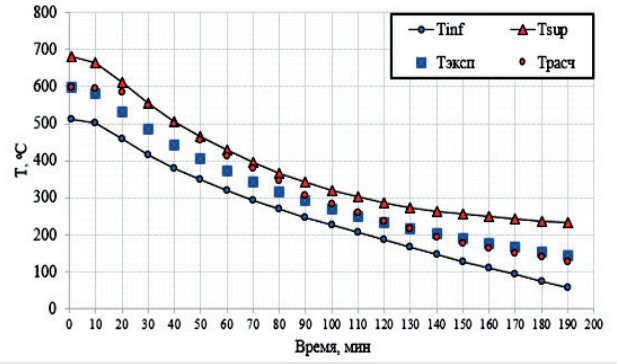

Figure 16. Comparison of calculated and experimental values of temperature when cooling down the block in the center

The data presented in Figs. 15, 16 demonstrate the following conclusions:

- the calculated model data are close in value to the mean estimates of the experimental data and are contained within the confidence interval along the entire time axis;
- the maximum deviation of the calculated data is observed at the beginning of the time axis, which is similar to the results of the estimation on the surface, also the data demonstrate the correct choice of the dispersion model of the experimental data;
- the deviation of the calculated data from the experimental data is directed toward the upper precise limit, which provides the necessary

margin in modeling the cooling process of the foam block.

CONCLUSIONS

A comprehensive assessment of the adequacy of a model has been carried out on the basis of processing the experimental data using Pearson's criterion and Student's criterion, taking into account of scattering the data relative to the center. The data for a comprehensive assessment are presented in Table 1.

To estimate the intervals in further engineering calculations, it is necessary to take into account the fact that the least upper bound (T_{sup}) is the evaluation of the experimental study.

Table 1. Results of assessment of the adequacy of a mathematical model

Control points for temperature measurements	STAGES OF ASSESSMENT OF THE ADEQUACY OF A MATHEMATICAL MODEL				
	Pearson's Cr. R^2	Student's Cr., t_p (P,k)	Complex data error, $S_e$max	Max. experimental scatter, ΔT_{max}	Conclusion
on the surface	R^2=0.969	P=0.2; k=19; t_p =1,33	$S_e$max=52.82 ^{O}C $S_e$min=27.68 ^{O}C	ΔT_{max}=70 ^{O}C ΔT_{min}=37 ^{O}C	adequate
in the center	R^2=0.985	P=0.2; k=19; t_p =1.33	$S_e$max=63.91 ^{O}C $S_e$min=33.50 ^{O}C	ΔT_{max}=85 ^{O}C ΔT_{min}=44 ^{O}C	adequate

Based on the data in Table 1, we can estimate the actual experimental temperature-time scatter by the formula $P_{empir}=\Delta T_{max}/T_{max}$:

– at Control Point No.1 of the foam glass block $P_{empir}=\Delta T_{max}/T_{max}$=0,13;

– at Control Point No. 2 of the foam block $P_{empir}=\Delta T_{max}/T_{max}$ = 0,14.

The data obtained show the correct choice of the confidence probability P=0.2 in estimating the quantile of the Student's t-distribution.

Taking into account Pearson's criterion values close to 1 and the maximum confidence probability in calculating Student's criterion, we can conclude that the calculated data have sufficient convergence with the experimental data and show the adequacy of the developed mathematical model.

The developed mathematical model of heat transfer at the stage of spontaneous cooling down of foam glass blocks enables us to conduct research of peculiarities of temperature distribution of foam glass blocks and to estimate convergence of functional dependence between time and temperature at the given control points according to the results of experimental data. The conducted study of mathematical model adequacy shows high convergence of the results of modeling and experimental measurements of temperature values at the given points of control. The obtained estimated values of Pearson's coefficient of determination - 0.969 for Control Point No. 1 and 0.985 for Control Point No. 2 demonstrate the presence of a stable functional relationship between the indicators of temperature dynamics obtained from the calculation of the mathematical model developed, and the data obtained from the experimental measurement of temperature using the applicable means of control.

REFERENCES

1. **Sopegin G.V., Rustamova D.Ch., Fedoseev S.M.** Analysis of existing technological solutions for the production of foam glass // Vestnik MGSU. - 2019. - T. 14. - No. 12 (135). - S. 1584-1609 (rus).
2. **Yatsenko E.A. et al.** Peculiarities of foam glass synthesis from natural silica-containing raw materials //Journal of Thermal Analysis and Calorimetry. – 2020. – T. 142. – C. 119-127.

3. **Siddika A., Hajimohammadi A., Sahajwalla V.** Powder sintering and gel casting methods in making glass foam using waste glass: A review on parameters, performance, and challenges //Ceramics International. – 2022. – T. 48. – №. 2. – C. 1494-1511.
4. **Greshnov V.A.** Foam glass as a promising heat-insulating material // Advanced innovative developments. Prospects and experience of use, problems of implementation in production. - 2019. - Part 1 - S. 233-235 (rus).
5. **Goltsman B.M.** Investigation of the foaming activity of various types of pore formers when foaming foam glass // Technique and technology of silicates. - 2020. - T. 27. - No. 3. - S. 66-69 (rus).
6. **Demidovich B.K.** Foam glass. Minsk: Science and technology, 1975. 248 p (rus).
7. **Bakanov M.O.** Modeling of high-temperature processes in foam glass technology. Part 1: Formation of the dynamics of cyclic non-stationary two-dimensional temperature fields // Bulletin of the Volga State Technological University. Series "Materials. Constructions. Technologies". – 2021. – no. 2 (18). - S. 87-102.
8. **Grushko I.S.** Investigation of the technological stages of obtaining porous glass using mathematical modeling (review) // Glass and ceramics. – 2016. – no. 10. - P. 3-9 (rus).
9. **Goltsman B.M., Yatsenko E.A.** Role of Carbon Phase in the Formation of Foam Glass Porous Structure //Materials. – 2022. – T. 15. – №. 22. – C. 7913.
10. **Gol'tsman B.M., Yatsenko E.A.** Modern Methods for Foaming of Glass and Silicate Raw Materials: Review and Analysis //Theoretical Foundations of Chemical Engineering. – 2022. – T. 56. – №. 5. – C. 678-686.
11. **Grushko I.S.** Investigation of foam glass stresses taking into account thermal loads during annealing // News of higher educational institutions. North Caucasian region. Technical science. – 2018. – no. 2 (198). - S. 90-95 (rus).
12. **Grushko I.S.** Calculation of the thermal field of foam glass during annealing // Glass Physics and Chemistry. - 2018. - T. 44. - No. 3. - S. 294-302 (rus).
13. **Rodin A.I. et al.** Porous glass ceramics from siliceous rocks with high operating temperature //Magazine of Civil Engineering. – 2022. – T. 116. – №. 8. – C. 3-5.
14. **Sedlačík M. et al.** Preparation and characterization of glass-ceramic foam from clay-rich waste diatomaceous earth //Materials. – 2022. – T. 15. – №. 4. – C. 1384.
15. **Alexander R. et al.** Porous glass ceramics from siliceous rocks with high operating temperature //Magazine of Civil Engineering. – 2022. – T. 116. – №. 8. – C. 11615.
16. **Pavlenko A., Szkarowski A.** Thermal insulation materials with high-porous structure based on the soluble glass and technogenic mineral fillers //Rocznik Ochrona Środowiska. – 2018. – T. 20. – C. 725-740.
17. **Salerno A. et al.** Design of porous polymeric scaffolds by gas foaming of heterogeneous blends //Journal of Materials Science: Materials in Medicine. – 2009. – T. 20. – C. 2043-2051.
18. **Miryuk O., Fediuk R., Amran M.** Foam glass crystalline granular material from a polymineral raw mix //Crystals. – 2021. – T. 11. – №. 12. – C. 1447.
19. **Sassi M., Simon A.** Waste-to-Reuse Foam Glasses Produced from Soda-Lime-Silicate Glass, Cathode Ray Tube Glass, and Aluminium Dross //Inorganics. – 2022. – T. 10. – №. 1. – C. 1.
20. **Mustafa W.S., Nagy B., Szendefy J.** Impact of compaction ratio and loading period on compressional behavior of foam glass aggregates //Construction and

Building Materials. – 2022. – T. 343. – C. 128111.
21. **Fedosov S.V., Bakanov M.O., Nikishov S.N.** Kinetics of structural transformations at pores formation during high-temperature treatment of foam glass, International Journal for Computational Civil and Structural Engineering. (2018) 14(2) 158–168.
22. **Grushko I.** Definition of the strain-stress distribution of porous glass in the retarded cooling temperature range //MATEC Web of Conferences. – EDP Sciences, 2017. – T. 132. – C. 03006.
23. **Siddika A., Hajimohammadi A., Sahajwalla V.** Stabilisation of pores in glass foam by using a modified curing-sintering process: sustainable recycling of automotive vehicles' waste glass //Resources, Conservation and Recycling. – 2022. – T. 179. – C. 106145.
24. **Apkar'yan A.S.** Investigation of the density of granular foam-glass ceramic by mathematical modeling //Glass and Ceramics. – 2014. – T. 71. – C. 194-197.
25. **Grushko I.S.** Mathematical Modeling of the Technological Stages of Porous Glass Production //Glass and Ceramics. – 2017. – T. 73. – №. 9-10. – C. 355-360.
26. **Choudhary M.K.** Mathematical modeling of rate phenomena in glass melting furnaces //Fiberglass Science and Technology: Chemistry, Characterization, Processing, Modeling, Application, and Sustainability. – 2021. – C. 483-539.
27. **da Silva R.C. et al.** Recycling of glass waste into foam glass boards: A comparison of cradle-to-gate life cycles of boards with different foaming agents //Science of The Total Environment. – 2021. – T. 771. – C. 145276.
28. **Dragoescu M.F. et al.** Simulating foam glass production in a tunnel furnace powered with microwaves //International Journal of Innovative Science and Research Technology. – 2018. – T. 3. – №. 1. – C. 718-722.
29. **Fedosov S.V., Bakanov M.O., Nikishov S.N.** Kinetics of Cellular Structure Formation at Thermal Treatment Processes Simulation in the Cellular Glass Technology, Materials Science Forum Submitted. (2018) Vol. 931, pp 628–633.
30. **Grushko I.** Definition of the strain-stress distribution of porous glass in the retarded cooling temperature range //MATEC Web of Conferences. – EDP Sciences, 2017. – T. 132. – C. 03006.
31. **Dragoescu M. F. et al.** Foam glass with low apparent density and thermal conductivity produced by microwave heating //Eur. J. Eng. Technol. – 2018. – T. 6.
32. **Cimavilla-Román P. et al.** Modelling of the mechanisms of heat transfer in recycled glass foams //Construction and Building Materials. – 2021. – T. 274. – C. 122000.
33. **Lykov A.V. and Mikhailov Yu.A.** Theory of heat and mass transfer. M.-L., «Gosenergoizdat», 1963, 536 pages (rus).
34. **Fedosov S.V.** Heat and mass transfer in technological processes of the construction industry: monograph. - Ivanovo: PressSto, 2010. - 364 p (rus).
35. **Bakanov M.O.** Modeling of high-temperature processes in foam glass technology. Part 1: Formation of the dynamics of cyclic non-stationary two-dimensional temperature fields // Bulletin of the Volga State Technological University. Series: Materials. Constructions. Technology. - 2021. - No. 2 (18) - P. 87-102 (rus).

СПИСОК ЛИТЕРАТУРЫ

1. **Сопегин Г.В., Рустамова Д.Ч., Федосеев С.М.** Анализ существующих технологических решений производства пеностекла // Вестник МГСУ. – 2019. – Т. 14. – №. 12 (135). – С. 1584-1609.
2. **Yatsenko E.A. et al.** Peculiarities of foam glass synthesis from natural silica-containing raw materials //Journal of

Thermal Analysis and Calorimetry. – 2020. – Т. 142. – С. 119-127.
3. **Siddika A., Hajimohammadi A., Sahajwalla V.** Powder sintering and gel casting methods in making glass foam using waste glass: A review on parameters, performance, and challenges //Ceramics International. – 2022. – Т. 48. – №. 2. – С. 1494-1511.
4. **Грешнов В.А.** Пеностекло как перспективный теплоизоляционный материал // Передовые инновационные разработки. Перспективы и опыт использования, проблемы внедрения в производство. – 2019. – Часть 1 – С. 233-235.,
5. **Гольцман Б.М.** Исследование вспенивающей активности различных типов порообразователей при вспенивании пеностекла // Техника и технология силикатов. – 2020. – Т. 27. – №. 3. – С. 66-69.
6. **Демидович Б.К.** Пеностекло. Минск: Наука и техника, 1975. 248 с.
7. **Баканов М.О.** Моделирование высокотемпературных процессов в технологии пеностекла. Часть 1: Формирование динамики циклических нестационарных двумерных температурных полей //Вестник Поволжского государственного технологического университета. Серия «Материалы. Конструкции. Технологии». – 2021. – №. 2 (18). – С. 87-102.
8. **Грушко И.С.** Исследования технологических стадий получения пористого стекла с применением математического моделирования (обзор) // Стекло и керамика. – 2016. – №. 10. – С. 3-9.
9. **Goltsman B.M., Yatsenko E.A.** Role of Carbon Phase in the Formation of Foam Glass Porous Structure //Materials. – 2022. – Т. 15. – №. 22. – С. 7913.
10. **Gol'tsman B.M., Yatsenko E.A.** Modern Methods for Foaming of Glass and Silicate Raw Materials: Review and Analysis //Theoretical Foundations of Chemical Engineering. – 2022. – Т. 56. – №. 5. – С. 678-686.
11. **Грушко И.С.** Исследование напряжений пеностекла с учетом тепловых нагрузок при отжиге // Известия высших учебных заведений. Северо-Кавказский регион. Технические науки. – 2018. – №. 2 (198). – С. 90-95.
12. **Грушко И.С.** Расчет теплового поля пеностекла в процессе отжига //Физика и химия стекла. – 2018. – Т. 44. – №. 3. – С. 294-302.
13. **Rodin A.I. et al.** Porous glass ceramics from siliceous rocks with high operating temperature //Magazine of Civil Engineering. – 2022. – Т. 116. – №. 8. – С. 3-5.
14. **Sedlačík M. et al.** Preparation and characterization of glass-ceramic foam from clay-rich waste diatomaceous earth //Materials. – 2022. – Т. 15. – №. 4. – С. 1384.
15. **Alexander R. et al.** Porous glass ceramics from siliceous rocks with high operating temperature //Magazine of Civil Engineering. – 2022. – Т. 116. – №. 8. – С. 11615.
16. **Pavlenko A., Szkarowski A.** Thermal insulation materials with high-porous structure based on the soluble glass and technogenic mineral fillers //Rocznik Ochrona Środowiska. – 2018. – Т. 20. – С. 725-740.
17. **Salerno A. et al.** Design of porous polymeric scaffolds by gas foaming of heterogeneous blends //Journal of Materials Science: Materials in Medicine. – 2009. – Т. 20. – С. 2043-2051.
18. **Miryuk O., Fediuk R., Amran M.** Foam glass crystalline granular material from a polymineral raw mix //Crystals. – 2021. – Т. 11. – №. 12. – С. 1447.
19. **Sassi M., Simon A.** Waste-to-Reuse Foam Glasses Produced from Soda-Lime-Silicate Glass, Cathode Ray Tube Glass, and

Aluminium Dross //Inorganics. – 2022. – Т. 10. – №. 1. – С. 1.
20. **Mustafa W.S., Nagy B., Szendefy J.** Impact of compaction ratio and loading period on compressional behavior of foam glass aggregates //Construction and Building Materials. – 2022. – Т. 343. – С. 128111.
21. **Fedosov S.V., Bakanov M.O., Nikishov S.N.** Kinetics of structural transformations at pores formation during high-temperature treatment of foam glass, International Journal for Computational Civil and Structural Engineering. (2018) 14(2) 158–168.
22. **Grushko I.** Definition of the strain-stress distribution of porous glass in the retarded cooling temperature range //MATEC Web of Conferences. – EDP Sciences, 2017. – Т. 132. – С. 03006.
23. **Siddika A., Hajimohammadi A., Sahajwalla V.** Stabilisation of pores in glass foam by using a modified curing-sintering process: sustainable recycling of automotive vehicles' waste glass //Resources, Conservation and Recycling. – 2022. – Т. 179. – С. 106145.
24. **Apkar'yan A.S.** Investigation of the density of granular foam-glass ceramic by mathematical modeling //Glass and Ceramics. – 2014. – Т. 71. – С. 194-197.
25. **Grushko I.S.** Mathematical Modeling of the Technological Stages of Porous Glass Production //Glass and Ceramics. – 2017. – Т. 73. – №. 9-10. – С. 355-360.
26. **Choudhary M.K.** Mathematical modeling of rate phenomena in glass melting furnaces //Fiberglass Science and Technology: Chemistry, Characterization, Processing, Modeling, Application, and Sustainability. – 2021. – С. 483-539.
27. **da Silva R. C. et al.** Recycling of glass waste into foam glass boards: A comparison of cradle-to-gate life cycles of boards with different foaming agents //Science of The Total Environment. – 2021. – Т. 771. – С. 145276.
28. **Dragoescu M.F. et al.** Simulating foam glass production in a tunnel furnace powered with microwaves //International Journal of Innovative Science and Research Technology. – 2018. – Т. 3. – №. 1. – С. 718-722.
29. **Fedosov S.V., Bakanov M.O., Nikishov S.N.** Kinetics of Cellular Structure Formation at Thermal Treatment Processes Simulation in the Cellular Glass Technology, Materials Science Forum Submitted. (2018) Vol. 931, pp 628–633.
30. **Grushko I.** Definition of the strain-stress distribution of porous glass in the retarded cooling temperature range //MATEC Web of Conferences. – EDP Sciences, 2017. – Т. 132. – С. 03006.
31. **Dragoescu M. F. et al.** Foam glass with low apparent density and thermal conductivity produced by microwave heating //Eur. J. Eng. Technol. – 2018. – Т. 6.
32. **Cimavilla-Román P. et al.** Modelling of the mechanisms of heat transfer in recycled glass foams //Construction and Building Materials. – 2021. – Т. 274. – С. 122000.
33. **Лыков А.В., Михайлов Ю.А.**, Теория тепло- и массопереноса. М.-Л., «Госэнергоиздат», 1963, 536 с.
34. **Федосов С.В.** Тепломассоперенос в технологических процессах строительной индустрии: монография / С. В. Федосов. – Иваново: ПрессСто, 2010. – 364 с.
35. **Баканов М.О.** Моделирование высокотемпературных процессов в технологии пеностекла. Часть 1: Формирование динамики циклических нестационарных двумерных температурных полей // Вестник Поволжского государственного технологического университета. Серия: Материалы. Конструкции. Технологии. – 2021. – № 2 (18) – С. 87-102.

Sergey V. Fedosov, academician of the RAASN, doctor of technical sciences, professor, professor of the department «Technologies and organization of construction production» of Moscow State University of Civil Engineering, Yaroslavl highway, 26, Moscow, Russian Federation, 129337, E-mail: fedosov-academic53@mail.ru; ID RISC: 1840-8194, ORCID: 0000-0001-6117-7529, Scopus Author ID: 7005670404.

Maksim O. Bakanov, doctor of technical sciences, docent, head of the educational and scientific complex «Fire extinguishing» of Ivanovo Fire Rescue Academy of State Firefighting Service of Ministry of Russian Federation for Civil Defense, Emergencies and Elimination of Consequences of Natural Disasters, Stroiteley ave., 33, Ivanovo, 153011, Russia, E-mail: mask-13@mail.ru; ID RISC: 3185-5193, ORCID: 0000-0001-8460-9056, Scopus Author ID: 57204434215.

Ilya A. Kuznetsov, researcher of the research department of the educational and scientific complex «Fire extinguishing» of Ivanovo Fire Rescue Academy of State Firefighting Service of Ministry of Russian Federation for Civil Defense, Emergencies and Elimination of Consequences of Natural Disasters, Stroiteley ave., 33, Ivanovo, 153011, Russia, E-mail: ikuz1999@list.ru

Федосов Сергей Викторович, академик РААСН, доктор технических наук, профессор, профессор кафедры «Технологии и организация строительного производства» Национального исследовательского Московского государственного строительного университета, Ярославское шоссе, 26, Москва, Российская Федерация, 129337, E-mail: FedosovSV@mgsu.ru; SPIN-код: 1840-8194, ORCID: 0000-0001-6117-7529, Scopus Author ID: 7005670404

Баканов Максим Олегович, доктор технических наук, доцент, начальник учебно-научного комплекса «Пожаротушение» Ивановской пожарно-спасательной академии ГПС МЧС России, пр-т Строителей, 33, Иваново, Российская Федерация, 153011, E-mail: mask-13@mail.ru; SPIN-код: 3185-5193, ORCID: 0000-0001-8460-9056, Scopus Author ID: 57204434215.

Кузнецов Илья Александрович, научный сотрудник научно-исследовательского отделения учебно-научного комплекса «Пожаротушение» Ивановской пожарно-спасательной академии ГПС МЧС России, пр-т Строителей, 33, Иваново, Российская Федерация, 153011, E-mail: ikuz1999@list.ru

International Journal for Computational Civil and Structural Engineering, 19(1) 204–211 (2023)

DOI:10.22337/2587-9618-2023-19-1-204-211

INFINITESIMAL AND FINITE DEFORMATIONS IN THE POLAR COORDINATE SYSTEM

Lyudmila Yu. Frishter

National Research Moscow State University of Civil Engineering, Moscow, RUSSIA

Abstract: The deformation problem of elasticity theory with regard to nonlinear deformations is examined. The expressions of deformations through displacements in the orthogonal curvilinear coordinate system are recorded. The relations for finite deformations in cylindrical and polar coordinate systems are derived. Physical relations for finite deformations and corresponding generalized stresses are recorded.

Keywords: small deformations, finite deformations, nonlinear continuum mechanics problem, curvilinear orthogonal coordinate system, cylindrical coordinate system, polar coordinate system, plane deformation, generalized stresses

БЕСКОНЕЧНО МАЛЫЕ И КОНЕЧНЫЕ ДЕФОРМАЦИИ В ПОЛЯРНОЙ СИСТЕМЕ КООРДИНАТ

Л.Ю. Фришmер

Национальный исследовательский Московский государственный строительный университет, г. Москва, РОССИЯ

Аннотация: Рассматривается деформационная задача теории упругости с учетом нелинейных деформаций. Записываются выражения деформаций через перемещения в ортогональной криволинейной системе координат. Выводятся соотношения для конечных деформаций в цилиндрической и полярной системах координат. Записываются физические соотношения для конечных деформаций и соответствующих обобщенных напряжений.

Ключевые слова: малые деформации, конечные деформации, нелинейная задача механики сплошной среды, криволинейная ортогональная система координат, цилиндрическая система координат, полярная система координат, плоская деформация, обобщенные напряжения

1. INTRODUCTION

This article examines the deformation problem. The positions of medium points before and after deformation are given. The change in the position of the vector connecting two arbitrary points of the medium, caused by the deformation of the medium, is determined. The solution of the problem does not depend on the assumptions regarding the properties of the medium and is solved geometrically, typically in the Cartesian coordinate system [1-7]. The initial and final positions of the medium points are defined by projections on the Cartesian coordinate system axes.

Problems with angular cutouts of the boundary, with angular lines of the boundary at surface intersections, with holes in the area for the case of small deformations are considered in polar, spherical or cylindrical coordinate systems. The choice of some curvilinear orthogonal coordinate system is determined by the formulation of the problem. At the same time, the curvilinear coordinate system is chosen so that the body boundary is defined as a coordinate surface or line.

The paper [8, 9] examines a surface with an angular line formed by irregular points. In order to study the peculiarities of the solution in the vicinity of the boundary, a curvilinear coordinate

system (ρ,φ,s) is introduced. The elastic problem in the vicinity of a point on the angle line of the boundary of the area is reduced to the solution of two problems: plane and antiplane deformation.

Analytical and experimental calculation methods [10-15] show that the investigation of the solution of the general elliptic boundary value problem in the vicinity of irregular boundary points is reduced to the consideration of boundary value problems for model regions: wedge or cone.

In order to solve the elastic problem for regions with an angular boundary cutout, it is convenient for wedges and regions with a hole to apply a particular kind of a curvilinear orthogonal coordinate system, the polar system [12-15].

The derivation of relations for finite deformations in the Cartesian coordinate system is discussed in detail in [1-7], whereas it is not given for the polar coordinate system.

Purpose of the work: to derive expressions for finite deformations in cylindrical and polar coordinate systems.

Objectives of the work: to obtain expressions for finite deformations through displacements, to record physical relations for finite deformations and generalized stresses in the polar coordinate system.

2. MODELING METHODS

2.1. Curvilinear orthogonal coordinate system

We consider the curvilinear orthogonal coordinate system α_1, α_2, α_3 with the origin point O, in which the unit vectors $\vec{k}_1, \vec{k}_2, \vec{k}_3$, lines tangent to coordinate lines $\alpha_1 = const$, $\alpha_2 = const, \alpha_3 = const$, are directed toward increasing parameters $\alpha_1, \alpha_2, \alpha_3$. The directions of vectors $\vec{k}_1, \vec{k}_2, \vec{k}_3$ change when passing from one point to another. The $\alpha_1, \alpha_2, \alpha_3$ parameters are related to the Cartesian coordinates x, y, z of an arbitrary point by the relations:

$$x = f_1(\alpha_1,\alpha_2,\alpha_3),\ y = f_2(\alpha_1,\alpha_2,\alpha_3),$$
$$z = f_3(\alpha_1,\alpha_2,\alpha_3) \quad (1)$$

The relations (1) are equivalent to the definition of the vector $\vec{R} = \vec{R}(\alpha_1,\alpha_2,\alpha_3)$ (fig. 1)

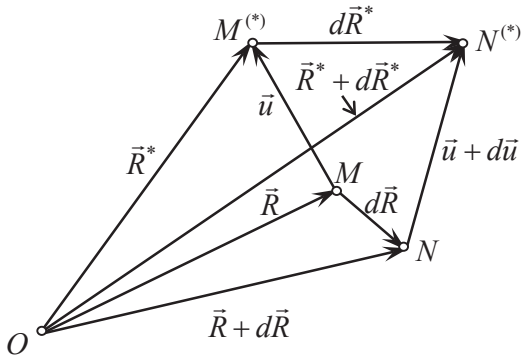

Figure 1. Displacements of points M and N to points M and N* during deformation*

The Lame parameters are described in the following form:

$$H_i = \left|\frac{\partial R}{\partial \alpha_i}\right| = \sqrt{\left(\frac{\partial x}{\partial \alpha_i}\right)^2 + \left(\frac{\partial y}{\partial \alpha_i}\right)^2 + \left(\frac{\partial z}{\partial \alpha_i}\right)^2}, \quad (2)$$

$i = 1,2,3$

The position of the arbitrary point M before deformation is determined by the radius vector $\vec{R} = \vec{R}(\alpha_1,\alpha_2,\alpha_3)$, where α_i – the orthogonal curvilinear coordinates of the vector $\vec{R}$. After the deformation, the point M transitions to the point M^* (fig. 1), which is defined by the radius vector;

$$\vec{R}^* = \vec{R} + \vec{u} = \vec{R} + u_1\vec{k}_1 + u_2\vec{k}_2 + u_1\vec{k}_3$$

where $u_i, i = 1,2,3$ are the projections of the displacement vector $\vec{u}$ on the axes of the local trihedron plotted at point *M*.

The point $N(\alpha_1 + d\alpha_1, \alpha_2 + d\alpha_2, \alpha_3 + d\alpha_3)$ prior to the deformation is defined by the vector

$$\vec{R} + \overrightarrow{dR} = \vec{R} + \sum_i \frac{\partial \vec{R}}{\partial \alpha_i} d\alpha_i = \vec{R} + \sum_i \mathrm{H}_i \overrightarrow{\kappa_i}\, d\alpha_i$$

Following the deformation, the point $N(\alpha_1 + d\alpha_1, \alpha_2 + d\alpha_2, \alpha_3 + d\alpha_3)$ transitions to the point N^* (fig. 1), which is defined by the radius vector in the following form:

$$\vec{R}^* + d\vec{R}^* = \vec{R} + \vec{u} + d(\vec{R} + \vec{u}) =$$
$$= \vec{R} + \vec{u} + \sum_i \frac{\partial \vec{R}}{\partial \alpha_i} d\alpha_i + \sum_i \frac{\partial \vec{u}}{\partial \alpha_i} d\alpha_i,$$

where $\vec{u} = u_1 \vec{k_1} + u_2 \vec{k_2} + u_1 \vec{k_3}$.

Given the differentiation of unit vectors $\vec{k}_i$, we obtain

$$d\overrightarrow{R^*} = \left[(1+e_{11})H_1 d\alpha_1 + (\frac{1}{2}e_{12} - \omega_3)H_2 d\alpha_2 + (\frac{1}{2}e_{13} + \omega_2)H_3 d\alpha_3\right]\overrightarrow{\kappa_1} +$$
$$+\left[(\frac{1}{2}e_{12} + \omega_3)H_1 d\alpha_1 + (1+e_{22})H_2 d\alpha_2 + (\frac{1}{2}e_{23} - \omega_1)H_3 d\alpha_3\right]\overrightarrow{\kappa_2} +$$
$$+\left[(\frac{1}{2}e_{13} - \omega_2)H_1 d\alpha_1 + (\frac{1}{2}e_{23} + \omega_1)H_2 d\alpha_2 + (1+e_{22})H_3 d\alpha_3\right]\overrightarrow{\kappa_3}$$

The expressions for e_{ij}, ω_i have the following form:

$$e_{11} = \frac{1}{H_1}\frac{\partial u_1}{\partial \alpha_1} + \frac{1}{H_1 H_2}\frac{\partial H_1}{\partial \alpha_2}u_2 + \frac{1}{H_1 H_3}\frac{\partial H_1}{\partial \alpha_3}u_3,$$
$$e_{22} = \frac{1}{H_2}\frac{\partial u_2}{\partial \alpha_2} + \frac{1}{H_2 H_3}\frac{\partial H_2}{\partial \alpha_3}u_3 + \frac{1}{H_2 H_1}\frac{\partial H_2}{\partial \alpha_1}u_1,$$
$$e_{33} = \frac{1}{H_3}\frac{\partial u_3}{\partial \alpha_3} + \frac{1}{H_1 H_3}\frac{\partial H_3}{\partial \alpha_1}u_1 + \frac{1}{H_3 H_2}\frac{\partial H_3}{\partial \alpha_2}u_2,$$
$$e_{12} = e_{21} = \frac{H_2}{H_1}\frac{\partial}{\partial \alpha_1}\left(\frac{u_2}{H_2}\right) + \frac{H_1}{H_2}\frac{\partial}{\partial \alpha_2}\left(\frac{u_1}{H_1}\right)$$
$$e_{13} = e_{31} = \frac{H_3}{H_1}\frac{\partial}{\partial \alpha_1}\left(\frac{u_3}{H_3}\right) + \frac{H_1}{H_3}\frac{\partial}{\partial \alpha_3}\left(\frac{u_1}{H_1}\right), \quad (2)$$
$$e_{23} = e_{32} = \frac{H_2}{H_3}\frac{\partial}{\partial \alpha_3}\left(\frac{u_2}{H_3}\right) + \frac{H_3}{H_2}\frac{\partial}{\partial \alpha_2}\left(\frac{u_3}{H_3}\right),$$
$$2\omega_1 = \frac{1}{H_2 H_3}\left[\frac{\partial}{\partial \alpha_2}(H_3 u_3) - \frac{\partial}{\partial \alpha_3}(H_2 u_2)\right],$$
$$2\omega_2 = \frac{1}{H_1 H_3}\left[\frac{\partial}{\partial \alpha_3}(H_1 u_1) - \frac{\partial}{\partial \alpha_1}(H_3 u_3)\right],$$
$$2\omega_3 = \frac{1}{H_1 H_2}\left[\frac{\partial}{\partial \alpha_1}(H_2 u_2) - \frac{\partial}{\partial \alpha_2}(H_1 u_1)\right].$$

We consider the relative elongation at the point M as:

$$E_{MN} = \frac{ds^* - ds}{ds} = \frac{\left|M^* N^*\right| - \left|MN\right|}{\left|MN\right|}.$$

Given the designations of the elongation E_{MN}, the difference $\left|\overrightarrow{M^* N^*}\right|^2 - \left|\overrightarrow{MN}\right|^2$ will be recorded as:

$$E_{MN}(1 + \frac{1}{2}E_{MN})ds^2 = \varepsilon_{11}H_1^2 d\alpha_1^2 + \varepsilon_{22}H_2^2 d\alpha_2^2 +$$
$$+ \varepsilon_{33}H_3^2 d\alpha_3^2 + \varepsilon_{12}H_1 H_2 d\alpha_1 d\alpha_2 +$$
$$+ \varepsilon_{13}H_1 H_3 d\alpha_1 d\alpha_3 + \varepsilon_{23}H_2 H_3 d\alpha_2 d\alpha_3,$$

where ε_{ij} are the deformation components in the curvilinear coordinate system $\alpha_1, \alpha_2, \alpha_3$:

$$\varepsilon_{11} = e_{11} + \frac{1}{2}\left[e_{11}^2 + (\frac{1}{2}e_{12} + \omega_3)^2 + (\frac{1}{2}e_{13} - \omega_2)^2\right],$$
$$\varepsilon_{12} = e_{12} + e_{11}(\frac{1}{2}e_{12} - \omega_3) + e_{22}(\frac{1}{2}e_{12} + \omega_3) +$$
$$+ (\frac{1}{2}e_{13} - \omega_2)(\frac{1}{2}e_{23} + \omega_1), \ldots \quad (3)$$

(cyclic permutation)

2.2. Cylindrical coordinate system

We consider the cylindrical coordinate system: $x = r\cos\varphi,\ y = r\sin\varphi,\ z = z$. The curvilinear coordinates are rewritten as: $\alpha_1 = r, \alpha_2 = \varphi, \alpha_3 = z$. The Lame parameters are: $H_1 = 1, H_2 = r, H_3 = 1$.

Given the expressions e_{ij}, ω_i in the form (2), we obtain expressions for deformations in the cylindrical coordinate system:

$$\varepsilon_{11} = \frac{\partial u_1}{\partial r} + \frac{1}{2}\left[\left(\frac{\partial u_1}{\partial r}\right)^2 + \left(\frac{\partial u_2}{\partial r}\right)^2 + \left(\frac{\partial u_3}{\partial r}\right)^2\right],$$

$$\varepsilon_{22} = \frac{1}{r}\frac{\partial u_2}{\partial \varphi} + \frac{u_1}{r} + \frac{1}{2}[(\frac{1}{r}\frac{\partial u_2}{\partial \varphi} + \frac{u_1}{r})^2 + (\frac{1}{r}\frac{\partial u_1}{\partial \varphi} - \frac{u_2}{r})^2 + (\frac{1}{r}\frac{\partial u_3}{\partial \varphi})^2],$$

$$\varepsilon_{33} = \frac{\partial u_3}{\partial z} + \frac{1}{2}\left[\left(\frac{\partial u_1}{\partial z}\right)^2 + \left(\frac{\partial u_2}{\partial z}\right)^2 + \left(\frac{\partial u_3}{\partial z}\right)^2\right],$$

$$\varepsilon_{12} = \frac{\partial u_2}{\partial r} - \frac{u_2}{r} + \frac{1}{r}\frac{\partial u_1}{\partial \varphi} + \frac{\partial u_1}{\partial r}(\frac{1}{r}\frac{\partial u_1}{\partial \varphi} - \frac{u_2}{r}) + \frac{\partial u_2}{\partial r}(\frac{1}{r}\frac{\partial u_2}{\partial \varphi} + + \frac{1}{r}u_1) + \frac{1}{r}\frac{\partial u_3}{\partial r}\frac{\partial u_3}{\partial \varphi}, \quad (4)$$

$$\varepsilon_{13} = \frac{\partial u_3}{\partial r} + \frac{\partial u_1}{\partial z} + \frac{\partial u_1}{\partial r}\frac{\partial u_1}{\partial z} + \frac{\partial u_2}{\partial r}\frac{\partial u_2}{\partial z} + \frac{\partial u_3}{\partial r}\frac{\partial u_3}{\partial z},$$

$$\varepsilon_{23} = r\frac{\partial u_2}{\partial z} + \frac{1}{r}\frac{\partial u_3}{\partial \varphi} + (\frac{1}{r}\frac{\partial u_1}{\partial \varphi} - \frac{u_2}{r})\frac{\partial u_1}{\partial z} + (\frac{1}{r}\frac{\partial u_2}{\partial \varphi} + \frac{u_1}{r})\frac{\partial u_2}{\partial z} + \frac{1}{r}\frac{\partial u_3}{\partial \varphi}\frac{\partial u_3}{\partial z}.$$

In the case of small deformations, the relations (4) are recorded in the following form:

$$\varepsilon_{11} = \frac{\partial u_1}{\partial r},\quad \varepsilon_{22} = \frac{1}{r}\frac{\partial u_2}{\partial \varphi} + \frac{u_1}{r},\quad \varepsilon_{33} = \frac{\partial u_3}{\partial z},$$
$$\varepsilon_{12} = \frac{\partial u_2}{\partial r} - \frac{u_2}{r} + \frac{1}{r}\frac{\partial u_1}{\partial \varphi},\quad \varepsilon_{13} = \frac{\partial u_3}{\partial r} + \frac{\partial u_1}{\partial z}, \quad (5)$$
$$\varepsilon_{23} = r\frac{\partial u_2}{\partial z} + \frac{1}{r}\frac{\partial u_3}{\partial \varphi}.$$

2.3. Polar coordinate system

We consider the polar orthogonal coordinate system: $\alpha_1 = r$, $\alpha_2 = \varphi$, $\alpha_3 = z$. The Lame parameters are: $H_1 = 1, H_2 = r, H_3 = 1$.

A plane deformation state is assumed, and the body points are displaced in planes perpendicular to the *OZ* axis:

$$u_1 = u_1(\alpha_1, \alpha_2, 0),\ u_2 = u_2(\alpha_1, \alpha_2, 0),\ u_3(\alpha_1, \alpha_2, 0) = 0, \quad (6)$$

then, for e_{ij} in the form (2), the following holds: $e_{13} = e_{31} = 0, e_{23} = e_{32} = 0, e_{33} = 0$, $e_{33} = 0$,

The deformations and generalized stresses take the following form:

$$\varepsilon_{33} = 0,\ \varepsilon_{13} = \varepsilon_{31} = 0,\ \varepsilon_{23} = \varepsilon_{32} = 0$$
$$\sigma_{13}^* = \sigma_{31}^* = 0,\quad \sigma_{23}^* = \sigma_{32}^* = 0. \quad (7)$$

In the polar coordinate system, the deformations through displacements are recorded as:

$$\varepsilon_{11} = \frac{\partial u_1}{\partial r} + \frac{1}{2}\left[\left(\frac{\partial u_1}{\partial r}\right)^2 + \left(\frac{\partial u_2}{\partial r}\right)^2\right],$$

$$\varepsilon_{22} = \frac{1}{r}\frac{\partial u_2}{\partial \varphi} + \frac{u_1}{r} + \frac{1}{2}\left[\left(\frac{1}{r}\frac{\partial u_2}{\partial \varphi} + \frac{u_1}{r}\right)^2 + \left(\frac{1}{r}\frac{\partial u_1}{\partial \varphi} - \frac{u_2}{r}\right)^2\right], \quad (8)$$

$$\varepsilon_{12} = \frac{\partial u_2}{\partial r} - \frac{u_2}{r} + \frac{1}{r}\frac{\partial u_1}{\partial \varphi} + \frac{\partial u_1}{\partial r}\left(\frac{1}{r}\frac{\partial u_1}{\partial \varphi} - \frac{u_2}{r}\right) + \frac{\partial u_2}{\partial r}\left(\frac{1}{r}\frac{\partial u_2}{\partial \varphi} + \frac{u_1}{r}\right).$$

The resulting deformations (8) contain expressions for the case of small deformations:

$$\varepsilon_{11}=\frac{\partial u_1}{\partial r},\quad \varepsilon_{22}=\frac{1}{r}\frac{\partial u_2}{\partial \varphi}+\frac{u_1}{r},$$
$$\varepsilon_{12}=\frac{\partial u_2}{\partial r}-\frac{u_2}{r}+\frac{1}{r}\frac{\partial u_1}{\partial \varphi}$$

2.4. Relations between nonlinear strains and generalized stresses

We assume, according to [1, 2], the same form of recording the dependences between invariants of tensors and deviators of strains and stresses in geometrically linear media and the form of recording the dependences for invariants of tensors and deviators of nonlinear strains and generalized stresses in nonlinear media. The overall form of the nonlinear strain tensor:

$$T_\varepsilon=\begin{pmatrix}\varepsilon_{11} & \varepsilon_{12} & \varepsilon_{13}\\ \varepsilon_{21} & \varepsilon_{22} & \varepsilon_{23}\\ \varepsilon_{31} & \varepsilon_{32} & \varepsilon_{33}\end{pmatrix}, \qquad (9)$$

where ε_{ij} are nonlinear strains in the curvilinear orthogonal coordinate system in the form (3) or nonlinear strains in the cylindrical (4) or polar (8) coordinate systems. The generalized stress tensor corresponding to the tensor T_ε is recorded as follows:

$$T_{\sigma^*}=\begin{pmatrix}\sigma^*_{11} & \sigma^*_{12} & \sigma^*_{13}\\ \sigma^*_{21} & \sigma^*_{22} & \sigma^*_{23}\\ \sigma^*_{31} & \sigma^*_{32} & \sigma^*_{33}\end{pmatrix} \qquad (10)$$

We assume [7, 4, 16] the measure of deviation of isotropic material from the similarity principle for stress and strain deviators (deviator similarity phase) equal to zero: $\omega^*=0$.

For a geometrically linear continuous medium, the relations for the stress and strain invariants are recorded as follows:

$$\sigma=3K(\varepsilon,\Gamma)\cdot\varepsilon,\ T=3G(\varepsilon,\Gamma)\cdot\Gamma$$

For a geometrically nonlinear continuous medium, the relations for the stress and strain invariants are recorded as follows:

$$\sigma^*=3K^*(\varepsilon,\Gamma^*)\cdot\varepsilon,\ T^*=3G^*(\varepsilon,\Gamma^*)\cdot\Gamma^*,$$

where ε is the first invariant of the nonlinear strain tensor (9), σ^* is the first invariant of the generalized stress tensor T_{σ^*} (10), T^* is the intensity of generalized shear stresses proportional to the second invariant of the generalized stress deviator, Γ^* is the intensity of nonlinear shear strains proportional to the second invariant of the strain deviator. The error in applying the similarity of the forms for recording the relations between stresses and strains depends on the adopted continuum model, the type of the stress-strain state, and the level of deformation development in the continuum.

Invariants K^*,G^*,ω^* characterize the mechanical properties of the isotropic material. The value K^* is referred to as the generalized volume expansion modulus; it characterizes the measure of resistance of the isotropic material to volume changes. G^* is the generalized shear modulus.

The physical relations for the plane deformation state of the body [12] are recorded in the following form:

$$\sigma^*_{ij}=2G^*\tilde{\gamma}_{ij}+\frac{1}{3}\sigma^*\delta_{ij},\qquad \tilde{\gamma}_{ij}=\gamma_{ij}-\frac{1}{3}\varepsilon\delta_{ij}, \qquad (11)$$

where $\varepsilon=\varepsilon_{11}+\varepsilon_{22}+\varepsilon_{33}=\varepsilon_{11}+\varepsilon_{22}$ is the first invariant of the nonlinear strain tensor in the form (9).

Let us record the expressions for the components of the strain tensor deviator $\tilde{\gamma}_{ij},i,j=1,2,3$:

$$\tilde{\gamma}_{11} = \varepsilon_{11} - \frac{1}{3}\varepsilon,\ \tilde{\gamma}_{22} = \varepsilon_{22} - \frac{1}{3}\varepsilon,$$
$$\tilde{\gamma}_{33} = \varepsilon_{33} - \frac{1}{3}\varepsilon = -\frac{1}{3}(\varepsilon_{11} + \varepsilon_{22}),$$
$$\tilde{\gamma}_{13} = \tilde{\gamma}_{31} = \frac{1}{2}\varepsilon_{13} = \frac{1}{2}\varepsilon_{31} = 0, \quad (12)$$
$$\tilde{\gamma}_{23} = \tilde{\gamma}_{32} = \frac{1}{2}\varepsilon_{23} = \frac{1}{2}\varepsilon_{32} = 0,$$
$$\tilde{\gamma}_{12} = \tilde{\gamma}_{12} = \frac{1}{2}\varepsilon_{12} = \frac{1}{2}\varepsilon_{21}.$$

The expressions for the generalized stresses given (12) are recorded as follows:

$$\sigma^*_{11} = 2G^*(\varepsilon,\Gamma)(\varepsilon_{11} - \frac{1}{3}\varepsilon) + \frac{1}{3}\sigma^*,$$
$$\sigma^*_{22} = 2G^*(\varepsilon,\Gamma)(\varepsilon_{22} - \frac{1}{3}\varepsilon) + \frac{1}{3}\sigma^*,$$
$$\sigma^*_{33} = 2G^*(\varepsilon,\Gamma)[-\frac{1}{3}(\varepsilon_{11} + \varepsilon_{22}) + \frac{1}{3}\sigma^*, \quad (13)$$
$$\sigma^*_{23} = 2G^*\tilde{\gamma}_{23} = 0,\ \sigma^*_{13} = 2G^*\tilde{\gamma}_{13} = 0,$$
$$\sigma^*_{12} = \sigma^*_{21} = 2G^*\tilde{\gamma}_{12} = G^*(\varepsilon,\Gamma)\varepsilon_{12},$$

where $\sigma^* = \sigma^*{}_{11} + \sigma^*{}_{22} + \sigma^*{}_{33}$ is the first invariant of generalized stresses.
Given the generalized modulus in the form:

$$K^*(\varepsilon,\Gamma) = \frac{1}{3}\frac{\sigma^*}{\varepsilon},$$

the physical relations for the generalized stresses in a geometrically nonlinear continuum are recorded as

$$\sigma^*_{11} = 2G^*(\varepsilon,\Gamma)(\varepsilon_{11} - \frac{1}{3}\varepsilon) + K^*(\varepsilon,\Gamma)\,\varepsilon,$$
$$\sigma^*_{22} = 2G^*(\varepsilon,\Gamma)(\varepsilon_{22} - \frac{1}{3}\varepsilon) + K^*(\varepsilon,\Gamma)\,\varepsilon,$$
$$\sigma^*_{33} = [K^*(\varepsilon,\Gamma) - \frac{2}{3}G^*(\varepsilon,\Gamma)]\,\varepsilon, \quad (14)$$
$$\sigma^*_{12} = \sigma^*_{21} = G^*(\varepsilon,\Gamma)\,\varepsilon_{12}.$$

Here, $\sigma^* = \sigma^*{}_{11} + \sigma^*{}_{22} + \sigma^*{}_{33}$ is the first invariant of generalized stresses tensor (10), $\varepsilon = \varepsilon_{11} + \varepsilon_{22}$ is the first invariant of the nonlinear strain tensor (9), the generalized mechanical properties $K^*(\varepsilon,\Gamma), G^*(\varepsilon,\Gamma)$ that depend on the first invariant of the nonlinear strain tensor ε and the nonlinear shear strain intensity:

$$\Gamma = \sqrt{\frac{2}{3}}\sqrt{(\varepsilon_{11} - \varepsilon_{22})^2 + \varepsilon_{11}^2 + \varepsilon_{22}^2 + \frac{2}{3}\varepsilon_{12}^2}.$$

The expressions for finite deformations (8) and generalized stresses (14) in the case of the plane deformation state of a nonlinear continuum were obtained for the formulation of the boundary value problem for continuum mechanics in consideration of geometric and physical nonlinearity.

RESULTS

The expressions for finite deformations (4) in the cylindrical coordinate system are obtained, the expressions for finite deformations (8) for the case of plane deformation in the polar coordinate system are obtained, and the relations between finite deformations and generalized stresses (14) in the polar coordinate system are recorded.

DISCUSSION

The deformation expressions (5) for small deformations in the polar coordinate system are obtained by examining the displacements of the minor area element $r\,dr\,d\varphi$. The application of the classical approach for obtaining expressions of finite deformations is complicated by taking into account the rotation of the element, including the radial displacements of points *M*

and N prior to deformation to points M^* and N^* post-deformation.

The known relations for finite deformations in Cartesian coordinate system are also difficult to translate into the polar coordinate system. When considering the displacement field, the displacement vector is projected to the axes of the local trihedron plotted at the point M of application of the displacement vector $\vec{u} = u_1\vec{k}_1 + u_2\vec{k}_2 + u_1\vec{k}_3$, $\vec{k}_i$ are the coordinate axis orthodes. The direction of vectors $\vec{k}_i$ changes when passing from point to point, so the projections on these axes change. The derivatives $\frac{\partial \vec{k}_i}{\partial \alpha_i}$ form a vector field. The differentiation rule valid for the Cartesian coordinate system is violated: the projection of the vector derivative on the coordinate α_i is equal to the derivative of its projection on this coordinate. Therefore, the orthogonal curvilinear coordinate system is used to derive expressions of finite deformations. The generalized stresses differ from the real ones by accounting for the change in the areas of the faces of the oblique parallelepiped during the deformation.

CONCLUSIONS

The expressions for nonlinear deformations (8) and generalized stresses (14) in the case of the plane deformation state of a nonlinear continuum were obtained for the formulation of the boundary value problem for continuum mechanics in consideration of geometric and physical nonlinearity.

REFERENCES

1. **Novozhilov V.V.** Elasticity Theory. Sudpromgiz, 1958. – 370 p.
2. **Rabotnov Yu.N.** Mechanics of Deformable Solids. Moscow: Nauka, 1979. – 744 p.
3. **Sedov L.I.** Continuum Mechanics: In 2 volumes. Moscow: Lan. V.1. 2004. – 528 p. V.2. 2004. – 560 p.
4. **Bakushev S.V.** Geometrically and Physically Nonlinear Continuum Mechanics: The Plane Problem. Moscow: LIBROKOM Book House, 2013. – 321 p.
5. **Leibenzon L.S.** Elasticity Theory Course. Moscow – L-d. 1947. – 464 p.
6. **Amenzade Yu.A.** Elasticity Theory. Moscow: Higher School, 1976. – 272 p.
7. **Lure A.I.** Elasticity Theory. Moscow: Nauka. 1970. – 940 p.
8. **Aksentjan O. K.** Features of the stress-strain state of the plate in the neighborhood of the edge. Applied Mathematics and Mechanics, 1967, volume 31, issue 1, pp. 178-186
9. **Parton V. Z. and Perlin P. I.** Methods of the mathematical theory of elasticity. Moscow: Nauka. 1981. – 688 p.
10. **Kondratyev V. A.** Boundary value problems for elliptic equations in domains with conical or corner points. Transactions of the Moscow Mathematical Society. Moscow: MSU. 1967. vol 16, pp. 209–292
11. **Cherepanov G. P.** Mechanics of brittle failure. Moscow: Nauka. 1974. – 640 p.
12. **Timoshenko S. P., Goodier Jn.** Theory of elasticity. Moscow: Nauka. 1975. –576 p.
13. **Razumovsky I. A.** Interference-optical Methods of Solid Mechanics, Moscow: Bauman MSTU, 2007. – 240 p.
14. **Frishter L.**: Photoelasticity-based study of stress-strain state in the area of the plain domain boundary cut-out area vertex. Advances in Intelligent Systems and Computing, vol 692. Springer, Cham 836-844 (2017) https://doi.org/10.1007/978-3-319-70987-1_89
15. **L. Frishter** The stress intensity factors in the corner cut-out area of the plane domain boundary, IOP Publishing FORM 2018, IOP Con. Ser.: Mat. Sci. Eng.365(2018) 042020, https://doi.org/10.1088/1757-899X/365/4/
16. **Bakushev S.V.** Resolving equations of plane deformation of geometrically nonlinear continuous medium in Cartesian coordinates

// Izvestiya VUZov. Construction. – 1998. № 6. p. 31-35

СПИСОК ЛИТЕРАТУРЫ

1. **Новожилов В.В.** Теория упругости. Судпромгиз. 1958. – 370 с.
2. **Работнов Ю.Н.** Механика деформируемого твердого тела. – М.: Наука.1979. – 744 с.
3. **Седов Л.И.** Механика сплошной среды: В 2-х т. М.: Лань. Т.1. 2004. –528 с. Т.2. 2004. – 560 с.
4. **Бакушев С.В.** Геометрически и физически нелинейная механика сплошной среды: Плоская задача. М.: Книжный дом «ЛИБРОКОМ», 2013. – 321с.
5. **Лейбензон Л.С.** Курс теории упругости. М.–Л-д. 1947. – 464 с.
6. **Аменздаде Ю.А.** Теория упругости. М.: Высшая школа, 1976. – 272с.
7. **Лурье А.И.** Теория упругости. М.: Наука. 1970. – 940 с.
8. **Аксентян О.К.** Особенности напряженно-деформированного состояния плиты в окрестности ребра. – ПММ, 1967, т.31, вып. 1, с. 178-186
9. **Партон В.З., Перлин П.И.** Методы математической упругости. М.: Наука. 1981. – 688 с.
10. **Кондратьев В. А.** Краевые задачи для эллиптических уравнений в областях с коническими или угловыми точками, Труды Московского математического общества – М.: МГУ, 1967, т. 16, с. 209–292.
11. **Черепанов Г. П.** Механика хрупкого разрушения. М.: Наука, 1974.– 640 с.
12. **Тимошенко. С.П., Гудьер Дж.** Теория упругости. М.: Наука. 1979, –560 с.
13. **Разумовский И.А.** Интерференционно-оптические методы механики деформируемого твердого тела. М.: Изд-во МГТУ им. Н.Э. Баумана, 2007. – 240 с.
14. **Frishter L.**: Photoelasticity-based study of stress-strain state in the area of the plain domain boundary cut-out area vertex. Advances in Intelligent Systems and Computing, vol 692. Springer, Cham 836-844 (2017) https://doi.org/10.1007/978-3-319-70987-1_89
15. **L. Frishter**, The stress intensity factors in the corner cut-out area of the plane domain boundary, IOP Publishing FORM 2018, IOP Con. Ser.: Mat. Sci. Eng.365(2018) 042020, https://doi.org/10.1088/1757-899X/365/4/
16. **Бакушев С.В.** Разрешающие уравнения плоской деформации геометрически нелинейной сплошной среды в декартовых координатах // Известия ВУЗов. Строительство.1998. № 6. с.31-35.

Lyudmila Yurievna Frishter, Professor, Department of Higher Mathematics, Doctor of Engineering Sciences, Senior Researcher, Associate Professor, National Research Moscow State University of Civil Engineering, 26 Yaroslavskoe Highway, 129337 Moscow, Russia, e-mail: lfrishter@mail.ru, tel.8(495)183 30 38

Фриштер Людмила Юрьевна, профессор кафедры высшей математики, доктор технических наук, старший научный сотрудник, доцент, Национальный исследовательский Московский государственный строительный университет, дом 26, Ярославское шоссе, г. Москва, 129337, Россия, e-mail: lfrishter@mail.ru, 8(495)183 30 38